Germanite derivative materials : synthesis, crystallographic structure from multi-scale characterizations and thermoelectric properties

Laura Paradis Fortin

Normandie Université

THÈSE

Pour obtenir le diplôme de doctorat

Spécialité CHIMIE

Préparée au sein de l'Université de Caen Normandie

Germanite derivative materials: synthesis, crystallographic structure from multi-scale characterizations and thermoelectric properties

Présentée et soutenue par
Laura PARADIS FORTIN

Thèse soutenue publiquement le 16/12/2019 devant le jury composé de		
M. CHRISTOPHE CANDOLFI	Maître de conférences HDR, Université Nancy 1 Henri Poincaré	Rapporteur du jury
M. LAURENT CARIO	Directeur de recherche au CNRS, Université de Nantes	Rapporteur du jury
M. PHILIPPE BOULLAY	Directeur de recherche au CNRS, ENSICAEN	Président du jury
Mme LAETITIA LAVERSENNE	Chargé de recherche au CNRS, Université Grenoble Alpes	Membre du jury
M. PIERRIC LEMOINE	Chargé de recherche au CNRS, Université Rennes 1	Membre du jury
M. CARMELO PRESTIPINO	Chargé de recherche au CNRS, Université Rennes 1	Membre du jury

Thèse dirigée par EMMANUEL GUILMEAU et STÉPHANE CORDIER, Laboratoire de cristallographie et sciences des materiaux (Caen)

UNIVERSITÉ CAEN NORMANDIE

ENSI CAEN
ÉCOLE PUBLIQUE D'INGÉNIEURS
CENTRE DE RECHERCHE

ED 591 PSIME

RISM

"It is better to fail in originality
than to succeed in imitation."
- Herman Melville

ACKNOWLEDGMENT

Ce travail a été réalisé en collaboration entre l'Institut des Sciences Chimiques de Rennes (ISCR – UMR CNRS 6226) à Rennes et le laboratoire CRISMAT à Caen (CRISMAT – UMR CNRS 6508). Ainsi je remercie M. Marc Fourmigué directeur de l'ISCR ainsi que M. Wilfrid Prellier directeur du laboratoire CRISMAT pour m'avoir accueillie dans leurs établissements respectifs. Je tiens à remercier M. Philippe Boullay d'avoir présidé le jury de thèse ainsi que M. Christophe Candolfi et M. Laurent Cario, pour m'avoir fait l'honneur d'accepter d'être les rapporteurs de cette thèse. J'adresse ma gratitude à Mme Laetitia Laversenne pour avoir examiné mon travail. J'adresse également toute ma gratitude à M. Carmelo Prestipino pour avoir fait partie de mon jury mais également pour son investissement dans l'encadrement de ma thèse, sans lequel je ne serais jamais parvenue à une telle profondeur en analyse structurale. Je garderai un bon souvenir de nos discussions lors de notre séjour au synchrotron ainsi que du match de rugby où la France a mis une raclée à l'Italie!

Je remercie sincèrement M. Emmanuel Guilmeau mon directeur de thèse, dont l'encadrement d'une qualité aussi scientifique et professionnelle qu'humaine m'a beaucoup appris et fut un atout majeur dans le bon déroulement de ces trois années. Je lui suis aussi redevante de ne m'avoir jamais abandonné dans mon cheminement pour parfaire ma culture du vin et ce malgré les quelques balles courbes que je lui ai lancé telles que celle du hot-dog et de la sardine. J'exprime également toute ma reconnaissance à mon co-encadrant de thèse, M. Pierric Lemoine, dont l'investissement et la disponibilité ont toujours été sans faille. Il a su me transmettre sa passion de la cristallographie et des neutrons. Merci aussi pour tous ces bons moments partagés autour de petites mousses! Je tiens aussi à remercier tout spécialement M. Stéphane Cordier d'avoir accepté d'être co-directeur de cette thèse. Avoir eu l'opportunité de travailler sous la direction de ces trois encadrants, qui furent pour moi à la fois collègues et mentors et dont la compétence scientifique est toujours accompagnée d'une grande gentillesse, est une chance incroyable que je souhaite à de nombreux futurs doctorants.

J'exprime ma reconnaissance à tous les membres de l'équipe Chimie du Solide et des Matériaux de l'ISCR particulièrement à ceux qui m'ont directement apporté leur aide, Valérie(s), Stéphanie, Nathalie, Véronique, Mona, Thierry, Vincent, Christophe, Francis, Loïc, Noée, Serge, Yann, Maria, Corentin, Soumayah, Patrick, Tatiana et Henry. Je remercie particulièrement Mathieu Pasturel d'avoir passé mon c.v. à son voisin d'en face. C'est la tête haute que je remercie mes vaillants compatriotes de thèse: Sam Moutarde, Maxou, Sylvano et Barth. Ce fut un réel honneur de thèser à vos côtés et parfois je me dis que si nous n'avions pas été là les un pour les autres… on aurait été de bien meilleur thésard! Merci 1000 fois d'avoir fait vivre la folie des gintos et surtout d'avoir été voir si le cactus était ouvert… Je ne manquerais pas de remercier aussi mon institution favorite : le Black Bear. Merci à Sophie et Clément pour les nombreuses pintes, shots exotiques et gintos servis!

J'adresse un grand merci à tous les membres de l'étage au CNRT, Christelle(s), Christophe(s), Sylvain, Charles, Solange, Jacques, Anthony, Moussa, Pavan, David, Gratien et Éric avec qui j'ai eu l'honneur de pouvoir créer une amitié pour tous les moments inoubliables que l'on a vécus ensemble. Je tiens particulièrement à remercier Jéjé pour son aide quotidienne dans les manips et pour fortement contribuer au fait que les salles de manips soient des plus propres, organisées et qu'il soit toujours agréable d'y travailler. Je remercie sincèrement Christelle pour nos petites sessions MEB que je trouve fortes agréables. Merci à Gabin, mon papi grincheux préféré avec qui nous gardons jalousement le meilleur bureau de l'étage (héhé), pour ces bières et whisky partagés et accessoirement merci de répondre à mes interrogations sur la thermoélectricité. Je tiens à remercier mon cher Cricri d'avoir co-parenté des plants de tomates avec moi ainsi que pour nos matins karaoké! Je suis reconnaissante d'avoir trouvé un ami en Guillaume Riquet dans cette épreuve qu'est la rédaction. Tu es un excellent compagnon pour se plaindre et comploter. Je remercie tous les doctorants du CRISMAT-CNRT, Cédric, Jean-Baptiste, Abdel, Tristan, Raphaël, Stas, Marie, Toinou, Félicien, Barbara (future), Justine, Audric, Aïmane, Adam, Chris, Hugo pour les repas toujours animés et amusants et les V&B encore plus animés. J'aurais des anecdotes cocasses à raconter avec vous tous mais je ne veux pas dépasser les 300 pages!

Enfin, j'adresse mes remerciements à maman et papa, Martin mon beau-papa, mes frères et sœurs Guillaum, Éli et Gallilée, mes tantes et oncles adorés ainsi que mes cousin(e)s et à mes amis de Val-d'Or et Sherbrooke, pour leur soutien inébranlable dans cette très difficile décision que fut de faire un doctorat de l'autre côté de l'Atlantique. Aussi je remercie ma belle-famille, Martine, Jean-Pierre, Marine, Ronan, Jean, Hélène qui m'ont fait sentir bien entourée. Finalement, je remercie mon chéri Vincent qui a durement gagné sa place dans cette section. C'est un peu grâce à lui qu'a germé dans ma tête l'idée de venir en France.

GENERAL INTRODUCTION

In front of the social-environmental stakes instigated by the ever growing demand in energy, drastic changes in energy management are to be expected. Indeed, the increase of the population (9.2 billion in 2040) together with the abrupt growth of energy-intensive sectors such as IT (multiplication of servers) and the automobile (individualisation of the transport) will be responsible for an escalation in energy demand estimated at 30 % between 2015 and 2040 according to the International Energy Agency (IEA).[1] This temperature anomaly of + 2 °C suggests that we must reduce our consumption of fossil fuels. In this context, in December 2015, the delegations present at COP21 in Paris pledged to undertake important measures to limit the rise in global temperature to less than 2 °C at the end of the century. This ambitious goal can only be achieved through drastic changes, such as the significant shift from fossil energy sources to different forms of renewable energy (solar, wind, biomass, tidal stream, geothermal, *etc* ...) along with the creation of local waste recovery systems.

Governments, industrials and individuals of the world today look forward in taking profit of the opportunities created in the recent decades to replace petroleum-derived materials with alternatives renewable energy sources, which include: biofuel, solar energy, mechanical energy (wind, ocean and piezoelectricity) and thermoelectricity. Among renewable energy technologies, thermoelectricity is attracting more and more attention because of the capability of producing electricity with no moving part, and the potential of harvesting wasted energy. Indeed, a substantial quantity of energy vanishes through heat dissipation, water cooling system, lubricant and exhaust gas.[2] Hence, thermoelectric devices can either be used to gather this industrial waste-heat or to harvest natural energy like sunlight heat.[3,4]

However, current devices have relatively low conversion efficiencies, *e.g.* below 10 %, and are very often made up of expensive, rare and/or toxic elements. As a result, they remain in niche markets, *e.g.* aerospace, isolated telecommunication equipment, *etc*.... In order to use thermoelectricity on a larger scale to meet the environmental, economic and social issues outlined earlier, it is

required to quickly create new high performance TE materials. For this, new concepts, integrating the need for electrical resistivity and low thermal conductivity, have led to remarkable advances in thermoelectricity. Two main paths have been explored: the search for materials with complex structure (κ intrinsically low) on the one hand, and the use of nanostructures (quantum well, nanowires, nanograins, thin layers), on the other hand.

This thesis stems from a collaboration between the Institut des Sciences Chimiques de Rennes (ISCR) and the Laboratoire de CRIstallographie et Science des MATériaux (CRISMAT) in Caen. The material studied during this thesis is the synthetic $Cu_{22}Fe_8Ge_4S_{32}$, a derivative of the natural germanite mineral, $Cu_{26}Fe_4Ge_4S_{32}$. Synthetic germanite $Cu_{22}Fe_8Ge_4S_{32}$ has the potential to be a performant TE material because of its isostructurality to colusite $Cu_{26}V_2M_6S_{32}$, which is at moment one of the best performant sulfide thermoelectrics due to is intrinsically low lattice thermal conductivity and relatively high power factor. Hence, this isostructurality entail the possibility that germanite share similar thermoelectric performances. The work in this manuscript addresses the synthesis of germanite compounds along with the characterization of structural and physicochemical properties, with the aim of evaluate and optimize the thermoelectric performance.

This document is composed of five chapters:

The first part gives an overview of the principles of thermoelectricity and the equations essential for the proper understanding of this work. The figure of merit, used to assess thermoelectric the performances of a material, is presented with the strategies to optimize it. Finally, a state of the art on the thermoelectric compounds currently available (*e.g.* telluride-based materials PbTe, GeTe or SnTe,) and on new thermoelectric compounds (not used in thermoelectric generators yet) is made, with a particular attention to the sulfide family.

The mastery of the synthesis conditions for the production of single-phase samples is capital prior to initiate structural and physical characterizations. Thus, in this chapter, the particular synthesis conditions to yield a ‘‘pure’’ germanite

sample by sealed tube are investigated by the means of *in situ* reactions. Also, a study of the phase stability/decomposition of germanite allowed an improved understanding of the TE properties behavior in temperature and acknowledges the workability of the material. Additionally, the influence of the synthesis and densification techniques on the structure, microstructure and thermoelectric properties of $Cu_{22}Fe_8Ge_4S_{32}$ are described through the comparison of two powder synthesis approaches, combined with two densification methods.

In parallel with this study, my work also focused on a Cu to Zn substitution in the germanite $Cu_{22-x}Zn_xFe_8Ge_4S_{32}$ ($0 \leq x \leq 2$) series, synthesized for the first time with the aim to modify the carrier concentration as it was reported in colusite and tetrahedrite.[5,6] Moreover, this substitution is going toward the natural stoichiometry of renierite $Cu_{20}Zn_2Fe_8Ge_4S_{32}$, which crystallizes in $P\bar{4}2c$, the direct tetragonal deformation of germanite $P\bar{4}3n$. The change in composition could introduce structural disorder, thus reducing the thermal lattice conductivity. Second, an isovalent substitution of Ge by Sn in the $Cu_{22}Fe_8Ge_{4-x}Sn_xS_{32}$ ($0 \leq x \leq 4$) series was investigated with the aim to reduce the lattice thermal conductivity by the creation of cationic disorder by alloying effect. Hence, the focus of this chapter is to address the influence of two types of cationic substitution (isovalent and aliovalent) on the structure along with their impact on the thermoelectric properties.

The exploration of different approaches to improve the thermoelectric properties of germanite, *e.g.* optimizing the process conditions and modifying the chemical composition, stimulated our interest to elucidate a crystal structure model for synthetic germanite, since the one for natural germanite is not applicable. Furthermore, the absence of structural model precludes us from a deep understanding of the transport properties, and consequently from a potential improvement of the thermoelectric properties. Actually, the low chemical contrast of the Cu^{1+}, Ge^{4+} and Fe^{3+} cations for both neutron and X-ray diffraction, coupled with the complex structure arrangement, hinders the structural resolution of germanite by conventional techniques. To the best of our knowledge, resonant

scattering (also known as anomalous scattering) is the only probe that allow a high chemical contrast in the case of germanite. Therefore, the fourth part of this manuscript reports a new structural model for synthetic germanite together with the path followed to determine the cationic distribution of the Cu, Ge and Fe on the five crystallographic sites of germanite.

The last part of this thesis proposes a brief summary of the results obtained for each optimization work on germanite. This conclusion will also provide some perspectives to this work. Finally, a last chapter summarizes all of the experimental techniques and conditions.

TABLE OF CONTENT

1 ASSESSMENT OF THE FUNDAMENTALS OF THERMOELECTRICITY

1.1 Preface

This first chapter aims to introduce thermoelectricity by establishing the foundation imperative to apprehend the work accomplished in the course of this thesis. For that purpose, the milestones that led to the discovery of thermoelectric effects will be related in a chronological fashion. This narration will include the description of the mathematical equations that certify a better grasp of the physical laws that rules the thermoelectric conversion phenomenon. This description will reveal the different intrinsic characteristics that dictate the thermoelectric performances of a material. The equations will allow a qualitative comprehension of the influence of each parameter on the figure of merit as well was their interdependency. Thereafter, the criteria adopted to select a thermoelectric material will be enumerated together with the strategies to optimize the performances. Finally, the last section of this chapter will be a non-exhaustive state of the art on the conventional and new thermoelectric materials, with a special focus on sulfides. This will settle the framework of this thesis.

1.2 Environmental crisis

The vast majority of scientists attribute the rise in temperature over the last 150 years to human activity.[7] This temperature anomaly of + 2 °C suggests that we must reduce our consumption of fossil fuels. Approximately 93 % of the additional heat associated to global warming is stored in the ocean and recent discoveries showed that the enhanced heat storage in the subsurface ocean contributed to the global surface warming outbreak.[8–10] The rising of the sea level is a direct consequence of the warming of the oceans, with an average increase of 23 cm since 1880 with about height of those centimeters gained in the last 25 years.[11] Every year, the sea rises another 3.3 mm and the rate is accelerating with the average temperature inflation. Figure 1.1 is an alluring infographic on the impact of the sea level rising on costal major cities.

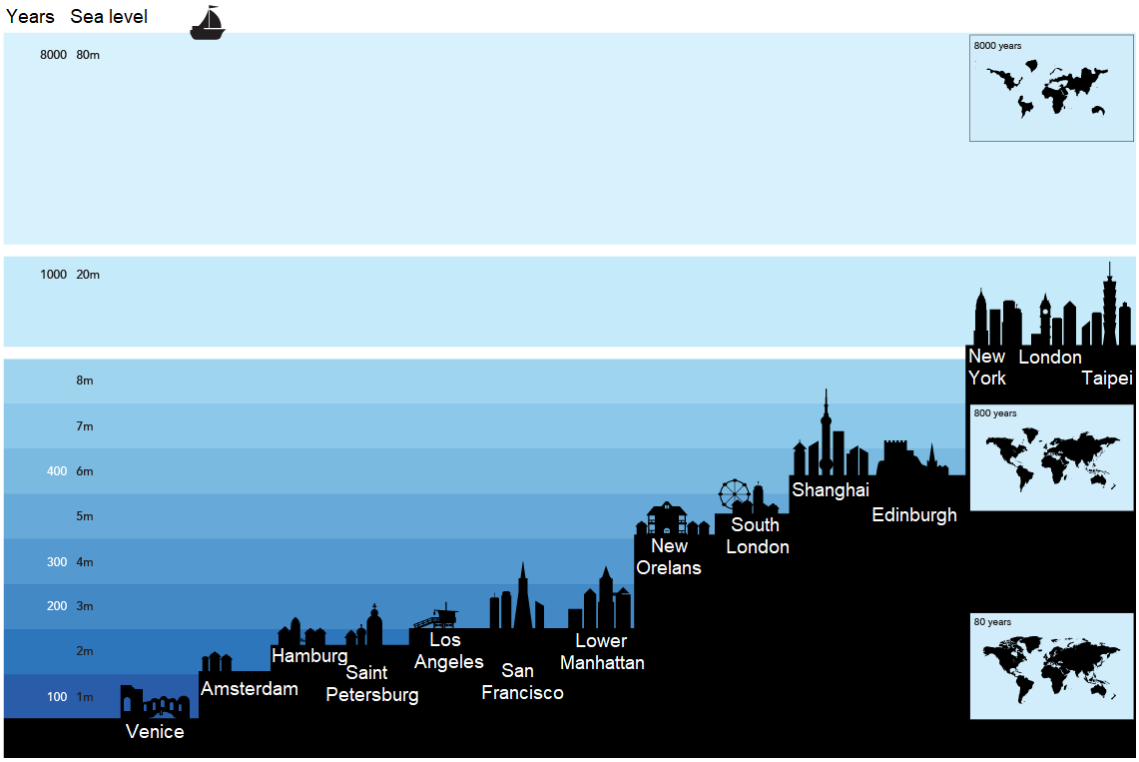

Figure 1.1. Illustration of the Sea level rising over the year relatively to some major cities level.[12]

Nonetheless, consciences have been raised and resolutions are taken accordingly. For instance a set of sustainable development goal (SDGs) was launched to serve as guidelines to the climate changes combat.[13,14] Under these circumstances, it is imperative to find sustainable and viable alternative energy sources that support the dashing advancement of economy, industry, and technology.

1.2.1 Sustainable energy

Research of alternate sources of energy can be traced back to the late 90's with the price hiking of the oil barrel.[15] Scientific literature is unequivocal that replacing fossil fuel-based energy sources with renewable energy sources would gradually help the world to achieve the idea of sustainability. Governments, industrials and individuals of the world today look forward in taking profit of the opportunities created in the recent decades to replace petroleum-derived materials with alternatives renewable energy sources, which include: biofuel, solar energy, mechanical energy (wind, ocean and piezoelectricity) and thermoelectricity. Among all renewable energy technologies, photovoltaic and thermoelectric are attracting more and more attention because of the capability of producing electricity with no moving part, and the potential of harvesting wasted energy. Indeed, a substantial quantity of energy vanishes through heat dissipation, water cooling system, lubricant and exhaust gas.[2] Hence, thermoelectric devices can either be used to gather this industrial waste-heat or to harvest natural energy like sunlight heat.[3,4]

1.3 Historic and fundamental principles of thermoelectricity

1.3.1 Seebeck effect

In the course of the XIXth century, three great discoveries allowed to set the base of thermoelectricity. The earliest one occurred in 1821, thanks to the work of Thomas Johan Seebeck (1770 - 1831) a German physicist. He found that a circuit made from two dissimilar metals with junctions at different temperatures would deflect a compass magnet.[16] Confronted to this new observation, he thought he was witnessing a thermomagnetic phenomenon (generation of a magnetic field by a temperature difference), but in reality he characterized the first thermoelectric manifestation of history. However, it was years later that a legitimate explanation of this experiment was given by Hans Christian Orsted: the imposed temperature variation has caused a potential difference, giving rise to the magnetic field that has been evidenced by the needle alignment.[17] This set the first fundamental relation of thermoelectricity known as Seebeck effect.

The Seebeck effect describes how a homogenous, conductor and isotropic material generates spontaneously an electrical current when contrived to a temperature gradient. In fact, as the charge carrier (electrons or holes) average kinetic energy is higher on the hot side, its concentration is building up on the cold side and therefore generates a potential difference (ΔV) directly proportional to the temperature difference (ΔT). The magnitude of this temperature dependence is called the Seebeck coefficient (S) or thermopower .

$$S = \frac{\Delta V}{\Delta T} \qquad \textit{Equation 1-1}$$

Where S is the Seebeck coefficient (V K^{-1}), ΔV is the potential differential (V) and ΔT is the temperature differential (K). The Seebeck coefficient sign depends on the main charge carrier nature: it is negative if the main charge carriers are electrons and positive if they are holes.

The experimental determination of the Seebeck coefficient of a material is possible by the measurement of a potential difference over a known temperature difference. Additionally, it is mandatory to connect the material to an electrical circuit comprising a voltmeter. The measurement apparatus can be assimilated to two conducting materials A and B connected in series, representing respectively the studied sample and the measurement circuit (Figure 1.2). Since both materials are responsive to the Seebeck effect under a temperature variation, the measured electric tension is affected accordingly.[18] As a result, to determine the Seebeck coefficient of the studied sample A, it is imperative to know the Seebeck coefficient of the electric circuit B in order to subsidize its contribution. Thus, the relation can be express as:

$$\Delta V = (S_A - S_B)\,\Delta T \qquad \textit{Equation 1-2}$$

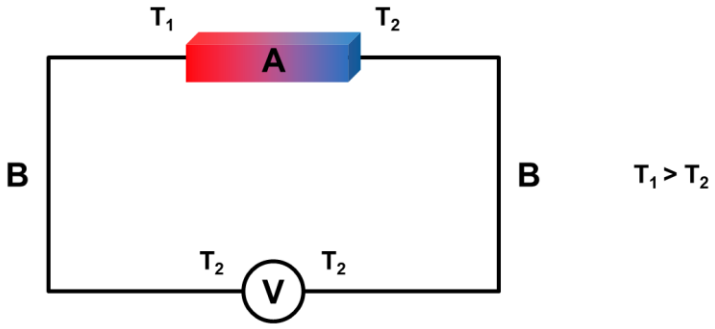

Figure 1.2. Scheme of the device to determine the Seebeck coefficient of material A.

1.3.2 Peltier effect

In 1834, the French physicist Jean Charles Athanase Peltier (1785 - 1845) observed a temperature gradient at the junction of two dissimilar materials crossed by an electric current.[19] This second thermoelectric effect, reciprocal to the Seebeck effect, is named Peltier effect.

To describe Peltier effect let's consider two homogenous, conductor and isotropic materials A and B, with Peltier coefficient $\pi_A > \pi_B$. The electric current flowing through the materials stimulates the charge carrier migration within the circuit. The current imposed direction creates charge carrier rich and poor areas. Each charge carrier hauls a certain amount of kinetic energy that can be dissipated through heat loss. So long as the electric current flow from A to B, a heat amount Q is dissipated at the materials junction. On the contrary, if the electric current flows from B to A, a heat amount is absorbed at the junction. Peltier effect is illustrated in Figure 1.3 and is defined by the following equation:

$$\pi_{AB} = (\pi_A - \pi_B) = \frac{Q}{I} \qquad \textit{Equation 1-3}$$

Where π_{AB} is the Peltier coefficient at A-B junction (V), Q the heat amount exchanged (W) and I the electric current strength (A).

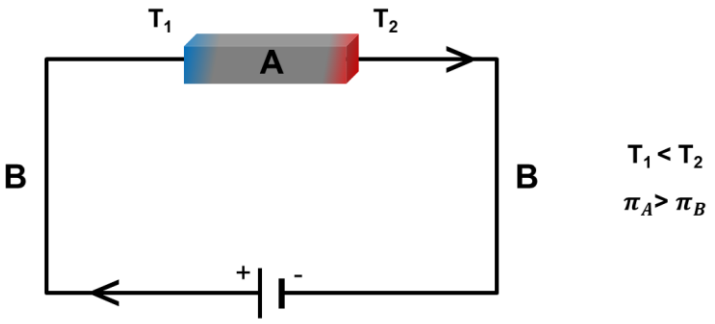

Figure 1.3. Schematic representation of the Peltier effect at an A-B materials junction.

1.3.3 Thomson effect

In some materials, the Seebeck coefficient is not steadily proportional to temperature, resulting in a gradient in the Seebeck coefficient. As long as a current is driven through this gradient, a continuous version of the Peltier effect occurs (Figure 1.4). This Thomson effect was predicted and subsequently observed in 1851 by Lord Kelvin (William Thomson (1824 - 1907)).[20] Equation 1-4

describes the heating or cooling of a current-carrying conductor with a temperature gradient.

$$\frac{dQ}{dx} = \tau J \frac{dT}{dx} \qquad \textit{Equation 1-4}$$

Where Q is the heat amount exchanged (W), τ the Thomson coefficient (V K^{-1}), J the current density (A m^{-2}) and x the spatial coordinate.

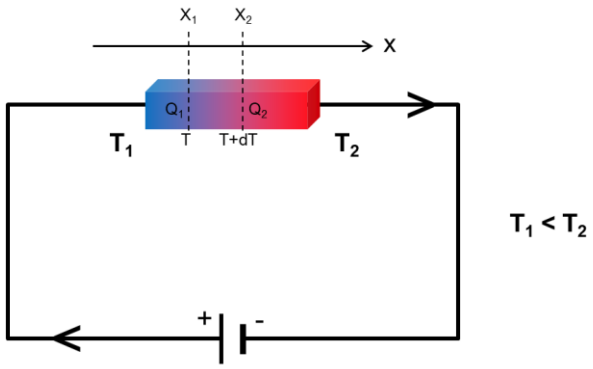

Figure 1.4. Schematic representation of the Thomson effect.

In contrast with the Seebeck and Peltier effects that involved a pair of material, Thomson effect concerns a lone material. Note that the three coefficients related to the Thomson effect are intrinsic properties of a material. Those three coefficients are put into proportional association by Lord Kelvin's relations:

$$\pi = S\,T \qquad \textit{Equation 1-5}$$

$$\tau = T\frac{dS}{dT} \qquad \textit{Equation 1-6}$$

The first equation sheds light of the reversibility between the Seebeck and Peltier effects, thus giving the opportunity to calculate the Peltier effect without the elaborate heat flux measurement that it necessitates.

1.4 Performance assessment of a thermoelectric material

1.4.1 Figure of merit

In order to appreciate and compare the thermoelectric performance of a material to another, it is crucial to have a magnitude that accommodates all the properties. Abram Fedorovich Ioffe (1880 - 1960) suggested in his work published in 1959 to evaluate the thermoelectric conversion efficiency with a dimensionless figure of merit ZT.[21,22] To this day, it is the most widely used magnitude to gauge a material thermoelectric performance and is defined as following:

$$ZT = \frac{S^2}{\rho\kappa}T = \frac{PF}{\kappa}T \qquad \textit{Equation 1-7}$$

Where T is the absolute temperature (K), S is the Seebeck coefficient or thermoelectric power (V K^{-1}), ρ is the electrical resistivity (Ω m), κ is the total thermal conductivity (W m^{-1} K^{-1}) and $PF = S^2/\rho$ the power factor (W m^{-1} K^{-2}).[23]

It is clear from the ZT equation that to attain the best performance, a material must have; (i) a high absolute Seebeck coefficient, translating the capacity of a material to generate a large electrical potential over a temperature gradient, (ii) a low electrical resistivity that enhances the charge carrier transport properties while keeping low heat loss by Joule effect and (iii) a low thermal conductivity that preserves the temperature gradient at the module junctions.

Nonetheless, those three parameters are not independent one from another and rely on shared electronic and structural features. The thermal conductivity, the Seebeck coefficient and the electrical resistivity are in close vicinity with the charge carrier concentration. In addition, the last two parameters are proportional to the charge carrier effective mass. Therefore, the three parameters act in an abortive way one to the others due to the common physical features they share.

A material with a ZT value above 1 is considered to be performant. For example, when using a material having a ZT of 1 with a T_H = 373 K and T_C = 273 K,

an efficiency of ~ 5 % is calculated. When the temperature of the hot region is increased to T_H = 773 K (*i.e.* increasing the temperature gradient) the thermoelectric efficiency increases up to ~ 15 % (Figure 1.5).

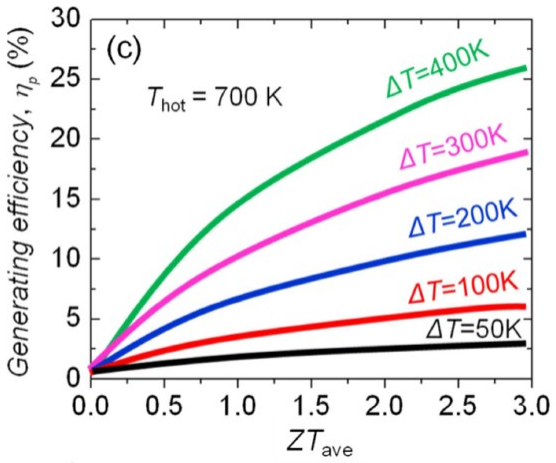

Figure 1.5. The energy conversion efficiency in (%) of a TE material as a function of its average ZT for various temperature differences.[24]

In order to better grasp the interdependency implications on the optimization of a material performance, it is crucial to acknowledge accurately each individual parameter involved in the figure of merit. Moreover, the exhaustive description of each parameter is going to be relevant to underline the main approaches to improve the *ZT*, as discussed in details in section 1.5.

1.4.2 Seebeck coefficient

For metals and degenerate semiconductors, the Seebeck coefficient can be expressed by the Pisarenko relation:[25]

$$S = \frac{8\pi^2 k_B^2}{3eh^2} m^* T \left(\frac{\pi}{3n}\right)^{2/3} \qquad \textit{Equation 1-8}$$

Where k_B is the Boltzmann constant (1.381×10^{-23} kg m^2 s^{-2} K^{-1}), e the elemental charge (1.602×10^{19} C), h is the Planck constant (6.626×10^{34} kg m^2 s^{-1}), n the charge carrier concentration (m^{-3}) and m^* the charge carriers effective mass (kg).

To conclude, a low charge carrier concentration (n) with a high effective mass ensures a high Seebeck coefficient. Also, there should only be one type of carrier. Mixed *n*-type and *p*-type conduction leads to both charge carriers moving to the cold end, cancelling out the induced Seebeck voltages.

1.4.3 Electrical resistivity

As the Seebeck coefficient, the electrical resistivity of a material is dependent of the charge carrier concentration and effective mass. However, electrical resistivity and Seebeck coefficient evolve contrariwise in relation to those constants. Thus, a small electrical resistivity implies a large charge carrier concentration and an inferior effective mass as described by the relations below:

$$\rho = \frac{1}{ne\mu} \qquad \textit{Equation 1-9}$$

$$\mu \; \alpha \; \frac{1}{m^*} \qquad \textit{Equation 1-10}$$

Where μ is the charge carrier mobility ($m^2\ V^{-1}\ s^{-1}$).

Considering those relations, it is apparent that the enhancement of both electrical resistivity and Seebeck coefficient is an arduous approach. Thus, depending on the nature of the compound, one is either seeking to increase the Seebeck coefficient (with an impairment of the electrical resistivity) or seeking for a low electrical resistivity (with prejudice to the Seebeck magnitude).

In pursuance of a better thermoelectric conversion rate, it is more reasonable to work on the power factor ($PF = \frac{S^2}{\rho}$). A large power factor allows to deliver a strong electrical power under the influence of a thermal gradient.

1.4.4 Thermal conductivity

Toward the achievement of high and enhanced thermoelectric properties, it is necessary for the material to have a thermal conductivity as low as possible. This condition assures the maintenance of a maximal temperature gradient between the junctions, thereby guaranteeing the generation of a strong potential difference by Seebeck effect.

The total thermal conductivity of a material is the sum of its electronic thermal conductivity (κ_e) and its lattice thermal conductivity (κ_L):

$$\kappa = \kappa_e + \kappa_L \qquad \textit{Equation 1-11}$$

By analogy to the kinetic theory of gases, the lattice thermal conductivity can be expressed by the relation:[23]

$$\kappa_L = \frac{1}{3} v_S C_p L_{ph} \qquad \textit{Equation 1-12}$$

where κ_L is the lattice thermal conductivity (W m^{-1} K^{-1}), v_S the sound velocity (m s^{-1}), C_p the lattice specific heat (J K^{-1} m^{-3}) and L_{ph} the phonon mean free path (m).

The electronic contribution arises from the heat hauled by the charge carriers. The former is inversely proportional to the electrical resistivity of the compound and can be estimated from the Wiedmann-Franz law:[26]

$$\kappa_e = \frac{LT}{\rho} \qquad \textit{Equation 1-13}$$

where κ_e is the electronic thermal conductivity (W m^{-1} K^{-1}) and L is the Lorenz number (W Ω K^{-2}).

In the case of a free electron gas, the Lorenz number can be defined as:

$$L = \frac{\pi^2 k_B^2}{3e^2} = 2.45 \times 10^{-8}\ W\ \Omega\ K^{-2} \qquad \textit{Equation 1-14}$$

This number particularly adapted to describe metals is widely used for the calculation of the electronic thermal conductivity. However, the equation is not suitable for semiconductors. Indeed, the Lorenz number is dependent of the diffusion process of the charge carriers at Fermi level. Typically, the compounds used in thermoelectricity present lower Lorenz number, *e.g.* 1.5×10^{-8} W Ω K^{-2}.[27]

For the length of this work, the Lorenz number was approximated from the Seebeck coefficients using the simplified relationship from Kim *et al.*[28,29]

$$L = 1.5 + \exp(\frac{-|S|}{116}) \qquad \textit{Equation 1-15}$$

Where L is the Lorenz number (10^{-8} W Ω K^{-2}), S the Seebeck coefficient (μV K^{-1}).

Even though the inquiry of a low electrical resistivity might be favorable to the enhancement of the power factor, Wiedmann-Franz relation also implies an increase of the electronic contribution to the thermal conductivity with the diminution of the electrical resistivity.

1.5 Enhancement of the figure of merit

The figure of merit detailed in 1.4.1 evidences two principal strategies to improve its value. The first is to increase the power factor, while the second is focused on the reduction of lattice thermal conductivity. Moreover, it is possible to demonstrate that the thermoelectric performance is related to the fundamental properties of a material by a quality factor β:[30]

$$\beta \propto m^{*3/2} \frac{\mu}{\kappa_L} \qquad \textit{Equation 1-16}$$

To improve the quality factor, the product $m^{*3/2}$ and the fraction μ/κ_L must be optimized. Some approaches to attain this goal are described in the following paragraphs. It is important to recall that some parameters involved in the ZT calculation are interdependent. As a consequence, the optimization techniques are susceptible to have a negative or positive influence on several physical parameters. Hence, they cannot be used all at once; obtaining a fully optimized ZT necessitates compromises. Moreover, the potential of each strategy is strongly correlated to the nature of the material as well as to the control of the synthesis and sintering process.

For clarity purposes, the strategies proposed in this text are segregated into three subsections: the optimization of the main charge carrier concentration, the increase of the power factor and the decrease of the lattice thermal conductivity. Further information are available in articles proposed in references.[24,31–34]

1.5.1 Optimization of the charge carrier concentration

The three parameters involved in the ZT calculation are intimately tied to common features such as the electronic structure or the charge carrier concentration. The latter can vary by many orders of magnitude depending on the nature of the material (insulators, semiconductors, metals).

Until half of the XXth century, the thermoelectric effects discovery and other scientific milestones happened thanks to the investigation on metals and alloys. Alloys enjoy a narrow electrical resistivity due to their high concentration in charge carrier. On the other hand, they have very poor Seebeck coefficient ($|S|$< 10 μV K^{-1}) as well as sizeable thermal conductivity (Figure 1.6). Consequently, the figure of merit of metals and alloys is mediocre and the conversion rate of the first thermoelectric modulus is inferior to 1 %.[35]

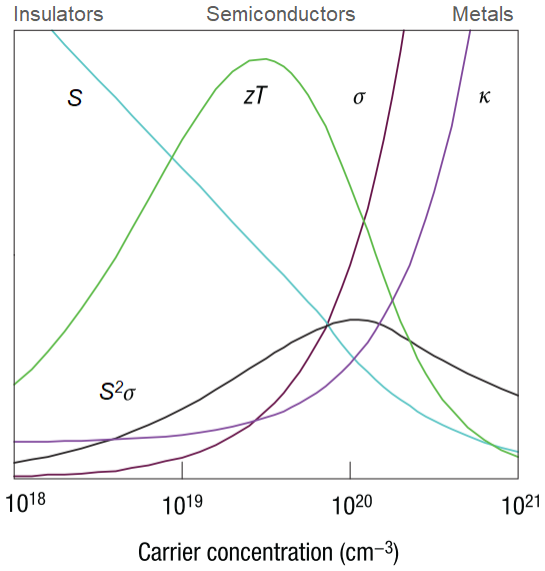

Figure 1.6. Graphic representation of the evolution of the Seebeck coefficient (S), the power factor (S^2 σ), the electrical conductivity (σ), the thermal conductivity (κ) and the figure of merit (ZT) as a function of the charge carrier concentration.[36]

As for insulators, they exhibit large Seebeck coefficient coupled to high electrical resistivity, which is a detrimental combination for good thermoelectric performances. This led to the identification of degenerated semiconductors as promising thermoelectric materials by A. F. Ioffe *et al.* in the fifties.[21] In fact, doped semiconductors attained much larger figure of merit in reason of their power factor with magnitudes reaching the hundreds of μV K^{-1} and relatively low electrical resistivity, owing to their low carrier concentration.

Even though S, ρ and κ do not have the same charge carrier concentration dependence, it is possible to find an optimum value for each parameter by conscientiously tailoring the charge carrier concentration through various

approaches. The optimal charge carrier concentration strongly depends on the nature of the material, but as a rule of thumb, a concentration between 10^{19} and 10^{21} charge carriers per cm^3, grants a maximal power factor and a modest electronic thermal conductivity as illustrated in Figure 1.6. Accordingly, the degenerated semiconductors and semimetals are the most promising materials to reach the best thermoelectric performance because of their insulator/conductor duality. Table 1.1 qualitatively summarizes the magnitude of the parameters ρ, *S*, κ, and *Z* for the three different classes of material: insulators, semiconductors and metals.

Table 1.1. Magnitude of the physical parameters ρ, S, κ, and Z at RT for the different material types: insulators, semiconductors and metals

	Insulators	**Semiconductors**	**Metals**
$\|S\|$ (μV K^{-1})	10^3	10^2	10^1
ρ (mΩ cm)	10^{13} – 10^{18}	10^0 – 10^2	10^{-3}
κ (W m^{-1} K^{-1})	10^{-1} – 10^2	10^0 – 10^2	10^1 – 10^2
Z **(K^{-1})**	10^{-16} – 10^{-14}	10^{-5} – 10^{-3}	10^{-6} – 10^{-4}

1.5.2 Improvement of the power factor

The power factor is mainly governed by the electronic structure of the material close to its Fermi energy (E_F) and can be tuned by the following approaches:

- The control of the charge carrier concentration (between 10^{19} and 10^{21} cm^{-3}) through doping, under-stoichiometries or isovalent substitutions that allows to find a compromise between *S*, ρ and κ.

- Doping with certain atoms can be responsible for a local increase of the electronic density of states leading to a band structure modification. If the density of occupied state is close to the Fermi level, the asymmetry development of the electronic density of states draws to an inflated effective mass hence a higher Seebeck coefficient.[37]

- The diminution of the energy difference between light and heavy bands close to the Fermi level allows a gain in the effective mass of the charge carriers and the Seebeck coefficient.[38] This strategy is called band convergence.

- A material made of a non-doped matrix with inclusions high in charge carrier concentration can potentially present a lower electrical resistivity. In fact, the charge carriers are transferred from the inclusions to the matrix where they benefit of a high mobility partially due to the quasi absence of impurities. However, this modulated doping approach is only possible at moderate temperature since a high temperature would lead to the inter-diffusion of the matrix and inclusions components.[39]

1.5.3 Decrease of the lattice thermal conductivity

Lattice thermal conductivity is proportional to the speed of sound in a material (v_s), the specific heat capacity (C_p) and the phonon mean free path (L_{ph}). While the C_p is linked to the composition and the structure of the phase, v_s is governed by the bonds strength within the lattice.[27] These two parameters are intrinsic to a material, thereby difficult to alter. As a consequence, the reduction of lattice thermal conductivity is made by lowering the phonon mean free path.

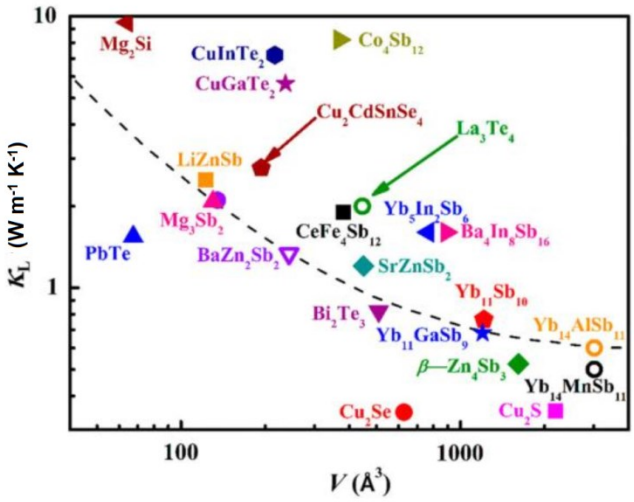

Figure 1.7. The lattice thermal conductivity correlated to the lattice cell volume.[27]

Early work by Wright discusses how alloying compounds with other isoelectronic cations and anions does not reduce the electrical conductivity but lowers the thermal conductivity.[40] Many of the recent high *ZT* thermoelectric materials were attained *via* a reduced lattice thermal conductivity through disorder within the unit cell. This disorder is achieved through rattling atoms, interstitial sites or partial occupancies in addition to the disorder inherent to the material. Thus, low thermal conductivity is generally associated with crystals containing large and complex unit cells (Figure 1.7). As phonon scattering by alloying depends on the mass ratio of the alloy constituents, it can be expected that random vacancies are also ideal scattering sites.

1.6 State of the art on thermoelectric materials

This state of the art is not intended to be a substitute to the exhaustive state of the art already realized in the literature.[31,41–51] Nevertheless, it provides a synthetic review of the thermoelectric systems with appropriate references.

1.6.1 Conventional thermoelectric materials

For clarity purposes, the variety of materials making the subject of this state of the art are summarized in Table 1.2. This classification allows a better insight of the pros and the cons of each system while ranking the compounds in function of their *ZT* and their optimal working temperature.

The discovery of conventional thermoelectric materials actually found in commercial devices was made back in 1950 and their properties were improved quickly during the next few decades until reaching *ZT* close to unity (Figure 1.8).[52,53] Since 1993, there is a renewed interest in the Bi_2Te_3 and SiGe phases, imputable to the work of L. D. Hicks and M. S. Dresselhaus on the impact of the miniaturization of thermoelectric materials.[54] The employment of quantum wells (2 D), quantum wires (1 D) and quantum dots (0 D) are at the origin of charge carrier containment; it increases the electronic state density near the Fermi level, expands the effective mass and rises the Seebeck coefficient.[55,56] Moreover, the interfaces multiplication is responsible of an escalation of phonon scattering, hence lowering the lattice thermal conductivity. During the last two decades, the appeal to these structures of low dimensionality allowed to widely increase the *ZT* of some materials over 2.[57–59] It is important to stay critic with those values since some performances could not be reproduced and the thermal stabilities are up for debate. Consequently, some *ZT* values were deliberately overlooked and do not appear in the summary Table 1.2.

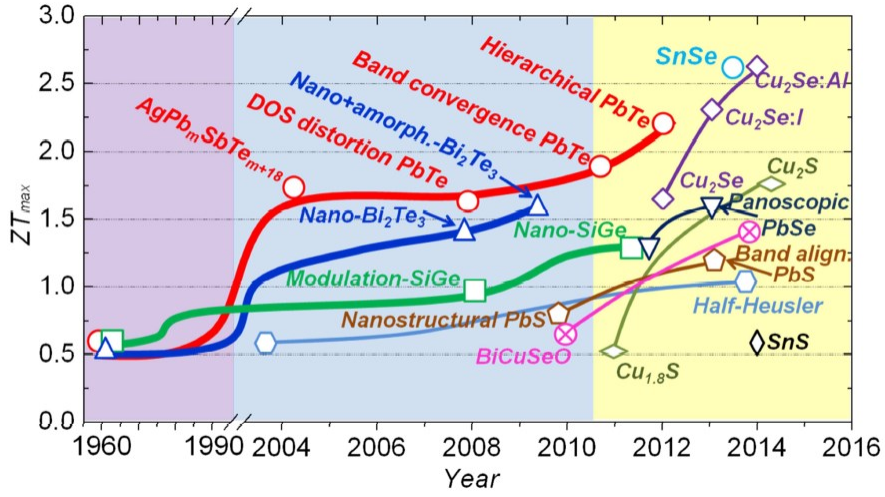

Figure 1.8. ZT evolution over the years of bulk thermoelectric materials. The conventional materials appear mostly on the left (before 2010) and the new material on the right (after 2010).[24]

For applications in the mid-temperature range (500–900 K), telluride-based materials such as PbTe, GeTe or SnTe, are generally employed.[60–62] Alloys with $AgSbTe_2$, commonly referred to as TAGS have led to *ZT* over unity for both *n*-type and *p*-type materials.

Table 1.2 Characteristics summary of the most performant conventional TE materials

Materials	**Composition**	**Temp. (K)**	**Pros**	**Cons**	**Type**	ZT_{max}	ZT_{max} **(K)**	**Ref.**
Bi_2Te_3	$Bi_2(Te_{0.8}Se_{0.2})_3$	200 - 450	High *S*, low ρ and low κ	toxic, heavy, costly	*n*	1	350	[36]
	$(Sb_{1-x}Bi_x)_2Te_3$				*p*	1.4	373	[63,64]
$Si_{1-x}Ge_x$	$Si_{0.8}Ge_{0.2}P_{0.02}$	900 - 1200	High *S*, low ρ good mecha. prop.	High κ and costly	*p*	0.95	1073	[65]
	$Si_{0.8}Ge_{0.2}$				*n*	1.3	1173	[66]
PbTe	$PbTe_{1-x}I_x$	450 - 800	High *S*, low ρ	Moderate κ, toxic, heavy, costly	*n*	1.4	730	[67]
	$Na_xPb_{1-x}Te$				*p*	1.4	750	[68]
TAGS	$(GeTe)_{0.70}(AgSbTe_2)_{0.30}$	350 - 750	High *S*, low κ	high thermal expansion	*p*	1.5	750	[69]
	$(PbTe)_{0.90}(AgSbTe_2)_{0.10}$	600 - 900			*n*	2.2	800	[70]

Nonetheless, applications involving these materials are not widespread due to the toxicity of some elements (Pb, Te), the low abundance (Te) and the high cost (Ge, Te). Therefore, application of these TE materials remain specific to niche sectors. On the other hand, numbers of promising alternative materials have been developed since the 90's. Those materials currently in development have the potential to outclass their ancestors by supressing the disadvantages, while keeping good TE properties and stability. The outcome of this research on new thermoelectric materials could endorse TE materials to reach widespread applications.

1.6.2 New thermoelectric materials

Nowadays, only a handful of applications have been able to compose with the important money constraint engendered by the utilization of thermoelectric technology. Nonetheless, new opportunities seem to emerge as many sectors consider the possibility to have recourse to thermoelectric modules. Even more, numbers of those potential applications are indifferent to the low conversion efficiency and take interest in the performance/cost ratio, the performance/mass ratio or to the absence of toxic elements.

The systematization of TE technology to a widespread market necessitates materials made of cheap elements easily available and in substantial quantities. Along these lines, several studies underline the limits of actual TE materials as Bi_2Te_3, PbTe and SiGe. Since 1950, telluride-based materials undoubtedly dominated the thermoelectric market with ZT always outranking that of their predecessor. Nevertheless, Te is a rare element in earth crust and present a lower abundance than gold.[71] Approximate evaluation of telluride concentration in earth's crust give a value of 1×10^{-3} ppm and that of selenide and sulfur are respectively of 50 (5×10^{-2} ppm) and 480 000 (5×10^{2} ppm) times more abundant.[72] Thus, to attain far-reaching market it is mandatory for TE modules to incorporate abundant elements.

The development of a number of technologies involving a specific element is strongly cost dependent. In a few years only, the Te price underwent a steep increase due to the developments in the fabrication of CdTe photovoltaic panels.[71] In 2015, 40 % of the extracted Te was devoted to the production of photovoltaic materials compared to 30 % for thermoelectric materials.[71] At this moment, the telluride price is more than an order of magnitude superior to that of sulfur, and that gap is widening each year as telluride demand is growing.[72] Moreover, toxic elements as Te, Pb, Sb and Se are inappropriate for mass production on behalf of the potential environment and sanitary hazard and important recycling cost they represent.

All of those factors are to be taken into consideration while finding a suitable application for a given TE material. Thus, the assessment of a compound is not solely based on its performance, but also on its production cost, the rarity of its constituting elements and its toxicity. This audit is crucial and gives credit to a number of materials that fail to present the highest efficiency and yet are relevant for particular applications.

1.6.2.1 Intermetallics

The phonon glass-electron crystal (PGEC) concept, first introduced by Glen Slack in 1995,[73] gave a second wind to the exploratory research of new phases. Those PGEC phases possess a structure that limits phonon propagation while having a negligible influence on charge carrier mobility.[3] The severe decrease of the lattice thermal conductivity caused by the rattling of heavy atoms permitted to attain *ZT* above unity in the skutterudite and clathrate structures. The structure of skutterudite, mostly based from $CoSb_3$ and $FeSb_3$, is depicted in Figure 1.9. Indeed, skutterudites are based on the chemical formula MX_3, where *M* is a metal such as Co which forms a cubic lattice and *X* represents a pnictogen atom (*e.g.* Sb, As, P) forming planar rings in the Co lattice voids. Not all voids are filled and heavy atoms such as Yb can be placed inside them (the large spheres in Figure 1.9). These

loosely bonded atoms rattle on their position with low frequency and high amplitude, impeding phonon transport and decreasing thermal conductivity.[74]

Clathrates share a similar idea with skutterudites on a slightly larger and more complex scale: a guest atom placed in a cage disrupts the phonon transport with its anharmonic behavior (Figure 1.9). The sp^3 covalently bonded framework of clathrate conducts electrons through the structure; while loosely holding guest atoms inside with the function to scatter phonons and thus significantly reduce the overall thermal conductivity. Moreover, the metallic cations quantity and nature alters the electron count that governs the electrical properties. This degree of freedom provides a simple fine-tuning parameter of the electron count for the optimization of the thermopower and electrical resistivity. Consequently, clathrates often have thermal conductivities below 3 W $m^{-1}K^{-1}$ with metallic or semiconducting electrical properties. These electrical properties, combined with inherently low thermal conductivity, raised exciting perspectives to achieve a high dimensionless thermoelectric figure of merit *ZT*. The stannide clathrate class contains several material with *ZT*s above 1 in the mid-range temperature (480 - 550 K),[75–79] as $Ba_8Ga_{5.23}Al_{10.52}Sn_{30.26}$ with a maximum of ZT_{480K} = 1.2,[75] due to their relatively low conductivities 0.48 - 0.81 W $m^{-1}K^{-1}$ and high absolute Seebeck coefficient 175 - 245 mV K^{-1} at 300 K. Chevrel phases of formula $M_xMo_6Q_8$ (M = transition metal or rare-earth metal, x = 0 – 4, and Q = S, Se, or Te) have also been investigated for their thermoelectric and supraconductor properties.[80–86] These octahedral molybdenum units compounds can accommodate different metal cations or ligands, thus giving the possibility to easily tune their optical and electrical properties.[81,87–89]

On a smaller scale, half-Heusler compounds are promising thermoelectrics with values of *ZT* close to unity.[74] A half-Heusler alloy has a chemical formula *XYZ*, where *X* is a metal from the Ti or V groups, *Y* a metal from the Fe, Co, Ni groups and *Z* a *p*-block element such as Sb, Sn, Ga. With three sublattices, each accepting a range of various elements, these materials allow a wide range of tuning parameters, either electronic or phononic.[90]

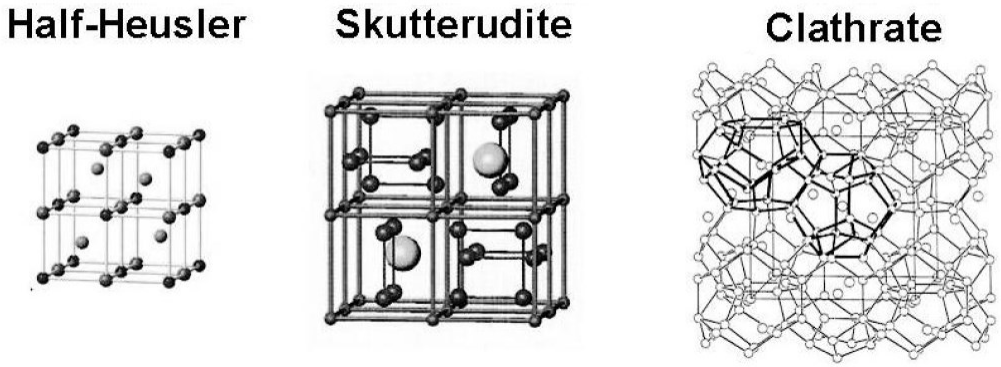

Figure 1.9. Structures of Half-Heusler, Skutterudite and clathrate.[74]

1.6.2.2 Oxides

For a long time, oxides have been overlooked for TE applications due to their limited figure of merit. Indeed, oxygen has a low atomic mass and an important electronegativity, resulting in highly polarized chemical bonds. As a result of the orbitals poor overlap, oxides are characterized by a large band-gap and a restrained electronic mobility, giving low electrical conductivity and low Seebeck coefficient. These strong bonds are also at the origin of important phonon propagation in the lattice. Nonetheless, oxides have benefitted of an improved reputation following the revelation in 1997 of cobaltites presenting a large thermopower.[91] Indeed, while the electrical resistivity of Na_xCoO_2 ($0.5 \leq x \leq 1$) is low around 2×10^{-6} Ω m, its Seebeck coefficient reaches unexpectedly large values around 1000 mV K^{-1}. Along with its low thermal conductivity, this leads to a *ZT* value reaching unity at 800 K (reported on single crystals).[91,92] A similar effect was soon observed in other oxides with a similar layered structure, namely $[Ca_2CoO_3][CoO_2]_{1.62}$ and $[Bi_{0.87}SrO_2]_2[CoO_2]_{1.82}$.[93,94] In spite of their relatively low TE performances, their main advantages lie in their air stability, thus avoiding the necessity of an inert atmosphere enclosure/protective layer and their composition made of abundant and low cost elements. In this manner, these materials are good prospect for high temperature thermoelectric applications.

1.6.2.3 Copper sulfide mineral phases

At last, the chalcogens (S, Se, Te) are the subject matter of several studies.[95] Compared to oxides, they possess bonds with a stronger covalent nature (for Te sometimes almost metallic), hence are characterized by smaller electrical resistivity and band-gaps. Moreover many chalcogen compounds present a layered structure, which regarding Hick and Dresselhaus low dimensionality theory, make them good candidates for attractive Seebeck coefficient,[54,96] thereby opening the possibilities to modulate the properties through texturing.

In addition, tellurium and selenium should be replaced with a less-toxic, less expensive homologous element such as sulfur. Compared with Te and Se, S has a lighter mass, smaller atomic radius, and larger electronegativity. However, the lighter mass of sulfur should lead to higher phonon frequencies/Debye temperature, *i.e.* a higher lattice thermal conductivity. As a consequence, TE sulfides have been overlooked with respect to tellurides, in spite of that fact that the sulfur family represent a greater structural diversity with diverse mechanical, optical and electrical characteristics and are much more earth abundant and cheaper than Te. Along these lines, the study of the thermoelectric properties of metal sulfides is essential.

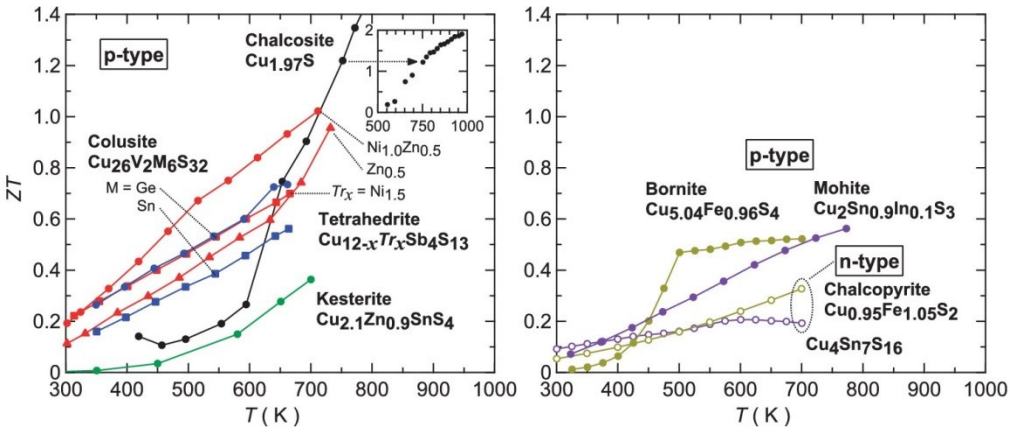

Figure 1.10. ZT values of the most studied Cu-S based synthetic minerals and related compounds of p-type (filled symbols) and n-type (open symbols).[97]

In the last few years, the growing research on sulfur phases originating from natural minerals as TE materials lead to the revelation of a wide variety of materials made of abundant elements with low toxicity and complex crystalline structure coupled to attractive electronic transport properties. Indeed, many synthetic compounds reproduced from copper rich natural minerals are reported as promising materials for applications in the 300 K to 700 K range, as shown by their attractive *ZT* values in Figure 1.10. Also, among these materials, many structures are complex (Figure 1.11) and thereby present intrinsically low thermal lattice conductivity coupled to interesting electronic properties in agreement with the criteria presented before.[98,99] In spite of relating a monotonous exhaustive list of all copper sulfides TE materials, examples of the most popular materials and the most closely related to the those presented in this thesis will be presented in the following paragraphs.

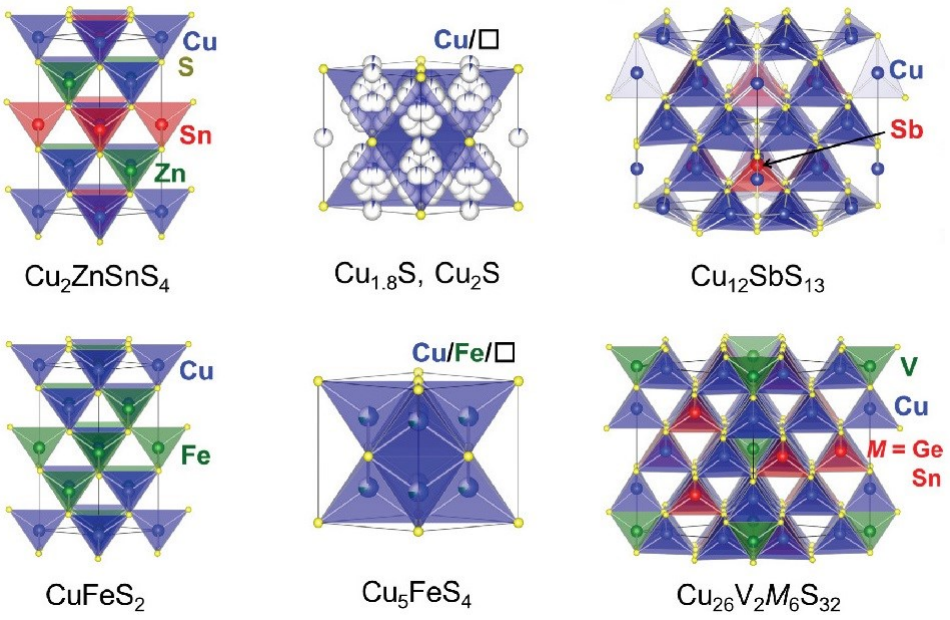

Figure 1.11. Crystal structures of Cu-S based minerals and related compounds. Binary $Cu_{1.8}S/Cu_2S$ and Cu_5FeS_4 are depicted in their cubic structures at high temperature.[97]

Digenite and chalcocite (*p*-type)

Digenite $Cu_{1.8}S$ and chalcocite $Cu_{2-\delta}S$ are well-known binary systems due to their peculiar structure that consist of Cu ions distributed on several possible positions and a rigid sublattice maintained by the sulfur atoms (Figure 1.11).[100] Two polymorphs of $Cu_{1.8}S$ exist with a transition at 345 K.[101] The higher-temperature (HT) phase, a face centered cubic structure, is stable, whereas the lower-temperature (LT) phase (rhombohedral) was reported to be metastable. The TE properties of *p*-type $Cu_{1.8}S$ were reported by Ge *et al.*[102] For $Cu_{1.8}S$ with the HT form, synthesized by an optimized mechanical alloying (MA) synthesis followed by a spark plasma sintering (SPS) densification, the combination of a metallic electrical resistivity ρ of 5 μΩ m and rather large Seebeck coefficient of 70 μV K^{-1} led to the high power factor (*PF)* of 1 mW m^{-1} K^{-2} at 673 K. Nonetheless, the total thermal conductivity remains high with a value of 2.3 W m^{-1} K^{-1} and therefore confines the *ZT* below 0.3.

$Cu_{2-\delta}$ S, on the other hand, presents three polymorphs: a cubic phase at $T \geq$ 708 K, a hexagonal one between T = 376 – 708 K, and a monoclinic one at $T \leq$ 376 K.[101] The formation of $Cu_{1.96}S$ and micro-sized pore resulted in the reduction of κ to 1.3 W m^{-1} K^{-1}, leading to a higher ZT = 0.5 at 673 K.[102] At that time, this value was the highest among *p*-type sulfide materials. Note that the higher-temperature phase is a superionic phase having liquid-like mobile copper ions, which causes stability hazards.[103]

Bornite (*p*-type, *n*-type)

Bornite Cu_5FeS_4 was reported to have many polymorphs, which strongly affects the TE properties, namely: the low temperature orthorhombic, the cubic intermediate and the cubic high temperature (Figure 1.11).[104–107] Bornite distinguishes above most of the TE materials by its considerably lower κ values.[36,105–109] These small values in both low-T and high-T phases were respectively ascribed to the complex microstructure and the complete disorder in the cation sublattice.[104] For Cu_5FeS_4, the affiliation of the relatively low power factor of 0.25 mW m^{-1} K^{-2} and the low lattice thermal conductivity (κ value lower than 0.5 W m^{-1} K^{-1}) results in ZT = 0.4 at 700 K.[105] With a Cu to Fe substitution in

$Cu_{5+x}Fe_{1-x}S_4$ (x = 0.02, 0.040 at ~ 490 K (where a phase transition occurs) the sign of the Seebeck coefficient is reversed from negative to positive and the value of the electrical resistivity is decreased. As a result, the ZT value for x = 0.04 was incremented to 0.5, as shown in Figure 1.10.[105]

Tetrahedrite (*p*-type)

Tetrahedrite is a sulfosalt mineral, named from the tetrahedral shape of its crystals, with the following general chemical formula: $(Cu, Ag)_6Cu_4(Fe, Zn, Cu, Hg, Cd)_2(Sb, As, Bi, Te)_4(S, Se)_{13}$. Regarding its crystal chemistry, a wide variety of elements can substitute into tetrahedrite without changing its crystal structure, apart from the cell parameter, to form a solid solution. The cubic crystal structure of tetrahedrite (Figure 1.11) is illustrated by $Cu_{12}Sb_4S_{13}$ which is often taken as the prototypical composition.

Tetrahedrite crystallizes in the body-centred cubic structure ($I\bar{4}3m$) and its cell parameter is around ~ 10.3 Å. While its crystal structure and rich chemistry has been studied extensively for many decades,[110–114] its interesting thermoelectric properties have been reported only in 2012 by Suekuni *et al.*[6] (at low temperature) and in 2013 by Lu *et al.*[115] and Suekuni *et al.*[116](at high temperature). Tetrahedrite displayed a relatively high power factor of 374 μW m^{-1} K^{-2} coupled to a low lattice thermal conductivity, *e.g.* less than 0.5 W m^{-1} K^{-1} at RT. Following that discovery, countless studies have been dedicated to the optimization of its figure of merit ZT through some of the approaches in section 1.5. Thanks to the low lattice thermal conductivity due to the complex structure and to the possibility to optimize the charge carrier concentration trough substitutions with Ni, Fe, Zn, Sb, Co, Te,[117–125] the maximal ZT for tetrahedrite reaches unity for the composition $Cu_{10.5}Ni_{1.5}Zn_{0.5}Sb_4S_{13}$ at 723 K. Also some process optimization work on tetrahedrite $Cu_{10.4}Ni_{1.6}Sb_4S_{13}$ allowed, by changing the synthesis method from conventional sealed tube (ST) to MA, to gain a better control of the final product composition and higher thermoelectric performances (ZT of 0.75 at 700 K).[122] The purity and structural stability of the $Cu_{12}Sb_4S_{13}$ and $Cu_{10.4}Ni_{1.6}Sb_4S_{13}$ tetrahedrite phases, were studied at high temperature in order to

determine the maximum operating temperature for TE applications. The maximum *ZT* of 0.8 was found for $Cu_{10.4}Ni_{1.6}Sb_4S_{13}$ at 700 K.[126]

Chalcopyrite (*p*-type)

Chalcopyrite, $CuFeS_2$ is an abundant Cu–Fe–S based natural minerals that crystallizes in a tetragonal structure related to cubic zinc blende as depicted in Figure 1.11.[127] It has gained much attention as a *n*-type TE material, since Li *et al.* reported the *ZT* of 0.21 at 573 K for $CuFeS_{2-x}$ (x = 0.2).[108] Additionally, Tsujii *et al.* substituted Fe and Zn for Cu in $Cu_{1-x}Fe_{1+x}S_2$ (x = 0 – 0.3) and $Cu_{1-y}Zn_yFeS_2$ (y = 0, 0.03) and obtained a *PF* at 400 K increased up to 1 mW m^{-1} K^{-2}.[128–130] Several groups reported similar *ZT* values on substituted systems, *e.g.* 0.3 at 700 K for $Cu_{1-x}Fe_{1+x}S_2$ (x = 0.03, 0.05) (Figure 1.10),[131] and 0.14 – 0.16 at 670 K for $CuFeS_{2(1-x)}Se_{2x}$ (x = 0.05, 0.20, 0.25).[132] The relatively low *ZT* of the chalcopyrite systems is due to the large κ_L exceeding 1 W m^{-1} K^{-1}. It should be noted that nanocrystalline bulk samples of $CuFeS_2$ showed positive Seebeck coefficient.[133,134]

Stannite, briartite and kesterite (*p*-type)

Stannite Cu_2FeSnS_4 crystallizes in a tetragonal structure ($I\bar{4}2m$, Figure 1.11), a superstructure derived from the sphalerite, composed of [CuS_4], [FeS_4], and [SnS_4] corner sharing tetrahedra. For stannite with sulfur defects (y), $Cu_{2+x}Fe_{1-x}SnS_{4-y}$ (x = 0 - 1), the samples with x = 0.8 - 1 exhibit degenerate conduction, whereas the Seebeck coefficient remains relatively high, $S \approx 100$ μV K^{-1} for x = 0.8 at 300 K and with κ in the range 0.1 W m^{-1} K^{-1} - 1 W m^{-1} K^{-1}, which is close to the κ value of silicon dioxide. The *ZT* is enhanced significantly through optimization of chemical composition, 0.044 for x = 0.8 at 300 K, it is two times larger than that of x = 0 at 300 K and by an increase in temperature.[135]

As tetrahedrite, many elements can substitute into stannite without changing its crystal structure, apart from the cell parameter. In fact, some of the substituted minerals have acquired their own name throughout the course of history. For instance, briartite is a form where the Sn is replaced by Ge such as Cu_2FeGeS_4. Another example is kesterite where the Fe is substituted by Zn. The

thermoelectric properties of the latter were reported by Liu *et al.* for a Cu for Zn substitution: $Cu_{2+x}Zn_{1-x}SnS_4$ (x = 0, 0.1).[53] A semiconducting behavior with holes as main charge carriers was reported for both samples. The control of the Cu/Zn stoichiometric ratio allowed to significantly lower both the electrical resistivity and the Seebeck coefficient by the conversion of some insulating ZnS_4 unit to conducting CuS_4 ones. Indeed, the substitution x = 0.1 gave a power factor of 0.58 mW m^{-1} K^{-2} at 700 K. Moreover, the relatively low thermal conductivity (0.9 W m^{-1} K^{-1} at 700 K) was attributed to the distortion inflicted to the structure by the Cu substitution.

Colusite (*p*-type)

Colusite of general chemical formula $Cu_{24+x}V_2(As, Sb)_{6-x}(Ge, Sn)_xS_{32}$ ($x \leq 2$) is a superstructure of sphalerite. The simple cubic unit cell ($a \sim 10.5$ Å, $P\bar{4}3n$) is composed of 66 atoms (Figure 1.11) positioned on seven crystallographic sites: one for V (2*a*), three for Cu (6*d*, 8*e*, 12*f*), one for *M* = As, Sb, Sn, Ge (6*c*), and two for S (8*e*, 24*i*).[136,137] In the structure, the [VS_4] tetrahedra share edges with [CuS_4] tetrahedra, whereas [MS_4] and [CuS_4] share corners, hence forming a three dimensional network. Colusites of formula $Cu_{26}V_2M_6S_{32}$ with *M* = (Ge, Sn), were developed and reported in the thermoelectric field for the first time by Suekuni *et al.* in 2014 with the desire of replacing Sb in tetrahedrite with less toxic elements.[138] The alliance of *p*-type metallic conduction and large Seebeck coefficient (< 200 µV K^{-1}) led to high power factors of 0.61 mW m^{-1} K^{-2} and 0.48 mW m^{-1} K^{-2} at 663 K for the Ge and Sn samples, respectively. In addition, from 350 K to 663 K the lattice thermal conductivity was lower than 0.6 mW m^{-1} K^{-1} due to the structural complexity. Consequently, the values of *ZT* for Ge and Sn reached 0.73 and 0.56 at 663 K, respectively. Following that, many successful attempts to optimize the *ZT* of colusite using the method previously described in section 1.5 were made.

In 2016, the *ZT* of colusite was enhanced to 0.8 at 670 K, for the composition $Cu_{26}Ta_2Sn_6S_{32}$, by an improvement of the power factor through doping. The heavy hole effective mass of 4 m_0 (m_0 is the free electron mass) caused

a high Seebeck coefficient, leading to high thermoelectric power factor of 0.7 mW m^{-1} K^{-2}at 660 K. Besides, the electrical resistivity was decreased, 63 μΩ m compared to 110 μΩ m for $Cu_{26}V_2Sn_6S_{32}$ at 660 K, because of the presence of CuS and Cu_2S secondary phases that provided charge carriers. The low lattice thermal conductivity was maintained.[139]

Also, Bouyrie *et al.* investigated the effect of Co, Ni, and Fe addition on the power factor enhancement in colusite $Cu_{26}Nb_2Ge_6S_{32}$. They showed that while the addition of Co increased the hole carrier concentration (1.8×10^{21} cm^{-3}, compared to 1.2×10^{21} cm^{-3}) and decreased the electrical mobility (0.87 cm^2 V^{-1} s^{-1}, ~ 35 % lower), the addition of Ni had a small effect on the electrical transport properties. A low electrical resistivity (~ 40 μΩ m) and high thermoelectric power factor (~ 600 mW m^{-1} K^{-2} at 665 K) were maintained with the addition of Co and Ni. On the other hand, the addition of Fe decreased both the hole carrier concentration (0.9×10^{21} cm^{-3}) and electrical mobility (0.79 cm^2 V^{-1} s^{-1}, ~ 40 % lower), leading to high electrical resistivity (~ 90 μΩ m) and low power factor of ~ 470 mW m^{-1} K^{-2} at 665 K. A little effect of the addition of Co, Ni, and Fe on the lattice thermal conductivity was found; all the samples exhibited low lattice thermal conductivity because of the complex crystal structure of colusites (~ 0.4 W K^{-1} m^{-1} at 665 K). High *ZT* of approximately 0.7 at 665 K were achieved in $Cu_{26}Nb_2Ge_6Co_{0.5}S_{32}$ and $Cu_{26}Nb_2Ge_6Ni_{0.5}S_{32}$.[140]

A distinctive feature of the colusite $Cu_{26}V_2M_6S_{32}$ family is their exceedingly low lattice thermal conductivity values, as low as tetrahedrite and chalcocite. Indeed, Bourgès *et al.* has recently reported a *ZT* close to unity at 700 K by reducing the lattice thermal conductivity (0.40 W m^{-1} K^{-1} – 0.55 W m^{-1} K^{-1} at 350 K), through cationic disordering induced by process control. Therefore, they showed that the reduced lattice thermal conductivity in colusite $Cu_{26}V_2Sn_6S_{32}$ was attributed to the structural complexity (large unit cell, large number of atoms per unit cell (*N*), and mass difference between Cu, V, and *M*) that serves several kinds of phonon scatterers, *i.e.* vacancies at S sites, Cu/Sn antisite defects, and chemical disorder on the metal ion sublattices.[5,141] Figure 1.12 shows the coexistence of

ordered an disordered regions within the same crystallite in the $Cu_{26}V_2M_6S_{32}$ sintered at higher temperature (1023 K).

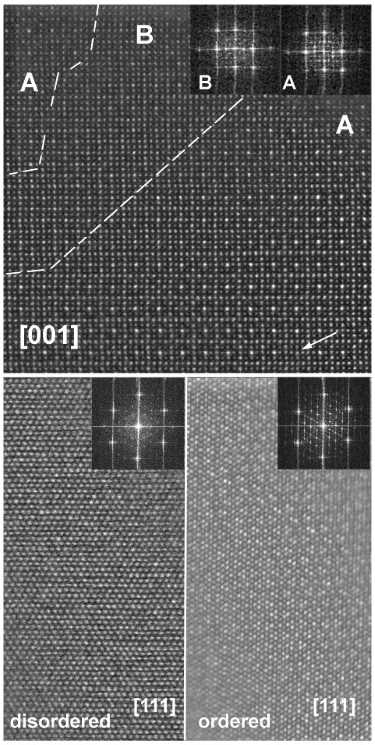

Figure 1.12. [001] and [111] HAADF-STEM images showing the coexistence of ordered an disordered regions within the same crystallite in the Cu26V2M6S32 sintered at 1023 K. Corresponding FT patterns are given as inset. Row indicates a point defect.[141]

Recently, outstanding power factors of 1.5 mW m^{-1} K^{-2} and 2.0 mW m^{-1} K^{-2} were achieved at 300 K and 700 K, respectively, through a band engineering approach for a new colusite $Cu_{26}Cr_2Ge_6S_{32}$.[142] The enhancement of the Seebeck coefficient in this compound was attributed to a modification of the Cu–S network to flatten the valence bands near the Fermi level, whereas the reduction in ρ (increased mobility of holes) was attributed to the enhanced metal-like Cr–Cu interactions in the CuL_6 cluster complex (L = Cu, Cr, Ge). Such "functionalization" of the Cu–S network could be used as a new approach to enhance the power factor for Cu–S based materials. By combining the two independent ways to enhance *PF* and to reduce κ_L described above, higher *ZT* up, to 0.7 at 300 K and 2.4 at 700 K, are potentially achievable.

Germanite (*p*-type)

Natural germanite, characterized by the copper rich formula "$Cu_{26}Fe_4Ge_4S_{32}$", has a cubic structure derived from that of the well-known ZnS sphalerite ($F\bar{4}3m$) and similar to colusite but with a different cationic distribution. The first formula for germanite, proposed by De Jong in 1930, was based on a sphalerite-type stoichiometry, *i.e.* 1:1 Metal:Sulfur (M/S) ratio with 3 Cu for 1 Fe or Ge, hence giving $Cu_3(Fe, Ge)S_4$.[143] The second formula proposition came from Sclar *et al.* in 1957 and is also based on a sphalerite-type stoichiometry, but includes this time a wider variety of elements that occurs often in germanite minerals as well as a possible partial S substitution with As, such as: $Cu_3(Fe, Ge, Zn, Ga)(S, As)_4$.[144] Sometimes later, Lévy was able to improve the formula gave by De Jong, by submitting a more precise stoichiometry with a neutral balance of the electrical charge: $Cu_3^+Cu_3^{2+}Fe^{3+}Ge^{4+}S_8^{2-}$.[145] Not long after, Springer introduced an alternate formula to the one proposed by Sclar with a sulfur under-stoichiometry: $(Cu, Fe, Zn, W, Mo, V, Ge, As, Ga)S_{0.95}$.[146]

In 1984, Tettenhorst and Corbato proposed the first formula with an M:S ratio greater than 1 (34:31) implying a superstructure of sphalerite with the occupation of interstitial sites, based on that of colusite. To this day, it remains the accepted formula and structural model for germanite.[147] Based on colusite stoichiometry, the chemical formula of germanite proposed by Spiridonov in 1987, $Cu_{20}^+(Cu^{2+}, Fe^{2+}, Zn^{2+})_6Fe_2^{3+}Ge_6^{4+}S_{32}^{2-}$, is not electrically neutral. Also, according to the author,[148] the Fe^{3+} cations occupy the same site that is occupied by V^{3+} in colusite namely the interstitial *2a* site; meaning that V^{3+} could substitute Fe^{3+} in germanite. Later, in the work on germanocolusite, Spiridonov and collaborators (1992) proposed another chemical formula for germanite. In this case, the formula is electrically neutral, but the sum of atoms in the unit cell is 68 rather than 66 as in colusite whose formula was adopted by E. Spiridonov as the basis for examination of the germanite formula; therefore, the *Me*:S ratio is equal to 36:32 rather than 34:32. All the formulas are summarized in Table 1.3.

Table 1.3. Different stoichiometry proposed for natural germanite over the years.

Formula	*M*:S	References
$\mathbf{Cu_3(Fe,Ge)S_4}$	32:32	[143] De Jong, 1930
$\mathbf{Cu_3(Fe,Ge,Zn,Ga)(S,As)_4}$	32:32	[144] Sclar *et al.*, 1957
$\mathbf{Cu_3^+Cu_3^{2+}Fe^{3+}Ge^{4+}S_8^{2-}}$	32:32	[145] Lévy, 1966
$\mathbf{(Cu,Fe,Zn,W,Mo,V,Ge,As,Ga)S_{0.95}}$	33.7:32	[146] Springer, 1969
$\mathbf{Cu_{16}^+Cu_{10}^{2+}Fe_4^{3+}Ge_4^{4+}S_{32}^{2-}}$	34:32	[147]Tettenhorst, Corbato, 1984
$\mathbf{Cu_{20}^+(Cu^{2+},Fe^{2+},Zn^{2+})_6Fe_2^{3+}Ge_6^{4+}S_{32}^{2-}}$	34:32	[148] Spiridonov, 1987
$\mathbf{Cu_{20}^+(Cu^{2+},Fe^{2+},Zn^{2+})_6Fe_2^{3+}(Ge^{4+}As^{5+})_6S_{32}^{2-}}$	36:32	[149] Spiridonov *et al.*, 1992

These contradictions and the scarcity of evidences on germanite's formula prompted Nenashevas to make an additional analysis of the literature data.[150] A total of 37 chemical and electron microprobe analyses of germanite available in the literature were found and recalculated into formula with regard to electrical neutrality. Thus, it has been revealed that 28 analyses out of 37 are adequately recalculated to the formula with 66 atoms in the unit cell; 6 analyses, to the formula with 64 atoms; and 3 analyses, with 68 atoms. The *M*:S ratio in the analyses varies from 32:32 to 34:32 and to 36:32. This fact suggests that we either deal with solid solutions or with three distinguished minerals, but similar in chemical composition and properties. The second assumption is more probable, as the presence of solid solutions would give a continuous *Me*:S ratio from 32:32 to 36:32.

The accepted structure determined by Tettenhorst and Corbato from powder X-ray analysis,[147] consists of a semi-ordered sphalerite framework [$Cu_{24}Fe_4Ge_4S_{32}$] built up of CuS_4, FeS_4 and GeS_4 corner-shared tetrahedra (Figure 1.13). According to Tettenhorst, in this framework, the 6*c*, 6*d* and 12*f* sites are occupied by Cu, whereas Fe and Ge are statistically distributed over the same *8e* site (Table 1.4). The sphalerite network forms interstitial tetrahedral sites, among which, according to the authors, the 2*a* site is filled with remaining Cu atoms. These [CuS_4] tetrahedra share their edges with the [CuS_4] tetrahedra of the 12*f* sites. Note that these cations would form centered octahedral metallic complexes [Cu(2*a*)S_4]Cu(12*f*)$_6$ similar to the CuL_6 complexes previously described for

colusites (Figure 1.13). However, from a formal charge point of view, $Cu_{16}^{+}Cu_{10}^{2+}Fe_{4}^{3+}Ge_{4}^{4+}S_{32}^{2-}$, contains a large amount of Cu^{2+}, a feature rarely observed in synthetic copper sulfides, which probably originates from the high-pressure conditions generally associated with natural mineral formation., or simply a wrong assumption of the chemical composition.

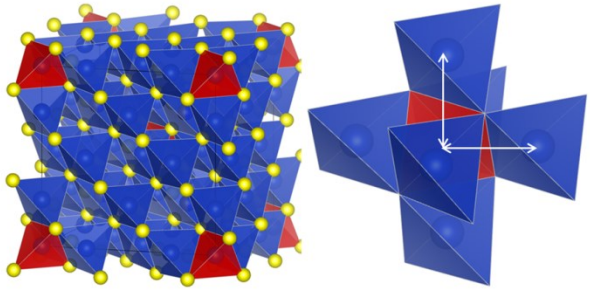

Figure 1.13. The cubic structure of space group $P\bar{4}3n$ of natural germanite $Cu_{26}Fe_4Ge_4S_{32}$ and an isolated representation of the metallic complex formed by CuS_4 tethahedra with the metallic interactions identified by white arrows.

Table 1.4. Published crystal structure data of germanite and colusite.[136,147]

Site	***x***	***y***	***z***	**$Cu_{26}Fe_4Ge_4S_{32}$**	**$Cu_{26}V_2As_4Sn_2S_{32}$**
2*a*	0	0	0	Cu_2	V_2
6*c*	0.25	0.5	0	Cu_6	As_4Sn_2
6*d*	0.25	0	0.5	Cu_6	Cu_6
12*f*	0.257(2)	0	0	Cu_{12}	Cu_{12}
8*e*	0.240(2)	0.240(2)	0.240(2)	Fe_4Ge_4	Cu_8
8*g*	0.121(3)	0.121(3)	0.121(3)	S_8	S_8
24*i*	0.379(3)	0.364(3)	0.121(1)	S_{32}	S_{32}

Synthetic germanite with a cubic structure (a = 10.59 Å, $P\bar{4}3n$) was recently obtained by Pavan Kumar *et. al*[151] by the combination of mechanical-alloying (MA) and spark plasma sintering (SPS), a method that was previously proven to be efficient to prepare large quantity of high-purity samples of many ternary and quaternary sulfides.[5,107,122,152,153] This study demonstrated the possibility to synthesize a Cu^{1+}-rich sulfide $Cu_{22}Fe_8Ge_4S_{32}$ with the germanite structure,[151] which deviates from the natural mineral $Cu_{26}Fe_4Ge_4S_{32}$ by its much higher Cu^{1+}/Cu^{2+} ratio. All efforts to synthesize the natural mineral, $Cu_{26}Fe_4Ge_4S_{32}$, were unsuccessful and led to mixtures containing the sulfide Cu_5FeS_4 and at least one other unidentified secondary phase. At this point, the attention to the charge

balance in the natural mineral $Cu_{16}^{1+}Cu_{10}^{2+}Fe_4^{3+}Ge_4^{4+}S_{32}^{2-}$ implied that the germanite structure should be difficult to stabilize due to the large amount of Cu^{2+} besides Cu^{1+} species in the same tetrahedral sites. Indeed, Cu^{2+} should favor the formation of distorted octahedral or pyramidal or square planar coordination due to its Jahn–Teller effect, with respect to the systematic tetrahedral coordination that is imposed by the structure of the Cu^{2+}-rich natural mineral. Therefore the opportunity to grow the Cu^{1+}/Cu^{2+} ratio by changing the charge balance between copper and iron was examined. The Fe/Cu ratio was increased conform to the formula $Cu_{26-x}Fe_{4+x}Ge_4S_{32}$, while maintaining the global cationic stoichiometry fixed to that of the mineral. The Rietveld refinement of an XRPD pattern with the crystal structure proposed by Tettenhorst led to an erroneous approximation of the superstructure peak of synthetic germanite as shown in Figure 1.14.

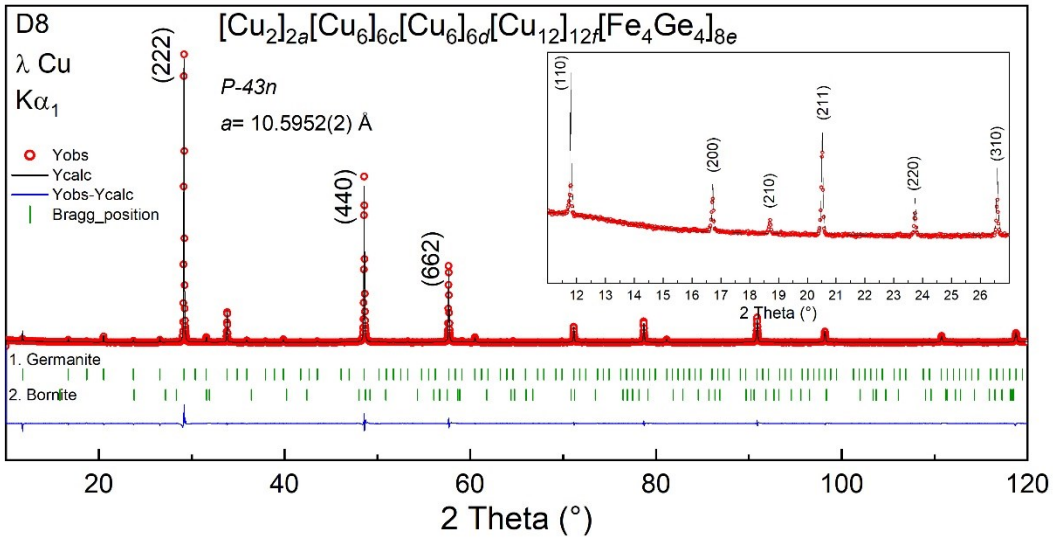

Figure 1.14. XRPD pattern of synthetic germanite $Cu_{22}Fe_8Ge_4S_{32}$ fitted by Rietveld with the structural model proposed by Tettenhorst.

Therefore, Pavan Kumar *et al.*[151] proposed a first approximate structural model for $Cu_{22}Fe_8Ge_4S_{32}$, established on the basis of a cationic distribution close to that natural mineral[147] and considering a chemical formula with iron in trivalent state only based on the room temperature ^{57}Fe Mössbauer spectroscopy. The difficulties to solve the structure of germanite stem from the similarity of the cationic sites (same coordination and comparable site sizes), the presence of mixed

occupancies and the nature of the cations (same electronic density and close scattering lengths).

Germanite $Cu_{22}Fe_8Ge_4S_{32}$ has the potential to be a performant TE material because of its isostructurality to colusite, hence giving the possibility that they share a common intrinsically low lattice thermal conductivity. The lattice thermal conductivity (κ_L) of germanite, 1.76 W m^{-1} K^{-1} at 300 K, and its maximum *ZT* value of 0.14 at 575 K, are comparable to those of colusite $Cu_{26}V_2Sn_6S_{32}$ sintered in similar conditions (*i.e.* at 873 K for 30 min under a pressure of 64 MPa).[141,151] Additionally, the significantly smaller figure of merit of synthetic germanite compared to that optimized colusite, strongly suggests that order–disorder cationic phenomena play a crucial role in carrier mobility leaving room for further improvement.

1.7 Conclusion

In this environmental context, it is imperative to encourage a durable and eco-responsible management of the energetic resources. This ambition compel to the development and to the settlement of new technologies that support emancipation from fossil energy sources. Regarding that, thermoelectricity provides the opportunity to partially valorize heat loss into electricity production. Despite the countless heat sources, conventional thermoelectric compounds struggle to democratize due to their low performance/price ratio and their low abundant and toxic composition. As a consequence, it is of prime importance to find alternative materials adequate to address those defaults and thus make thermoelectricity a suitable large scale solution. The state of the art realized in this chapter emphasize that the Cu-S family seems to be the most adapted class of materials to answer those requirements. Nevertheless, in spite of the low cost of those compounds, their relatively low performances are an obstacle to their usage. In this context, this thesis endeavor is focused on the study of the thermoelectric properties of a copper rich sulfide family, the germanite.

2 STUDY OF GERMANITE SYNTHESIS, PURITY, TEMPERATURE STABILITY AND PROCESS

2.1 Preface

The mastery of the synthesis conditions for the production of single-phase samples is of prime importance prior to initiate structural and physical characterizations. The classical approach for phase exploration is to predetermine a set of conditions (*e.g*. time, temperature, heating and cooling rates) and to wait until completion of the reaction to identify the formed compounds. This experimental approach is oblivious to important information such as the formation temperature of the product (*e.g*. during an isotherm, heating or cooling) and the formation of reactive intermediates and secondary phases. This lack of awareness hinders our ability to identify new materials or to devise successful synthetic processes for desired complex materials such as germanite. Indeed, as briefly exposed in the last chapter, the synthesis of pure sample of germanite is problematic because this compound crystallizes close to other related phases such as bornite, renierite, fahlores, sphalerite and galena.[150] In this context, real time *in situ* reaction is mandatory. Thereby, the first part of this chapter focuses on the formation conditions of a ''pure'' germanite $Cu_{22}Fe_8Ge_4S_{32}$ sample by the means of *in situ* reactions.

The conception of new materials for thermoelectric applications face major challenges in generators integration.[154] Thermal stability is one of the main obstacles that limit the commercialization of many materials with good thermoelectric properties. An investigation on the phase stability/decomposition and underlying mechanism is essential to understand the temperature dependence of the TE properties and acknowledges the workability of the material. Along these lines, the second section of this chapter aims to determine the temperature stability of germanite.

Due to the high sensitivity of sulfur to volatilize during the processing route, the synthesis technique is of prime importance and can critically alter the final chemical composition, the structure, the microstructure and the electrical and thermal properties.[153] A composition deviation can cause a drastic change in charge carrier concentration to an extent where the whole electrical and thermal

transport behavior is different.[152,155,156] In this fashion, the third part of this chapter describes the influence of the synthesis and densification techniques on the structure, microstructure and thermoelectric properties of $Cu_{22}Fe_8Ge_4S_{32}$. Two powder synthesis approaches are compared, namely mechanical alloying and conventional sealed tube synthesis, combined with two densification methods: spark plasma sintering and hot pressing. This investigation drags attention to the significant impact of powder synthesis and sintering methods on the transport properties of complex quaternary Cu-based chalcogenides.

2.2 Sealed tube synthesis investigation

2.2.1 Sample preparation

Cu (99 %), Fe (99.5 %), S (99.5 %), and Ge (99.999 %) commercial powders, were stored and manipulated in a glove box under argon atmosphere. The powders were weighed in a stoichiometric ratio and ground together in an agate mortar. The 4 g batches of powder were then pressed into eight pellets of ≈ 0.5 g with a Φ = 5 mm die because compacted powders favor solid state diffusion. The pellets were placed in sealed silica tubes evacuated down to a pressure of ≈ 10^{-2} mbar from an argon atmosphere. The reaction took place in a tubular furnace in vertical position with a heating rate of 2 K min^{-1} and a plateau at 973 K for 24 h. The sample was cooled down to 770 K at a natural cooling rate by switching off the heat power of the furnace and then air quenched. For further information refer to the appendices in Chapter 5 (section 5.2.1.1).

2.2.2 NPD *in situ* heating reaction

For these experiments, unreacted elements mixed in a stoichiometric ratio to form germanite $Cu_{22}Fe_8Ge_4S_{32}$ were heated and cooled in a sealed tube within a furnace during a neutron diffraction experiment. The first pattern recorded at RT was refined by the Rietveld method with the elementary components; Cu ($Fm\bar{3}m$, a = 3.608(1) Å), Fe ($Im\bar{3}m$, a = 2.867(5) Å), Ge ($Fd\bar{3}m$, a = 5.646(7) Å) and α-S_8 ($Fddd$, a = 10.416 (5) Å, b =12.893(6) Å, c = 24.399 (8) Å) (Figure 2.1). Also, the precursors started to react together during the tube sealing as a CuS hexagonal phase can be indexed with the space group $P6_3/mmc$ (a = 3.783(2) Å, c = 16.329(2) Å). Due to the semi-amorphous nature of the silica tube, all the diffraction patterns present a noisy background.

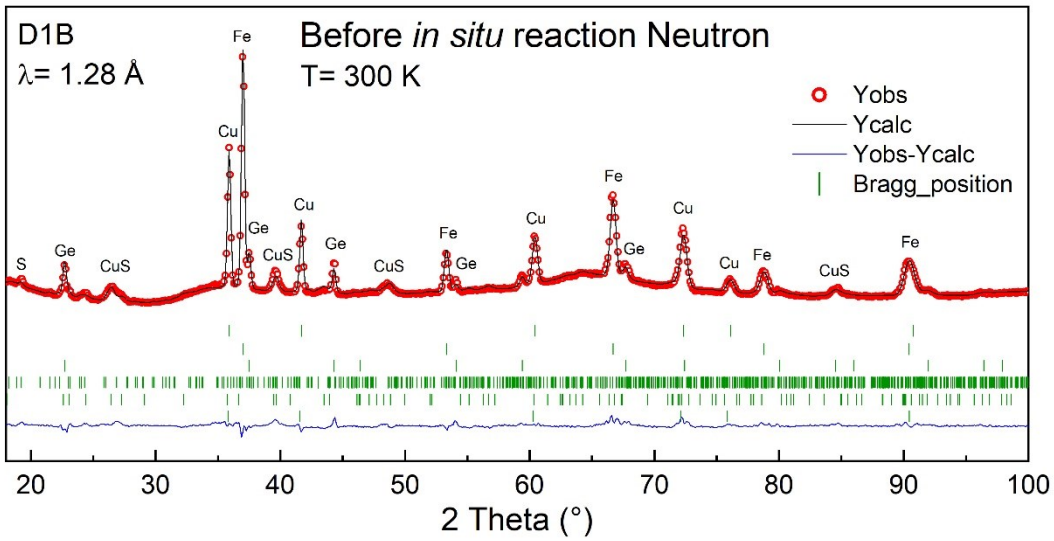

Figure 2.1. Rietveld refinement of the NPD pattern at RT of the precursors to form germanite $Cu_{22}Fe_8Ge_4S_{32}$ before the in situ reaction.

2.2.2.1 Heating from RT to 973 K

The heating from room temperature to 973 K of the aforementioned precursors can be divided in four reactivity zones regarding the formation and reactivity of intermediate compounds (Figure 2.2). During the three first reactivity zones (RT to 840 K), where Ge was still in its metallic state, the *in situ* experiment simply relates of the ternary Cu-Fe-S equilibria, which is extensively described in the literature[101,157,158] and consequently will not be discussed in details here. Note that in the following, the phases are named after their chemical formula for identification purposes, but are unlikely representative of the accurate stoichiometry. The nature of each phase was determined by the Rietveld refinement of patterns acquired at specific temperatures, *i.e.* the four zone transitions (T = 300 K, 470 K, 570 K and 840 K) and four intermediates (T = 525 K, 600 K, 675 K and 800 K). The first regime, from 300 K to 470 K, is a stable zone where all metallic precursors remained in their elementary state. The only observable change is the disappearance of sulfur diffraction peak close to its melting point ~ 390 K. Starting at 470 K, the second regime is characterized by the reaction of metallic copper with sulfur in its liquid state to form covellite CuS as first binary phase. Then, above 570 K, CuS reacted with metallic iron to form the first ternary phases, namely nukundamite $Cu_{0.85}Fe_{0.15}S$ and bornite Cu_5FeS_4.

Coincidentally with the formation of those ternary phases, metallic iron also reacted with sulfur in its liquid state, leading to a pyrite FeS_2 binary compound. The formation of the bornite Cu_5FeS_4 phase ~ 570 K will be confirmed in section 2.3.1 by Rietveld refinements and by the recognition of its characteristic topotactic transition temperatures. The highlights of this experiment are the formation of bornite, the most recurrent secondary phase, before the formation of the first quaternary phase and reaction at HT of the metallic Ge with a ternary Cu-Fe-S phase to form a quaternary compound.

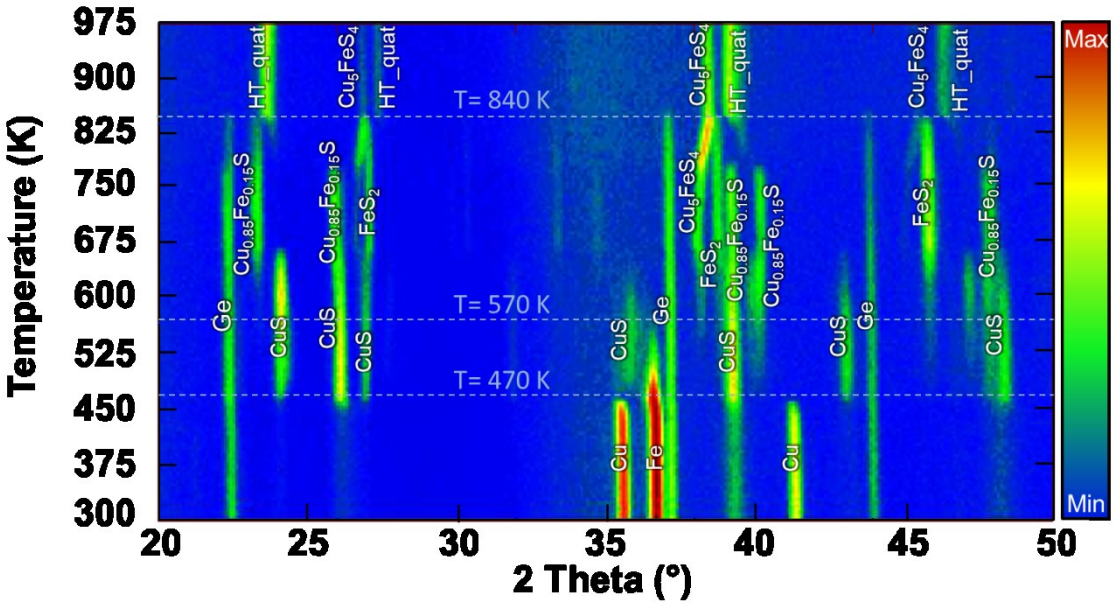

Figure 2.2. 2D contour plot showing the neutron powder diffraction patterns of an in situ sealed tube reaction of germanite. The minimum intensity is represented in blue and maximum in red.

2.2.2.2 Formation of a high temperature quaternary compound

The fourth and last region (840 K ≤ *T* ≤ 973 K) is characterized by the disappearance of metallic germanium, FeS_2 and $Cu_{0.85}Fe_{0.15}S$ replaced by a high temperature quaternary compound (HT_quat, Figure 2.2). Also, it is known that nukundamite is not stable above 800 K and decomposes into a bornite-digenite solid solution.[157] Experimentally, the heating ramp was followed by an isotherm of 2 h at 973 K, where the measured diffractograms did not vary significantly. The

summation of the neutron powder diffraction patterns measured during the isotherm at 973 K is shown in Figure 2.3. Yet, it is difficult to determine the symmetry of the high temperature quaternary phase and whether its an intermediate phase or the expected germanite compound. From the allowed reflections and their relative intensities, it is clear that this HT_quat has a close metric to cubic germanite ($P\bar{4}3n$), but it is also the case for many tetragonal quaternary compounds. Also, the lack of resolution makes it difficult to discriminate a cubic from tetragonal symmetry as the splitted peaks, distinctive of a tetragonal symmetry, are convoluted into a single peak (alike cubic).

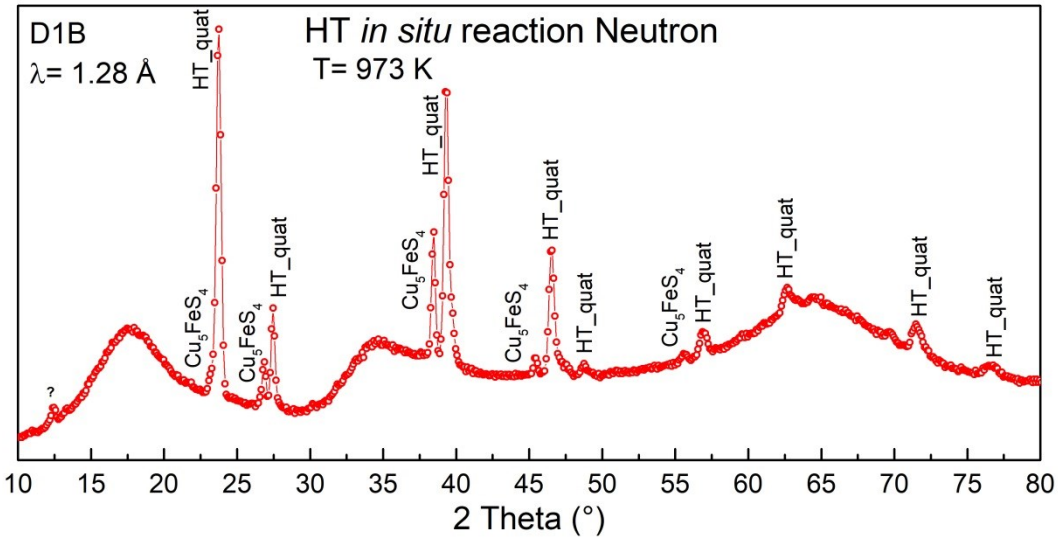

Figure 2.3. Summation of the NPD patterns measured at 973 K during the isotherm of the in situ reaction of $Cu_{22}Fe_8Ge_4S_{32}$. A question mark pinpoints the contribution of an unidentified phase.

Nevertheless, pattern-fitting considerations suggest a tetragonal symmetry as it leads to an improvement of the peak shape fitting. Indeed, most of the peaks were satisfyingly fitted with a tetragonal crystal system and an anisotropic strain. The tetragonal symmetry the most highly related to germanite space group ($P\bar{4}3n$) has a $P\bar{4}2c$ space group and is found in renierite compounds ($2a \times 2a \times \sim 2a$). Yet, the experimental conditions did not allow to detect the presence (or absence) of the renierite superstructure. Thus, a briartite phase ($I\bar{4}2m$, $a \times a \times \sim 2a$) was used for the refinement because it generates fewer reflections than renierite ($P\bar{4}2c$, $2a \times 2a \times \sim 2a$) and hence lowers the risk of an artificially low χ^2. Figure 2.4a shows

how the supplementary reflections of renierite, which are extinguished in a calculated intensity profile, artificially improves the χ^2 from 1004 for $I\bar{4}2m$ to 700.9 for $P\bar{4}2c$. Additionally, a closer look at the peak shape reveals a wide Gaussian tail on the right of the {*hhl*}, {*hll*} and {*hkl*} reflections. One cause of peak broadening is the distribution of the cell parameters induced by microdeformation (commonly referred to as microstrain). While isotropic microstrain produces $tan\theta$ dependent broadening, an additional *hkl*-dependence suggests that the microstrain is anisotropic. Although both isotropic and anisotropic strain models described adequately the peak profile of the (222) reflection (Figure 2.4b), that of {440} (Figure 2.4c) was greatly improved by applying the anisotropic microstrain model by Stephens (pink).[159] The standard isotropic strain model (blue) slightly underestimates the width of the {440} peaks. In the case of an anisotropic strain of a cubic space group ($P\bar{4}3m$ red, $P\bar{4}3n$ yellow, Figure 2.4d), the broadening would be symmetrical on both sides of the peak, thus excluding this option. For a tetragonal symmetry, Stephens model entails five parameters: *U*, *Y*, S_{220}, S_{202}, S_{400} and S_{004}; *U* is a Gaussian strain contribution, *Y* a Lorentzian size contribution and S_{hkl} the magnitude of the *hkl*-dependent peak broadening implying the following conditions: $a = b \neq c$ and $S_{220} \neq S_{202}, S_{400} \neq S_{004}$. Table 2.1 resumes the refined models and parameters of the anisotropic strain fittings. From a practical point of view, larger *S* values of the reflections with higher *l* contribution means that the *c* parameter has a broader cell parameter distribution than *a* and *b*.

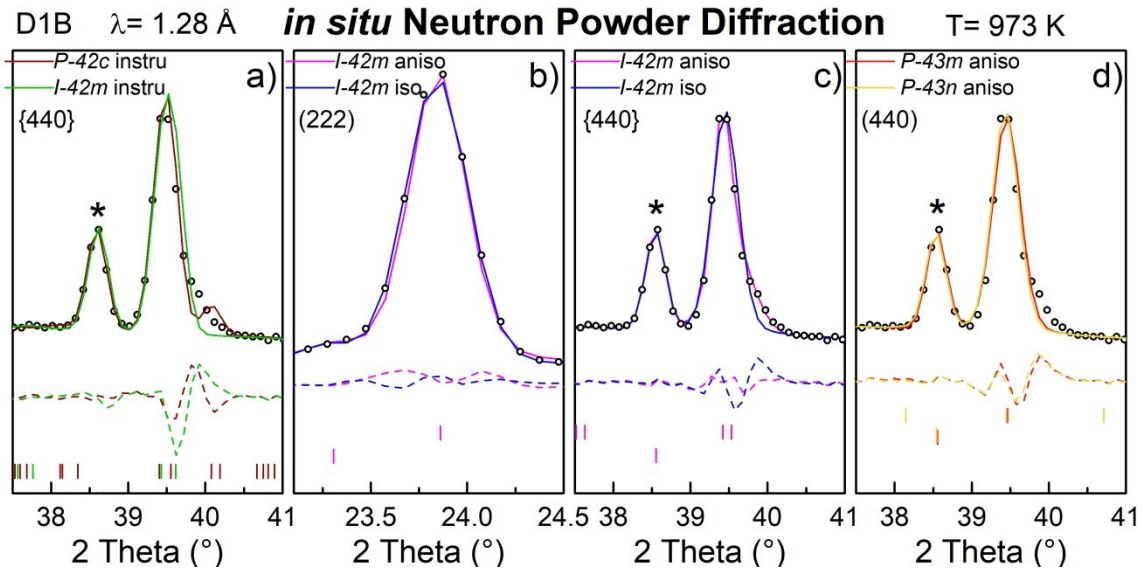

Figure 2.4. Different Le Bail fits of the NPD isotherm at 973 K of the HT_quat phase: a) $P\bar{4}2c$ (brown) and $I\bar{4}2m$ (green) refined with instrument resolution parameter only, b) and c) $I\bar{4}2m$ refined with an isotropic (blue) and anisotropic (pink) strain for reflections (222) and {440}, respectively and d) $P\bar{4}3m$ (red) and $P\bar{4}3n$ (yellow) refined with an anisotropic strain. An asterisk pinpoints a contribution of Cu_5FeS_4.

Table 2.1. Specifications of the refinement of the HT_quat phase on the pattern recorded at 973 K and anisotropic parameters.

	Tetra no strain	**Tetra no strain**	**Tetra isotropic strain**	**Tetra anisotropic strain**	**Cubic anisotropic strain**
Space group	$P\bar{4}2c$	$I\bar{4}2m$	$I\bar{4}2m$	$I\bar{4}2m$	$P\bar{4}3m$
***a* (Å)**	10.8111(6)	5.3978(1)	5.3957(5)	5.3890(3)	5.3898(4)
***c* (Å)**	10.732(4)	10.704(5)	10.752(3)	10.719(1)	
U			0.2494	0.2430	0.6299
Y			0.0695	0.0008	0.0643
S_{220}				-1.420	-0.6337
S_{202}				2.327	
S_{400}				-8.389	-2.517
S_{004}				4.962	
χ^2	700.9	1004	288.9	117.4	351.4

Stephens microstrain model largely captures the anisotropy of the broadening determined by individual fits and induces a clear improvement of the peak shape fitting. Furthermore, it would be interesting to verify the presence of such microdeformation by TEM, but since this phase exists at 973 K it is technically impossible. Yet, those crystallographic considerations do not invalidate the

presence of a cubic symmetry. On the contrary, it is highly probable that this anisotropic strain is in fact a homogeneous blend of closely related cubic and tetragonal phases. To address this hypothesis, the germanite synthesis was air quenched at 973 K in laboratory, to yield the sample utmost closely related to the HT composition. Figure 2.5 displays the refinement by Le Bail method of the XRPD pattern of the ST $Cu_{22}Fe_8Ge_4S_{32}$ synthesized and quenched at 973 K, which shows the coexistence of the germanite and renierite phases. The relative intensities deviation from the expected 2:1 ratio for a tetragonal symmetry, notably for the {440} and {622} reflections, suggests that the phase at HT is a mixture of cubic and tetragonal phases with the same metric. Finally, the absence of superstructure peaks is probably related to cationic disorder due to the high temperature quench. The a/c ratio of the HT_quat phase is $\sim$ 1.006, which is the one expected for a renierite phase.

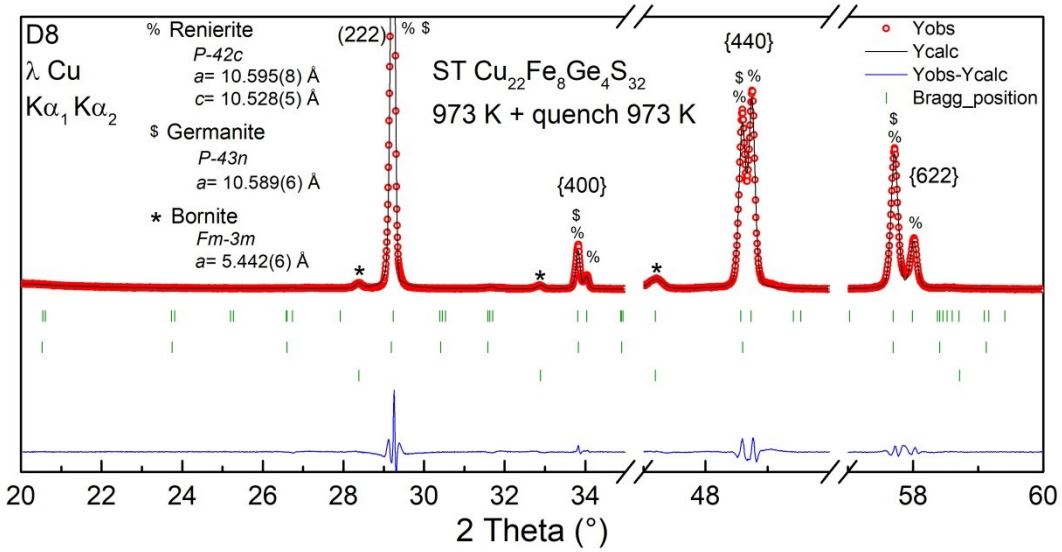

Figure 2.5. Le Bail refinement of the XRPD pattern of a $Cu_{22}Fe_8Ge_4S_{32}$ sample post ST reaction synthesized and air quenched at 973 K.

Now that we have identified the nature of the first quaternary compound synthesized from the metallic precursors of germanite, we will show the crystallization during cooling and see whether the germanite phase is formed or not.

2.2.3 NPD *in situ* cooling reaction

2.2.3.1 RT post reaction

To investigate the effects of the cooling conditions on the formation of germanite, a few *in situ* experiments were repeated, *i.e.* with the same heating conditions but with different cooling parameters. Before tackling the refinement of the patterns acquired during cooling, it is important to identify the nature of the phase resulting from the various cooling conditions. Accordingly, post reaction NPD patterns were measured on powders out of the silica tube during 2 h isotherms (Figure 2.6). Independently of the cooling method (*i.e.* by furnace inertia (Figure 2.6a) and by quenching at 973 K (Figure 2.6b)) the isolated compound was fitted with germanite space group ($P\bar{4}3n$). The structure of germanite was confirmed by the presence of its characteristic superstructure peaks at low angle (Figure 2.6a and b, first inset on the left). The blue line represents the simulated pattern of germanite ($P\bar{4}3n$, $a \approx 10.6$ Å) with Tettenhorst structural model.[147] The intensity discrepancies are probably owed to the different cationic distribution of the mineral and synthetic germanite (Chapter 4). Furthermore, the incompatibility of a tetragonal symmetry is obvious when comparing the observed data to a renierite-type structure simulation ($P\bar{4}2c$, $a \approx 10.6$ Å and $c \approx 10.5$ Å, red line) of the reflection (800) (Figure 2.6a and b first inset on the right).

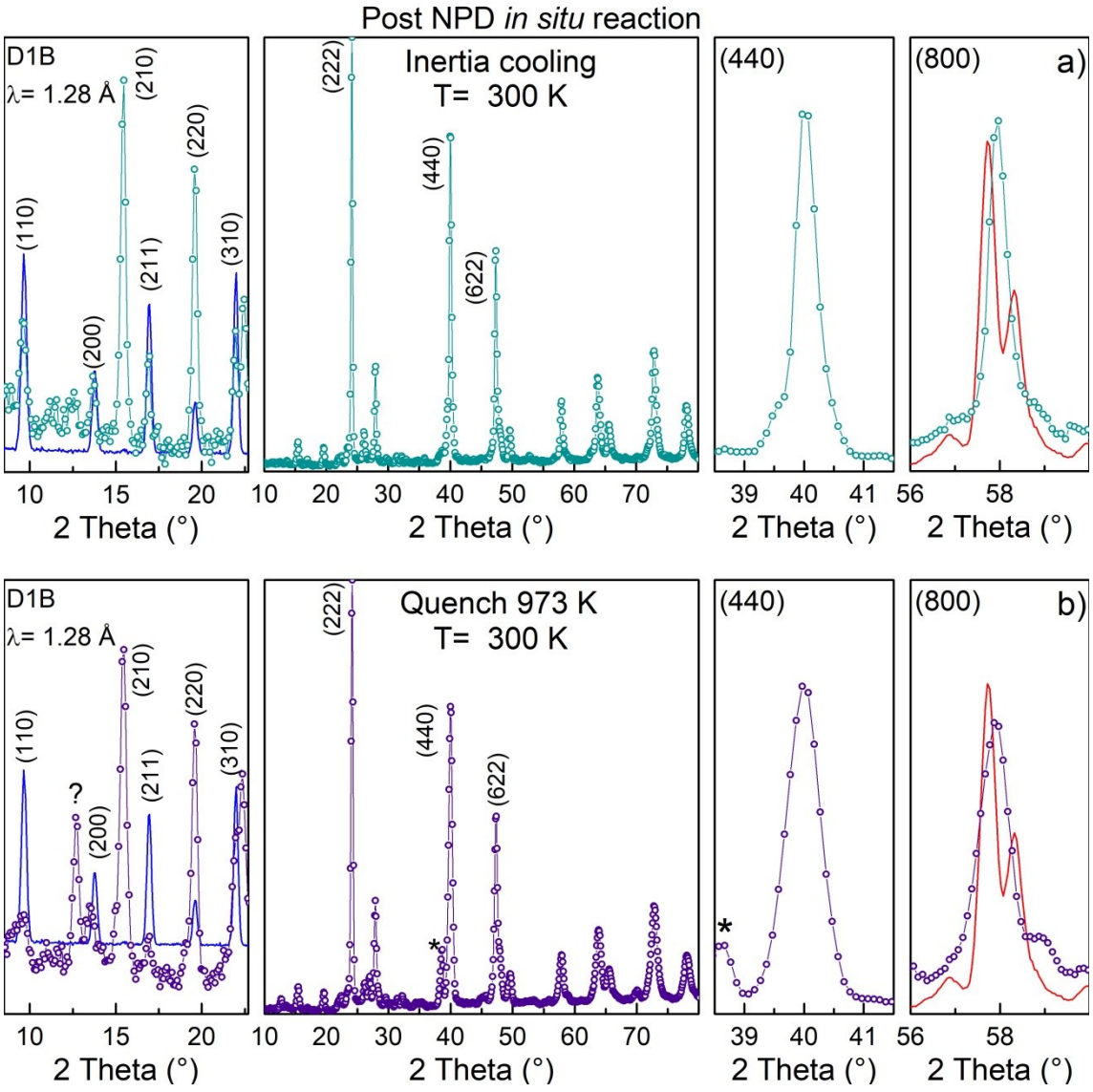

Figure 2.6. NPD patterns recorded at RT of a) a sample cooled by inertia and b) a sample quenched at 973 K. Both samples have an inset on the left to show the superstructure peaks compared to that of a simulated germanite (blue), an inset on the right to show the peak shape of (440) and another on the extreme right to compare the data with a simulated renierite structure (red). An asterisk identifies the main peak of bornite and a question mark an unknown phase.

The main difference between the sample cooled by furnace inertia and the sample cooled by quenching at 973 K is the presence/proportion of one or more secondary phases. Considering *ex situ* experiments done in the laboratory (Figure 2.5), the formation of germanite was unexpected for the sample quenched at 973 K during the *in situ* neutron experiments. Nevertheless, it is important to note that

environmental condition on D1B beamline prevented to do a proper air quench. Instead, the set point was fixed to zero, causing a rapid drop of the temperature to $\sim$ 470 K, where argon was introduced in the chamber and the sample took out. Thus it is possible that germanite was formed during this ''quench'' that lasted $\sim$ 1 h. The next section will address the circumstances of the formation of germanite along with the formation of some secondary phases.

2.2.3.2 Tetragonal to cubic phase transition from 973 K to 846 K

The refinement of the patterns acquired during the cooling ramp were executed with a more general model than the one defined for the high temperature isotherm. Indeed, the noisier data due to a shorter collection time and the shrinking cell parameters hinder the simultaneous refinement of the a, c and anisotropic microstrain parameters, as they are correlated. Thus, the patterns were refined using a tetragonal renierite space group ($P\bar{4}2c$) with a constant isotropic strain parameter and free cell parameters. In these conditions, the eventual emergence of new microstructural defects, expected during a phase transition,[160,161] would have repercussion on the cell parameters as they are the only degree of freedom. Thus, Figure 2.7a represents the evolution of a and c cell parameters, and their ratio as a function of temperature.

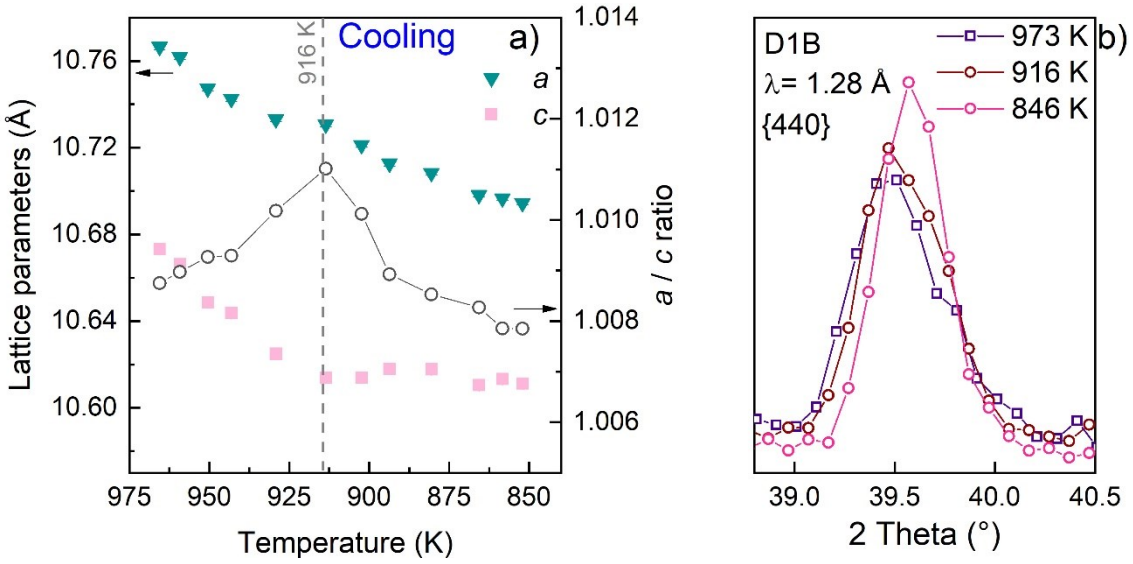

Figure 2.7. a) The cell parameters evolution of a $P\bar{4}2c$ phase during cooling (error bars smaller than symbols) and b) a section of the NPD patterns at 973 K, 916 K and 916 K showing the splitting of the {440} reflection.

The fluctuating slopes of the cell parameters and their ratio, a, c and a/c, against temperature suggest a structural change at 916 K, *e.g.* phase transition (Figure 2.7a). The steep increase of the a/c ratio from 973 K to 916 K can be regarded as FWHM widening. Indeed, by overlapping the {440} peak of the patterns measured at 973 K and 916 K (Figure 2.7b, purple and wine, respectively), one can notice that the peak lose its double summit for an equal in height, but slightly larger single peak. Such feature could be the signature of a tetragonal to cubic phase transition where both phases coexist. While it is expected for the {440} peak to be sharper in a cubic symmetry than in a tetragonal one (more reflections contribute), it is reasonable to witness such intermediate pattern with larger peaks due to microstructural disorder induced by the phase transition or by the coexistence of the two phases. Afterward, we observe the anticipated thinning of the {440} peak at 846 K (Figure 2.7b, pink). Two features suggest that germanite may crystallize between 916 K and 846 K. First, the a/c ratio decrease indicates that we might be going toward a cubic symmetry. Nevertheless, this ratio never reached unity because several convoluted parameters can contribute such as, the reminiscent microstructural defects, a possible admixture of germanite with a low-crystallinity phase and the thermal agitation parameters (B_{iso}). On the other

hand, the emergence of the (321) (Figure 2.8, blue) superstructure peak in the temperature range 860 K – 820 K, is a reliable feature that evidences the crystallization of germanite. In fact, all the superstructure peaks appear simultaneously, but (321) is first detected due to its higher angle (25.8°), hence sparing it from silica noisy background. Indeed, the noisy background coupled to the intrinsically low intensity of the superstructure peaks make their detection rather difficult.

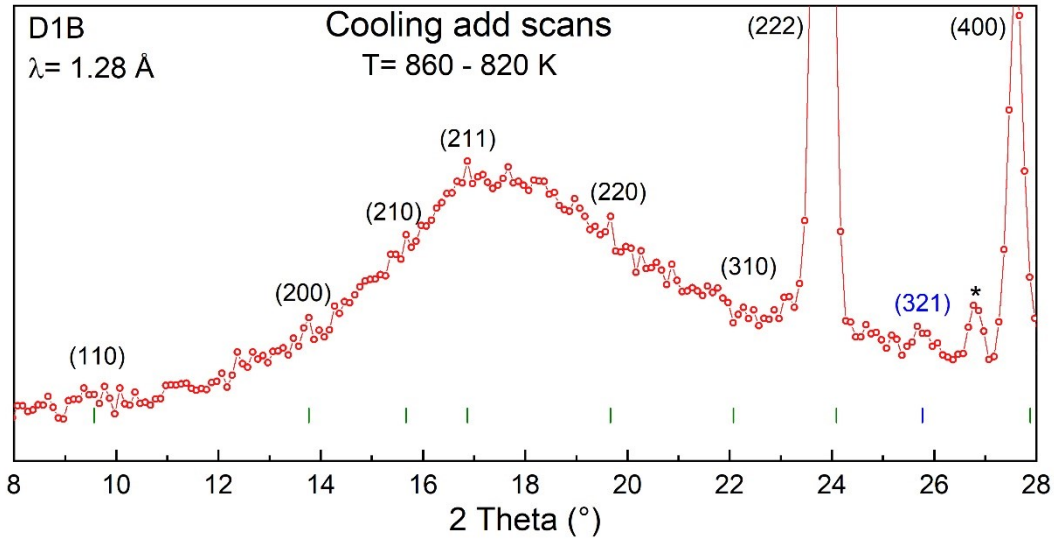

Figure 2.8. NPD pattern summation between 860 K and 820 K, showing the presence of a superstructure peak, (321) referring to the cubic crystal structure of germanite (space group $P\bar{4}3n$, $a \approx 10.68$ Å). An asterisk pinpoints a contribution of Cu_5FeS_4.

2.2.3.3 Refinement of cubic germanite from 900 K to 550 K

The refinement of the diffraction patterns were performed again from 900 K with a cubic germanite structure ($P\bar{4}3n$, a = 10.682(3) Å, Figure 2.9a). The cell parameters and the isotropic microstrain parameter are decreasing with the reducing temperature. The microstrain parameter can be seen as a probe of the a parameter distribution, thus the lower its value, the closer we are to a periodic and well-crystallized sample.

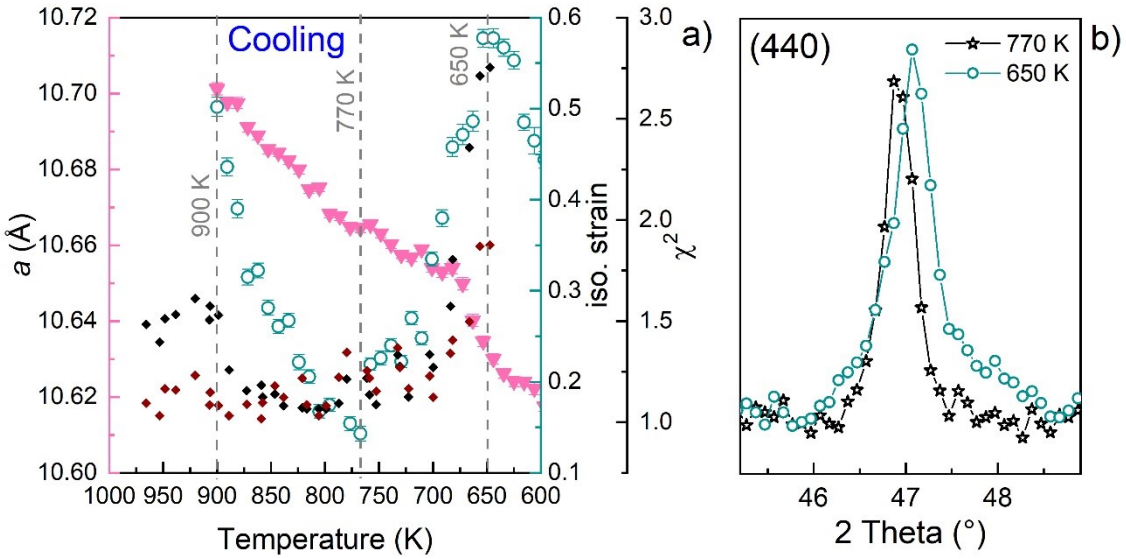

Figure 2.9. Results from the NPD in situ cooling: a) cell parameter (pink, left axis) and isotropic microstrain (teal, right axis) evolution of a cubic phase obtained by Le Bail refinement, χ^2 of the refinement with a $P\bar{4}3n$ space group (black, second axis on the right) and $P\bar{4}2c$ space group (wine, second axis on the right) and b) the diffraction peak (440) widening.

The sudden change of trend of the isotropic microstrain at 770 K may be assigned to the appearance of a low crystallinity phase with close Bragg reflections to that of germanite, thus adding a wide contribution at the base (Figure 2.9b). The formation of this phase at 770 K limits the possibility to obtain a pure sample below this point. Therefore, we conclude that the optimal condition to synthesize a high purity and high crystalline germanite sample is to quench the reaction between 900 K and 770 K.

2.2.3.4 Quench at 770 K

The goal of this *in situ* experiment is to reproduce exactly the same heating conditions as before and quenching the reaction at ~ 770 K to obtain a pure germanite sample. Figure 2.10a represents the neutron diffractogram measured at RT of the germanite sample after the reaction (out of the silica tube). The pattern was refined by Le Bail method with a cubic space group ($P\bar{4}3n$, a = 10.5912(1) Å). Figure 2.10b shows the Le Bail refinement of a germanite sample with a cubic

space group ($P\bar{4}3n$, a = 10.5934(6) Å) and synthesized in sealed tube for 24 h at 973 K and quenched at 770 K. Both patterns represent high purity germanite samples with similar cell parameters and no apparent bornite, thus confirming this cooling condition. A close-up of the main diffraction peak, (222), evidences an anomalous peak shape (Figure 2.10b). The next subsection is dedicated to the study of this peak shape by high resolution synchrotron powder diffraction.

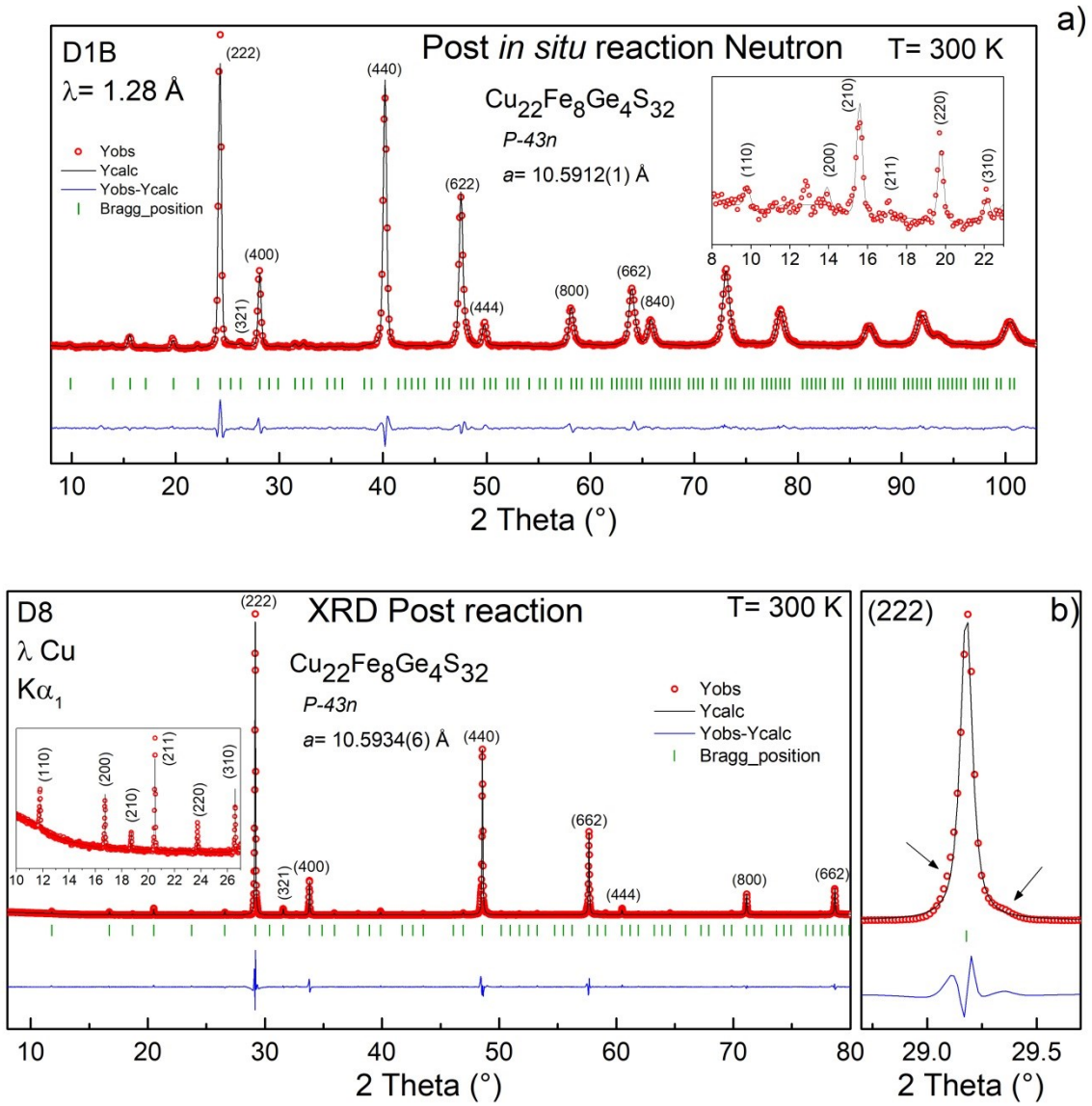

Figure 2.10. a) NPD pattern post in situ reaction, after a quench at 770 K and b) XRPD pattern after a 24 h reaction at 973 K and 770 K quench.

2.2.3.5 Anomalous peak shape characterization

The high resolution of synchrotron radiation yields an improved deconvolution of the peaks, which is useful in the case of germanite to separate the contribution of the odd peak shape. Figure 2.11 exhibits the XRPD pattern of a germanite sample ($P\bar{4}3n$, a = 10.5951(4) Å) produced by ST synthesis and refined by Le Bail method with an isotropic microstrain contribution to the peak width. First, we detected a bornite Cu_5FeS_4 phase that was indexed with a $Fm\bar{3}m$ space group (a = 10.9299(9) Å). Second, as each germanite peaks sit on a large bump, except for the superstructure peaks, this means that the phase responsible for this bump has the same average cell parameter as germanite but with a wider distribution. Also, the fact that the superstructure peaks are not affected by this widening of the base means that this phase has no superstructure or is characterized by a highly disordered cationic lattice. Thus, the bumps were refined with a sphalerite lattice ($F\bar{4}3m$, a = 5.307(5) Å) and a large isotropic microstrain *i.e.* a low crystallinity germanite. Third, the shoulder often seen on the right of the peaks was fitted correctly by a tetragonal renierite-type space group ($P\bar{4}2c$) with a a/c ratio of $\sim$ 1.006, which resembles that of the refined HT_quat phase at the quench temperature (section 2.2.2.2).

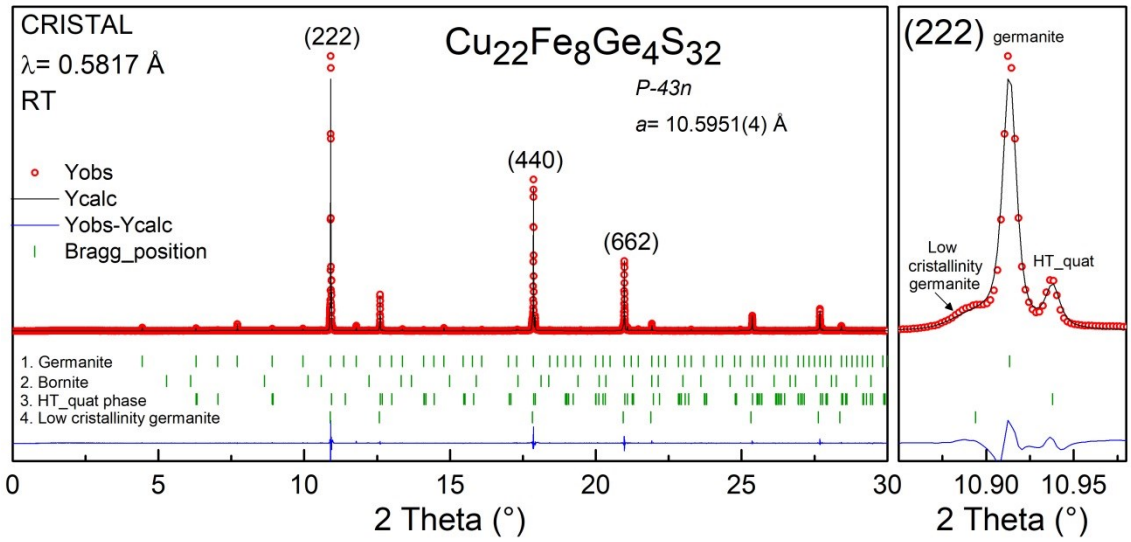

Figure 2.11. Le Bail refinement of a high resolution diffraction pattern of ST germanite acquired by synchrotron radiation.

2.2.4 Summary

- Real time *in situ* synthesis experiments in silica sealed tube are possible by NPD.
- The synthesis of germanite from elemental precursors follows a gradual path; binary forms from metallic precursors, followed by the formation of ternary and finally quaternary phases.
- The cubic germanite phase forms during cooling and starts around 916 K.
- The superstructure peaks appear in the temperature range: 860 K- 820 K.
- A semi-crystalline phase with cell parameters similar to germanite appears below 770 K.
- The cooling conditions to synthesize a pure germanite $Cu_{22}Fe_8Ge_4S_{32}$ sample are confirmed: slow cooling (2 K min^{-1}) from 973 K to 770 K and air quench from 770 K to RT.
- Contribution of the odd peak shape observed in every germanite sample: HT_quat phase and a semi-crystalline germanite-like phase (forms during cooling).

In the following, the thermal stability of germanite will be investigated in order to have a better perception of the transport properties behavior together with the acknowledgement of its workability.

2.3 Temperature stability

2.3.1 Identification of the ternary Cu-Fe-S phase

The investigations of the thermal stability of a complex compound such as germanite needs a detailed analysis of the secondary phases. The most recurrent secondary phase is most likely a bornite phase Cu_5FeS_4 ($Fm\bar{3}m$, a = 5.4290(1) Å, cubic high temperature polymorph). Rietveld refinements of the X-ray diffractograms using bornite structural model measured on germanite samples produced by ST led to satisfactory fits. Nonetheless, many related Cu-Fe-S compounds could fit this pattern as only three largely Gaussian peaks are observed. Therefore, the identity of bornite was confirmed by its characteristic phase transitions during an XRPD cooling experiment. Diffractograms were acquired each 50 K during 2 h isotherms (4 × 30 min). The diffractometer was a D8 Advance (*Bruker*) equipped with a molybdenum anticathode. For the sake of clarity and coherence, the data were converted to λ_{Cu}. For this experiment, a germanite sample containing bornite synthesized by ST was heated up to 1000 K and cooled down to RT (2 K min^{-1} rate) in a X-ray diffractometer. During the cooling ramp (Figure 2.12), a first phase transition of bornite was observed with the appearance of a peak around 27° at 550 K, namely the transition from the high cubic phase ($Fm\bar{3}m$, a = 5.4290(1) Å) to the intermediate cubic phase ($Fm\bar{3}m$, a = 10.9806(2) Å).[104] Afterward, another peak appeared around 32° at 450 K, which is the temperature reported for the transition of bornite from its intermediate cubic phase to the low orthorhombic phase (*Pbca*, a = 10.937(6) Å, b = 10.959(2) Å and c = 21.929(8) Å).[104] In conclusion, in the light of those phase transitions and conclusive Rietveld refinements, it is reasonable to assume that the ternary Cu-Fe-S phase present in the germanite samples is a bornite Cu_5FeS_4 phase.

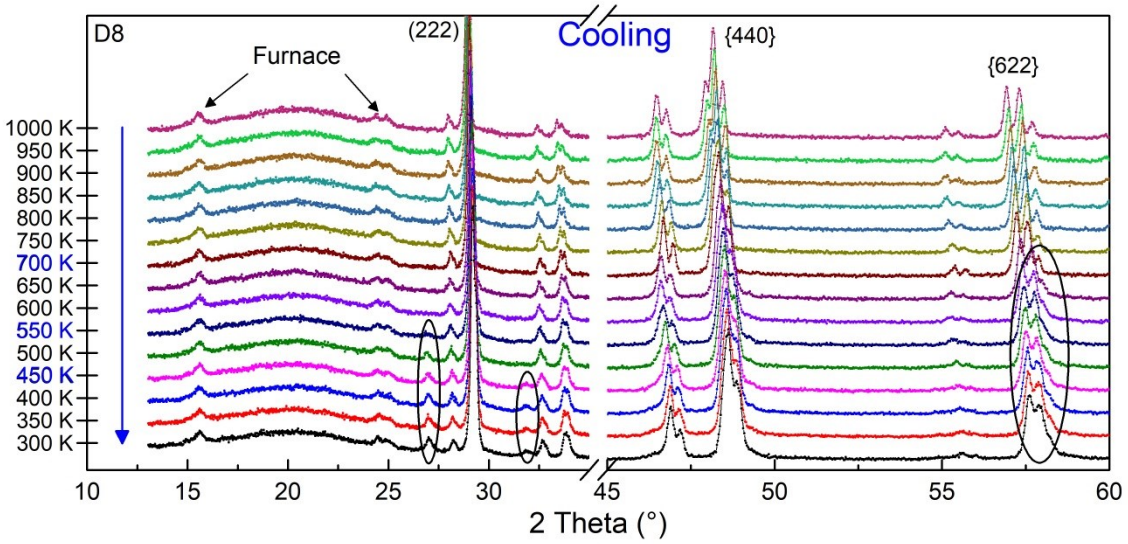

Figure 2.12. XRPD patterns from 1000 K to RT of a ST germanite $Cu_{22}Fe_8Ge_4S_{32}$ sample showing two phase transitions of bornite (data converted from λ_{Mo} to λ_{Cu}).

2.3.2 Identification of the reactivity windows by DSC

Differential scanning calorimetry was used as first assessment of the thermal stability of germanite. Figure 2.13 displays the DSC signal of a ST germanite $Cu_{22}Fe_8Ge_4S_{32}$ sample (in a vacuum-sealed ampoule) between RT and 1273 K (heating rate of 5 K min^{-1}). Throughout heating, three events were observed; (i) an endothermic peak possibly linked to a phase transition at ~ 910 K, (ii) an exothermic peak at ~ 1065 K and (iii) an endothermic peak around 1190 K, which is probably owed to the melting of the phase. The interpretation of those thermal events will require complementary analyses and thus will be addressed in the next sections. The subsequent cooling ramp features two main events: (i) an exothermic event (two peaks) which typically look like a liquid to solid transition and share a common temperature (1190 K) with the alleged melting peak and (ii) an exothermic peak at ~ 700 K, which could be the crystallization of a semi-crystalline germanite-like phase, as it was observed in the *in situ* synthesis experiment. However, it is important to note that since germanite melted and lost sulfur during the heating ramp, it is possible that the phase measured during the cooling ramp is not germanite. Nonetheless, this experiment settles the zones of

interest and working limits for the diffraction investigation, which will grant an insight of the crystallographic changes.

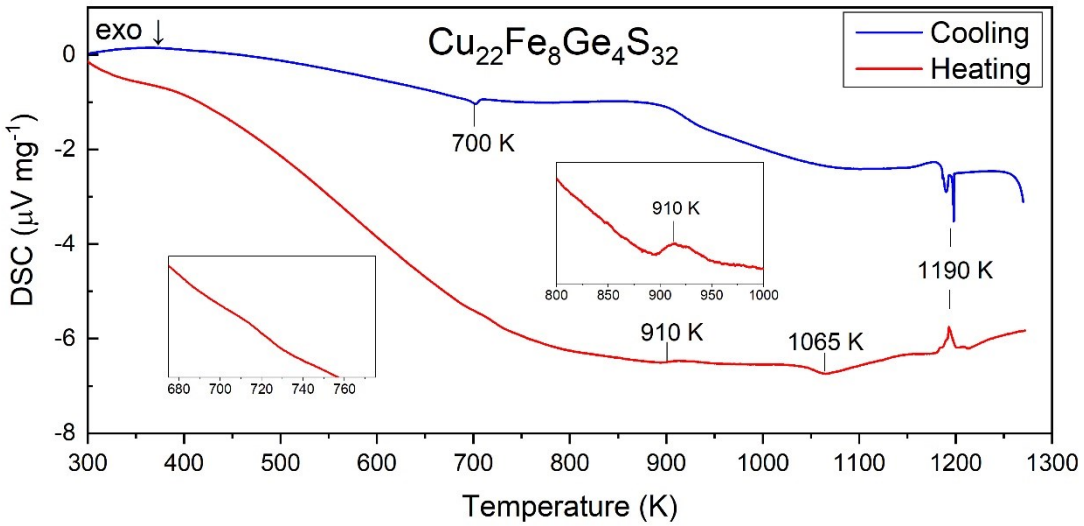

Figure 2.13. Temperature stability investigations on germanite by DSC in sealed ampoule. The heating curve is red and the cooling curve is blue.

2.3.3 Structural transitions during heating

2.3.3.1 Powder diffraction

This section is dedicated to the description of the thermal stability of germanite from a crystallographic point of view with analyses performed by neutron and X-ray diffraction versus temperature. Figure 2.14 shows the Le Bail refinement of a NPD pattern (D1B, λ = 2.52 Å) at 300 K of a germanite sample ($P\bar{4}3n$, a = 10.599(1) Å). This wavelength was chosen over λ = 1.28 Å because it grants a higher neutron flux, necessary for the study of the superstructure. However, a downside of this wavelength (λ = 2.52 Å) is the rapid increase of the peaks FWHM with 2θ, which is rather penalizing for phase transition observations.

In the spirit of full disclosure, note that experimental difficulties encountered during the heating ramp (abrupt rise of the temperature due to a power change of the furnace) preclude the interpretation of the NPD data recorded

between 700 K and 827 K. Consequently, we can observe a mild peak shift around 700 K in Figure 2.15 and the absence of cell parameters between 700 K and 827 K in Figure 2.16. For both beam time allocation and mass sample availability reasons, we were not able to reproduce the experiment.

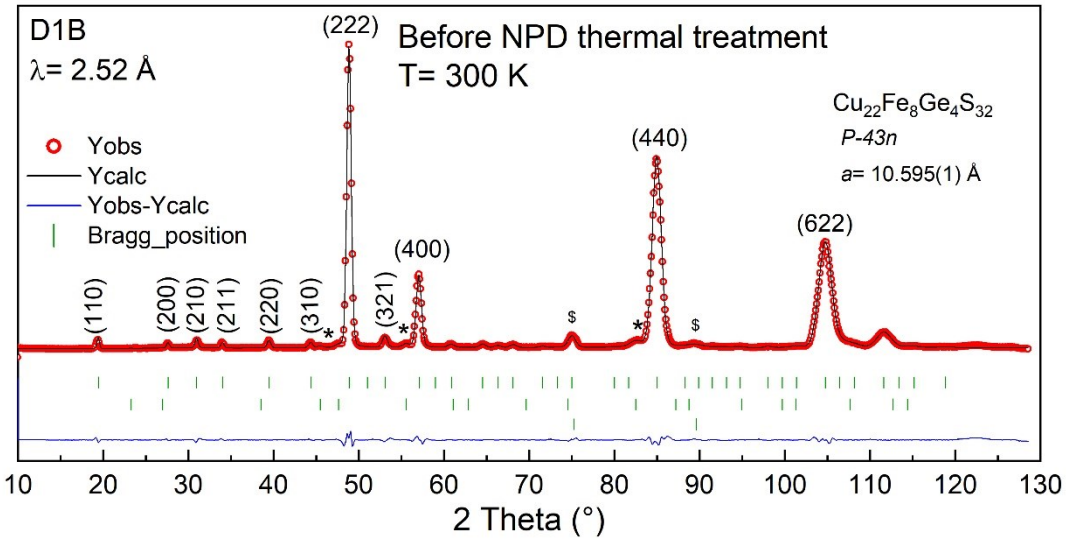

Figure 2.14. Le Bail refinement of germanite $Cu_{22}Fe_8Ge_4S_{32}$ ($P\bar{4}3n$, a = 10.595(1) Å) measured by NPD at RT. The bornite ($Fm\bar{3}m$, a = 10.852(7) Å) contributions are pinpointed by an asterisk and that of the thermocouple by a dollar sign.

The diffractograms collected each 10 K from 338 K to 973 K evidenced three events (Figure 2.15). The first one at ~ 700 K could reasonably be assigned to the crystallization/formation of bornite, which was not observed by DSC due to the low weight fraction of the phase (Figure 2.13). Whether the bornite was formed during the synthesis (in an amorphous form) or during the post-synthetic thermal treatment, is a good indicator of the germanite thermal stability. In any case, the presence of bornite implies a stoichiometry deviation from the nominal stoichiometry of germanite, as the latter represents the only source of elements (Chapter 4, section 4.3.6). The second event, also at ~ 700 K, is the disappearance of two superstructure peaks of germanite, namely (210) and (220), which happened 130 K before the disappearance of all superstructure peaks. This could be the signature of a magnetic transition and will be discussed in Chapter 4 (section 4.3.7).

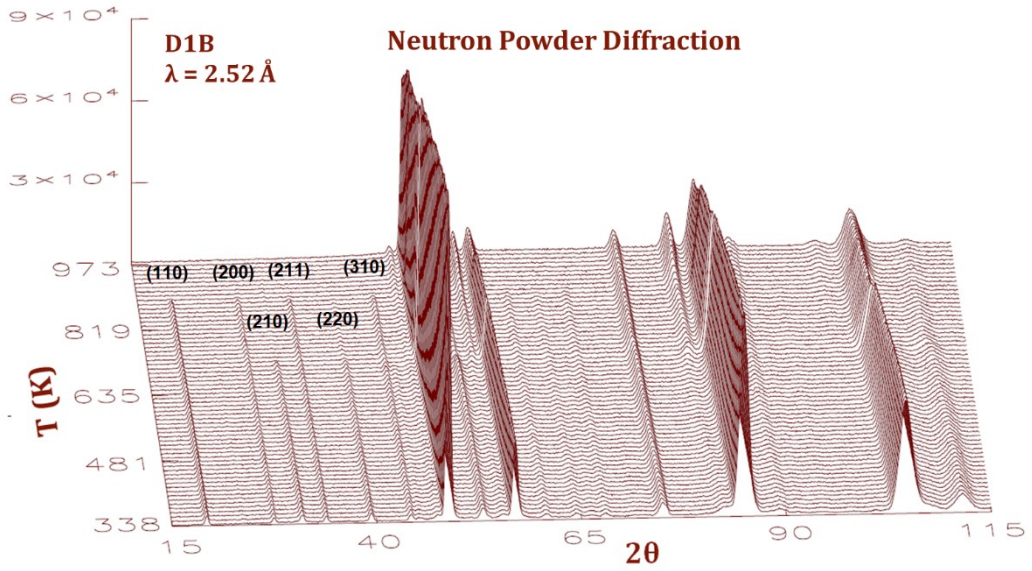

Figure 2.15. Neutron powder diffractograms of germanite $Cu_{22}Fe_8Ge_4S_{32}$ between 338 K and 973 K.

The third event at ~ 910 K (pinpointed by DSC, Figure 2.13) was the complete disappearance of germanite remaining superstructure peaks. The loss of those peaks implies the loss of the supercell, which is probably owed to some cationic disorder induced by the high temperature conditions. Such cationic disorder is expected to cause an increase of the unit cell.[141,162] Therefore, we have investigated the cell parameter expansion of germanite ($P\bar{4}3n$) versus temperature (Figure 2.16). The linear thermal expansion of the cell parameters from 400 K to 700 K attests the chemical stability of germanite in this temperature window. In contrast, the predicted cell parameter at 830 K (a = 10.685 Å), calculated by extrapolation of the data between 400 K and 700 K, is lower than that obtained by Le Bail refinement (a = 10.704(1) Å). This apparent cell parameter increase at 830 K is in agreement with the presence of cationic disorder in the germanite structure induced by the high temperature conditions.

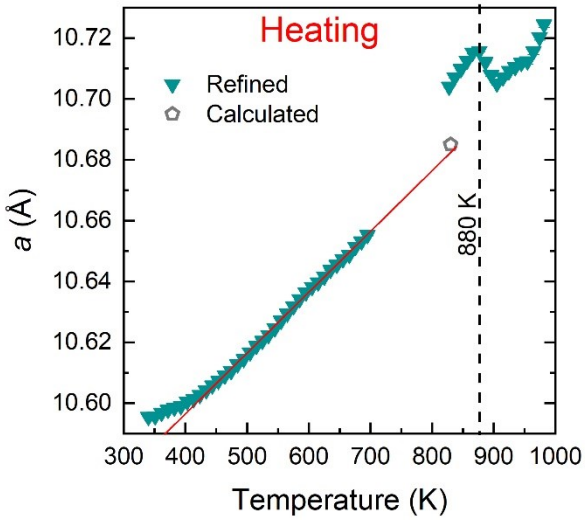

Figure 2.16. Refined cell parameter variation with temperature (teal). The cell parameter expected at 830 K from a linear regression is shown in grey.

Moreover, Figure 2.16 shows a major incongruity of the cell parameter evolution at 880 K. Such behavior could be the signature of a phase transition. Yet, it is delicate to identify a symmetry modification from these high temperature neutron diffractograms because of the rapid increase of the peaks FWHM with 2θ. To address that, the experiment was repeated with X-rays (Figure 2.17). The XRD thermal investigation was carried out on a sealed capillary between 300 K and 1000 K. The diffractograms were collected each 50 K, during 2 h isotherms (4 × 30 min), using a D8 advance with a non-monochromatized X-ray Mo source. For clarity and coherence purposes, the diffractograms were converted to λ_{Cu}. Also, the detection of superstructure peaks was problematic because the furnace diffracted at ~ 15° and ~ 25° and thus hid most of the germanite superstructure peaks, except for (211) and (321).

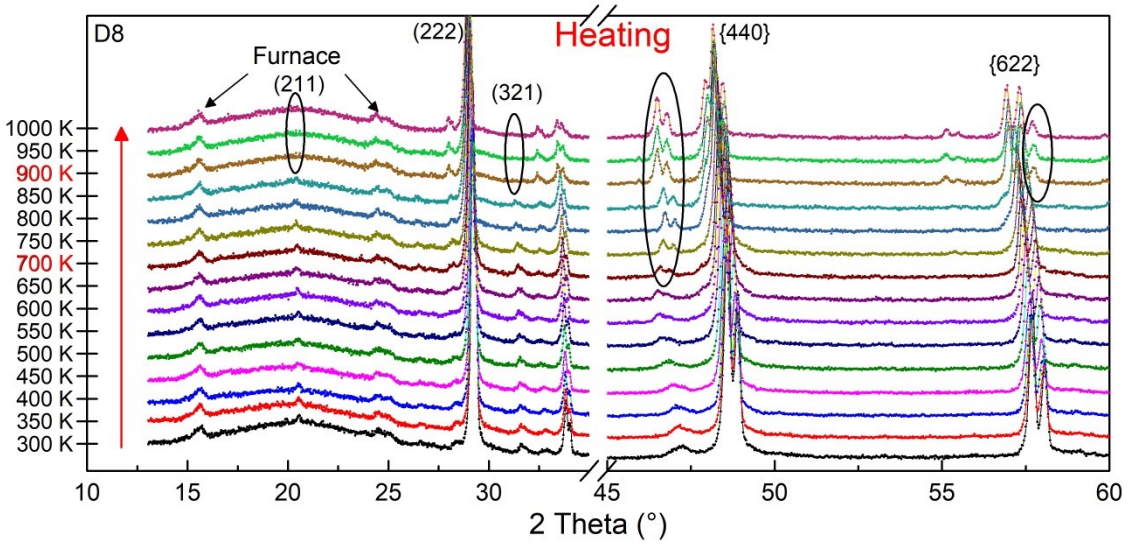

Figure 2.17. XRPD temperature stability experiments from RT to 1000 K on a germanite $Cu_{22}Fe_8Ge_4S_{32}$ synthesized by ST (data converted from λ_{Mo} to λ_{Cu}).

The *in situ* NPD experiment was successfully reproduced by XRD in spite of the inherent experimental differences. Indeed, the (211) and (321) superstructure peaks disappeared at ~ 900 K, which is close to the temperature measured during the NPD experiments (~ 910 K). As we anticipated, X-ray diffraction allowed to witness the appearance of new peaks at the temperature of the phase transition (~ 900 K). In a cubic $P\bar{4}3n$ symmetry, the appearance of a peak next to the (440) reflection and one next to the (622) reflection, which are (*hhl*) and (*hll*) Bragg reflections, is an argument in favor of a cubic to tetragonal structural transition. Indeed, a tetragonal distortion of germanite cubic structure engenders a splitting of equivalent reflections into two reflections for the (*hhl*) and (*hkk*) reflections (allowed by the cubic space group) or into three reflections for the (*hkl*) reflections (allowed by the cubic space group). Then, by comparing the Rietveld refinements of the HT phase using the germanite structure ($P\bar{4}3n$, a = 10.70(7) Å)[147] and the renierite structure ($P\bar{4}2c$, a = 10.72(8) Å and c = 10.63(9) Å)[163], we confirmed that the ‘‘germanite’’ phase at high temperature (973 K) crystallizes in a tetragonal space group (Figure 2.18a and b, respectively). In this case, a Rietveld refinement was necessary. Indeed because Le Bail method extracts the intensities (I_{hkl}) from the powder diffraction data, it would have been problematic to discriminate a cubic and a tetragonal symmetry due to the presence of the $K\alpha_2$ reflections. Note

that the refinement using a briartite structural model ($I\bar{4}2m$, a = 5.36(5) Å and c = 10.63(4) Å) led to an equivalent fit. The renierite was chosen over briartite as it is the direct tetragonal deformation of germanite.

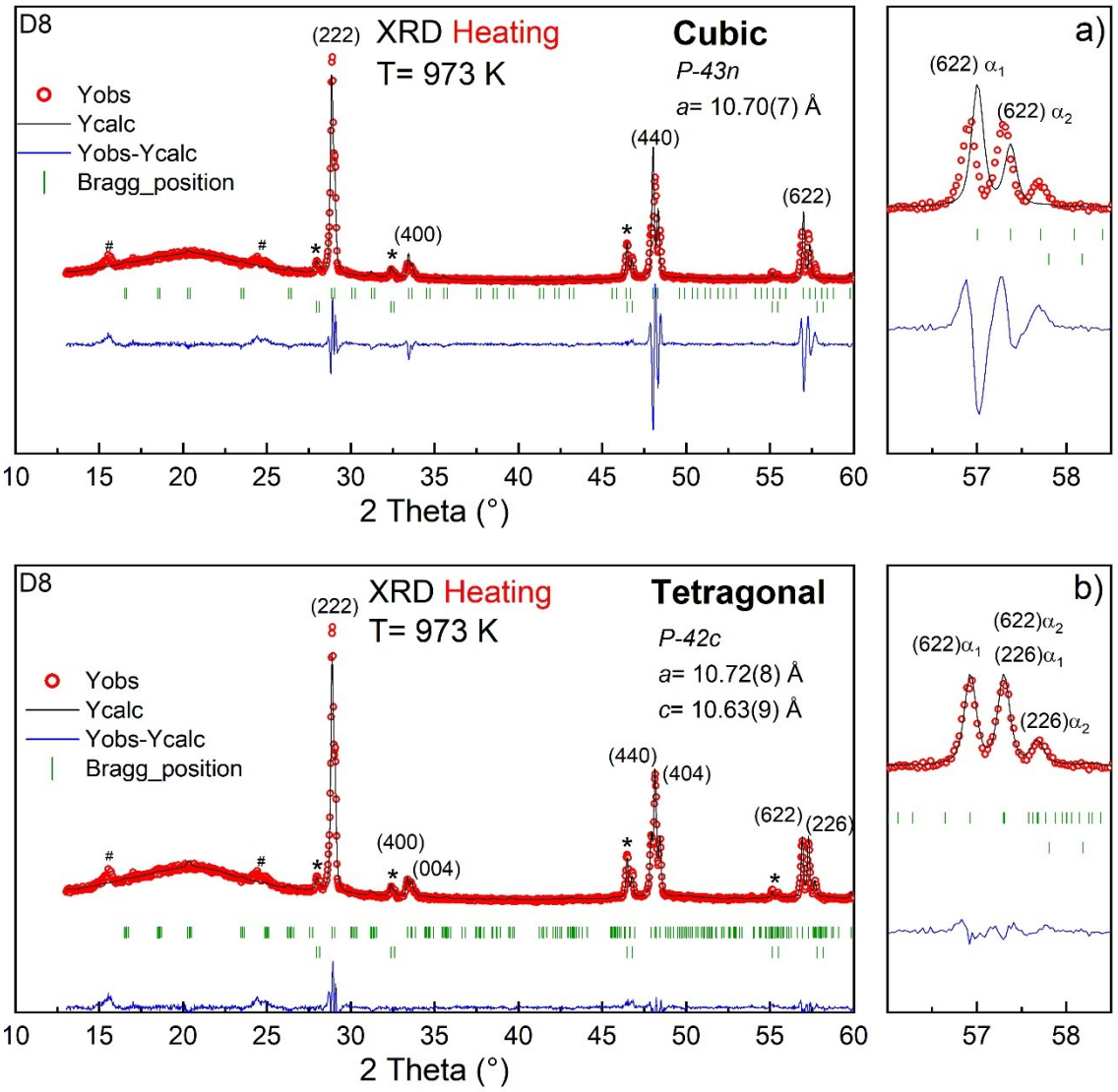

Figure 2.18. Rietveld refinements of the XRPD pattern at HT (973 K) in a) with a cubic germanite structure ($P\bar{4}3n$, a = 10.70(7) Å) and in b) with a tetragonal renierite structure ($P\bar{4}2c$, a = 10.72(8) Å c = 10.63(9) Å) (data converted from λ_{Mo} to λ_{Cu}). An asterisk and a hash sign identify the contributions of the bornite and the furnace, respectively.

2.3.3.2 TGA-DSC experiments

In order to determine the nature of the phase formed above 900 K, it is important to understand the origin of this phase transition. Hence, this experiment aims to rationalize the phase transitions interdependency, *i.e.* formation of a secondary phase/main phase transition, in term of sulfur loss. To do so, a $Cu_{22}Fe_8Ge_4S_{32}$ sample synthesized by sealed tube was cycled in temperature from 373 K to 973 K in a platinum pan in an argon flux. Figure 2.19 displays the TGA signal (left axis) and DSC signal (right axis). A weight diminution is observable on the whole temperature range. Weight loss in sulfide minerals can mostly be assigned to sulfur volatilization. During heating, slope changes at 650 K and 880 K are observable: the slope become more steep, and thereby translates an acceleration of sulfur volatilization rate. Those temperatures coincide with the formation of bornite (650 K) and the phase transition from cubic to tetragonal HT (880 K – 910 K). Note that during the length of this work, the TE properties of all samples were measured from RT to a maximal temperature of 650 K, where the ''weight loss'' for $Cu_{22}Fe_8Ge_4S_{32}$ was about 1.03 %. At the maximal temperature of the stability studies, 973 K, the ''weight loss'' of the sample was 5.45 %.

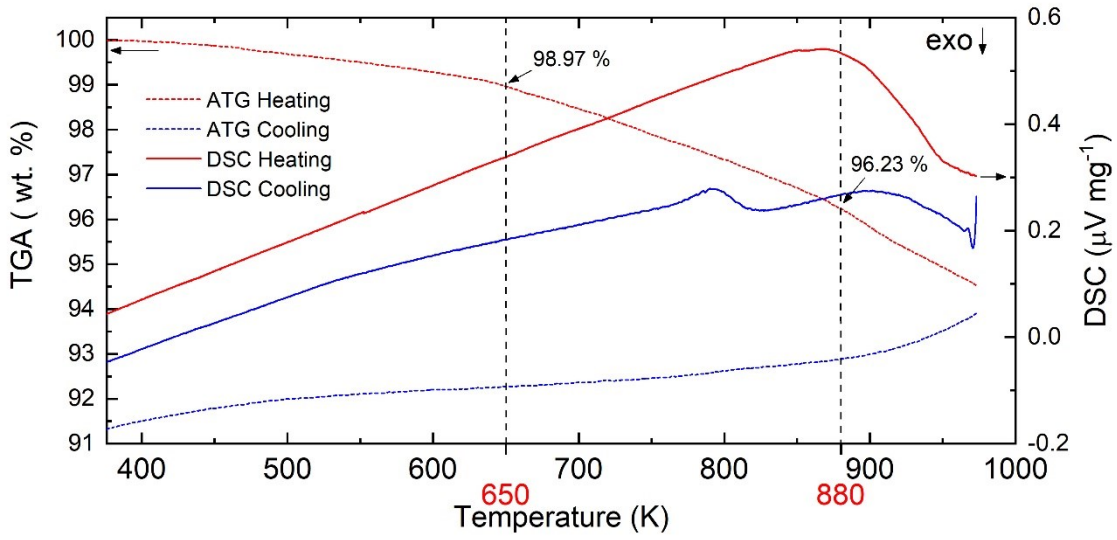

Figure 2.19. TGA-DSC of a ST germanite $Cu_{22}Fe_8Ge_4S_{32}$ sample in a platinum pan.

2.3.3.3 Rietveld analysis

Figure 2.20 displays the weight fraction evolution versus temperature of germanite and bornite obtained by Rietveld refinement of the NPD patterns (left axis) and the M_{tot}/S ratio of the sample obtained from TGA analysis (right axis). The weight percentages of the two phases are inaccurate because germanite was refined with Tettenhorst structural model,[147] *i.e.* the structural model for mineral germanite which does not have the same stoichiometry. Nevertheless, it provides an adequate approximation of the relative weight fraction evolution of the two phases with temperature.

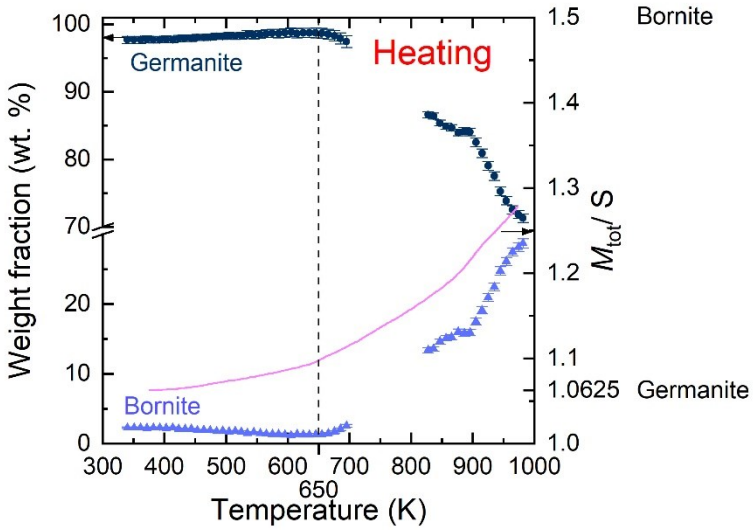

Figure 2.20. Approximate weight fraction of germanite (dark blue) and bornite (light blue) obtained by Rietveld refinements of NPD data (left axis) and the M_{tot}/S ratio calculated from TGA measurements (pink curve, right axis).

Considering that bornite Cu_5FeS_4 has a higher M_{tot}/S ratio than germanite $Cu_{22}Fe_8Ge_4S_{32}$ (1.5 against 1.0625, respectively), it is not surprising to detect the formation of bornite together with sulfur loss. Three mechanisms could possibly explain how the germanite structure deals with this sulfur sub stoichiometry: (i) sulfur vacancies are generated, (ii) the sulfur network is maintained and the resulting extra cationic elements occupy new interstitial sites and (iii) the sulfur network is maintained and the extra cationic element are balanced by the formation of secondary phase such as bornite. In fact, at 650 K, the weight percentage is ~ 99.0 %, which corresponds to 1 *eq.* of sulfur lost (formula weight of

3160.96 g mol^{-1}) and represents a M_{tot}/S ratio of 1.097, which gives a formula: $Cu_{22}Fe_8Ge_4S_{31}$ (assuming that the starting stoichiometry is $Cu_{22}Fe_8Ge_4S_{32}$). This yields a structural arrangement of high energy as some cations can ''see'' each others, hence giving rise to cationic repulsions. Thus, from a qualitative Coulombic forces point of view this meachnism is not favored. The second sulfur loss coping mechanism, where the sulfur network is maintained and the extra cationic elements occupy interstitial sites, is assumedly to be more energetically favorable. However, the refinement of X-ray diffraction data measured on a germanite $Cu_{22}Fe_8Ge_4S_{32}$ single crystal rejected the significant occupation other interstitial sites than $2a$ (Chapter 4, section 4.3). Thus, this leaves the thirst mechanism, where the sulfur loss is said to be compensated by the formation of secondary phases. The formation of bornite with germanite Cu, Fe and S atoms tends the latter to have a Ge-rich composition. In conclusion, the renierite phase formed ~ 880 – 910 K is likely to respect the M_{tot}/S = 1.0625 but is likely to have a Ge-rich composition.

2.3.3.4 High temperature phase: discrimination between renierite and briartite

The discrimination between a renierite and briartite phase is complicated due to their close metric and space group. Also, due to the absence of a trustable structural model for synthetic renierite, one has to rely on other intrinsic features to distinguish its occurrence from a briartite one, such as the cell parameter a/c ratio, the cation over anion ratio M_{tot}/S and the relative ratio of some cationic species as Ge/M_{tot}. By averaging the different entries in ICSD, a $2a/c$ ratio of ~ 1.0132 was obtained for briartite and a a/c of 1.0068 for renierite.[163–170] A summary of the differences between a renierite and a briartite structure, apart from the structural model, is described in Table 2.2. These latter are also compared to bornite, as it is a recurrent phase in the germanite system.

Table 2.2. Differences between three structural types: renierite, briartite and bornite.

Renierite	**Briartite**	**Bornite**
$\boldsymbol{P\bar{4}2c}$	$I\bar{4}2m$	$Fm\bar{3}m$*
$\boldsymbol{a/c = 1.0068}$	$2\,a/c = 1.0132$	$a/c = 1.0000$
$Cu_{20}Zn_2Fe_8Ge_4S_{32}$	Cu_2FeGeS_4	Cu_5FeS_4
$\boldsymbol{M_{tot}/S}$ = 1.0625	M_{tot}/S = 1.0	M_{tot}/S = 1.5
$\boldsymbol{Ge/M_{tot} = 0.117}$	$Ge/M_{tot} = 0.25$	$Ge/M_{tot} = 0$

*Two of the three polymorphs are cubic

Figure 2.21 shows the Le Bail refinement of a NPD pattern of the sample $Cu_{22}Fe_8Ge_4S_{32}$ at high temperature (973 K) with renierite ($P\bar{4}2c$, a = 10.756(2) Å, c = 10.667(1) Å). Renierite was chosen over a briartite for different arguments. The Le Bail refinement of the pattern gives a $a/c = 1.0083$ ratio, which is closer to renierite (1.0068) than to briartite ($2a/c = 1.0132$). Also, a transition from $P\bar{4}3n$ to $P\bar{4}2c$ was observed in a Zn substituted germanite series described in Chapter 3 (section 3.2).

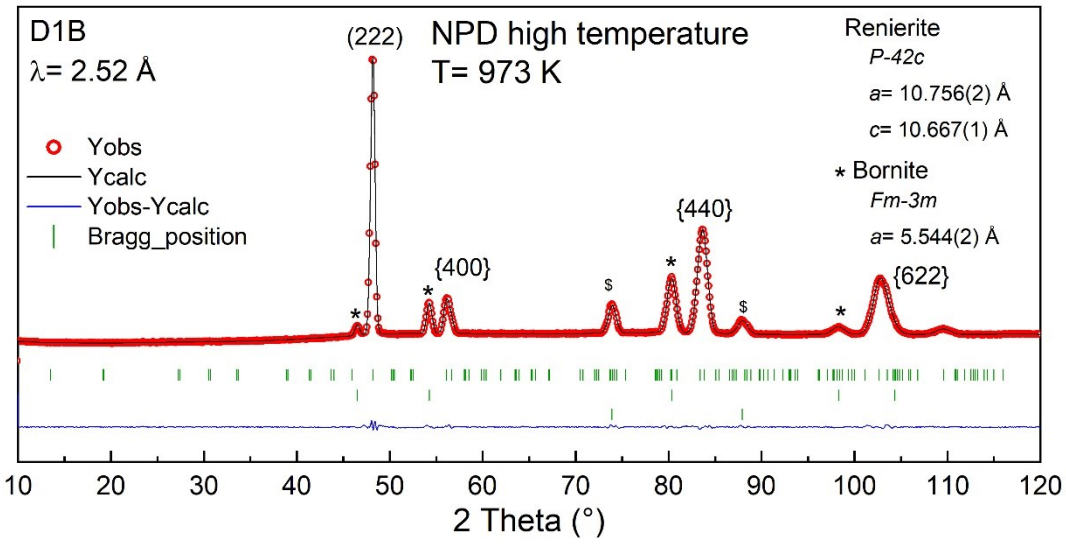

Figure 2.21. Le Bail refinement of the NPD pattern at 973 K. The main phase is refined with a P$\bar{4}$2c (a = 10.756(2) Å, c = 10.667(1) Å) space group and a Fm$\bar{3}$m (a = 5.544(2) Å) space group for bornite (identified by an asterisk). A dollar sign marks the thermocouple contribution.

2.3.4 Cooling

2.3.4.1 RT post reaction

In order to facilitate the interpretation of the *in situ* diffraction patterns collected during the cooling ramp, the final state of the sample will be determined. The isotherm NPD pattern, recorded at 330 K post reaction, was refined by the Rietveld method with a briartite structural model ($I\bar{4}2m$, a = 5.337(6) Å, c = 10.548(2) Å) and a bornite structural model ($Fm\bar{3}m$, a = 10.966(2) Å, Figure 2.22). The refinement yielded a weight fraction of 56 % for briartite with R_f = 2.67 % and R_{Bragg} = 1.02 % and a weight fraction 44 % for bornite with R_f = 3.37 % and R_{Bragg} = 3.38 % and an overall χ^2 = 34.63. In this case, the structural model of briartite was preferred over that of renierite for several reasons. First, the Rietveld refinement with the briartite structure led to a χ^2 = 34.63, compared to χ^2 = 1248 with the renierite structure. Second, the refined $2a/c$ ratio of the main phase is equal to 1.0119, which is closer to the average $2a/c$ of briartite than that of renierite (1.0130 and 1.0068 (a/c)), respectively. Finally, yet importantly, briartite has a Ge-rich nominal stoichiometry, Cu_2FeGeS_4, with a Ge/M_{tot} = 0.25, compared with a Ge/M_{tot} = 0.117 for renierite, which is in agreement with the Ge-enrichment of the phase due to the formation of bornite Cu_5FeS_4.

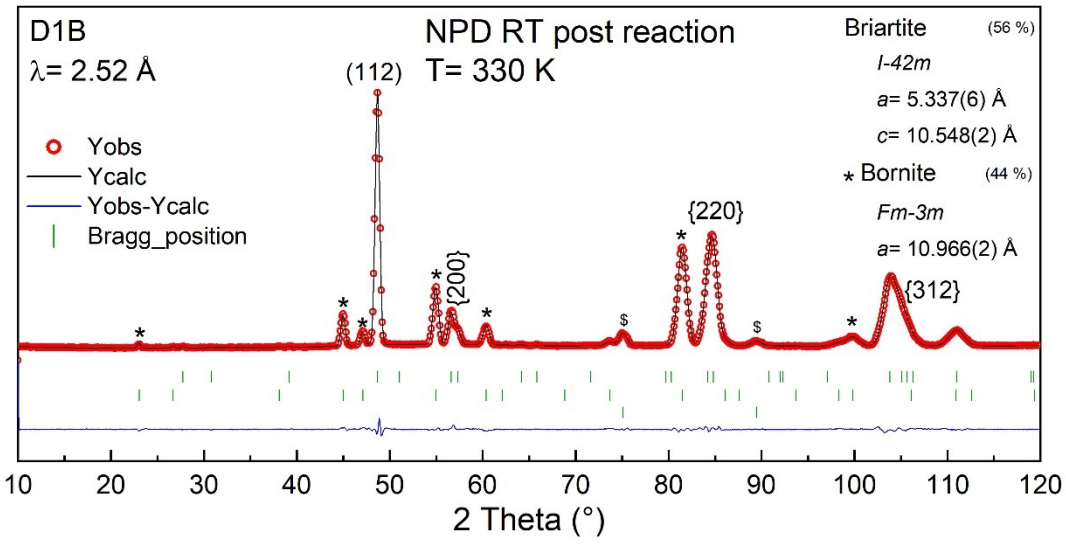

Figure 2.22. Rietveld refinement of the NPD pattern at 330 K post reaction. An asterisk and a dollar sign marks the bornite and thermocouple contribution.

2.3.4.2 Renierite $P\bar{4}2c$ to briartite $I\bar{4}2m$ phase transition during cooling

The crystallographic changes induced by the phase transition are gradual and subtle, thus are not easily observable on the diffractograms, hence the patterns collected during cooling are not displayed. In this context, pattern refinement is useful as it is sensitive to subtle changes. Figure 2.23 displays the decrease of the lattice parameters of a renierite phase refined by Le Bail method and its a/c ratio. Note that the results below 530 K are not presented because the cooling system of the sample chamber was unable to follow the cooling rate. The cell parameters at 330 K (measured on an isotherm) are displayed on the figure for extrapolation purposes. While the *a* and *c* cell parameters both decreased with temperature between 950 K and 530 K, their ratio decreased from 1.0077 (950 K) to 1.0065 (730 K, *i.e.* close to renierite (1.0068)) and then sharply increased up to 1.0104 (530 K). The intercept of the two trends of the cell parameters *a* and *c* indicates 700 K as the turnover temperature (Figure 2.23, red lines), thus indicating 700 K as the phase transition from renierite to briartite. In the next section, attempts will be made to rationalize this phase transition from a chemical point of view.

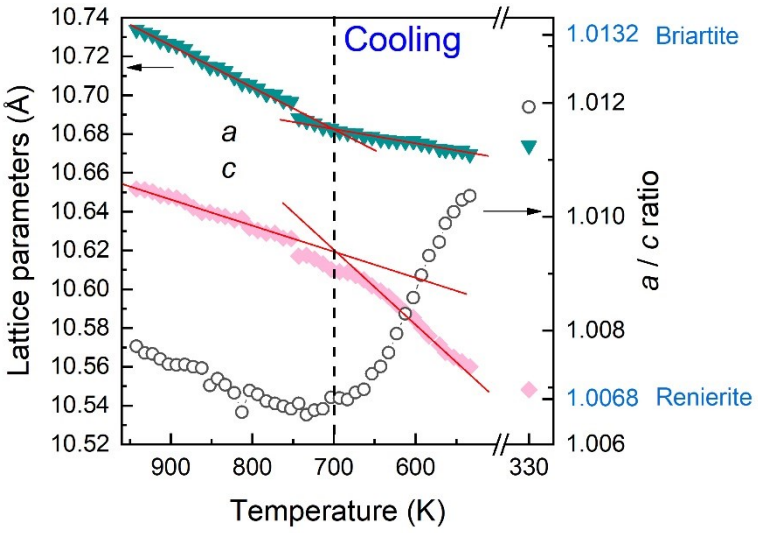

Figure 2.23. NPD thermal stability experiment: cell parameter a and c (left axis), a/c ratio (right axis) of a renierite phase refined by Le Bail method. The points at 330 K were obtained by Rietveld refinement of a briartite structural model (2a).

Figure 2.24 shows a correlation between the bornite content increase, the renierite content decrease and the sulfur loss, represented by the M_{tot}/S ratio obtained from TGA analysis. We can conclude that, the bornite phase continues to grow during cooling at the expense of the main renierite-type phase and hence fuels the Ge-enrichment of the latter. Along these lines, we can suppose that this Ge-enrichment process may be one of the trigger of the renierite to briartite phase transition. In fact, it is conceivable that at 700 K, the cationic ratio of Ge in the composition approaches that of briartite Cu_2FeGeS_4 (Ge/M_{tot} = 0.25) and thus induces a phase transition from $P\bar{4}2c$ to $I\bar{4}2m$. Note that the weight fractions of both phases were obtained by Rietveld refinement, thus these results must be considered witch caution as Bernstein structural model of natural renierite was used and a constant nominal stoichiometry was assumed. Nonetheless, it remains a legitimate approximation to survey the relative variation of the two phases.

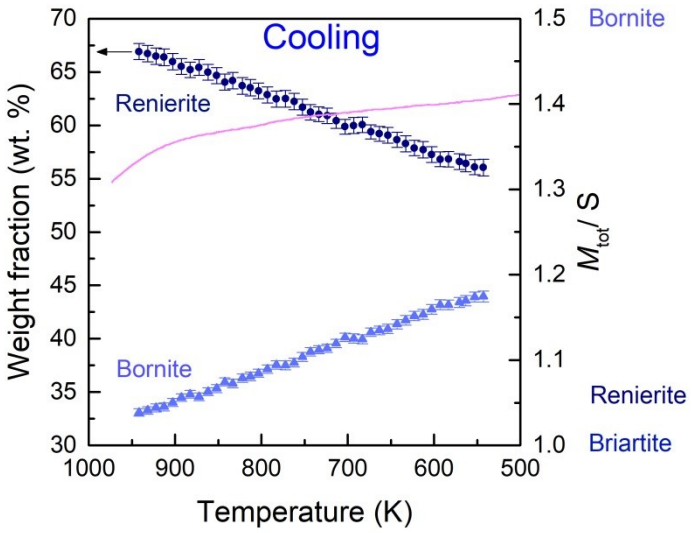

Figure 2.24. Weight fractions of renierite (navy) and bornite (blue) with cooling temperature obtained by Rietveld refinement of NPD data (left axis). The M_{tot}/S ratio was obtained from a TGA measurement (pink line, right axis).

2.3.5 Germanite stability up to 860 K

This study, conducted in the same conditions as the temperature stability investigation up to 1000 K, was meant to verify the stability of the germanite phase below the phase transition temperature (880 K - 910 K). Thus, a sealed capillary filled with a $Cu_{22}Fe_8Ge_4S_{32}$ sample was heated from RT to 860 K at 2 K min^{-1} (Figure 2.25) and cooled down to RT at the same rate. The patterns were measured during 2 h isotherms (4 × 30 min) on a D8 Advance (*Bruker*) equipped with a molybdenum anticathode. The data were converted to λ_{Cu} for consistency concerns. Contrary to what was observed in the previous temperature stability experiments, either by X-ray or neutron, the formation of bornite Cu_5FeS_4 at 650 K or higher was not observed (maybe the little bulge ~ 47° at 860 K). The main difference between all the stability experiments was the starting material. Indeed, even when prepared in reproducible conditions, the batches of sealed tube germanite may vary in: their bornite, HT_quat and semi-crystalline germanite-like phase contents. In fact, the headspace volume of the sealed tube was probably the most influent and laborious parameter to control. Indeed, while a large headspace volume favors sulfur loss, thereby stoichiometric deviation (resulting in bornite formation) and inertia detrimental to the quench, small headspace volume entails explosion hazards. Furthermore, the superstructure peaks (211) and (321) were still present at 860 K although they seem to have lost a bit of intensity, thus indicating that the integrity of the $P\bar{4}3n$ germanite phase is preserved.

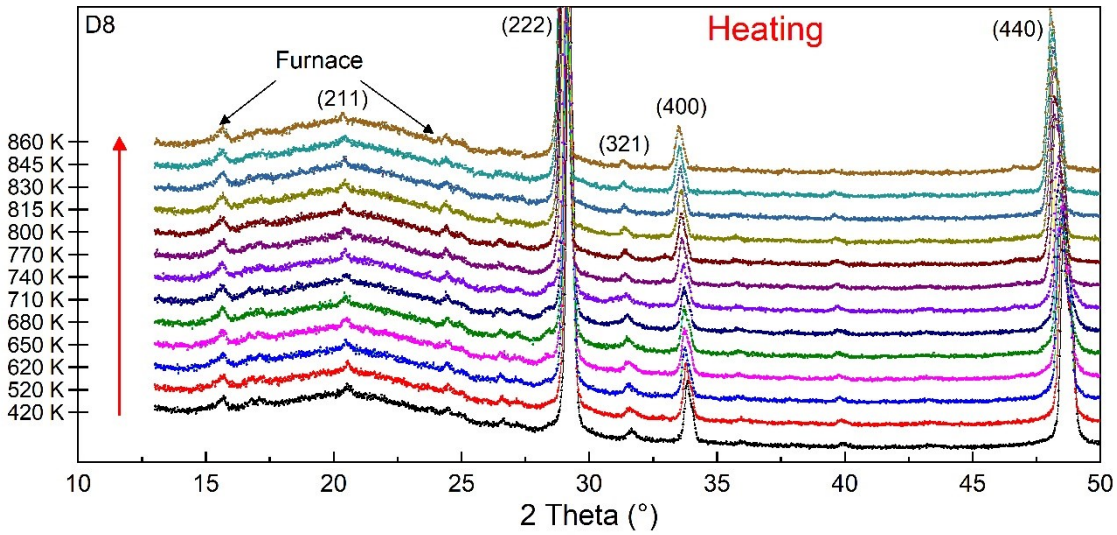

Figure 2.25. XRD investigations of the temperature stability of germanite $Cu_{22}Fe_8Ge_4S_{32}$ below 860 K: diffraction pattern as a function of temperature (data converted from λ_{Mo} to λ_{Cu}).

The XRPD patterns acquired during this experiment were refined by Le Bail method with the cubic germanite space group ($P\bar{4}3n$). These refinements enabled the examination of the thermal expansion of the cell parameters of germanite $Cu_{22}Fe_8Ge_4S_{32}$ (Figure 2.26). The non-linearity of the cell parameters with increasing temperature supports the hypothesis that the composition of germanite is not static. Nonetheless, it is important to remember that this is not a real time *in situ* experiment as the patterns were recorded during isotherms. Therefore, deviations can occur from the expected linear thermal expansion.

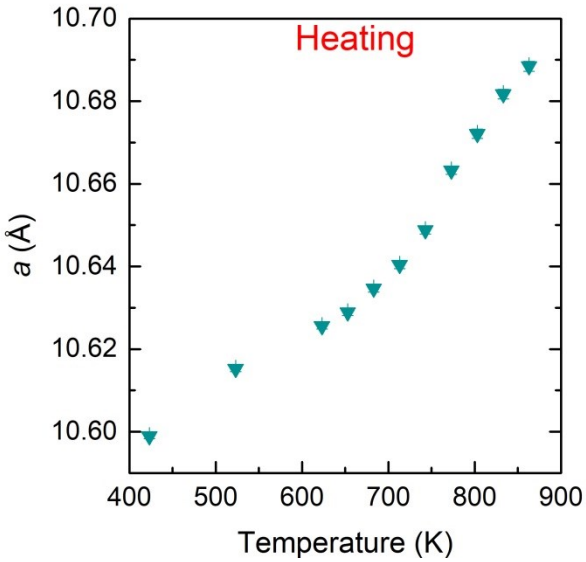

Figure 2.26. Cell parameter thermal expansion of germanite $Cu_{22}Fe_8Ge_4S_{32}$ obtained from XRD investigations of the stability below 860 K.

2.3.6 Summary

- The identity of bornite Cu_5FeS_4 as impurity is confirmed by Rietveld refinement and phase transitions temperatures.
- Bornite Cu_5FeS_4 (M_{tot}/S = 1.5) crystallizes above ~ 650 K during heating to balance the cationic excess in response to sulfur loss.
- The formation of Cu_5FeS_4 participates to a Ge-enrichment of the germanite phase. Thus the stoichiometry $Cu_{22}Fe_8Ge_4S_{32}$ is stable up to 650 K.
- The germanite $P\bar{4}3n$ structure is stable up to 860 K.
- The cubic $P\bar{4}3n$ symmetry of germanite is lost above ~ 900 K in a transition toward a tetragonal $P\bar{4}2c$ symmetry of renierite-type.
- During cooling, at 700 K the $P\bar{4}2c$ renierite-type phase undergoes a phase transition to a briartite-type phase $I\bar{4}2m$.

This insight on the thermal stability of germanite produced by ST together with the formation of the secondary phases allow to pursuit the most advantageous process conditions to yield the highest *ZT*. This research is important because, the synthesis and densification process can have a considerable effect on the transport properties of a thermoelectric materials.

2.4 Investigation on the synthesis and sintering conditions

2.4.1 Sample preparation

For this study, four samples of germanite $Cu_{22}Fe_8Ge_4S_{32}$ were synthesized by combining different powder syntheses (MA or ST) and sintering processes (SPS or HP), namely MA_SPS, MA_HP, ST_SPS and ST_HP. For all synthesis methods, Cu (99 %), Fe (99.5 %), S (99.5 %), and Ge (99.999 %) commercial powders, were stored and manipulated in a glove box under argon atmosphere. The pure reactants for the mechanically alloyed samples were weighted in a stoichiometric ratio and ground in an agate mortar. Two batches of 4 g each were prepared and put respectively into two 45 mL tungsten carbide jars along with a total of 14 WC balls with a diameter of Φ = 10 mm, for a 13:1 ball-to-powder weight ratio. The milling lasted for 360 min at 600 rpm decomposed in 24 cycles of 15 min each with 1 min pause and a reverse of the milling direction. The sealed tube synthesis was done in the conditions described in section 2.2.1.

Powders (*ca*. 3 g) from the ST or MA synthesis were weighted and put into a graphite die (Φ = 10 mm) and densified by SPS at 873 K under a uniaxial pressure of 64 MPa with a heating rate of 30 K min^{-1} and a holding time of 30 min in a spark plasma sintering furnace (SPS-FCT HPD 25) under static vacuum. The hot-pressed samples (*ca*. 3 g) were sintered in a graphite die (Φ = 10 mm), at 873 K for 60 min under a uniaxial pressure of 64 MPa with a heating rate of 15 K min^{-1} and a holding time of 60 min under static vacuum in a VAS (*Vide et Appareils Scientifiques*) instrument. The sintering temperature of 873 K for MA powders was fixed during preliminary experiments presented in Chapter 2,[151] where high purity samples were obtained.

2.4.2 Structure and microstructure

The XRPD patterns of the two batches of powders before the sintering process are presented in Figure 2.27. The XRPD pattern of the pre-reacted mechanically alloyed powder shows broad diffraction peaks belonging to the main reflections of the sphalerite lattice (sub-structure of germanite). Small diffraction peaks are assigned to unreacted elementary Ge. The powders obtained from sealed tube synthesis were found to be well crystallized with only traces of cubic bornite (Cu_5FeS_4) as seen in Figure 2.27b.

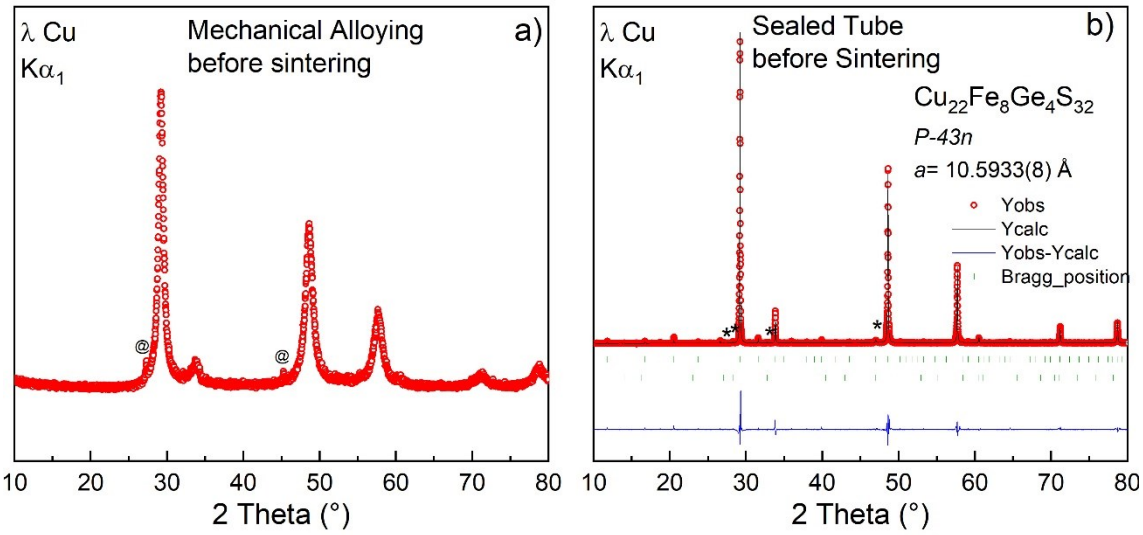

Figure 2.27. Le Bail refinement of the XRPD patterns of (a) mechanically alloyed and (b) sealed tube powders. The MA sample displays two well-crystalized peaks (identified by a @ sign) belonging to unreacted Ge. The ST sample contains a small portion of bornite Cu_5FeS_4, which main peaks are identified by an asterisk.

The sintering of the mechanically alloyed (MA) samples yields pure and well crystallized samples (Figure 2.28a and b), but while MA_SPS is a highly pure germanite sample, MA_HP contains a small fraction of nukundamite ($Cu_{0.85}Fe_{0.15}S$). Note that, MA is known to limit sulfur loss and hence yield samples with stoichiometry close to the nominal one. On the other hand, the sintering of the ST powders by SPS (ST_SPS) or HP (ST_HP) at 873 K, tends to slightly increase the content of Cu_5FeS_4 (Figure 2.28c and d) in agreement with the results presented section 2.3. Also, it is compliant with the fact that a yellow precipitate on the silica walls was commonly observed after the ST synthesis. Additionally, cell parameter

disparities can be observed between the four samples. While this difference is negligible for the samples synthesized by the same method (*i.e.* negligible influence of the sintering process), it is pronounced between the samples synthesized using mechanically-alloyed and sealed tube powders such as: ST_HP (a = 10.5986(1) Å) & ST_SPS (a = 10.5969(1) Å) > MA_HP (a = 10.5908(2) Å) & MA_SPS (a = 10.5884(1) Å). Considering these observations and the fact that all sintering processes were performed at the same temperature, it is possible to correlate the temperature exposition to the cell parameter. Thus, the larger cell parameter in ST-based samples likely originates from sulfur loss due to longer exposure to high temperature. Indeed, as in colusite $Cu_{26}V_2Sn_6S_{32}$ and $Cu_{26}Nb_2Sn_6S_{32}$,[141,162] the sulfur loss benefits structural disorder including interstitial sites and anti-sites defects, hence leading to an increase of the cell parameter.

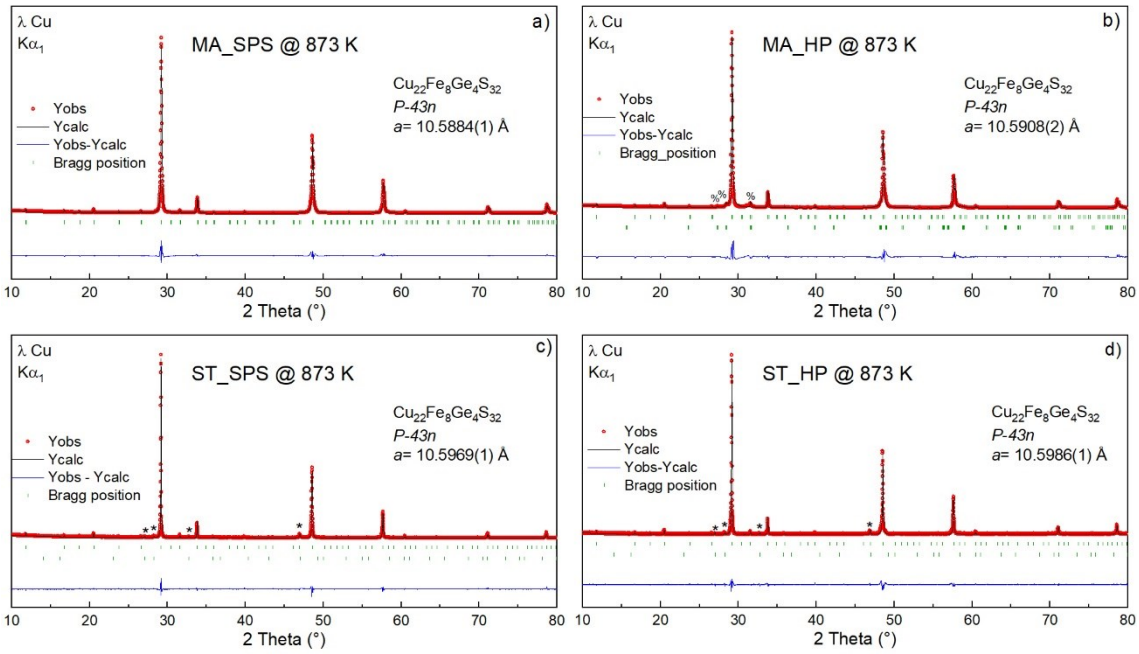

Figure 2.28. Le Bail refinements of the XRPD patterns of a) MA_SPS, b) MA_HP, c) ST_SPS and d) ST_HP samples. Both ST samples contain a small portion of bornite, which main peaks are identified by an asterisk and MA_HP contains a small fraction of nukundamite (contribution identified by a percentage sign).

SEM micrographs on the fractured surfaces of the sintered samples are displayed in Figure 2.29. The micrographs evidence a small, uniform and homogeneous microstructure for both MA_SPS and MA_HP samples (Figure 2.29a

and b, respectively). Relative densities of MA_SPS and MA_HP samples are about 95.0 % and 96.2 %. The estimated average particle size, determined by the intercept method, for the MA_HP sample is around 0.60 ± 0.10 μm, which is slightly larger than that of the MA_SPS sample (0.40 ± 0.10) μm. The grain sizes of ST_SPS and ST_HP samples were found to be significantly larger (Figure 2.29c and d, respectively), with an average value around 7.0 ± 0.5 μm. As expected, sealed tube and mechanical alloying synthesis yielded a mean grain size difference by an order of magnitude. The long synthesis duration at high temperature (973 K/ 24 h) favors the element diffusion and the growth of large crystallites/grains compared to the repeated welding, fracturing, and rewelding mechanisms involved during mechanical alloying that leads to small particle sizes.[171] Moreover, ST_SPS and ST_HP samples present relative densities of 96.7 % and 99.4 %, respectively, which are slightly higher than MA_SPS and MA_HP samples.

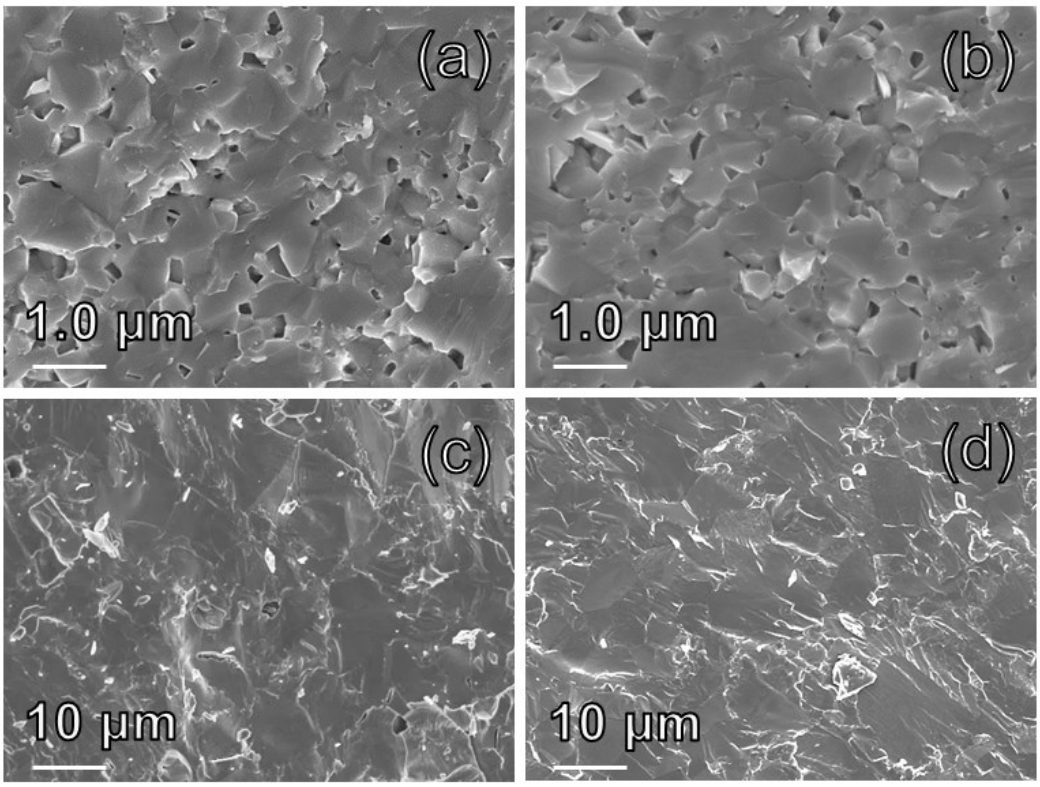

Figure 2.29. Micrographs of fractured cross-sections for a) MA_SPS b) MA_HP c) ST_SPS and d) ST_HP sintered samples.

2.4.3 Thermoelectric properties

The thermoelectric properties of the four $Cu_{22}Fe_8Ge_4S_{32}$ samples have been investigated, namely, MA_SPS, MA_HP, ST_SPS and ST_HP (Figure 2.30). The temperature dependence of the Seebeck coefficient (*S*), given in Figure 2.30a, shows that all the compounds are *p*-type with *S* values ranging from 93 μV K^{-1} to 329 μV K^{-1} at 300 K. The Seebeck coefficient of the MA_SPS and MA_HP samples increases with temperature from 300 K to 450 K, but suddenly manifests a change in its temperature dependence. This behavior can be explained by the fact that the electrical conduction is in an intermediate regime between metallic and semiconducting behavior.[151] The Seebeck coefficient of ST_SPS and ST_HP is decreasing over the full temperature range exhibiting a semiconducting behavior. Both ST samples display higher Seebeck coefficient than their MA counterparts, with values of 329 μV K^{-1} for ST_SPS, 279 μV K^{-1} for ST_HP, 133 μV K^{-1} for MA_SPS and 93 μV K^{-1} for MA_HP at RT. As the Seebeck coefficient is directly proportional to the charge carriers effective mass (*m**) and inversely proportional to the charge carrier concentration, it is likely that the changes in the amplitude of the Seebeck coefficient between the four samples is caused by variations of the charge carrier concentration. Therefore, such difference in Seebeck coefficient could originate from slight deviations from the nominal composition. Interestingly, the magnitude of the Seebeck coefficient can be correlated to the cell parameters (ST_SPS & ST_HP > MA_SPS & MA_HP), that presumably originates from sulfur loss during ST synthesis. Also, as previously shown in other colusite compounds[141,162] it is well accepted that sulfur deficiency can create changes in charge carrier concentration. In the present study, sulfur deficiency reduces the charge carrier concentration, thus explaining the higher Seebeck coefficient of the ST samples as compared to MA synthesized samples. A reduction in the charge carrier concentration may be due to a decrease of the Cu^{2+} content due to the Ge enrichment of the composition (Chapter 4 section 4.3.6 proposes several Ge rich composition with 1 Cu^{2+}).

The temperature dependence of the electrical resistivity for all four samples is given in Figure 2.30b. Over the whole investigated temperature range, the electrical resistivity decreases with increasing temperature, hence displaying a semiconducting behavior. However, it can be presumed from the slight variation of MA_SPS and MA_HP, that the semiconducting behavior is near a transition towards a degenerate semiconductor. In agreement with the Seebeck coefficient, the electrical resistivity at room temperature varies such as: ST_SPS (760 mΩ cm) > ST_HP (640 mΩ cm) > MA_SPS (8.67 mΩ cm) > MA_HP (5.17 mΩ cm). The ST samples exhibit a higher electrical resistivity than the MA samples, consistent with a higher sulfur deficiency, similarly to what was previously reported on colusite.[141]

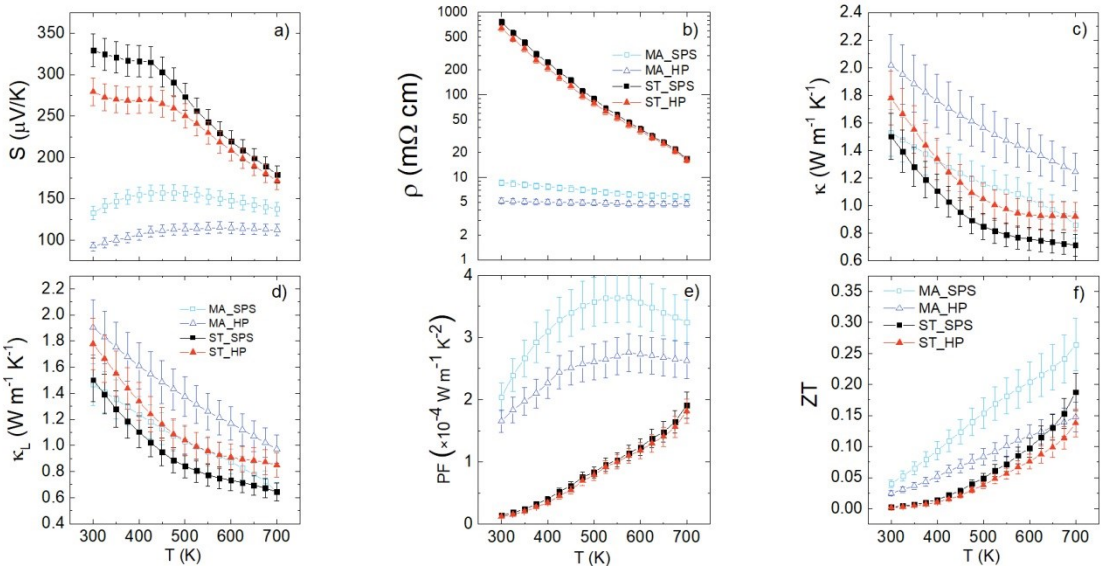

Figure 2.30. Thermoelectric properties of the four germanite $Cu_{22}Fe_8Ge_4S_{32}$ samples: MA_SPS (square), MA_HP (triangle), ST_SPS (filled square) and ST_HP (filled triangle). The Seebeck coefficient is represented in a), electrical resistivity in b), total thermal conductivity in c), lattice thermal conductivity in d), power factor in e) and the figure of merit ZT in f).

The power factor of each sample increases with temperature as seen in Figure 2.30e. MA_SPS sample has the highest power factor with a maximal value of 3.64×10^{-4} W m^{-1} K^{-2} at 550 K followed by MA_HP with a maximum power factor of 2.75×10^{-4} W m^{-1} K^{-2} at 575 K. As evidenced by the relatively low power factor at 700 K of 1.92×10^{-4} W m^{-1} K^{-2} for ST_SPS and 1.81×10^{-4} W m^{-1} K^{-2} for ST_HP, it is

probable that the lower carrier concentration in ST samples distances from the optimal value. Unfortunately, it is not possible to confirm this hypothesis as attempts to measure the carrier concentration in the PPMS system under high magnetic field were unsuccessful due to correlation effects. In the light of these results, it is clear that the germanite prepared by ST synthesis are not markedly affected by the sintering process, as opposed to the samples synthesized by MA, which is consistent with the fact the MA samples undergo reactive sintering.

The thermal conductivity (κ) and its lattice contribution (κ_L), in Figure 2.30c and 2.30d**,** respectively**,** are decreasing with temperature for all samples over the whole investigated temperature range. No specific trend can be observed regarding the impact of the powder synthesis and/or sintering method, which suggests that the presence of secondary phases and the substantial difference of grain sizes do not have a significant influence on phonon scattering. To investigate further the possible formation of structural defects at the atomic level, especially in sulfur deficient ST samples, TEM studies, including electron diffraction (ED) and high angle annular dark field scanning TEM (HAADF-STEM) were undertaken (Figure 2.31). Several crystallites of the MA_HP and ST_HP samples were analyzed. The ST_HP sample should be the one presenting the highest degree of disorder because it is produced by the combination of the synthesis and sintering conditions that promotes the most sulfur loss. Also, a comparison with MA_HP allows to observe the influence of powder synthesis on the formation of structural disorder. Indeed, as discussed above, it was recently demonstrated that the sulfur sublimation in the closely related colusite $Cu_{26}V_2Sn_6S_{32}$ structure induces atomic-scale defects/disordered states including interstitial sites, anti-sites defects, and site splitting, which function as strong phonon scatterers.[141,162]. However, HR-TEM analyses brought further evidence that samples are well crystallized and ordered, in agreement with XRPD data. Indeed, the main zones of the ED patterns (as exemplified along the [001] and [$\bar{1}$11] direction) and the corresponding HAADF-STEM images of both MA_HP and ST_HP, show a highly crystallized structure, which can be indexed based on the cubic $P\bar{4}3n$ ($a \sim 10.6$ Å) structure, obtained from XRPD data. The absence of observable structural defects is mainly

explained by the lower sintering temperature (873 K in the present study, against 1023 K in disordered colusites) and the difference in cationic site occupancy in germanite-type structure.[141,142,162]

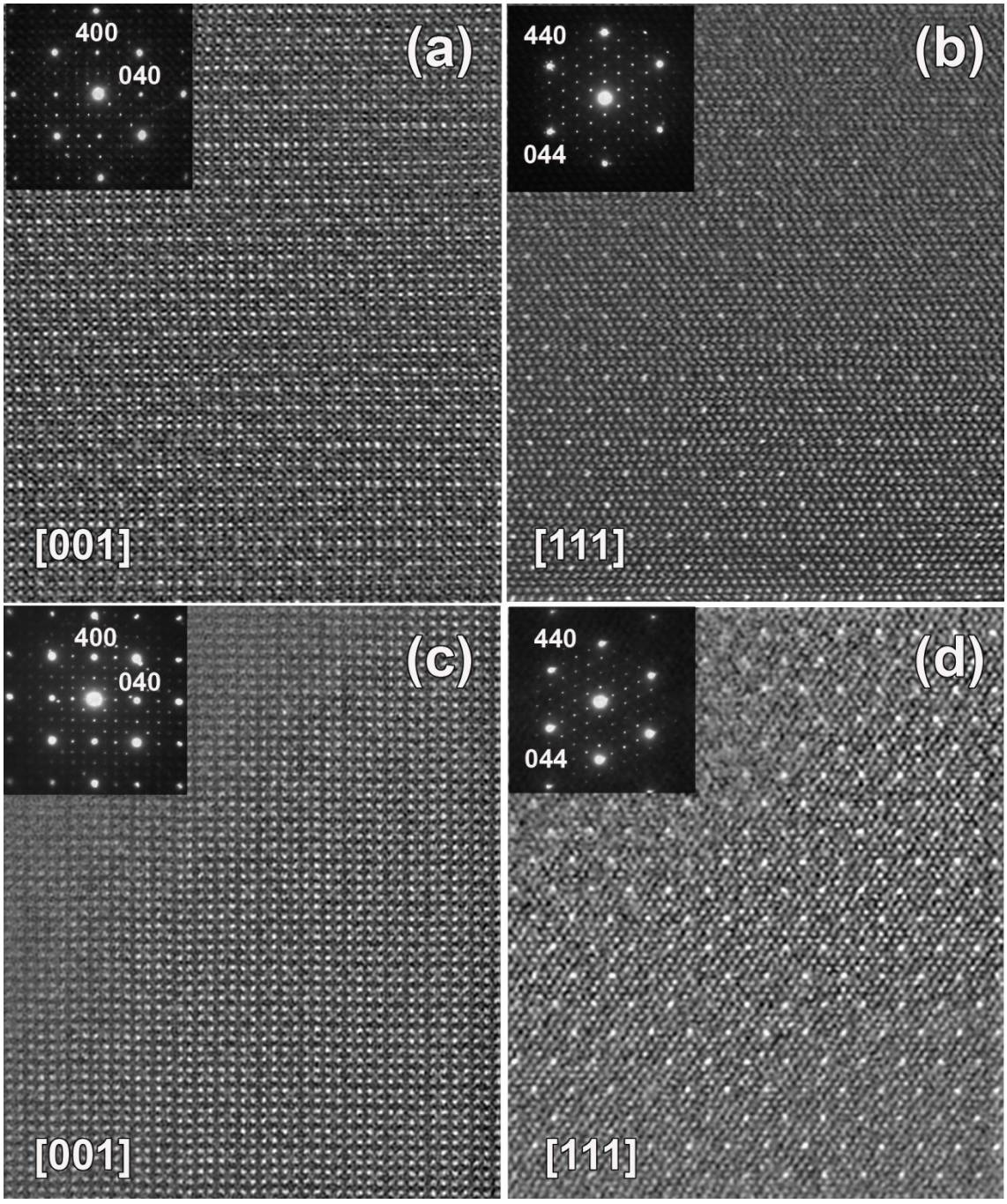

Figure 2.31. Electron diffraction patterns and micrographs of germanite synthesized by MA_HP along the main crystallographic zone axis a) [001] and b) [111] and germanite synthesized by ST_HP along the main crystallographic zone axis c) [001] and d) [111].

As shown in Figure 2.30f, the dimensionless figure of merit *ZT* for all samples increases with temperature. In fact, it appears that the samples synthesized from MA powder have larger *ZT* values compared with the samples prepared from ST powder. The $ZT_{700\ K}$ of 0.26 for MA_SPS sample is mainly explained by the lower electrical resistivity due to its higher carrier concentration. Moreover, MA synthesis counts many technical advantages over ST synthesis, such as its low operational temperature and easy scaling up.

2.5 Conclusion

The goal of Chapter 2 was to establish the best synthesis and sintering conditions in order to produce the most attractive germanite $Cu_{22}Fe_8Ge_4S_{32}$ sample for thermoelectric applications.

The *in situ* experiments allowed to describe for the first time the binary, ternary and quaternary intermediate products formed during heating prior to the formation of germanite. The formation of germanite happened around 860 K during cooling and was identified by the appearance of the superstructure peaks characteristics to the structure. However, the appearance of a low crystallinity phase around 760 K, limited the possibility to cool the reaction below this point. The changes in the secondary products proportion with the sample cooling conditions evidenced the close equilibria of the material with chemically related products, especially bornite Cu_5FeS_4. Finally, the anomalous shape of the diffraction peaks of the germanite samples was assigned to a shared contribution of a quaternary high temperature intermediate product and a germanite derivative phase with low crystallinity. In summary, this study highlighted the importance of the cooling control for the synthesis of high purity germanite $Cu_{22}Fe_8Ge_4S_{32}$ samples in sealed tube.

The investigation on the phase stability/decomposition of germanite $Cu_{22}Fe_8Ge_4S_{32}$ synthesized in sealed tube has allowed an improved perception of the TE properties behavior in temperature. We showed that the balance between

the main germanite phase and the secondary bornite phase is ruled by sulfur loss due to its sensitivity to volatilization above 650 K. Also, it was demonstrated that germanite undergoes a phase transition above 880 K to transform into a renierite-type phase. Additionally, the germanite $P\bar{4}3n$ structure is stable up to 860 K.

Finally, the investigation on the synthesis and sintering conditions showed the influence of the synthesis and sintering techniques on the structure, microstructure and thermoelectric properties of germanite $Cu_{22}Fe_8Ge_4S_{32}$. The mechanically-alloyed samples present higher *ZT* than the samples prepared by ST because of their radically lower electrical resistivity values and significant Seebeck coefficients. Results showed the high sensitivity of the material and electrical properties to stoichiometry deviations. In opposite, the thermal conductivity is less influenced by the stoichiometry deviations and microstructural changes. Note that the ST germanite samples were sintered above the stability temperature determined in the previous investigation (*e.g.* formation of bornite ~ 650 K, sintering T = 873 K), based on the optimized sintering conditions for the germanite samples produced by MA (which responded differently to the densification since they undergo reactive sintering) and because the temperature stability investigation by NPD was performed after. This might explain most of the transport properties differences. These results demonstrate that MA is an effective route to synthesize Cu-S compounds for thermoelectric end. Moreover, the *ZT* figure of merit of germanite, which is significantly smaller than that of the closely related colusite, strongly suggests that order–disorder cationic phenomena play a crucial role in carrier mobility leaving room for further improvement.

3 STUDY OF CU TO ZN AND GE TO SN SUBSTITUTION IN GERMANITE

3.1 Preface

The previous chapter discussed the synthesis, thermal stability and process optimization of germanite. Now that the base to produce a high purity germanite sample is set, the focus will be on the enhancement of the transport properties. Among the several approaches presented in Chapter 1, the effect of cationic substitution on the electrical and transport properties will be investigated. As a reminder, beside the possible modification of the charge carrier concentration, the introduction of substitutional impurities into a crystal lattice is known to potentially enhance phonon scattering due to differences in atomic mass and size between the host and impurity atoms.[172,173]

First, a Cu to Zn substitution in the $Cu_{22-x}Zn_xFe_8Ge_4S_{32}$ ($0 \leq x \leq 2$) series is synthesized for the first time with the aim to modify the carrier concentration as it was reported in colusite and tetrahedrite.[5,6] Moreover, this substitution is going toward the natural stoichiometry of renierite $Cu_{20}Zn_2Fe_8Ge_4S_{32}$, which can be view as the direct tetragonal deformation of germanite. The change in crystal structure symmetry could introduce structural disorder, thus reducing the thermal lattice conductivity. Second, an isovalent substitution of Ge to Sn in the $Cu_{22}Fe_8Ge_{4-x}Sn_xS_{32}$ ($0 \leq x \leq 4$) series is investigated with the aim to reduce the lattice thermal conductivity by the creation of cationic disorder by alloying effect.

3.2 Cu to Zn substitution in $Cu_{22-x}Zn_xFe_8Ge_4S_{32}$

3.2.1 Sample preparation

Polycrystalline samples of $Cu_{22-x}Zn_xFe_8Ge_4S_{32}$ ($0 \leq x \leq 2$) were synthesized by mechanical alloying followed by spark plasma sintering following the same protocol presented in Chapter 2. Also, all the samples preparation conditions are detailed in the appendices (Chapter 5, section 5.2.1.2 and 5.2.1.4).

3.2.2 Analysis of the germanite and renierite structures.

In order to understand the relationship between the structure and the thermoelectric properties of these sulfides, a careful analysis of their structures is absolutely necessary, all the more so because they exhibit complex cationic ordering phenomena which have not been fully described in the literature. Both structures derive from the ZnS sphalerite structure (cubic space group $F\bar{4}3m$, Figure 3.1a) but differ from each other by their crystal symmetry: germanite is cubic $P\bar{4}3n$ ($a \sim 10.6$ Å) whereas renierite is tetragonal $P\bar{4}2c$ ($a \sim 10.6$ Å, $c \sim 10.5$ Å), a feature which allows them to be easily differentiated by X-ray powder diffraction study (See below). Thus, natural renierite $(Cu,Zn)_{22}Fe_8(Ge,As)_4S_{32}$ can be described as a semi-ordered but tetragonally distorted sphalerite framework built up of corner-shared CuS_4, FeS_4, ZnS_4 and $(Ge, As)S_4$ tetrahedra. The cationic distribution in the different sites of this network appears to be more ordered compared to synthetic germanite: 4*g,* 4*i,* 4*m* and 8*n* sites are occupied by copper, and 4*h* and 2*f* sites are occupied by iron, whereas zinc and the remaining copper are randomly distributed over the 2*e* site, and germanium and arsenic are located on a 4*j* site.[170] Remarkably, this sphalerite framework also hosts Fe^{3+} as an interstitial cation in the 2*b* site (referring to $P\bar{4}2c$ space group). As with synthetic germanite, the corresponding FeS_4 tetrahedron shares its edges with the surrounding polyhedra, *i.e.* with 4 CuS_4 tetrahedra arising from copper on the 4*g* and 4*m* sites and 2 FeS_4 tetrahedra arising from iron on the 4*h* site. Thus, alike germanite, renierite exhibits octahedral metallic FeL_6 complexes, but differently, metal *L* apices are occupied in an ordered way, with two apical iron cations and

four equatorial copper cations. This results in an elongation of those Fe[Cu_4Fe_2] octahedra with 4 equatorial Fe-Cu distances of 2.65 - 2.67 Å and 2 longer apical Fe-Fe distances of 2.81 Å,[170] in agreement with the Fe^{3+}-Cu^{2+} and Fe^{3+}-Fe^{3+} Coulomb repulsions. Note that the average distance between central Fe^{3+} and the surrounding *L* cations in octahedral metallic FeL_6 complexes is equivalent in both structures, synthetic germanite and renierite.

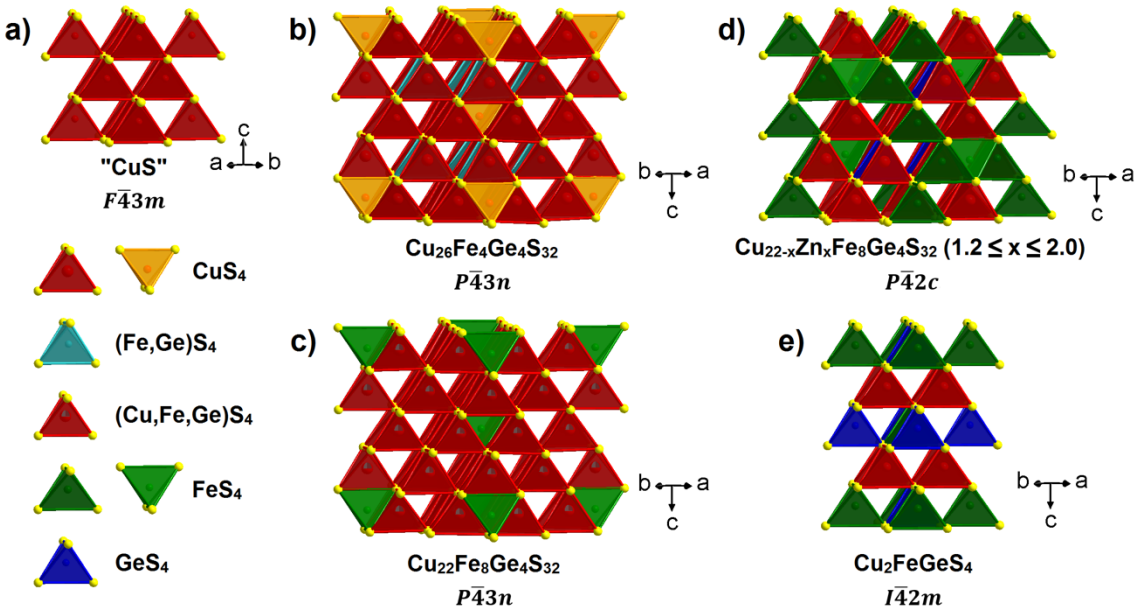

Figure 3.1. Crystal structure representations highlighting the semi-ordered cation distribution of a) sphalerite "CuS", b) mineral germanite $Cu_{26}Fe_4Ge_4S_{32}$, c) synthetic germanite $Cu_{22}Fe_8Ge_4S_{32}$, d) renierite $Cu_{22-x}Zn_xFe_8Ge_4S_{32}$ ($1.2 \leq x \leq 2.0$) and e) briartite Cu_2FeGeS_4.

3.2.3 Structural analysis

In the following, we will show that, with the experimental conditions used for the preparation of synthetic germanite $Cu_{22}Fe_8Ge_4S_{32}$ by mechanical alloying two series of compounds can be synthesized in the system $Cu_{22-x}Zn_xFe_8Ge_4S_{32}$: a single phase germanite domain for $0 \leq x \leq 0.4$ and a single phase renierite one for $1.2 \leq x \leq 2.0$, with a biphasic domain for $x = 0.8$ corresponding to a mixture of the two sulfides.

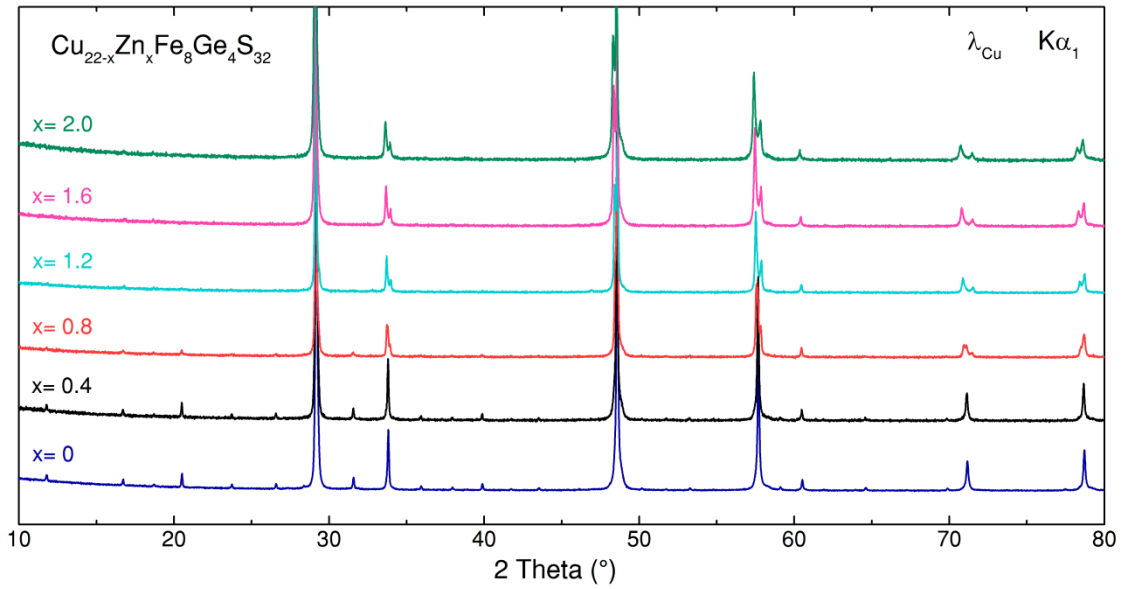

Figure 3.2. XRPD patterns of the $Cu_{22-x}Zn_xFe_8Ge_4S_{32}$ ($0 \leq x \leq 2$) series.

The XRPD patterns (Figure 3.2) of the germanite samples (*i.e.* $x = 0$ and $x = 0.4$) show similarities with those of the renierite samples (*i.e.* $x = 1.2$, 1.6 and 2.0), due to the fact that the two structures have similar cell dimensions. However, the distortion of the structure from cubic in germanite to tetragonal in renierite induces a splitting of equivalent reflections either into two reflections (for (*hhl*) and (*hkk*) reflections allowed by the cubic space group) or into three reflections (for (*hkl*) reflections allowed by the cubic space group). This is illustrated by the splitting of the (622) peak of the cubic germanite into the non-equivalent intensity (622) and (226) peaks of the tetragonal renierite (Figure 3.3a). In contrast, the (*hhh*) reflections are the only ones which are not splitted by the cubic to tetragonal distortion, as shown from the main intensity (222) diffraction peak (Figure 3.3b) which is similar in renierite and germanite (Figure 3.2). Also, it is important to know that the reflection conditions imposed by the two different space groups allow the germanite and renierite to be clearly distinguished from their XRPD patterns. In fact, the (*hhl*), (*hkk*), and (*hkh*) reflections with $l = 2n + 1$, $h = 2n + 1$, and $k = 2n + 1$, respectively, are systematically absent in the $P\bar{4}3n$ space group of germanite, whereas the tetragonal space group $P\bar{4}2c$ of renierite requires that only (*hhl*) reflections with $l = 2n + 1$ are absent.

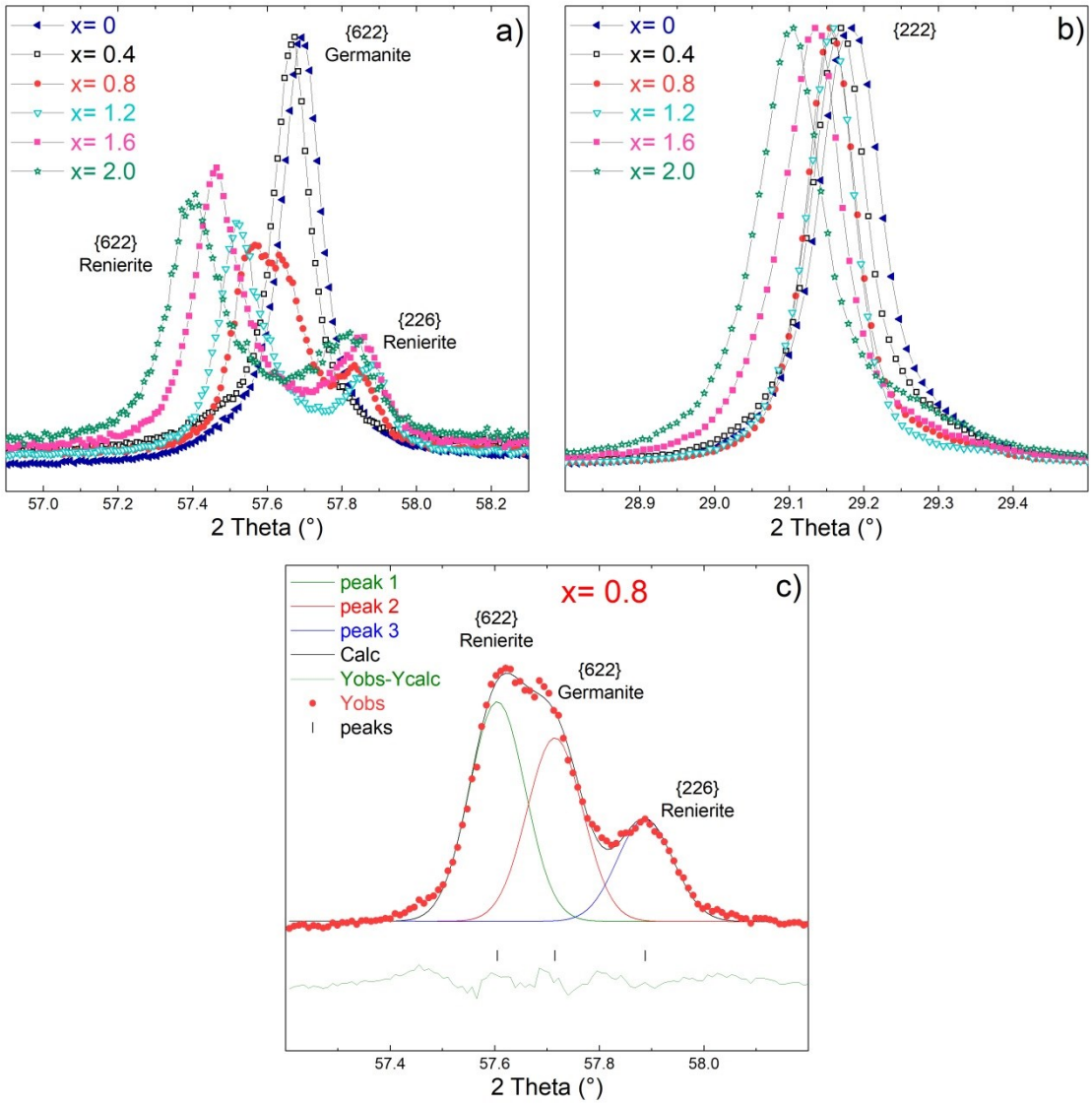

Figure 3.3. Evolution of a) {622} and b) (222) reflections with Zn content in the $Cu_{22-x}Zn_xFe_8Ge_4S_{32}$ ($0 \leq x \leq 2$) series. c) Profile fitting of the {622} peaks for $x = 0.8$ sample.

To confirm the germanite structure for samples with $x \leq 0.4$, precession electron diffraction tomography (PEDT) data were collected on a single crystal (size ~200 nm) for a sample $x = 0$. In Figure 3.4a, the reciprocal space section $0kl$ reconstructed from PEDT data exhibit extra reflections compatible with the cubic primitive lattice of the germanite. The $P\bar{4}3n$ space group is further confirmed from the *hkh* and *hhl* sections in Figure 3.4c and d, respectively, where the conditions limiting the reflections *hkh*: $k = 2n$ and *hhl*: $l = 2n$ are clearly observed.

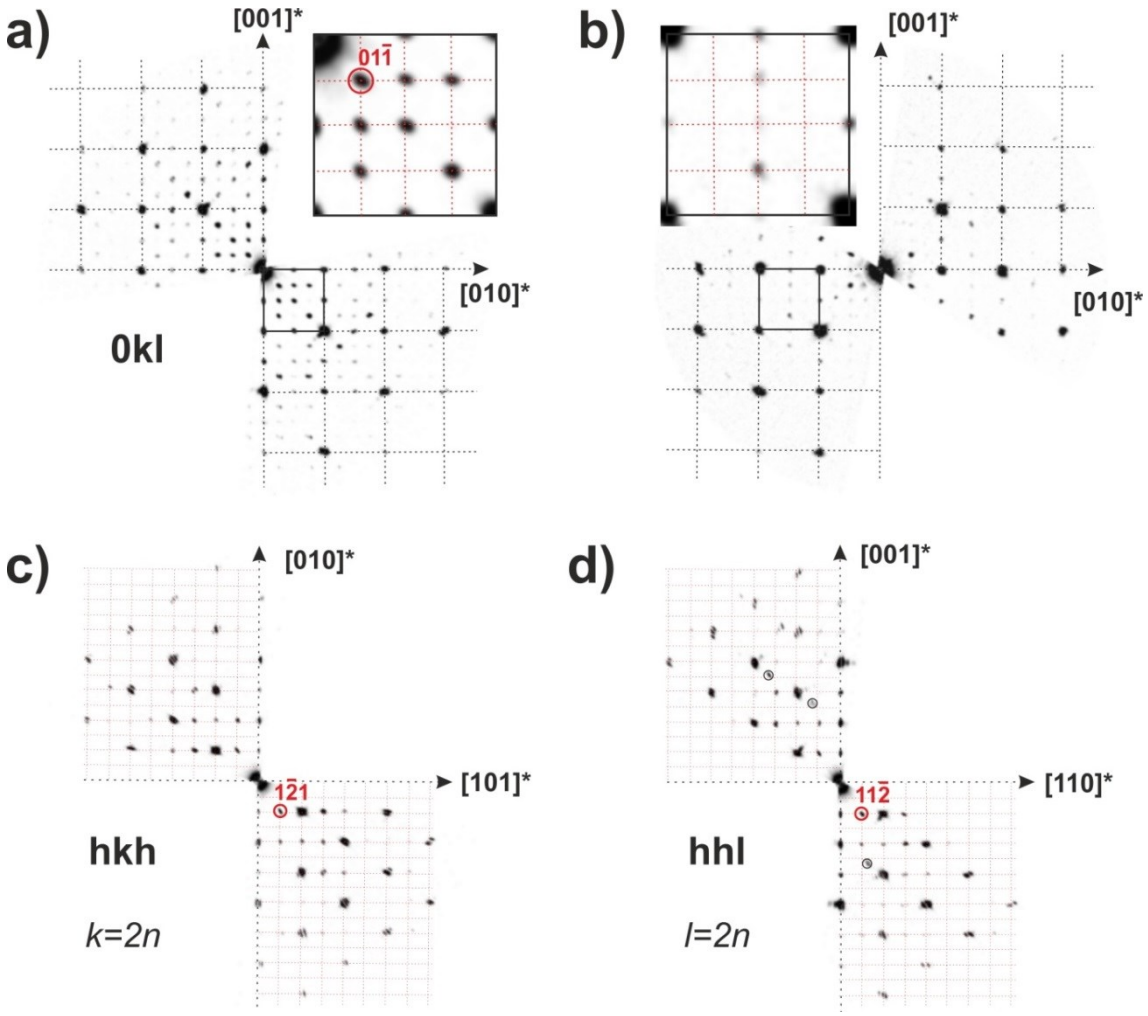

Figure 3.4. Reciprocal space sections reconstructed from PEDT data for samples $Cu_{22-x}Zn_xFe_8Ge_4S_{32}$ with in: a) 0kl section for x = 0, b) 0kl section for x = 2, c) hkh section for x = 0 and d) hhl section for x = 0. In a) and b), the reflections related to the sphalerite subcell are highlighted using black dotted lines. In a) and b), the enlarged inserts are used to better view extra supercell reflections signing the existence of an ordering with respect to the sphalerite subcell. Red dotted lines are used as a guide to the eyes to visualize the reciprocal lattice mesh.

Bearing in mind that the cationic distribution in both structures is complex due to disorder phenomena (Chapter 4), Rietveld refinements from XRPD data are not expected to be of much help to elucidate ordering phenomena in such samples due to the equivalent scattering factors of the cations. It is especially the case in renierite where most of the crystallographic sites exhibit a simultaneous occupancy by two different cations involving either statistical or semi-ordered distributions.[170] Considering this difficulty, only Le Bail refinements were used to fit the diffraction data in order to distinguish the two different structures. This is

illustrated for the x = 0.8 biphasic sample which peak profiles suggest that the latter corresponds to a mixture of germanite and renierite phases (Figure 3.3c). This is confirmed by refinements leading to a mixture of germanite with a = 10.598(1) Å and renierite with a = 10.620(1) Å and c = 10.554(2) Å. Due to the overlapping of the diffraction peaks of germanite and renierite, it is difficult to determine accurately the proportion of each phase in this sample. However, a peak profile fitting of the (622) peaks indicates that the area corresponding to the (622) peak of the germanite phase represents ≈ 36 % of the total area, while it is of ≈ 42 % and ≈ 22 % for the (622) and (226) peaks of the renierite phase, respectively (Figure 3.3c). Considering that the 2 for 1 intensity ratio expected for the (622) and (226) peaks of renierite is well reproduced, we can estimate the proportion of germanite and renierite phases in the x = 0.8 sample to be ≈ 1/3 and ≈ 2/3, respectively.

Note that the intensity of the superstructure diffraction peaks of renierite are strongly reduced for higher Zn content samples. This is confirmed by PEDT collected on a x = 2 sample (Figure 3.4b), where the 0kl reciprocal space section shows mostly strong reflections related to the sphalerite subcell. In the insert of Figure 3.4b, weak superstructure reflections confirm the existence of an ordering with respect to the sphalerite with, at least, one cell parameter of about 10.6 Å. Due to the weakness of the extra reflections and the presence of systematic twinning in the PEDT data, no conclusive result can be obtained regarding the possible space groups for this sample. This nonetheless suggests that an ordering compatible with both the briartite (Cu_2FeGeS_4, $I\bar{4}2m$, a = 5.32 Å, c = 10.55 Å, Figure 3.1e) and the renierite structure should be considered for the refinements of samples where $x \geq$ 1.2. However, in the briartite, both metal/sulfur ratio (equal to 1) and chemical composition differ significantly from our nominal chemical compositions, especially the Cu:Ge ratio. This should induce the existence of at least one secondary phase, which is not observed on the experimental XRPD patterns. Moreover, our nominal chemical compositions are coherent with the chemical compositions of natural renierite $(Cu, Zn)_{22}Fe_8(Ge, As)_4S_{32}$.[170] Last but not least, ^{57}Fe hyperfine parameters of samples, for which $x \geq$ 1.2 determined from fits of RT

Mössbauer spectra (see below), are much smaller than those expected for a briartite structure. Consequently, the multiple evidences are clearly in favor of a renierite structure. As a result, it is reasonable to consider that higher Zn content samples exhibit a renierite-type structure in which the cationic site distribution is highly disordered, inducing the reduction of intensity of the superstructure diffraction peaks. This is supported by the complex crystal structure of renierite, where a partial occupancy of the cationic sites was reported by Bernstein *et al.*,[170] and by the synthesis and sintering conditions used to prepare our samples. Indeed, mechanical alloying is well-known to be favorable to structural disorder. Such structural disorder associated with superstructure diffraction peaks extinction was also observed in closely related colusite structures.[162] From these considerations, the refinements of the XRPD patterns of the x = 1.2, x = 1.6, and x = 2.0 samples were finally carried out by considering a renierite crystal structure.

The evolution of the refined unit cell parameters of germanite/renierite-type phases versus Zn content is shown in Figure 3.5**.** From this figure, it could be noted that the a parameter of the cubic germanite is intermediate between the a and c parameters of the tetragonal renierite. Moreover, a linear variation of the a parameter of renierite with Zn content is observed, and the same trend is evidenced for germanite. Hence, by considering those linear tendencies and the refined unit cell parameters a for germanite and renierite phases in the x = 0.8 sample, it is possible to estimate the "real" Zn content which delimits the germanite and renierite domains to be $0 \leq x \leq 0.6$ and $1.0 \leq x \leq 2.0$, respectively.

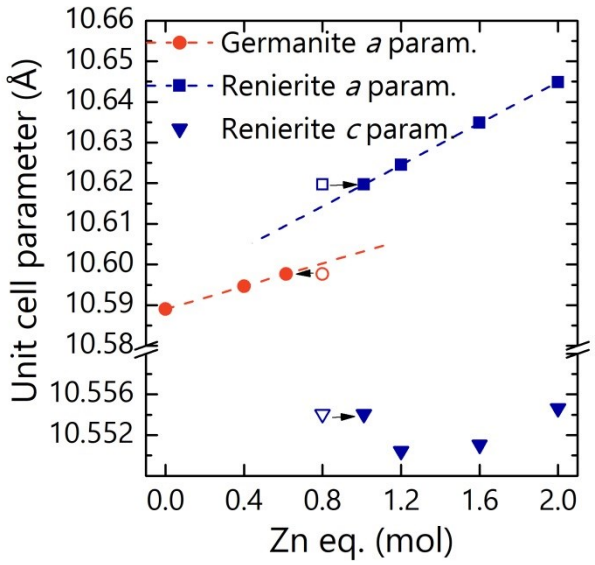

Figure 3.5. Evolution of the refined unit cell parameters of germanite/renierite phases versus Zn content in the $Cu_{22-x}Zn_xFe_8Ge_4S_{32}$ ($0 \leq x \leq 2$) series.

3.2.3.1 Qualitative characteristics of room-temperature Mössbauer spectra

Mössbauer spectra of $Cu_{22-x}Zn_xFe_8Ge_4S_{32}$ with x ($0 \leq x \leq 2.0$), recorded at room temperature (RT) between - 2.5 mm s^{-1} and + 2.5 mm s^{-1}, are shown in Figure 3.6 for x = 0, 0.4, 0.8, 1.2, and 2.0. Solid lines, except for x = 0.8, are obtained from least-squares fits of the spectra that will be discussed later on. An asymmetrical shape of the main central component characterizes the spectrum with x = 0 while the spectra (x = 1.2, 2.0) have central parts that are also asymmetrical but broader than the one with x = 0. Intermediate spectra (x = 0.4, 0.8) are less asymmetrical with somewhat flattened central parts.

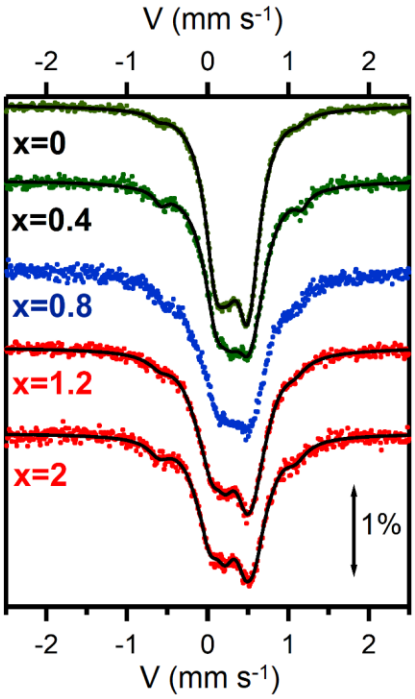

Figure 3.6. Room-temperature ^{57}Fe Mössbauer spectra of $Cu_{22-x}Zn_xFe_8Ge_4S_{32}$ for x = 0, 0.4, 0.8, 1.2, and 2.0. Black solid lines are results of least-squares fits in conditions described in the text.

All the spectra show peaks at *ca*. - 0.5 mm s^{-1} and *ca*. + 1 mm s^{-1}, whose central lines are associated with a magnetic phase as clearly shown by the spectrum of $Cu_{20}Zn_2Fe_8Ge_4S_{32}$ (x = 2.0) recorded between - 8 mm s^{-1} and + 8 mm s^{-1} (Figure 3.7). Altogether, the magnetic spectrum of Figure 3.7 is complicated with its broad external and intermediate lines. The largest hyperfine magnetic field at RT is <B> ~ 36 T for x = 0 and <B> ~ 35.4 T for x = 2.0. Note that the hyperfine magnetic field of α-Fe at RT is 33.1 T. The assumption of similar Lamb-Mössbauer factors for all phases leads to estimate that on the average ~ 25 % of the total Fe might be contained in the magnetic phase, the maximum value of ~ 37 % occurring for the "$Cu_{20}Zn_2Fe_8Ge_4S_{32}$" sample. There is no possibility to obtain the observed <B>'s from a combination of Fe with one or more than one element chosen among Cu, Zn and Ge. Then, the magnetic phase includes Fe atoms; up to ~ 3 Fe for x = 2.0, and probably other metallic elements and sulfur atoms. It is worth mentioning that the studied samples are not attracted to a strong permanent magnet at RT. A Mössbauer spectrum of the x = 2.0 sample, recorded at 4.2 K, shows that the main phase becomes also magnetic (data not shown). The maximum hyperfine magnetic field of this mixture of two magnetic phases is ~ 36.4 T, a maximum close to the

maximum field, 35.4 T, found at RT. The Mössbauer spectrum recorded at 4.2 K is however too complex to be fitted reliably.

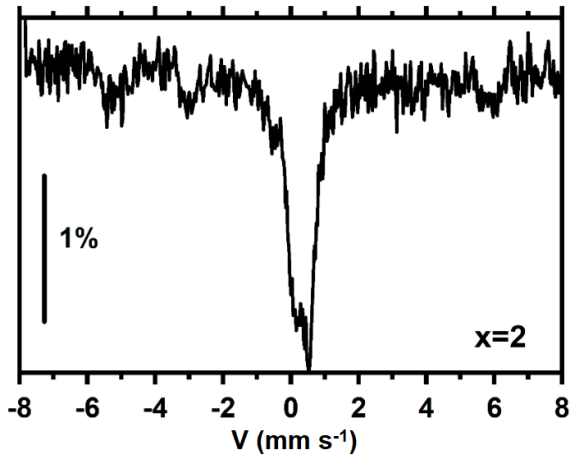

Figure 3.7. Room-temperature ^{57}Fe Mössbauer spectrum of $Cu_{20}Zn_2Fe_8Ge_4S_{32}$ in a velocity range (- 8 mm s^{-1}, + 8 mm s^{-1}).

The velocity intervals between the central lines of the previous magnetic phases are 1.73(5), 1.70(4), 1.63(4), and 1.69(3) for x = 0, 0.4, 1.2, and 2.0 respectively. The average position of the center of gravity of these lines is 0.26(3) mm s^{-1}. The area fractions of the central peaks of magnetic components, y, normalized to the total spectral areas measured between - 2.5 mm s^{-1} and + 2.5 mm s^{-1}, increase with x. The y values are 0.02(1), 0.04(2), 0.06(2), and 0.09(2) for x = 0, 0.4, 1.2, and 2.0 respectively. The area fractions associated with the magnetic phase are estimated by assuming that the intensity ratios of peaks of sextuplets are the theoretical ones for thin absorbers, *i.e.* 3 for external lines, 2 for intermediate lines and 1 for central lines. If the central area fraction of the magnetic phase is y, then its total area is (3+2+1) y = 6 y when all peaks are included. The total area of the non-magnetic phase is by definition 1- y. The total area of the two phases is 1+5y. Finally, the area fractions of the magnetic phase are estimated to be given by 6 y/(1+5 y), that is 0.11, 0.20, 0.28, and 0.37 for x = 0, 0.4, 1.2, and 2.0, respectively, with an average of 0.24. The number of Fe atoms in the magnetic phase increases accordingly between ~ 1 and ~ 3 when x increases from 0 to 2.0 with the additional assumption of equal Lamb-Mössbauer factors for all Fe sites. For reasons explained below, no value is given for x = 0.8.

These magnetic contributions may result from the presence of magnetic secondary phases, thus implying some significant changes of actual compositions with respect to nominal ones as it was suggested for the $x = 0$ sample in Chapter 2. However, the selectivity of ^{57}Fe Mössbauer spectroscopy makes these magnetic phases clearly visible despite the fact that their atomic fractions in the studied samples are possibly small. An alternative hypothesis to account for the presence at RT of a magnetic contribution in all samples is that the magnetic contribution is intrinsic to the germanite/renierite structure in which iron sublattices with different magnetic ordering temperatures would coexist. It is in concordance with the two superstructure peaks presumably due to a magnetic structure visible by NPD (Chapter 2, section 2.3.3). Also, this might explain why powder X-ray diffraction fails to detect any "secondary phase". The close values of maximum hyperfine magnetic fields at 4.2 K and at RT mean that the magnetic phase has its magnetic transition temperature well above RT. However, the validation of those assumptions requires a perfect knowledge of both crystal and magnetic structure of germanite/renierite systems. The crystal structure of germanite will be addressed in Chapter 4, but the magnetic structure is out of the scope of this work.

Hereafter, we discuss no more the previous central lines due to the magnetic contribution at RT and we continue to use the nominal compositions. Only the two or three components of the central part of any spectrum that is relevant to the studied phases are numbered, starting with 1 and the sum of their area fractions is normalized to 1.

Figure 3.6 shows that the main components of the spectra are packed with peaks (at least four) from the different sites in narrow velocity ranges. The determination of the exact number of Mössbauer sites is thus problematic all the more than lines may become broader as a consequence of aforementioned structural disorder. Nevertheless, asymmetrical spectra allow us to conclude unambiguously that their central components consist of at least two doublets.

3.2.3.2 Thinning of RT Mössbauer spectra

To highlight the various iron containing phases and the evolution of spectra with *x*, we "thin" them with a method described in section 7.2 of reference [174]. The peaks in thinned spectra are thus considered significant only if their amplitudes are clearly larger than low amplitude fluctuations above the zero background (~ 0.1 in Figure 3.8). The thinning method yields *in fine* "spectra" whose resolutions are improved and, importantly, whose areas are normalized to 1 so that they are directly comparable (Figure 3.8). The previous method was used by Hightower *et al.*[175] to study Li-SnO anode materials for Li-ion cells (^{119}Sn Mössbauer isotope). A final remark is that thinned spectra may be fitted in turn with Gaussian or Voigt lines to provide starting values for classical least-squares fitting methods of as-recorded spectra.

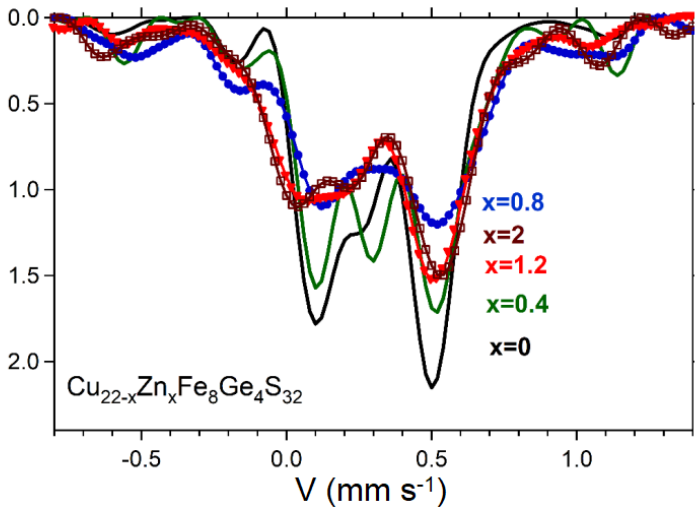

Figure 3.8. Thinned RT ^{57}Fe Mössbauer spectra of $Cu_{22-x}Zn_xFe_8Ge_4S_{32}$ obtained from as-recorded spectra of Figure 3.6 for x = 0, 0.4, 0.8, 1.2, and 2.0. For the sake of clarity, thinned spectra are plotted in a velocity range narrower than the one of Figure 3.6 Central peaks of magnetic phase emerge at ca. - 0.5 mm s^{-1} and ca. + 1 mm s^{-1}.

Figure 3.8 highlights a first pair (x = 0, x = 0.4), whose peaks are narrower than those of other spectra, with two high amplitude central peaks and a smaller amplitude peak located between them. A second pair (x = 1.2, x = 2.0) is made up of almost identical spectra with peaks broader than those of the first pair. Narrow "valleys" are seen at *ca.* + 0.3 mm s^{-1}. The x = 0.8 spectrum differs from the

previous ones. It bears a reminiscence of the two intense peaks of the first pair, though broader, with a broad and flat region between them. This region might result from a weighted sum of a peak and of a valley.

The previous characteristics are fully consistent with the conclusions, based on X-ray diffraction patterns, according to which germanite and renierite structures are formed for $x \leq 0.4$ and $1.2 \leq x \leq 2.0$, respectively, while the $x = 0.8$ sample belongs to a two-phase domain.

3.2.3.3 Least-squares fits of RT Mössbauer spectra

As suggested by the thinned spectra of Figure 3.8, as-recorded spectra may be least-squares fitted with either two doublets, two doublets and a singlet or three doublets accordingly to the Zn content. As far as possible, FWHM's are free to vary from doublet to doublet but peaks of a given doublet are constrained to have identical amplitudes and FWHM's. However, the narrowness of the central component leads sometimes to unreliable results with FWHM's less than the natural linewidth as peaks overlap strongly. In that case, all fitted peaks are constrained to have the same FWHM's.

3.2.3.4 Cases of $x = 0$ and $x = 0.4$ samples

Mössbauer sites, more particularly for $x = 0$ and $x = 0.4$, are crowded into a restricted velocity range. This makes it difficult to determine their number. Accordingly, we fitted these spectra with two doublets, two doublets and a singlet, and three doublets with FWHM's either free to vary or constrained to be all equal. The solid lines of Figure 3.6 for $x = 0$ and $x = 0.4$ samples are obtained when fitting with two doublets and a singlet, all with the same FWHM. The fittings that we performed in the various conditions described above show that IS and QS of the two main doublets are robust parameters whose respective average values are similar for $x = 0$ and $x = 0.4$ samples (Table 3.1).

Table 3.1. Average isomer shifts (IS) and quadrupole splittings (QS) of the two main doublets for x = 0 and x = 0.4 samples found from all fits.

Doublet N°		**IS (mm s^{-1})**	**QS (mm s^{-1})**	**Γ (mm s^{-1})**
1	$x = 0$	0.28 ± 0.02	0.37 ± 0.03	0.32 ± 0.02
	$x = 0.4$	0.29 ± 0.02	0.37 ± 0.03	0.37 ± 0.02
2	$x = 0$	0.40 ± 0.03	0.31 ± 0.02	0.30 ± 0.04
	$x = 0.4$	0.44 ± 0.04	0.31 ± 0.04	0.34 ± 0.04

The results shown in Table 3.1 are quite similar to those recently published.[151] There are no differences between fits performed with the previous doublets adding either a singlet or a doublet because the latter has an almost zero QS (~ 0.03(3) mm s^{-1}). All FWHM's (*i.e.* Γ) are constrained to be the same in the final fits (Figure 3.6). Singlets have FWHM's of 0.32(1) mm s^{-1} and 0.36(1) mm s^{-1} while the IS are equal to 0.30(3) mm s^{-1} and 0.27(7) mm s^{-1} for $x = 0$ and $x = 0.4$ samples, respectively. The most sensitive parameters to the fitting assumptions are the area fractions.

Fits with two doublets:

If all FWHM's are the same, the area fractions p_1 and p_2 of doublets N°1 and N°2 are $p_1 = 0.54(3)$, $p_2 = 0.46(3)$ for $x = 0$, and $p_1 = 0.52(4)$, $p_2 = 0.48(4)$ for $x = 0.4$. If the latter constraint is removed, the area fractions become $p_1 = 0.81$, $p_2 = 0.19$ for $x = 0$, and $p_1 = 0.73$, $p_2 = 0.27$ for $x = 0.4$. However, in the second case the FWHM's are very different for sites 1 and 2, being 0.34 mm s^{-1} and 0.24 mm s^{-1}, respectively, for $x = 0$, and 0.38 mm s^{-1} and 0.29 mm s^{-1} for $x = 0.4$. The value of 0.24 mm s^{-1} is approximately equal to the smallest possible FWHM that we measure generally. We are thus led to select the first set of results described above with doublets of identical FWHM's and of nearly equal fractions $p_1 \approx p_2$.

Fits with two doublets and a singlet:

When a singlet (N° 3) is included in fits, the area fractions become: $p_1 = 0.64(3)$, $p_2 = 0.28(3)$, $p_3 = 0.08(3)$ for $x = 0$, and $p_1 = 0.64(4)$, $p_2 = 0.24(4)$, $p_3 = 0.12(4)$ for $x = 0.4$. To conclude, the existence of two Fe^{3+} Mössbauer sites in germanite phases (*i.e.* x = 0 and $x = 0.4$ samples) is unambiguously proven and their hyperfine parameters are obtained. The presence of a third minor Fe^{3+}

Mössbauer site in a symmetrical environment (QS ≈ 0) is less firmly established from Mössbauer data only. However, this is in fair agreement with single crystal X-ray results obtained recently on synthetic germanite highlighting that the high symmetry 2*a* site is fully occupied by Fe (Chapter 4, section 4.3.1).

3.2.3.5 Cases of the *x* = 1.2 and *x* = 2.0 samples

The central parts of the spectra of the second family, that are broader than those of the first family (Figure 3.8), cannot be accounted for with only two doublets. Consequently, final least-squares fits have been carried out with three doublets (Figure 3.6). The fitting parameters do not differ significantly when the FWHM's are constrained to be all equal or are let free to vary separately.

Table 3.2. Isomer shifts (IS) and quadrupole splittings (QS) of the three doublets used to fit Mössbauer spectra for x = 1.2 and x = 2.0 samples.

Doublet N°		**IS (mm s^{-1})**	**QS (mm s^{-1})**	**Γ (mm s^{-1})**	**Area fraction *p***
1	*x* = 1.2	0.25 ± 0.03	0.41 ± 0.06	0.33 ± 0.04	0.45 ± 0.12
	x = 2.0	0.24 ± 0.02	0.44 ± 0.04	0.32 ± 0.02	0.49 ± 0.05
2	*x* = 1.2	0.39 ± 0.03	0.33 ± 0.03	0.33 ± 0.03	0.39 ± 0.08
	x = 2.0	0.41 ± 0.02	0.37 ± 0.02	0.31 ± 0.02	0.43 ± 0.05
3	*x* = 1.2	0.29 ± 0.10	0.83 ± 0.10	0.39 ± 0.10	0.16 ± 0.12
	x = 2.0	0.31 ± 0.07	0.93 ± 0.07	0.31 ± 0.05	0.08 ± 0.05

The hyperfine parameters gathered in Table 3.2 are typical of Fe^{3+} ions and are similar for both Zn contents. It should be noted that (i) the hyperfine parameters of sites 1 and 2 are comparable to those of sites 1 and 2 of the first family (*x* = 0 and 0.4, Table 3.1), suggesting some similarities in term of chemical environments, and (ii) the quadrupole splitting of site 3 is the largest one found in the present study, suggesting that the related Fe^{3+} ions are in strongly distorted chemical environment. These pieces of information on the local environment of Fe atoms in this sulfide are in favor of the complex renierite crystal structure instead of the "simple" briartite one, as supposed from XRPD analyses for the *x* = 1.2 and *x* = 2.0 samples. This is confirmed by the huge difference of hyperfine parameters determined from ^{57}Fe Mössbauer spectroscopy between synthetic briartite Cu_2FeGeS_4 [176] and our samples. First, iron atoms are in a +II oxidation state in

briartite[176] and in +III oxidation state in our samples (as expected in renierite). Secondly, the quadrupole splitting associated to the doublet in briartite is ~ 2.56(2) mm s^{-1} at RT,[176] while those associated to the different iron sites in our samples are much smaller (*i.e.* ~ 0.4 mm s^{-1} and ~ 0.9 mm s^{-1}, Table 3.2). Hence, ^{57}Fe Mössbauer spectroscopy results indicate unambiguously that the crystal structure of our Zn-rich samples ($x \geq 1.2$) is different from that of briartite. Consequently, these results in association with those obtained from powder X-ray diffraction are in favor of a disordered renierite crystal structure for $x = 1.2$ and $x = 2.0$ samples.

3.2.3.6 Case of the $x = 0.8$ sample

As discussed previously, the Mössbauer spectrum recorded for the $x = 0.8$ sample is intermediate between those of the two families discussed above. From XRPD patterns, the studied sample consists of a two-phase mixture. Thus, its spectrum (Figure 3.6 and Figure 3.8) is expected to consist of at least five doublets that overlap strongly. The a *priori* values of the hyperfine parameters of all these contributions, which change slightly with x, are not known with enough precision to attempt to fit reliably the observed spectrum so as to get trustworthy hyperfine parameters. This is the reason why this spectrum is not discussed further.

3.2.3.7 Summary

- All the samples contain a phase magnetically ordered at room temperature.
- ^{57}Fe Mössbauer spectra reflect the structural changes evidenced by XRPD patterns that occur in $Cu_{22-x}Zn_xFe_8Ge_4S_{32}$ series when x increases between 0 and 2.0 with a first pair of spectra ($x = 0$ and 0.4), an intermediate spectrum ($x = 0.8$), and a second pair of spectra ($x = 1.2$ and 2.0).
- The central parts of the spectra (other than those of the magnetic contribution) consist unambiguously of at least two sites. In agreement with structural arguments from single crystal X-ray diffraction, the spectra include a third site. The hyperfine parameters are obtained for samples of

the two pairs. The narrow velocity ranges which contain the central parts prevent to fit reliably the spectrum with x = 0.8 as this sample is a mixture of two different phases.

- All the measured hyperfine parameters are consistent with iron being in the form of Fe^{3+}.
- Hyperfine parameters determined for Zn-rich samples ($x \geq 1.2$) indicate unambiguously that the crystal structure of the Zn-rich compounds is different from that of briartite.

3.2.4 Thermoelectric properties

The temperature dependences of the electrical resistivity, ρ, and Seebeck coefficient, S, in the $Cu_{22-x}Zn_xFe_8Ge_4S_{32}$ series are displayed in Figure 3.9a and Figure 3.9b respectively. Regardless of the Zn content, a positive value for the Seebeck coefficient is measured, confirming holes as dominant charge carriers. For x = 0, the electrical resistivity, which decreases slightly as the temperature increases, shows that this material exhibits a semiconducting behavior, though approaching the transition towards a metallic state. The Seebeck coefficient varies slightly with temperature and in opposite trend relative to the electrical resistivity. This behavior is explained by the fact that the conduction regime is intermediate between metallic and semiconducting. When the Zn content increases, the magnitude of the electrical resistivity increases drastically at 300 K from 9.3 mΩ cm for x = 0 to 2.57×10^3 mΩ cm for x = 2.0. The Seebeck coefficient also increases with the Zn content from + 122 μV K^{-1} for x = 0 to + 262 μV K^{-1} for x = 2.0 at 300 K. The temperature dependences of ρ and S for x = 2.0 tend toward a semiconducting behavior, as observed from the sharper decrease of ρ (plotted in log scale) with the increase of temperature. This behavior is consistent with a decrease of the carrier concentration. Indeed, from a formal charge point of view, stoichiometric $Cu_{22}Fe_8Ge_4S_{32}$ is assumed to be $(Cu^+)_{20}(Cu^{2+})_2(Fe^{3+})_8(Ge^{4+})_4(S^{2-})_{32}$. By analogy to $Cu_{12}Sb_4S_{13}$ tetrahedrite, there are two unoccupied states in the valence band above E_F. Therefore, the unoccupied states in such a compound could be filled by substituting Cu by a divalent transition element (Zn), as also reported in

tetrahedrite and colusite,[116,177] leading to a semiconducting behavior. In other words, since Zn, Fe and Ge ions are strictly in the Zn^{2+}, Fe^{3+} and Ge^{4+} states, the increase of *S* and ρ with *x* is consistent with a decrease in Cu^{2+} content, *i.e.* of hole concentration. On the other hand, the introduction of additional Zn^{2+} cations on the copper sites likely decreases the mobility of carriers due to the creation of point defects, which perturbates the percolation paths in the tridimensional "Cu-S" conductive network. Unfortunately, the variation of the carrier concentration with *x* was not verified as it was impossible to extract reliable carrier concentration values from Hall effect measurements due to an anomalous signal. Finally, the significant increase of the electrical resistivity with *x* induces a decrease of the power factor from 0.29 mW m^{-1} K^{-2} for *x* = 0 to 0.11 mW m^{-1} K^{-2} for *x* = 2.0, at 700 K (Figure 3.9d).

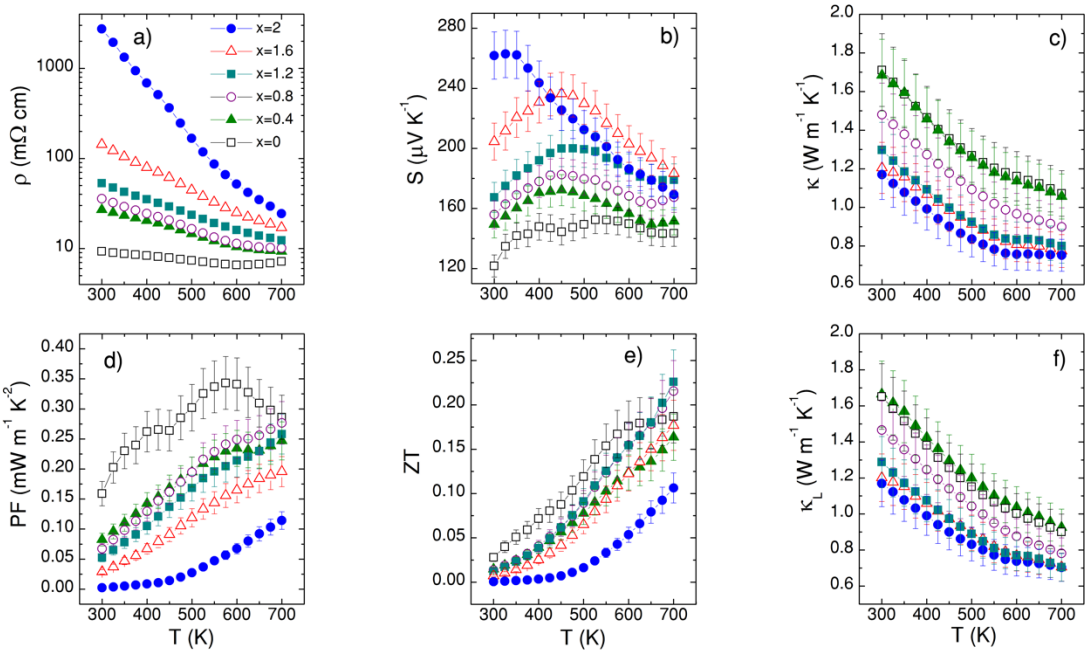

Figure 3.9. Temperature dependences of a) electrical resistivity (ρ), b) Seebeck coefficient (S), c) thermal conductivity (κ), d) power factor (PF), e) figure of merit (ZT, and f) lattice thermal conductivity (κ_L), in the in the $Cu_{22-x}Zn_xFe_8Ge_4S_{32}$ ($0 \leq x \leq 2.0$) series.

The temperature dependence of the thermal conductivity in the $Cu_{22-x}Zn_xFe_8Ge_4S_{32}$ series (Figure 3.9c) exhibits a systematic decrease of the thermal conductivity with increasing Zn content. This reflects the combined effects of a reduced electronic component of the thermal conductivity and a decreasing lattice contribution. By simply subtracting the electronic part from the total thermal conductivity, it can be observed that a higher Zn content (especially above $x = 0.8$) causes marked reductions in the lattice thermal conductivities of these compounds over the full temperature range (Figure 3.9f). In fact, two distinct sets of values can be observed depending of the Zn content. For $0 \leq x \leq 0.4$, the lattice thermal conductivity values are in the ranges of 1.60 - 1.65 W m^{-1} K^{-1} at 300 K and 0.90 - 0.95 W m^{-1} K^{-1} at 700 K, while for $1.2 \leq x \leq 2.0$, the lattice thermal conductivity drops down to 1.13 - 1.25 W m^{-1} K^{-1} at 300 K and 0.70 W m^{-1} K^{-1} at 700 K. Interestingly, the $x = 0.8$ sample, composed of both renierite and germanite, exhibits intermediate values around 1.45 W m^{-1} K^{-1} at 300 K and 0.80 W m^{-1} K^{-1} at 700 K. This trend suggests that the additional number of crystallographic sites and the higher cationic disorder in the renierite-type compounds ($1.2 \leq x \leq 2.0$), induced by the tetragonal distortion, provides an effective way of scattering heat carrying phonons. Unfortunately, the crystal structure of our synthetic renierite-type compounds being quite complex (as discussed in the structure analysis section), it was not possible to perform phonon calculations and to address the role of specific crystal structure features on phonon scattering. Finally, it must be pointed out that the κ_L values of the Zn-rich compounds ($1.2 \leq x \leq 2.0$) are in the same range as those of other copper-based sulfide minerals such as pristine $Cu_8Fe_3Sn_2S_{12}$ stannoidite,[178] and ordered colusites.[141,179]

From the above parameters, the figure of merit, *ZT*, was calculated for all the samples and displayed in Figure 3.9e. Overall, the *ZT* increases with temperature for all compositions. Due to the counter-balanced effects of the decrease of both the power factor and the thermal conductivity, the *ZT* remains constant for Zn content below $x \leq 1.6$ and decreases significantly for $x = 2.0$ due to the large increase of the electrical resistivity.

3.2.4.1 Summary

- Regardless of the Zn content, a positive value for the Seebeck coefficient is measured, confirming holes as dominant charge carriers.
- The introduction of additional Zn^{2+} cations on the copper sites likely decreases the mobility of carriers due to the creation of point defects, which perturbates the percolation paths in the tridimensional "Cu-S" conductive network.
- The symmetry reduction and the higher cationic disorder in the renierite-type compounds ($1.2 \leq x \leq 2.0$), induced by the tetragonal distortion, provides an effective way of scattering heat carrying phonons.

Now that we have seen the effect of a Cu to Zn substitution in germanite synthesized by mechanical alloying, the rest of this chapter is dedicated to the isovalent substitution of Ge by Sn in germanite prepared by sealed tube synthesis. This method was used instead of mechanical alloying because at the moment of this study, I was in the laboratory of Rennes, where no planetary ball mills were available. Additionally, the densification of the powders by SPS was done in different conditions than the ones presented in Chapter 2 because this series of sample was prepared before.

3.3 Results of Ge to Sn substitution in $Cu_{22}Fe_8Ge_{4-x}Sn_xS_{32}$

3.3.1 Sample preparation

Solid solutions of $Cu_{22}Fe_8Ge_{4-x}Sn_xS_{32}$ ($0 \leq x \leq 4$) were prepared by sealed tube synthesis followed by spark plasma sintering. The synthesis conditions for the ST samples are presented in Chapter 3, namely 24 h at 973 K, followed by an air quench at 773 K (summarized in Chapter 5, section 5.2.1.1). The resulting powders were then placed in WC dies of 10 mm diameter and densified by spark plasma sintering (SPS-FCT HPD 25) at 773 K for 30 min under a pressure of 150 MPa (heating and cooling rate of 50 and 20 K min^{-1}, respectively). This produced 10 mm diameter pellets, *ca*. 7 mm thick, with geometrical densities greater than 99 % of the crystallographic value.

3.3.2 Structural analysis

In the following paragraphs, the structural analysis of a series of tin-substituted germanite samples will be presented. Figure 3.10a displays the XRPD patterns of the five compositions of the series after their synthesis by sealed tube, namely $Cu_{22}Fe_8Ge_4S_{32}$, $Cu_{22}Fe_8Ge_3SnS_{32}$, $Cu_{22}Fe_8Ge_2Sn_2S_{32}$, $Cu_{22}Fe_8GeSn_3S_{32}$ and $Cu_{22}Fe_8Sn_4S_{32}$. To highlight the superstructure and secondary phase contributions, the highest peak of each pattern is cut at 50 % of its intensity. A shift of the diffraction peaks toward lower angles is observable with the increasing Sn content due to the increasing size of the unit cell as a result of the larger ionic radius of Sn^{4+} compared to Ge^{4+} (0.55 Å and 0.39 Å, respectively). The refined cell parameters of the end members of the series, $Cu_{22}Fe_8Ge_4S_{32}$ and $Cu_{22}Fe_8Sn_4S_{32}$, are in reasonable agreement with previously reported values (comparing with nekrasovite for the Sn_4,).[147,151,180] The refined cell parameters of the whole series (Table 3.3, Figure 3.11), revealed a linear trend with the increasing Sn content and follow Vegard's law, which was expected since the structure is maintained. The linear dependency of the cell parameter with the Sn content is a proof that the five samples crystallize in the same cubic space group ($P\bar{4}3n$). An interesting feature of the Ge to Sn substitution is the gradual decrease of the bornite content together

with the semi-crystalline germanite-related phase (shoulder on the main peaks). Regarding the purity, while the first two samples (x = 0, 1) present slight content of bornite, the last three samples (x = 2, 3, 4) are pure.

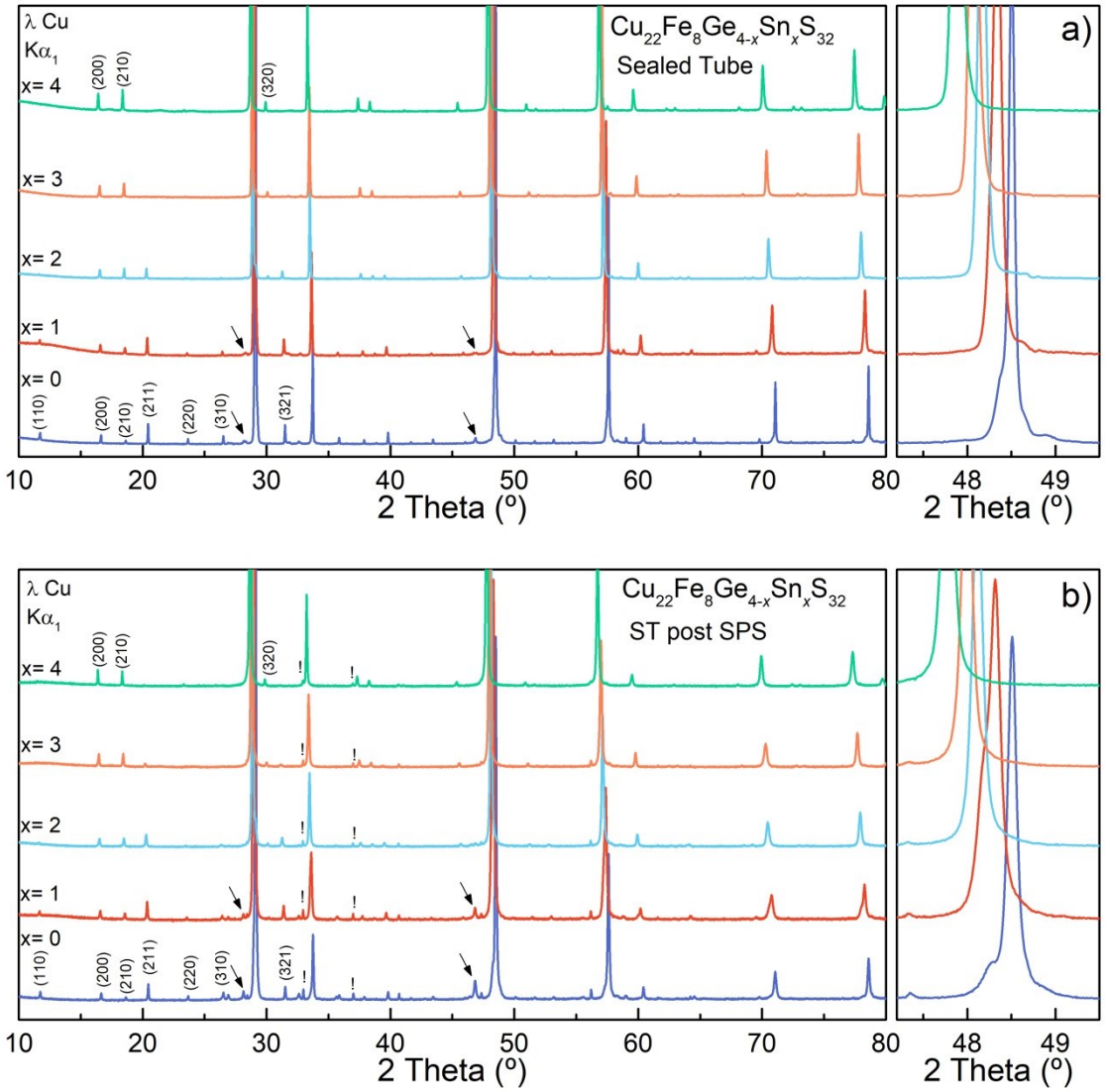

Figure 3.10. XRPD patterns of $Cu_{22}Fe_8Ge_{4-x}Sn_xS_{32}$ with ($0 \leq x \leq 4$) in a) after the sealed tube synthesis and b) after SPS densification. Arrows point the main diffraction peaks of a bornite secondary phase and exclamation points to a FeS_2 phase.

The densification of the powder samples systematically led to the formation of FeS_2 as secondary phase ($Pa\bar{3}$, a = 5.415(9) Å). The formation of this phase was not observed previously and is probably due to the two times higher sintering pressure, compared to the conditions presented in Chapter 2. The cell parameters

dependency with the substitution also follows Vegard's law (Figure 3.11). The slight increase in cell parameters of the samples after the SPS treatment can be explained by a cationic disorder induced by sulfur loss (Chapter 2). This is also in agreement with the increase in bornite content after SPS for both x = 0 and x =1 samples, which was shown to compensate the cationic imbalance due to sulfur volatilization.

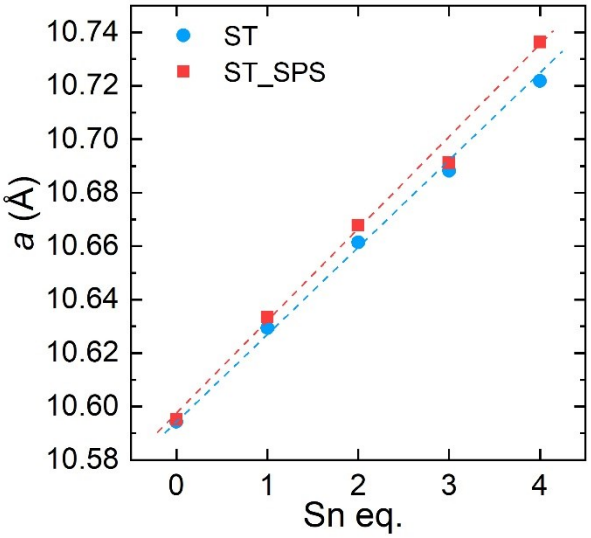

Figure 3.11. Cell parameters evolution of $Cu_{22}Fe_8Ge_{4-x}Sn_xS_{32}$ with Sn content. ST is represented in blue and ST_SPS in red, a trend is used as a guide for the eye.

Table 3.3. Refined cell parameters before and after SPS of the samples $Cu_{22}Fe_8Ge_{4-x}Sn_xS_{32}$ with x = 0 – 4.

x	**0**	**1**	**2**	**3**	**4**
a (Å)	10.5942(6)	10.6293(5)	10.6613(8)	10.6881(9)	10.7218(1)
a (Å) SPS	10.5951(1)	10.6334(5)	10.6677(7)	10.6911(3)	10.7363(5)

Finally yet importantly, another consequence of the Ge to Sn substitution is the disappearance of bornite together with the semi-crystalline germanite-related phase (shoulder on the main peaks). As a reminder, it was shown in Chapter 2 that bornite Cu_5FeS_4 is formed, when germanite $Cu_{22}Fe_8Ge_4S_{32}$ is synthesized at high temperature, to balance the "extra" cationic stoichiometry engendered by sulfur loss. Therefore, the decreasing bornite content of the sample with the substitution until its complete disappearance for x = 2, may lead one to think that the Sn atoms

stabilize the structure. The three hypotheses that prevail to explain this phenomenon will be presented in the next section.

3.3.2.1 Stabilization of the germanite structure by the Ge to Sn substitution

The first hypothesis is that the Sn atoms stabilize the germanite structure by forming stronger bonds with sulfur compared to Ge. However, this hypothesis was put aside based on TGA-DSC results evidencing that at 700 K, $Cu_{22}Fe_8Sn_4S_{32}$ (Figure 3.12); and $Cu_{22}Fe_8Ge_4S_{32}$ (Figure 2.19, section 2.3.3.2) have an equivalent mass loss, *i.e.* 98.27 wt. % and 98.45 wt. %, respectively. The exothermic peak at 665 K will be discussed in relation with other results in the section 3.3.2.2.

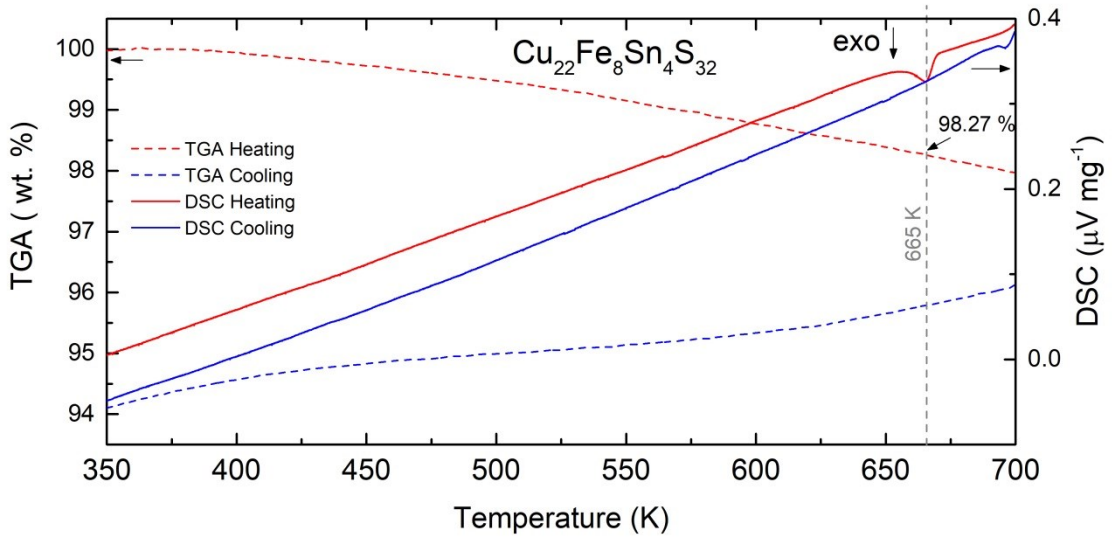

Figure 3.12. TGA-DSC of $Cu_{22}Fe_8Sn_4S_{32}$ synthesized by ST and post SPS. The DSC signal is in full lines (right axis) and TGA signal in dashed lines (left axis).

The second hypothesis is that the Sn atoms can compensate the structure charge imbalance induced by sulfur loss by altering its oxidation state from Sn^{4+} to Sn^{2+}. However, the ^{119}Sn Mössbauer spectroscopy of all the Sn-containing samples (x = 1, 2, 3, 4) revealed the presence a single peak with an IS of 1.54 mm s^{-1} (referred to $BaSnO_3$ at RT, Figure 3.13a, x = 2, 3, 4, not shown because very similar to x = 1) and therefore confirms the presence of Sn^{4+} only for all the compositions.[5] The presence of Sn in its +II oxidation state would be manifested

by a peak with an IS ~ 3.5 mm s^{-1}. The hyperfine parameters are summarized in Table 3.4. The ^{57}Fe Mössbauer spectra at RT of the sample $Cu_{22}Fe_8Sn_4S_{32}$ (Figure 3.13b) is not fitted yet and the distribution of the Fe atoms in the structure seems more complicated than that of the $Cu_{22}Fe_8Ge_4S_{32}$ sample (Figure 4.6, section 4.3.1).

Table 3.4. Isomer shift (IS), quadrupole splitting (QS) and FWHM (Γ) of the doublet used to fit the ^{119}Sn Mössbauer spectra at RT for $1 \leq x \leq 4$ in $Cu_{22}Fe_8Ge_{4-x}Sn_xS_{32}$

x	**IS (mm s^{-1}) (± 0.03)**	**QS (mm s^{-1}) (± 0.03)**	**Γ (mm s^{-1}) (± 0.03)**
1	1.53	0.43	0.82
2	1.54	0.48	0.98
3	1.54	0.43	0.94
4	1.54	0.43	0.92

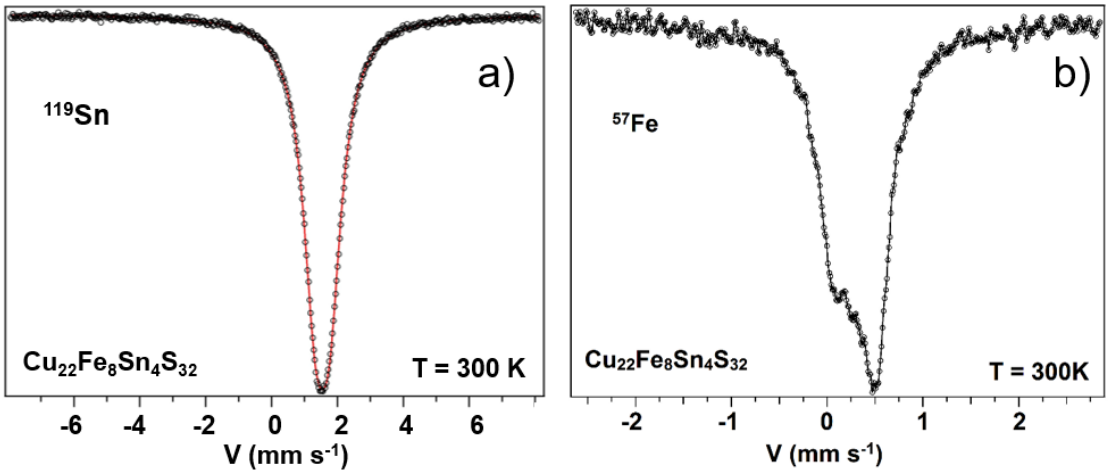

Figure 3.13. a) ^{119}Sn and b) ^{57}Fe Mössbauer spectra at RT of $Cu_{22}Fe_8Sn_4S_{32}$ sample.

Note that the Ge to Sn substitution did not suppressed the magnetic ordering at low temperature. Figure 3.14 displays the ^{57}Fe Mössbauer spectra measured at 4.25 K of the samples $Cu_{22}Fe_8Ge_4S_{32}$, $Cu_{22}Fe_8Ge_2Sn_2S_{32}$ and $Cu_{22}Fe_8Sn_4S_{32}$.

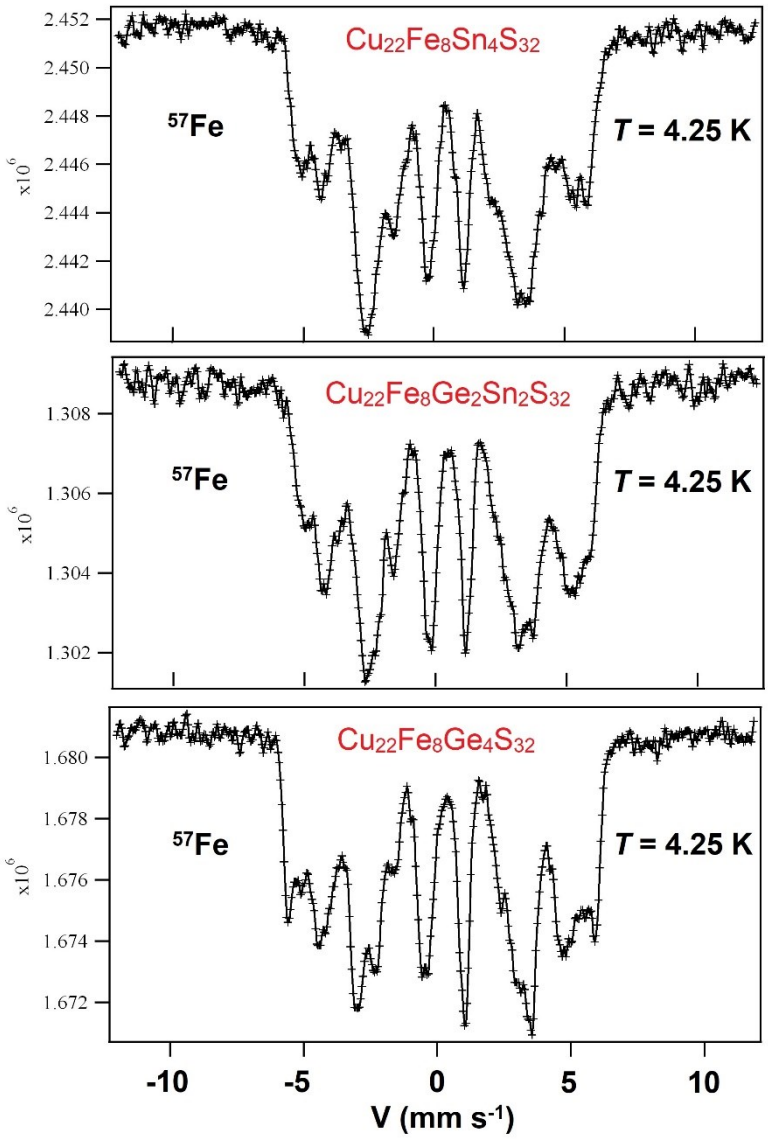

Figure 3.14. ^{57}Fe Mössbauer spectra measured at 4.25 K of the $Cu_{22}Fe_8Ge_4S_{32}$, $Cu_{22}Fe_8Ge_2Sn_2S_{32}$ and $Cu_{22}Fe_8Sn_4S_{32}$ samples.

Finally, the third hypothesis regarding the apparent gain in stability of the crystal structure of germanite with Sn substitution is that the replacement of Ge atoms by Sn leads to a larger unit cell, thus larger interstitial sites. Consequently, it facilitates the occupation of some interstitials sites by extra cations on the basis that Sn^{4+} has a larger radius (0.55 Å), than Ge^{4+}(0.39 Å). While the structure of $Cu_{22}Fe_8Sn_4S_{32}$ has not been resolved yet, preliminary refinements of synchrotron data together with single crystal X-ray data revealed the partial occupation of an additional interstitial site, *i.e.* 6*b* site. The results from the Rietveld refinement on

synchrotron data measured in resonant condition at Cu K-edge, *i.e.* more sensitive to subtle change of Cu occupation in the structure, are shown in Figure 3.15. The latter evidenced the improvement of the *Bragg R-Factors* upon the partial occupation of the interstitial 6*b* site by 1 atom. For further information on the resonant scattering experiments see Chapter 4, section 4.2.2.

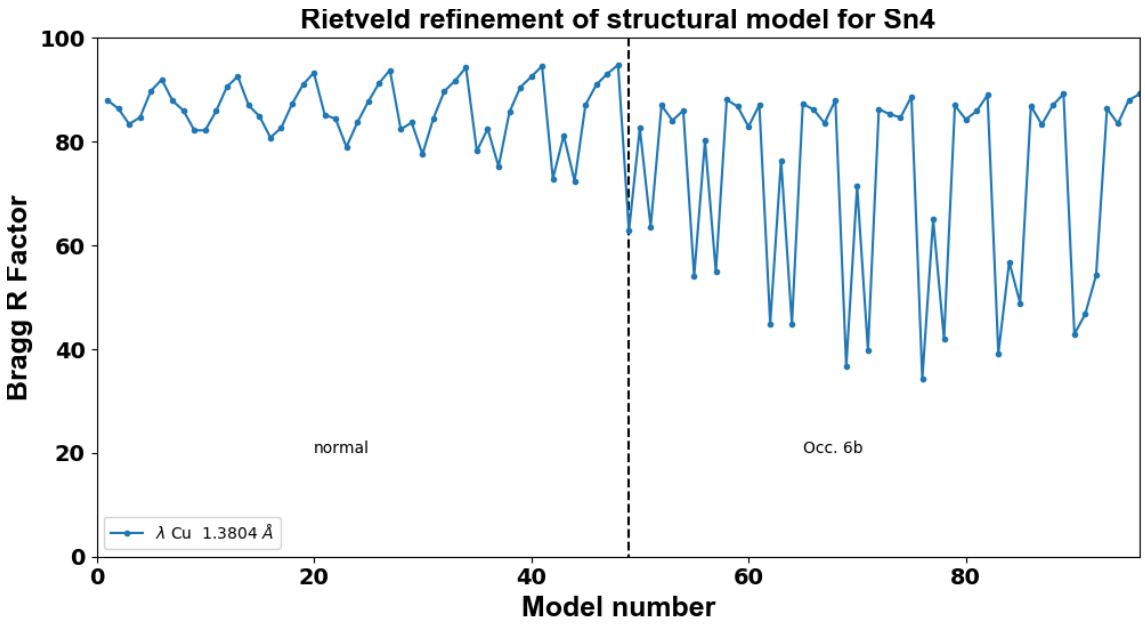

Figure 3.15. Results of the Rietveld refinement of a $Cu_{22}Fe_8Sn_4S_{32}$ sample measured by synchrotron at Cu K-edge with some structural models based on a germanite derivative crystal structure (models 1 – 46) and the same but with a partial occupation (Sof= 1/6) of the interstitial site 6b (models 49 – 97).

3.3.2.2 *In situ* thermal stability experiments of $Cu_{22}Fe_8Sn_4S_{32}$

Finally, to investigate the thermal stability of the end member $x = 4$ sample, an *in situ* neutron diffraction experiment on ST powders was performed. Figure 3.16 displays the NPD patterns measured each 10 K from RT to 948 K. It evidenced the disappearance of three low intensity superstructure peaks at low angle (circled in red) at ~ 660 K. Thus, one can conclude that at 660 K, a temperature induced phase transition toward a phase with higher structural disorder inhibits the supercell.

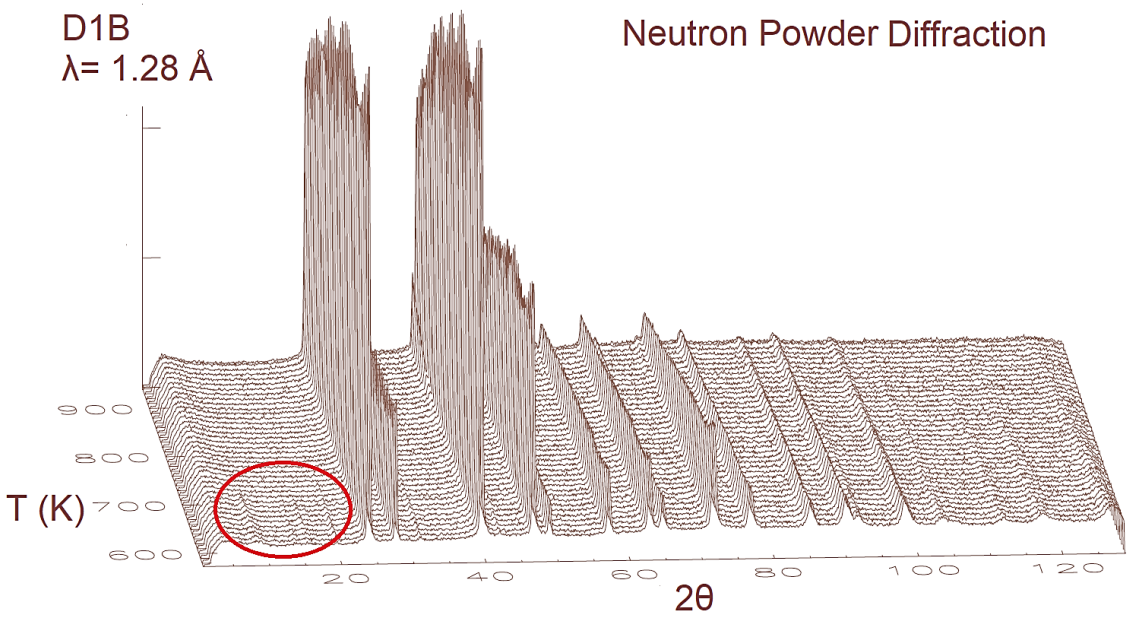

Figure 3.16. Neutron powder diffraction patterns of $Cu_{22}Fe_8Sn_4S_{32}$.

A Le Bail refinement of the diffraction patterns recorded from 578 K to 948 K with the $P\bar{4}3n$ (~ 10.6 Å) space group allows to plot the cell parameter of $Cu_{22}Fe_8Sn_4S_{32}$ as a function of temperature (Figure 3.17). The cell parameter linearly increases with temperature from 578 K to 635 K and then reach a plateau until 700 K and increase from this temperature to 948 K with the same initial slope. The peculiar behavior of the thermal expansion coupled to the concurrent disappearance of the superstructure peaks together with the exothermic peak measured at 665 K by DSC (Figure 3.12) are in good agreement with a phase transition from a semi-ordered germanite-type structure to a disordered structure. Indeed, a temperature induced crystallographic rearrangement of the cations can lead to the lost of the superstructure peak intensity or of symmetry elements. Unfortunately, we are not able yet to bring answers to this.

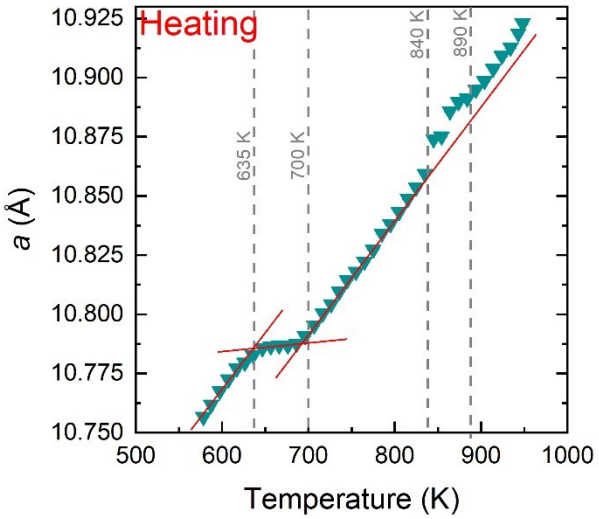

Figure 3.17. NPD stability in temperature. The cell parameter thermal expansion of $Cu_{22}Fe_8Sn_4S_{32}$.

3.3.2.3 Summary

- The Ge for Sn substitution ($0 \leq x \leq 4$) yielded the solid solution $Cu_{22}Fe_8Ge_{4-x}Sn_xS_{32}$ germanite samples which crystallize in the $P\bar{4}3n$ space group.
- The Ge to Sn substitution reduces the content of secondary phases.
- The densification of the samples by SPS induce a slight increase of the lattice parameters and the appearance of FeS_2 in small quantity (< 1 wt. %).
- Sn is in its IV oxidation state only.
- All samples are magnetically ordered at RT.
- The Sn atoms stabilize the structure by facilitating the filling of unoccupied sites by extra cationic elements.
- The end member $Cu_{22}Fe_8Sn_4S_{32}$, is stable in temperature up to 635 K.

3.3.3 Thermoelectric properties

The temperature dependence of the Seebeck coefficient (S), given in Figure 3.18b, shows that all the compounds are *p*-type materials with S values ranging from + 130.2 µV K^{-1} to + 214.7 µV K^{-1} at 300 K. The evolution with temperature of the Seebeck coefficient of the $Cu_{22}Fe_8Ge_4S_{32}$, $Cu_{22}Fe_8Ge_3SnS_{32}$, $Cu_{22}Fe_8Ge_2Sn_2S_{32}$, and $Cu_{22}Fe_8GeSn_3S_{32}$ samples evidences a curve bell shape. Also, it seems that the

maximal Seebeck value is shifting toward higher temperature for the sample with higher Sn content: 425 K for x = 0, 450 K for x = 1, 500 K for x = 2, 550 K for x = 3 and higher or equal to 650 K for x = 4. The Ge-rich samples display higher Seebeck coefficient than their Sn-rich counterparts, with values of + 214.7 µV K^{-1} for $Cu_{22}Fe_8Ge_4S_{32}$, + 205.4 µV K^{-1} for $Cu_{22}Fe_8Ge_3SnS_{32}$, + 194.8 µV K^{-1} for $Cu_{22}Fe_8Ge_2Sn_2S_{32}$, + 138.8 µV K^{-1} for $Cu_{22}Fe_8GeSn_3S_{32}$ and + 130.2 µV K^{-1} for $Cu_{22}Fe_8Sn_4S_{32}$ at RT (*i.e.* $x = 0 > x = 1 > x = 2 > x = 3 > x = 4$). Considering that the substitution is isovalent, such decrease of the Seebeck coefficient is unlikely due to a charge carrier concentration variation. Indeed the charge carrier concentration and mobility of the samples $Cu_{22}Fe_8Ge_4S_{32}$, $Cu_{22}Fe_8GeSn_3S_{32}$ and $Cu_{22}Fe_8Sn_4S_{32}$, obtained from Hall effect measurements (Table 3.5), evidenced that the three samples have similar charge carrier concentration, *e.g.* 3.05×10^{21} m^{-3}, 3.43×10^{21} m^{-3} and 3.27×10^{21} m^{-3}, respectively. A high Seebeck coefficient together with a high charge carrier concentration and a low mobility can be explained by a high effective mass (m^*) of the charge carriers. This is in agreement with the effective masses obtained experimentally from the Seebeck coefficient (Table 3.5),[36] *e.g.* 22.5 m_0 (x = 0), 15.7 m_0 (x = 3), 14.3 m_0 (x = 4). Generally, large m^* are attributed to the heavy band mass and/or high band degeneracy near the Fermi level. This is the case in germanite where the top of the valence band is composed of the Cu-3*d* and S-3*p* hybridized orbitals, a feature commonly observe in cubic crystal structure.[138] Note that the *p*-type Cu-S and Cu-Se based compounds have relatively large m^* values regardless of the crystal structures: $Cu_{26-x}Zn_xV_2Sn_6S_{32}$ (4 m_0 - 5 m_0 at 300 K),[181] $Cu_{26}V_2Sn_{6-z}S_{32}$ (5 m_0 - 7 m_0 at 300 K),[181] $Cu_{2-\delta}S$ (2.1 m_0 at 750 K),[182] $Cu_{2-\delta}Se$ (6.5 m_0 at 750 K),[182] $Cu_3Sn_xSb_{1-x}S_4$ (3.0 m_0 at 300 K),[183] $Cu_{2.95}Sb_{1-x}Sn_xSe_4$ (1.5 m_0 at 300 K),[184] and $Cu_2Zn_{1-x}Fe_xGeSe_4$ (1.2 – 3.6 m_0 at 360 K).[185]. Unfortunately, the variation of the carrier concentration with below 300 K was not verified as it was impossible to extract reliable carrier concentration values from Hall effect measurements due to an anomalous signal, thus even the values at 300 K values should be considered with caution.

Table 3.5. Transport properties at 300 K of the samples $Cu_{22}Fe_8Ge_4S_{32}$, $Cu_{22}Fe_8GeSn_3S_{32}$ and $Cu_{22}Fe_8Sn_4S_{32}$

x	**Resistivity (Ω m)**	**Seebeck (μV K^{-1})**	**Charge carrier conc. (m^{-3})**	**Charge carrier mobility (cm^2 V^{-1} s^{-1})**	**Effective mass (m_0)**
0	2.85×10^{-4}	214	3.05×10^{21}	0.0718	23
3	1.75×10^{-4}	138	3.43×10^{21}	0.1043	16
4	1.04×10^{-4}	130	3.27×10^{21}	0.1832	14

The temperature dependence of the electrical resistivity for the five samples is given Figure 3.18a. Over the whole investigated temperature range, the electrical resistivity decreases with increasing temperature, hence revealing a semiconducting behavior. In agreement with the Seebeck coefficient, the electrical resistivity varies such as: $Cu_{22}Fe_8Ge_4S_{32}$ (28.47 mΩ cm) > $Cu_{22}Fe_8Ge_3SnS_{32}$ (24.11 mΩ cm) > $Cu_{22}Fe_8Ge_2Sn_2S_{32}$ (21.55 mΩ cm) > $Cu_{22}Fe_8GeSn_3S_{32}$ (17.45 mΩ cm) > $Cu_{22}Fe_8Sn_4S_{32}$ (10.42 mΩ cm). Interestingly, the electrical resistivity falls off regularly with the Sn for Ge substitution from $Cu_{22}Fe_8Ge_4S_{32}$ to $Cu_{22}Fe_8GeSn_3S_{32}$, and drops when all 4 Ge atoms are substituted for 4 Sn. The decrease in electrical resistivity support the decrease in the holes effective mass in the Sn-rich samples.

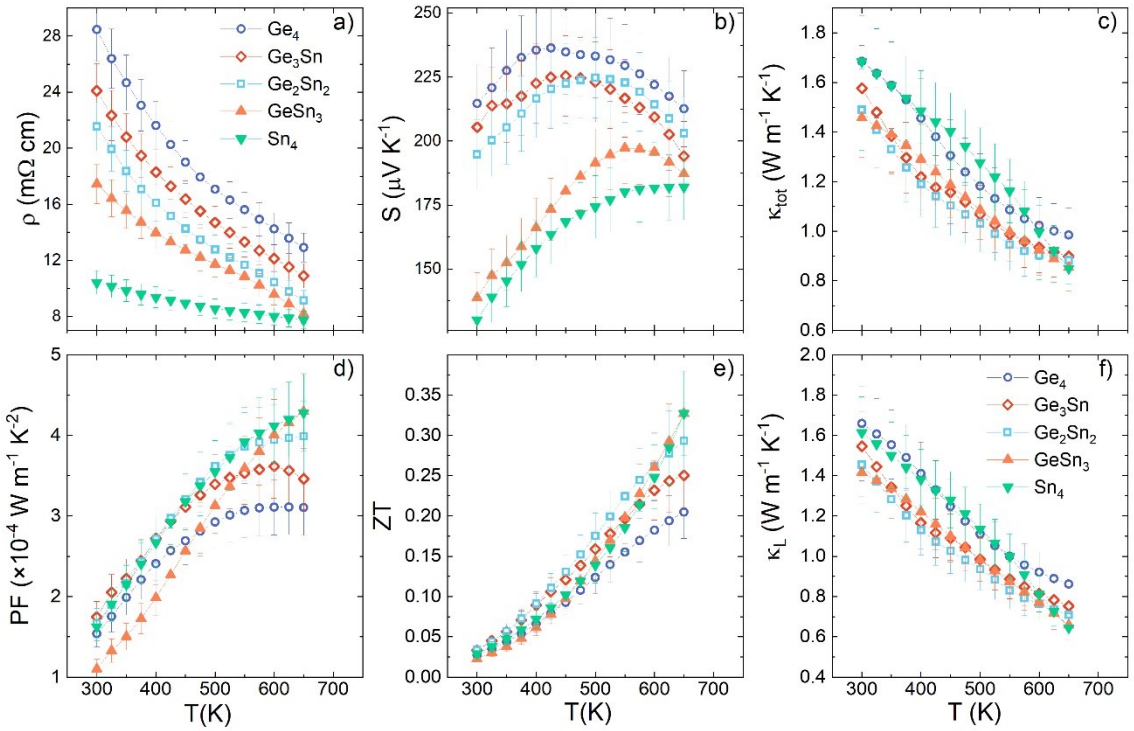

Figure 3.18. a) electrical resistivity b) Seebeck coefficient c) total thermal conductivity d) power factor e) ZT and f) lattice thermal conductivity of the Ge to Sn substituted germanite $Cu_{22}Fe_8Ge_{4-x}Sn_xS_{32}$ with x= 0, 1, 2, 3, 4.

The power factor of each sample increases with temperature as seen in Figure 3.18d. The $Cu_{22}Fe_8GeSn_3S_{32}$ and $Cu_{22}Fe_8Sn_4S_{32}$ samples have the highest power factor with a maximal value of 4.3×10^{-4} W m^{-1} K^{-2} at 650 K, $Cu_{22}Fe_8Ge_2Sn_2S_{32}$ stands behind with a maximum power factor of 4.0×10^{-4} W m^{-1} K^{-2}. The other two samples have power factor at 650 K of 3.5×10^{-4} W m^{-1} K^{-2} for $Cu_{22}Fe_8Ge_3SnS_{32}$ and 3.1×10^{-4} W m^{-1} K^{-2} for $Cu_{22}Fe_8Ge_4S_{32}$.

The temperature dependence of thermal conductivity (κ), displayed in Figure 3.18c, shows that the thermal conductivity is decreasing with temperature with similar magnitude for all the samples. Note that the samples containing both Ge and Sn, namely $Cu_{22}Fe_8Ge_3SnS_{32}$, $Cu_{22}Fe_8Ge_2Sn_2S_{32}$ and $Cu_{22}Fe_8GeSn_3S_{32}$, present a mildly lower total thermal conductivity compared to $Cu_{22}Fe_8Ge_4S_{32}$ and $Cu_{22}Fe_8Sn_4S_{32}$. While assuming an equal contribution of boundary scattering in all these compounds, this reduction of the total thermal conductivity can be assigned

to the decrease of lattice thermal conductivity due to enhancement of point defect scattering, stemming from differences in mass, size, as well as bonding strength of the unequal species (Figure 3.18f).[186,187]

The figure of merit *ZT* (Figure 3.18e) at 650 K is linearly increased with the Sn content from 0.21 ($Cu_{22}Fe_8Ge_4S_{32}$) to 0.33 ($Cu_{22}Fe_8Sn_4S_{32}$) due to the contribution of higher power factor and to the lower thermal conductivity.

3.4 Conclusion

The goal of Chapter 3 was to enhance the thermoelectric performances of germanite through cationic substitution. In this manner, a compound, $Cu_{22-x}Zn_xFe_8Ge_4S_{32}$ ($1.2 \leq x \leq 2.0$), with the renierite-type structure has been synthesized for the first time. The close structural relationship between this sulfide and the germanite shows that its conductive "Cu-S" network, as in germanite, constitutes a driving force for the appearance of *p*-type hole carriers and consequently of thermoelectric properties in this material. It appears clearly that the zinc concentration has a correlated effect on both the electrical and thermal conductivity in these sulfides. Increasing the Zn concentration in the copper network leads to a decrease in the concentration of hole carriers, *i.e.* to an increase of the electrical resistivity and Seebeck coefficient in renierite compared to germanite. Also, the cationic disorder in the copper network increases with the Zn content and results in a decrease in the thermal conductivity that ultimately becomes lower for renierite with respect to germanite. This explains the very similar figures of merit that are observed for both structural types independently of the zinc content. Further investigations on univalent copper-rich systems should be encouraged for enhancing the performances of *p*-type thermoelectric materials.

Additionally, we have completed the first known investigation of the $Cu_{22}Fe_8Ge_{4-x}Sn_xS_{32}$ series. The successful synthesis of the Sn-substituted germanite solid solution was confirmed by X-ray powder diffraction. The lattice constant of the cubic crystal structure $P\bar{4}3n$ expands linearly with increasing Sn content.

Preliminary structural analyses revealed that the Sn substitution allowed extra-cationic site occupancy. The substitution of Ge by a larger isovalent cation led to the decrease of electrical resistivity and Seebeck coefficient due to the decreasing of the effective mass. Also, the Sn-incorporation probably enhances point defect scattering of the heat carrying phonons as a result of mass, size, and bonding strength disparities. Thus a slight reduction of lattice thermal conductivity for the samples that contain both cations Ge and Sn is observed, but is not affected by their proportion. This approach could also be applied to other Cu-based ternary and quaternary semiconductors such as colusite and kesterite.

4 STRUCTURAL RESOLUTION OF SYNTHETIC GERMANITE $Cu_{22}Fe_8Ge_4S_{32}$

4.1 Preface

Previously, Chapter 2 and Chapter 3 aimed to improve the thermoelectric properties of germanite by optimizing the process conditions and by modifying the chemical composition. Nevertheless, the absence of a crystal structure model for synthetic germanite precludes us from a deep comprehension of the transport properties and consequently, the improvement of the thermoelectric properties. Actually, the low chemical contrast of the Cu^{1+}, Ge^{4+} and Fe^{3+} cations for both neutron and X-ray diffraction, coupled with the complex structure arrangement denies the structural resolution of germanite by conventional methods. Resonant scattering (also known as anomalous scattering) is the only probe that allows a high contrast in the case of germanite.

The first part of this chapter describes the experimental approach used for the structural determination of germanite by detailing the advantages and the limitations of each technique. The systematic examination of all the possible occupations of the five crystallographic sites (2*a*, 6*c*, 6*d*, 12*f* and 8*e*) by the 34 cations of $Cu_{22}Fe_8Ge_4S_{32}$, would imply to consider of a total of 18 000 structural models. Such endeavor would be costly in terms of time and computation resources. Thus, to reduce this number of models, the complementarity of powder and single crystal XRD and ^{57}Fe Mössbauer spectroscopy was put to profit to exclude aberrant occupation of the sites. Those occupation constraints bring down the number of possible models to 186.

The second part of this chapter is dedicated to the Rietveld refinement of the 186 structural models on resonant scattering data. The quality of the agreement between the observed and calculated profiles is evaluated by the *Bragg R-Factor* and is used to discriminate the models. This yielded four structural models for germanite $Cu_{22}Fe_8Ge_4S_{32}$. Then, we proceeded to refine the stoichiometry and found that germanite real stoichiometry could be slightly different from the nominal composition.

4.2 Experimental approach

4.2.1 Neutron and non-resonant X-ray diffraction

During a standard diffraction experiment, a sample is irradiated with a beam of photons, electrons or neutrons with a wavelength similar to the interatomic distances of the crystal structure. The intensity of the diffraction peaks depends, among other things, of the nature of the radiation and the nature of the diffracting atom. For X-rays and electrons, scattering arises mainly from the interaction of the incident beam with the atoms electron cloud. Generally, at a fixed wavelength the scattering power, also known as atomic form factor (f), scales up with the electronic density of the atom, thus with the atomic number (Z). However, for energies near an absorption edge (resonant condition) the monotonic relationship between f and Z could be strongly perturbed.

On the other hand, neutrons interact directly with the nucleus of the atoms. The contribution to the diffracted intensity (the scattering length) depends on each elements and isotopes in a way that appears random. At present, it is still not possible to calculate precisely the scattering lengths, thus their values are evaluated experimentally and tabulated.[188] Table 4.1 resumes the number of electrons, the atomic number and the neutron coherent scattering length (for natural elements) of the cations contained in germanite $Cu_{22}Fe_8Ge_4S_{32}$.

Table 4.1. Atomic and electronic information of Cu, Fe and Ge.[188]

	20 Cu^{+}	**2 Cu^{2+}**	**8 Fe^{3+}**	**4 Ge^{4+}**
Electrons	28	27	23	28
Atomic No.	29	29	26	32
Scattering length (10^{-15} m)	7.718	7.718	9.450	8.185

The electron count and scattering length of the three cations are similar, thus giving them low contrast by X-ray or neutron diffraction. More importantly, it is probable that germanite has crystallographic sites with mixed occupancy. As a result, the same site form factor (the crystallographic site contribution to diffraction pattern) could be obtained by several atomic combination. For instance,

using X-ray, the *8e* site occupation by Cu_6Fe_2, Cu_5Fe_2Ge, $Cu_4Fe_2Ge_2$, $Cu_3Fe_2Ge_3$ and $Cu_2Fe_2Ge_4$ results every times in 214 electrons (while considering only Cu^{1+}) *i.e.* the same site contribution. Similarly, for neutrons mixed occupations on the *8e* site lead to a weak increase of the site contribution from 65.208 for Cu_6Fe_2 to 67.076 for $Cu_2Fe_2Ge_4$ (+ 2.9 % only).

In this context, non-resonant XRD and NPD data are insufficient to determine the cationic distribution of germanite, but can be used to evaluate the consistency of the models. Single crystal diffraction will be used to determine occupation constraint to limit the number of structural models to investigate. The conditions of data collection and structure refinements of each diffraction techniques are gathered in the appendices (Chapter5).

4.2.2 Resonant scattering

Resonant (*i.e.* anomalous) scattering is an X-ray diffraction phenomenon due to the variation of the scattering factor of an atomic species when the incident beam has an energy similar to one of its core electrons, *i.e.* same energy as its X-ray absorption edges. Generally, the Thompson scattering term f^0 (only dependent of the exchanged wavevector $\vec{k}$) is considered a sufficient approximation of the atomic form factor f. However, in resonant condition two additional correction terms are necessary; a real term f^I that describes the reduction in the scattering amplitude and an imaginary term f^{II} that expresses the phase variation due to the absorption. Both terms are dependent of the exchange wavevector $\vec{k}$ and energy E.

$$f = f^0(\vec{k}) + f^I(\vec{k}, E) + if^{II}(\vec{k}, E) \qquad \textit{Equation 4-1}$$

Such deviation from Thomson scattering reaches its maximum when the wavelength is at the corresponding absorption edge of an atom, and generally its magnitude is proportional to the wavelength and inversely proportional to the number of electrons of an atom. This effect can be used to generate a set of independent diffraction data with high scattering contrast even for elements with

close atomic numbers. This contrast enhancement is useful for germanite compounds because copper, iron and germanium have similar number of electrons but have different K-edge absorption values: 7072 eV for iron, 8953 eV for copper, and 11102 eV for germanium. Figure 4.1 displays the theoretical scattering factors f^I and f^{II} of the atoms Cu, Fe, and Ge contained in germanite as a function of the beam energy.

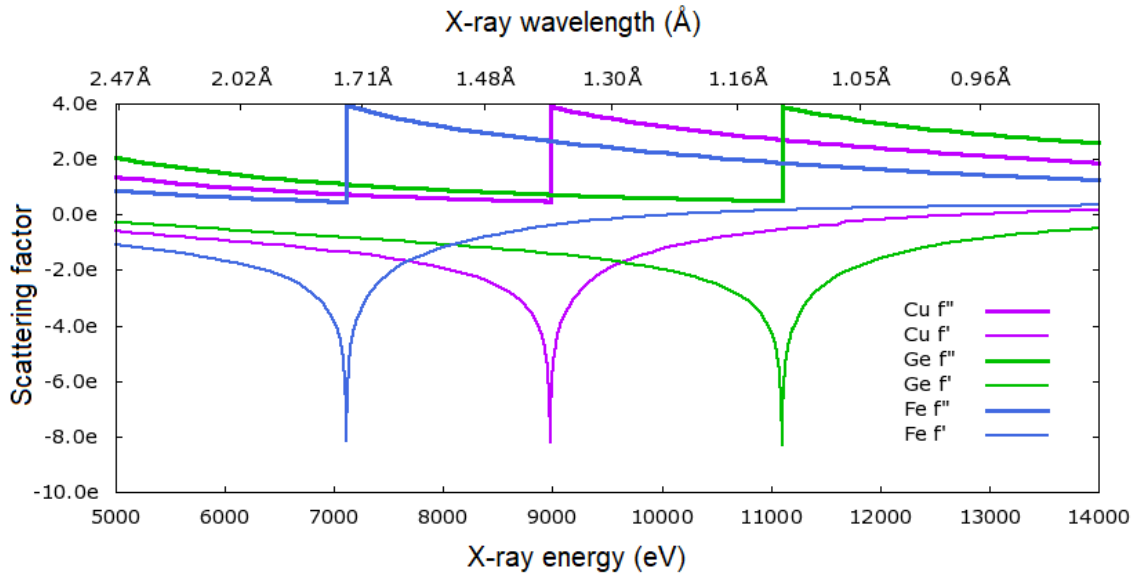

Figure 4.1. Theoretical f^I and f^{II}, derived using the theoretical approximation developed by Cromer and Liberman, as a function of X-ray energy for Fe, Cu and Ge.[189] *Plot calculated using the subroutine library by Brennan and Cowan.*[190]

Although such kind of experiments seem conceptually simple, several experimental difficulties exist. First, the collection of a diffraction pattern at several energies require a tunable energy source such as synchrotron radiation. Second, the values of the f^I and f^{II} terms are strongly dependent of the chemical environment of the atomic species, thus the values tabulated in the databases as Cromer-Liberman are not sufficiently precise for quantitative analyses. For this reason, the collection of an X-ray absorption spectrum of the investigated samples on the same beamline is mandatory to experimentally determine the f^I and f^{II} terms. The f^{II} term is directly proportional to the X-ray absorption cross-section and related to f^I by a Kramers-Kronig relation.[191] Hence, these absorption spectra allow to determine the optimal collection energies and to precisely define

the calibration energy, which is of high importance since a 10 eV difference, although negligible for structural purpose, can strongly alter both correction terms. A third set of difficulties arises from the intrinsic different energies collection. In fact, a variation of the source energy implies differences in the absorption correction and fluorescence contribution, but also variations of the angular and reciprocal space resolution and optics and detector performances. Consequently, the diffraction patterns collected at different energies are not so straightforwardly comparable. This issue can be resolved by collecting several diffraction patterns around each edge. Therefore, diffraction patterns will be collected to at least three different energies for each element: one at the edge where resonant effects are maximized, one at several decades of eV before the edge where resonant effects are still present but with negligible fluorescence and one far from the edge in the optimal experimental condition and where experimental conditions remain comparable (Figure 4.2).

4.2.2.1 Resonant scattering at Cu, Fe and Ge K-edges.

The resonant scattering experiments were performed on CRISTAL beamline at SOLEIL light source facility, Saclay, France. The conditions of the data collection are gathered in the appendices (Chapter 5, section 5.2.3.2). The fluorescence X-ray absorption spectra of germanite have been obtained by a synchronous scan of the monochromator and the ondulator gap, while incoming X-ray and fluorescence were monitored by an ionization chamber and a silicon drift detector, respectively. Then, the f^{II} and f^{I} factors were calculated from the X-ray absorption cross-section and by a Kramers-Kronig relation, respectively (Figure 4.2 for Ge K-edge). The collection energies were chosen from this calculation. The nominal and calibrated incident beam energies, wavelength of the calibrated energies and the resonant factors are summarized in the appendices (Chapter 5, section 5.2.3.2).

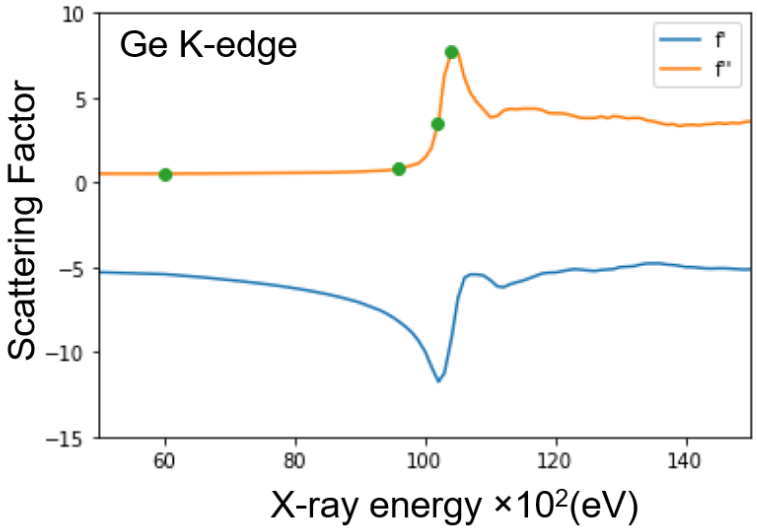

Figure 4.2. The f^{II} (orange) factor calculated from the fluorescence X-ray absorption spectrum for the Ge K-edge and the f^{I} (blue) factor calculated by a Kramers-Kronig relation of germanite $Cu_{22}Fe_8Ge_4S_{32}$. Green dots represent the energies selected for data collection close to the Ge K-edge.

The variations of the scattering factors due to the resonant effect had a significant influence on the superstructure peaks intensity of germanite. Figure 4.3, divided in four subplots; one for each element Cu, Fe and Ge and one for the high energy, displays the low angle section of the diffraction pattern of germanite at different energies. The intensity is plotted against $1/d$ ($Å^{-1}$) for comparison among the energies. An asterisk identifies the contribution of bornite Cu_5FeS_4. The extinction of all superstructure peaks except (211) and (310) on the patterns collected close to Fe K-edge makes them desirable and compensate the decrease in quality due to fluorescence. The patterns acquired around Cu K-edge benefited of a better statistic compared to that close to Fe K-edge. Also, compared to the high energy pattern (λ = 0.5817 Å), where no resonant effects are considered, all superstructure peaks benefited of an improved intensity, except for (220). Among all the patterns acquired close to the edges, those acquired around Ge K-edge had the best peak statistic. The appearance of the (210) peak upon diminution of the wavelength close to the Ge K-edge is an interesting feature to consider during the selection of the structural models. This set of diffraction patterns will be used to determine a crystal model for germanite by Rietveld refinement.

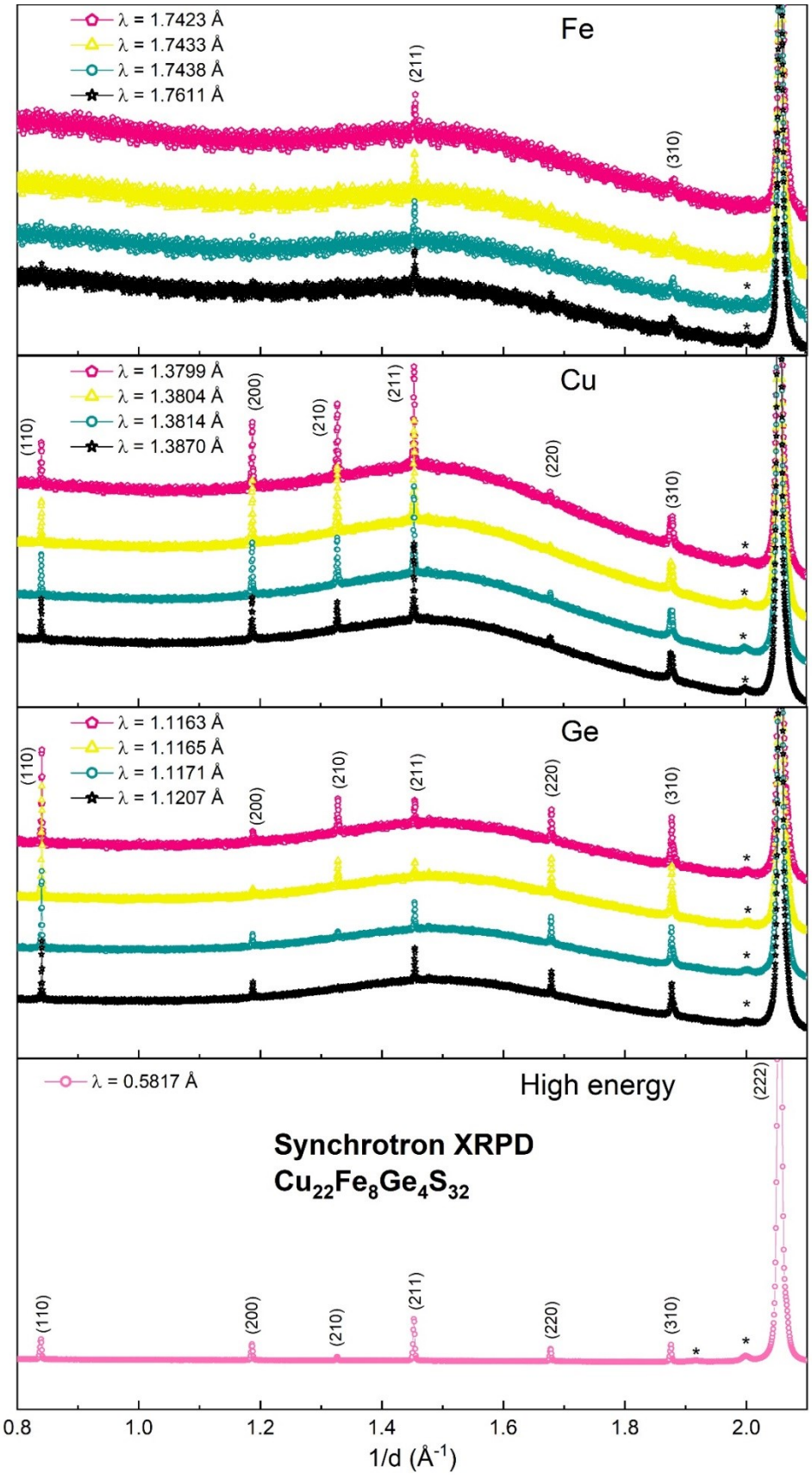

Figure 4.3. Resonant diffraction patterns at different energies of $Cu_{22}Fe_8Ge_4S_{32}$.

4.2.3 Mössbauer spectroscopy

Mössbauer spectroscopy is a technique based on the Mössbauer effect, which is a process where nucleus emit and absorb γ-rays without the loss of energy due to nuclear recoil. A Mössbauer spectrum provides quantitative information on "hyperfine interactions", which are due to the interactions between the nucleus and the neighboring electrons. The three important hyperfine interactions come from: the gradient of the electric field (the nuclear quadrupole splitting (QS)), the electron density at the nucleus (the isomer shift (IS)) and the value of the magnetic field at the nucleus (the hyperfine splitting).[192] From the number of lines, their positions and intensities, it is possible to draw conclusions on the nuclear moments and on the magnitude of internal electrical and magnetic fields.[193] Concretely, the IS value indirectly gives the oxidation state of the probed atom and the value of the QS gives information on the site symmetry of the probed atom through a deviation of the nucleus sphericity.

Considering all of the above, one can say that Mössbauer spectroscopy is unique in its sensitivity to subtle changes in the chemical environment of the nucleus. For that matter, ^{57}Fe is a valuable local probe to examine the crystallographic and chemical state of Fe in cubic germanite $Cu_{22}Fe_8Ge_4S_{32}$. Thus, ^{57}Fe Mössbauer spectroscopy will be used to restrain the number of structural models to investigate. The measurement conditions of the ^{57}Fe Mössbauer spectrum are summarized in the appendices (Chapter 5, section 5.2.3.1).

4.2.4 Summary

Table 4.2. Advantages, disadvantages and purposes of each characterization technique used to solve the crystal structure of synthetic ST germanite $Cu_{22}Fe_8Ge_4S_{32}$.

Technique	Advantages	Disadvantages	Purpose
XRPD	-accessible -reflection superimposition -powder sample	-limited by low flux -similar atomic form factor	-verify the model by Rietveld refinement
NPD	-scattering power independent from *k* -alternative set atomic contribution - magnetic scattering	-restricted access -limited by the cations close scattering lengths	-verify the model by Rietveld refinement
Single crystal XRD	- accessible -deconvolution of (*h*00) in (*h*00), (0*k*0) and (00*l*)	-limited by cations electronic vicinity -recquire a single crystal	-establish occ. constraint to exclude improbable models
^{57}Fe Mössbauer spectroscopy	-accessible* -sensitive chemical environment	-only for Fe	-Fe valence -Number of site and symmetry
Resonant scattering	-high scattering contrast -high resolution patterns	-restricted access	-structural determination

* Through a collaboration with Pr. Bernard Malaman, IJL, Nancy, France.

4.3 Structural determination

In 2017, based on Tettenhorst model for natural germanite, $Cu_{26}Fe_4Ge_4S_{32}$,[147] and ^{57}Fe Mössbauer spectroscopy, two structural models were proposed for the synthetic germanite $Cu_{22}Fe_8Ge_4S_{32}$.[151] Starting from the cationic distribution reported for the natural germanite, namely $[Cu_2]_{2a}[Cu_6]_{6c}[Cu_6]_{6d}[Fe_4Ge_4]_{8e}[Cu_{12}]_{12f}S_{32}$, where the Fe and Ge atoms are on the 8*e* site and the rest of the sites are occupied by Cu, we proposed: $[Cu_2]_{2a}[Cu_6]_{6c}[Fe_4Cu_2]_{6d}[Fe_4Ge_4]_{8e}[Cu_{12}]_{12f}S_{32}$, where 4 Fe atoms substitute 4 Cu atoms on the 6*d* site and $[Cu_2]_{2a}[Cu_6]_{6c}[Fe_4Ge_2]_{6d}[Fe_4Cu_2Ge_2]_{8e}[Cu_{12}]_{12f}S_{32}$, where the Ge atoms are equally distributed on the sites 6*d* and 8*e*. Thereafter, the refinement of a single crystal, collected from powders produced by sealed tube, confirmed the space group $P\bar{4}3n$ for germanite ($Cu_{22}Fe_8Ge_4S_{32}$) and the full occupation of the 2*a*, 6*c*, 6*d*, 12*f* and 8*e* crystallographic sites and rejected the significant occupation of further supplementary interstitial sites. However, the refinements of the two structural models on single crystal led to high R_1 values (~ 8.8 %), together with high electronic residual density (Δe- ~ - 1.1/+ 6.9, Table 4.3). Such large values prompted us to reinvestigate the crystal structure of germanite. The number of different combination of Fe, Cu and Ge occupations for the five crystallographic sites yields ~ 18 000 possible models. The evaluation of such number of models is not feasible in a limited amount of time and computation resources; thereby supplementary constraints were established to skim the models. First, the position of the Fe atoms will be determined by reinterpreting the Mössbauer spectrum and refining single crystal data together with X-ray powder diffraction patterns collected in resonant condition. Then, the occupation site of at least 1 Ge atom will be determined.

Table 4.3. Structural model of natural germanite according to Tettenhorst et al. and two structural models suggested for synthetic germanite by Pavan Kumar et al.

Cationic distribution	**R_1 (%)**	**Δe-**
$[Cu_2]_{2a}[Cu_6]_{6c}[Cu_6]_{6d}[Fe_4Ge_4]_{8e}[Cu_{12}]_{12f}S_{32}$	-	-
$[Cu_2]_{2a}[Cu_6]_{6c}[Fe_4Cu_2]_{6d}[Fe_4Ge_4]_{8e}[Cu_{12}]_{12f}S_{32}$	8.76	- 1.12/+ 6.88
$[Cu_2]_{2a}[Cu_6]_{6c}[Fe_4Ge_2]_{6d}[Fe_4Cu_2Ge_2]_{8e}[Cu_{12}]_{12f}S_{32}$	8.80	- 1.11/+ 6.91

4.3.1 Two Fe atoms on the interstitial *2a* site

The interstitial site 2*a* is a crystallochemical singularity of the germanite and colusite ($P\bar{4}3n$) structures and is accountable of the supercell. Also, the site 2*a* forms a perfect tetrahedra with four ionocovalent bonds $M(2a)$-S_4 and also forms an octahedral metallic complex with the adjacent metals of the 12*f* site $[M(2a)S_4]M(12f)_6$, *e.g.* Fe_{2a}-M_{12f} metallic bond ~ 2.73 Å (Figure 4.4). The 2*a* site, occupied by V in $Cu_{26}V_2Ge_6S_{32}$ colusite, is occupied by 2 Cu in natural germanite according to Tettenhorst.[147] However, in the case of synthetic germanite $Cu_{22}Fe_8Ge_4S_{32}$, crystalline evidences suggested the occupation of this site by two Fe atoms (discussed below). This constraint allowed to lower the number of possible structural models to ~ 3 000.

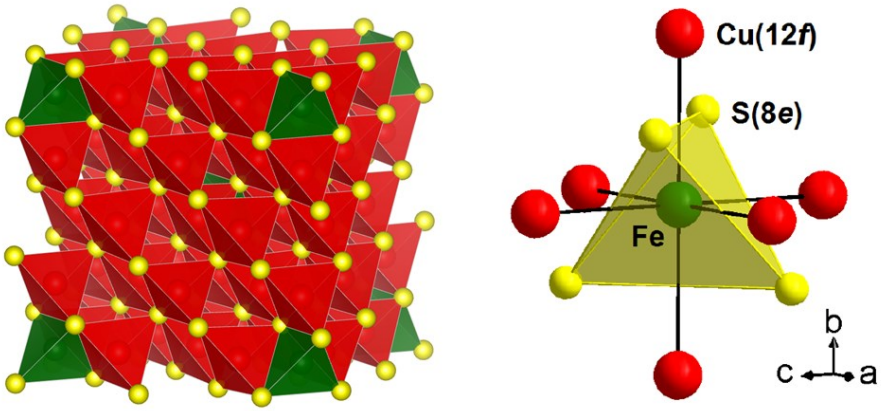

Figure 4.4. The structure of germanite ($P\bar{4}3n$ space group) and an isolated representation of the metallic octahedral complex $[Fe(2a)S_4]Cu(12f)_6$.

The generation of a first set of structural models was based on the approximations that Cu is only in its +I oxidation state and that the isoelectronic cations, Cu^{1+} and Ge^{4+}, have the same scattering contribution. Thus, the sites that are not occupied by Fe are approximated with a unique species (*e.g.* Cu^{1+}), hence limiting all the possible combination to only 360 models. Figure 4.5 displays the decrease of the *R-Factors* with the increasing Fe content on site 2*a*, obtained from the refinement of single crystal data (λ_{Mo}). Accordingly, we concluded that the interstitial 2*a* site is likely occupied by 2 Fe atoms.

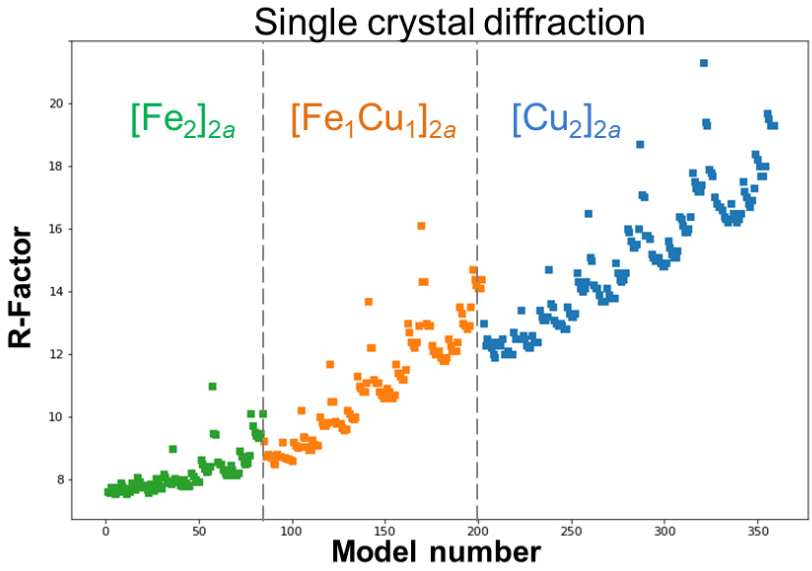

Figure 4.5. R-Factors obtained from the refinement of the 360 structural models, on single crystal data (λ_{Mo}). Three cationic occupation of the 2a site are represented: $[Fe_2]_{2a}$ (green), $[Fe_1Cu_1]_{2a}$ (orange) and $[Cu_2]_{2a}$ (blue).

Accordingly, we adapted the two models suggested by Pavan Kumar *et al.* (Table 4.3) by replacing the $[Cu_2]_{2a}$ by $[Fe_2]_{2a}$. This yielded a drastic decrease of the R_1 and of the residual electronic density, *e.g.* from ~ 8.8 % to ~ 5.5 % and from ~ - 1.1/+ 6.9 to ~ - 0.9/+ 2.1, respectively (Table 4.4).

Table 4.4. New structural models with the 2a site occupied by 2 Fe, derived from the models suggested by Pavan Kumar et al.

Cationic distribution	R_1 **(%)**	**Δe-**
$[Fe_2]_{2a}[Cu_6]_{6c}[Fe_2Cu_4]_{6d}[Fe_4Ge_4]_{8e}[Cu_{12}]_{12f}S_{32}$	5.24	- 0.90/+ 1.99
$[Fe_2]_{2a}[Cu_6]_{6c}[Fe_4Cu_2]_{6d}[Fe_2Ge_4Cu_2]_{8e}[Cu_{12}]_{12f}S_{32}$	5.83	- 1.07/+ 2.81
$[Fe_2]_{2a}[Cu_6]_{6c}[Fe_2Ge_2Cu_2]_{6d}[Fe_4Ge_2Cu_2]_{8e}[Cu_{12}]_{12f}S_{32}$	5.23	- 0.84/+ 1.97
$[Fe_2]_{2a}[Cu_6]_{6c}[Fe_4Ge_2]_{6d}[Fe_2Ge_2Cu_4]_{8e}[Cu_{12}]_{12f}S_{32}$	5.40	- 0.96/+ 2.44

These strong evidences of the 2*a* interstitial site occupation by 2 Fe atoms in synthetic germanite entail a reinterpretation of the ^{57}Fe Mössbauer spectrum. In the present study, the isomer shift (IS) was used to determine the oxidation state of Fe, the quadrupolar splitting (QS) to estimate the symmetry of the site occupied by Fe and the peak relative area of each contribution to estimate the proportion of Fe atoms on each site. The isomer shift of the spectra confirmed Fe^{3+} as the only oxidation state of iron in germanite (0.31(1) – 0.34(1) mm s^{-1}). These IS values are

similar to those of the two Fe^{3+} sites of stannoidite $Cu_8Fe_3Sn_2S_{12}$ at RT, namely 0.29(3) and 0.40(3) mm s^{-1},[178] in agreement with the structural similarities of the two compounds, which both consist of CuS_4 and FeS_4 tetrahedra frameworks. Also, the different chemical environment of some of the crystallographic sites should yield mildly disparate QS.

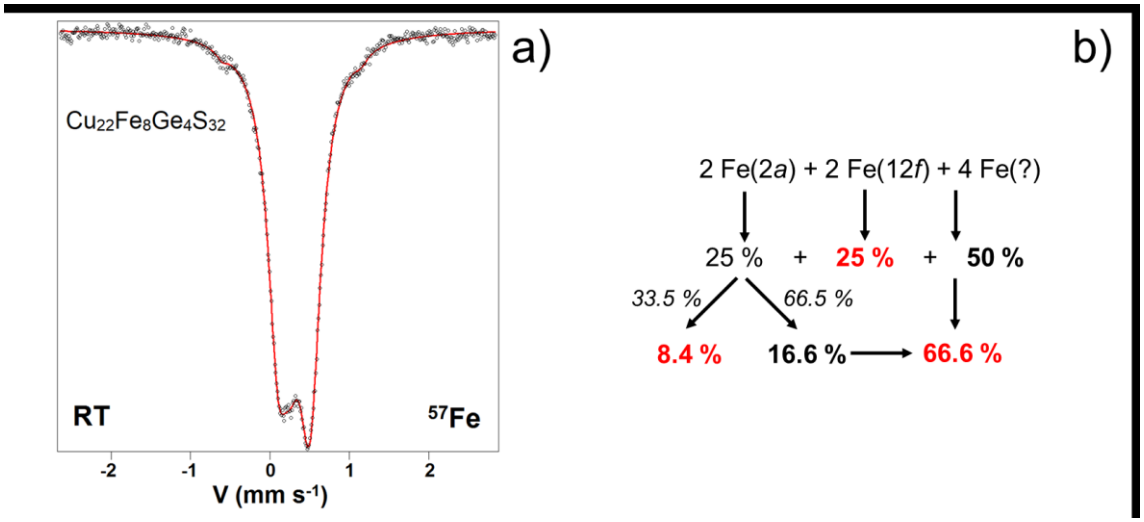

Figure 4.6. a) ^{57}Fe Mössbauer spectra at RT of a germanite $Cu_{22}Fe_8Ge_4S_{32}$ sample synthesized by ST and b) the different site contribution % area.

Figure 4.6a displays the room temperature ^{57}Fe Mössbauer spectrum of the synthetic germanite $Cu_{22}Fe_8Ge_4S_{32}$ produced by ST synthesis. Due to the asymmetric shape of the spectrum, it have to be fitted by at least two doublets. Fitting the spectrum by more than three components is limited by the signal convolution due to the high symmetry of the structure. Consequently, the Mössbauer spectrum was fitted by three components, *e.g.* two doublets and one singlet with similar IS and significant different QS (Table 4.5).

Table 4.5. ^{57}Fe hyperfine parameters: Isomer Shifts (IS, referred to α-Fe at RT), Quadrupole Splittings (QS), FWHM (Γ) and Relative Areas at 300 K.

Components	**IS (mm s^{-1}) (± 0.01)**	**QS (mm s^{-1}) (± 0.01)**	**Γ (mm s^{-1}) (± 0.01)**	**Area (%) (± 3)**	**Fe atoms**
1	0.31	0.42	0.33	67	5.4
2	0.34	0.25	0.33	25	2.0
3	0.32	0.00	0.33	8	0.6

The assignment of these components to three local environments (crystallographic sites) is not straightforward. Nonetheless, it is reasonable to ascribe the component 3 to the site *2a* since a non-resolvable quadrupole splitting (QS = 0 mm s^{-1}) is typical of an high symmetry environment. However, the relative area of component 3 (8 % of 8 Fe ≈ 0.6 Fe atoms) is in disagreement with an occupation of the *2a* site by 2 Fe atoms. This suggests that the occupation of Fe on 2*a* yields a second contribution (overlapping with 1 or 2), that probably originates from the disturbance of the chemical environment by the second neighbor $[M_{12}]_{12f}$. In other words, we expect the interstitial site to yield a singlet in a symmetrical octahedral environment, *e.g.* $[Fe_2]_{2a}[Cu_{12}]_{12f}$ (area ~ 8 % ≈ 0.6 Fe atom, QS = 0 mm s^{-1}), and a doublet in a non-symmetrical octahedral environment, *e.g.* $[Fe_2]_{2a}[Cu_{12-x}Fe_x]_{12f}$ (remaining 1.4 Fe atom ≈ area of 17 %, QS = 0.42 mm s^{-1} or 0.25 mm s^{-1}). To verify this hypothesis, we evaluated the probability to find an Fe atom in the metal octahedron surrounding Fe in position 2*a* as a function of the Fe content on the 12*f* site with a binomial distribution of order 6 (Table 4.6).

Table 4.6. Probability of the Fe atoms distribution on the 12f site in the octahedral environment of 2a.

Site 12*f*	**$Cu_{11}Fe_1$**	**$Cu_{10}Fe_2$**	**Cu_9Fe_3**	**Cu_8Fe_4**	**Cu_7Fe_5**	**Cu_6Fe_6**
P(0)	0.5933	0.3349	0.178	0.0878	0.0394	0.0156
P(1)	0.3236	0.4019	0.356	0.2634	0.1689	0.0938
P(2)	0.0735	0.2009	0.2966	0.3292	0.3015	0.2344
P(3)	0.0089	0.0536	0.1318	0.2195	0.2872	0.3125
P(4)	0.0006	0.008	0.033	0.0823	0.1538	0.2344
P(5)	0	0.0006	0.0044	0.0165	0.044	0.0938
P(6)	0	0	0.0002	0.0014	0.0052	0.0156

Where P(1) represents the probability of finding an iron atom in the metal octahedron surrounding the iron in position 2*a* and *x* the concentration of iron atoms on the site 12*f*. For instance, when $[Fe_2]_{2a}[Cu_{10}Fe_2]_{12f}$ (x = 2/12), the probability P(0) of having a symmetrical environment around the 2*a* site is 33.5 %, (P(6) is negligible), and the probability of having a non-symmetrical environment around the position 2*a* is 66.5 % (sum of the probabilities P(1) to P(5)). Hence, this suggests that the crystallographic 12*f* site contains 2 Fe atoms and thus is assigned to the contribution 2 (QS = 0.25 mm s^{-1}). Consequently, this leaves the contribution

1 (QS = 0.42 mm s^{-1}), with 4 out of the 8 Fe atoms (area of 50 %), assigned to either of the sites 6*c*, 6*d* or 8*e*. The contribution of each crystallographic sites to the integrated relative areas is summarized in Figure 4.6b.

These results obtained from Mössbauer spectroscopy should be used cautiously since they are based on many assumptions. First, the Mössbauer is fitted by three contributions, but such assumption is uncertain due to the high symmetry of the cubic structure yielding many convoluted contributions. The second hypothesis is that the sample contains 8 Fe atoms (nominal composition). However, synthetic germanite probably present stoichiometry deviations (p. 168). Third, the main peak is considered to represent 100 % of the 8 Fe atoms contribution. Nonetheless, the presence of small satellite peaks on each side of the main peak (*ca*. - 0.5 mm s^{-1} and + 1 mm s^{-1}) might indicates the contrary, *i.e.* contributions of a secondary magnetic phase or of a magnetic arrangement of germanite.

4.3.2 Site 12*f* contains at least 1 Fe atom & site 6*d* contains less than 4 Fe atoms

The determination of the second occupation constraint was based on the same single crystal data refinements presented in Figure 4.5. Only this time, the structural models are represented as a function of the Fe content on the site 12*f* (Figure 4.7). For the same 2*a* occupation, the *R-Factors* are increasing almost linearly with the decreasing Fe content on the 12*f* site. Thus, the minimal Fe occupation on the site 12*f* is set to 1 atom. This constraint allowed to lower the number of possible structural models to ~ 1 800. In the next paragraph, crystallographic evidences suggesting that the 6*d* site contains less than 4 Fe atoms will be presented, in agreement with the ^{57}Fe Mössbauer analyses.

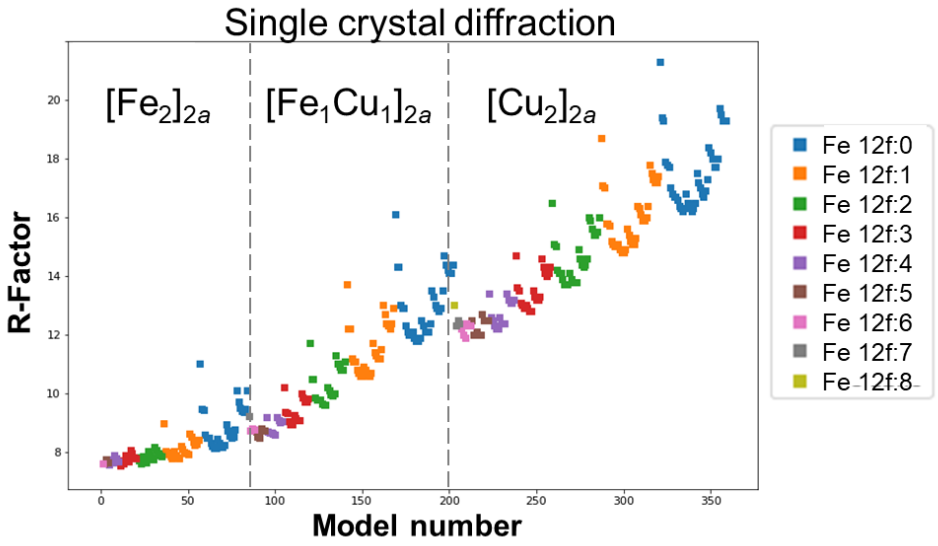

Figure 4.7. R-Factors obtained from the refinement of the 360 structural models with variable Fe content on the 12f site on single crystal data (λ_{Mo}).

Preliminary refinements of single crystal diffraction data showed that the best fits are obtained with structural models containing less than 4 Fe atoms on the 6*d* site (Figure 4.8). This limitation of Fe occupation on the site 6*d* below four atoms lowered the number of possible models to ~ 800. Next, the occupation of at least 1 Ge atom on the 6*c* or 6*d* site will be determined.

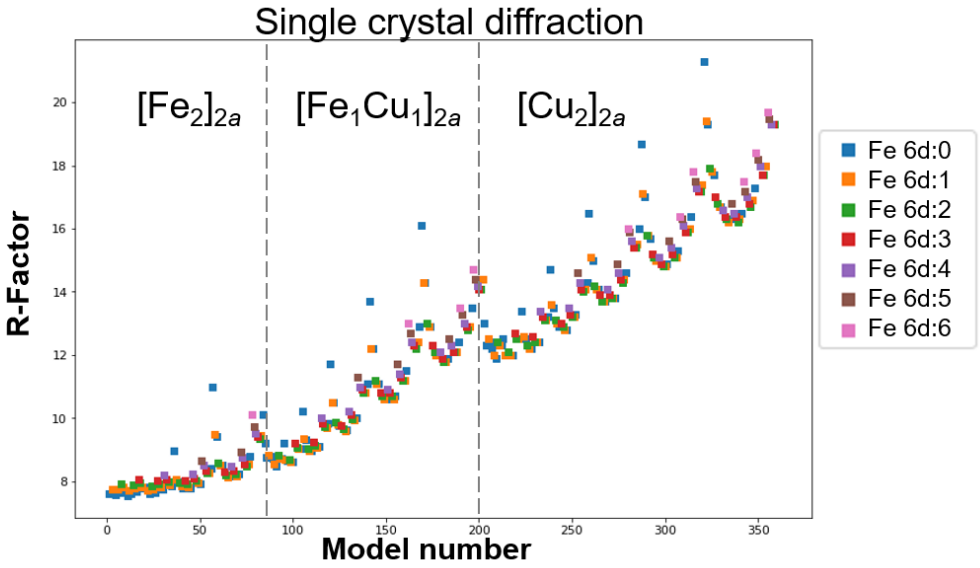

Figure 4.8. R-Factors obtained from the refinement of the 360 structural models with variable Fe content on the 6d site on single crystal data (λ_{Mo}).

4.3.3 Site *6c* and *6d*: one site contains 3 - 4 Ge atoms, the other one contains 0 Ge atom.

As previously mentioned, the reflection (210) is highly sensitive to the occupation of the sites 6*c* and 6*d*. Indeed, the (210) reflection violates the general reflection conditions ($h + k + l = 2n$) and arises from an extra set of reflection conditions (*e.g.* $h = 2n + 1,\ k = 4n, l = 4n + 2$) allowed by the $\bar{4}$ site symmetry of the 6*c* and 6*d* sites.[194]

Earlier in this chapter, we observed a steep increase of the (210) peak with the wavelength evolution toward the edge energy (where the resonant effect is maximal) for the patterns acquired close to Ge K-edge (Figure 4.3). Such sensitivity of the (210) peak intensity to the resonant effect at Ge K-edge suggests a non-negligible content of Ge on the 6*c* and/or 6*d* sites. In this fashion, the structure factor of (210) will be calculated for various Ge occupations of the 6*c* and 6*d* sites (Table 4.7). This should help in the determination of the Ge occupation limits.

Table 4.7. Structure factors of the reflection (210) for the diffraction pattern collected a Ge K-edge.

6c	***6d***	**Structure Factor (210)**
$[Cu_6]$	$[Cu_6]$	8.27
$[Cu_4Ge_2]$	$[Cu_4Ge_2]$	8.27
$[Cu_6]$	$[Cu_4Ge_2]$	5.38
$[Cu_5Ge_1]$	$[Cu_3Ge_3]$	5.38
$[Cu_3Ge_3]$	$[Cu_6]$	27.7
$[Cu_2Ge_4]$	$[Cu_6]$	34.2
$[Cu_6]$	$[Cu_2Ge_4]$	18.2

The first structural model investigated do not contain any Ge atoms on the 6*c* or 6*d* site, *i.e.* $[Cu_6]_{6c}[Cu_6]_{6d}$ (structure factor of 8.27) and lead to an underestimation of the peak intensity (Figure 4.9a). The increase in Ge content on the 6*c* and/or 6*d* sites do not straightforwardly lead to an increase of the structure factor of the reflection (210). For instance, an identical Ge content on the *6c* and 6*d* sites, cancels the Ge contributions since the two sites contribute equally to the structure factor but in opposite sign ($F^{210} = 4\ f_{6d} - 4\ f_{6c}$), *e.g.* the occupation

$[Cu_4Ge_2]_{6c}[Cu_4Ge_2]_{6d}$ lead to a structure factor of 8.27 (same as $[Cu_6]_{6c}[Cu_6]_{6d}$). Additionally, the contrast in Ge content between the 6*c* and 6*d* sites is important. In fact, a difference of 2 Ge atoms is insufficient to yield high structure factors, *e.g.* the structural models $[Cu_5Ge_1]_{6c}[Cu_3Ge_3]_{6d}$ and $[Cu_6]_{6c}[Cu_4Ge_2]_{6d}$ both yield a structure factor of 5.38. At last, an occupation difference of 3 or 4 Ge atoms between the two sites yields higher structure factors, such as 27.7 for $[Cu_3Ge_3]_{6c}[Cu_6]_{6d}$ (Figure 4.9b), 34.2 for $[Cu_2Ge_4]_{6c}[Cu_6]_{6d}$ (Figure 4.9c) and 18.2 for $[Cu_6]_{6c}[Cu_2Ge_4]_{6d}$. Hence, a proper fit of the (210) peak intensity (of the diffraction pattern measured a Ge K-edge) requires the occupation of the 6*c* or 6*d* site by 3 to 4 Ge atoms together with the occupation of the second site by 0 Ge atom. This last constraint yielded 186 possible structural models, which is compatible with the computational resources available.

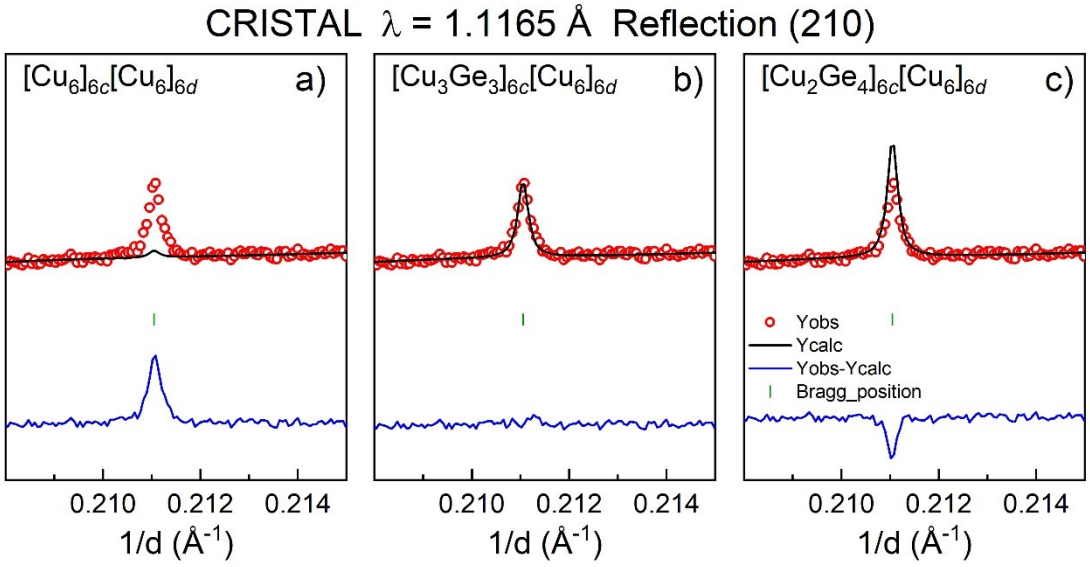

Figure 4.9. Rietveld refinements of the diffraction pattern measured at Ge K-edge with various occupation of the 6c and 6d sites: a) $[Cu_6]_{6c}[Cu_6]_{6d}$, b) $[Cu_3Ge_3]_{6c}[Cu_6]_{6d}$ and c) $[Cu_2Ge_4]_{6c}[Cu_6]_{6d}$. Showing the reflection (210).

4.3.4 Rietveld refinements of 186 structural models on data measured in resonant scattering conditions.

The previously defined constraints, namely (i) the site 2*a* is occupied by 2 Fe atoms, (ii) the site 12*f* contains at least 1 Fe atom, (iii) the site 6*d* contains less

than 4 Fe atoms and (iv) the site 6*c* or 6*d* contains 3 – 4 Ge atoms, while the other site have 0 Ge atom, yielded 186 possible structural models for synthetic germanite $Cu_{22}Fe_8Ge_4S_{32}$. Hence, this section is dedicated to the structural analyses of the diffraction patterns acquired in resonant conditions using these 186 structural models.

Note that the main peaks of the germanite phase have an anomalous shape due to the presence of a semi-crystalline germanite-like phase. Thus, it prevented an acceptable estimation of the peak intensity and consequently precluded a more traditional approach for data analysis. Along these lines, the investigation was focused exclusively on the superstructure peaks as they have a conventional peak shape and are very sensitive to the cationic site occupation. The accordance of the models with the observed data was evaluated by the *Bragg R-Factors* obtained by Rietveld refinement, where all the parameters remained fix to a value determined by the nominal stoichiometry (occupancy), by Le Bail (*i.e.* zero, *abc*, UVW) and single crystal (*i.e.* B_{iso}, *xyz*) refinement and only the scale factor was refined. The choice for such strongly constrained fits was dictated by the exigence of the computational time reduction and to avoid unphysical solutions. Indeed, compared to single crystal, powder refinement is intrinsically more computationally consuming and tends to diverge more easily. After such refinements were performed at all energies, a subgroup with an acceptable accordance was selected for each set of resonant data, and finally the intersection of all the subgroup was evaluated. Note that, among all the elemental edges surveyed, the Fe K-edge presents the least *Bragg R-Factor* variations. Nevertheless, the resonant effect close to Fe K-edge is particularly sensitive to Fe, thus making it a good measurement to exclude structural models with aberrant Fe occupation. Also, all figures of this section have red and black crosses that identify the final four structural models.

4.3.4.1 Occupation of the 8*e* and 12*f* sites

Figure 4.10 represents the *Bragg R-Factors* obtained from the Rietveld refinement of the 186 structural models for germanite $Cu_{22}Fe_8Ge_4S_{32}$ on a diffraction pattern collected at Fe K-edge. The *Bragg R-Factor* is increasing with the model number, which in its turn is inversely proportional to the Fe content on the site 12*f*. Hence, the plot was divided in five zones that evidence the Fe content on the site 12*f*. Since the lowering of the Fe content lead to an increase of the agreement factors, we concluded that the 12*f* site is most likely occupied by 3 - 6 Fe atoms. Moreover, while the occupation of the 8*e* site by 2 Fe atoms lead to reasonable *Bragg R-Factors*, the best agreement factors were obtained with the models containing 0 – 1 Fe atom and the worst with the models containing 3 -4 Fe atoms.

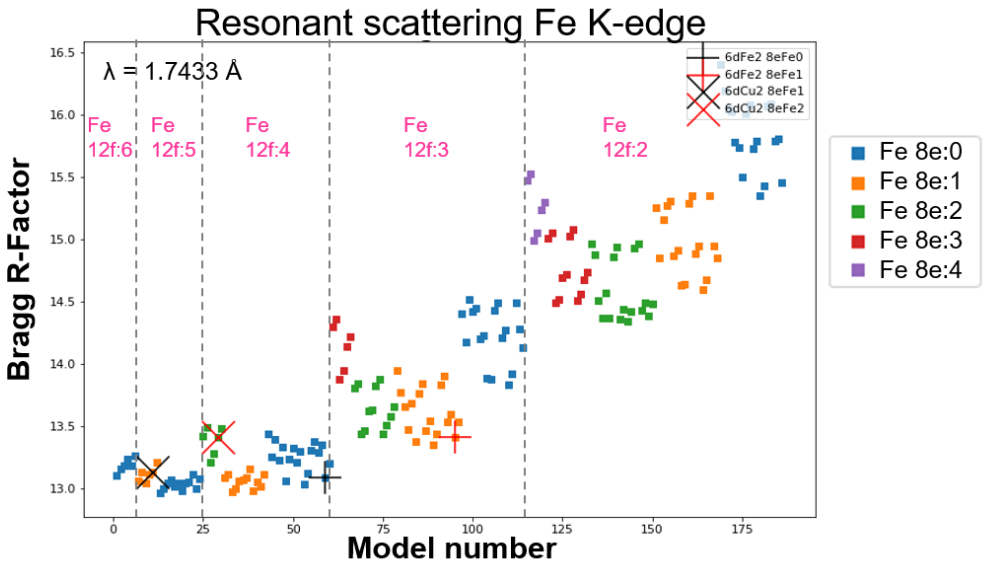

Figure 4.10. Bragg R-Factors obtained from the Rietveld refinement of the 186 structural models at Fe K-edge. The plot is divided in 5 zones corresponding to the Fe occupation of the 12f site. A color identifies each 8e occupation.

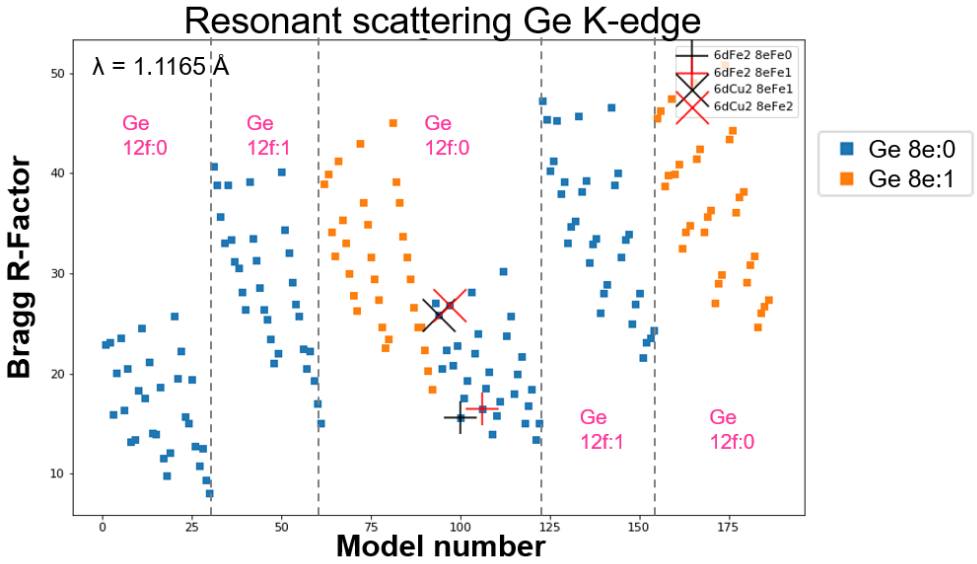

Figure 4.11. Bragg R-Factors obtained from the Rietveld refinement of the 186 structural models at Ge K-edge. The plot is divided in 5 zones corresponding to the Ge occupation of the 12f site. A color identifies each 8e occupation.

The best agreement factors of the pattern measured at Ge K-edge (Figure 4.11) were obtained with the models containing no Ge on the 8*e* and 12*f* sites. Also, the *Bragg R-Factors* obtained from the Rietveld refinements of the pattern collected at Cu K-edge (Figure 4.12) suggests that the 8*e* site is most likely occupied by 6 – 8 Cu atoms, which is in agreement with the Ge and Fe occupation of the 8*e* site. However, the occupation of the 12*f* site by 0 Ge and 6 Fe atoms (from the 3 - 6 Fe atoms predicted at Fe K-edge) implies an occupation of the site by 6 Cu atoms, which leads to higher *Bragg R-Factors* (Figure 4.13), *i.e.* higher Cu content yields lower *Bragg R-Factors*. Consequently, the occupation of the 12*f* site will be limited at a maximum of 5 Fe atoms and 7 – 9 Cu atoms. The optimal occupation of the 8*e* and 12*f* sites are summarized in Table 4.8.

Table 4.8. Summary of the optimal cationic occupation at each sites.

	8*e*	**12*f***	**6*c***	**6*d***
Fe atoms (Fe K-edge)	0 -2	3 – 5		
Ge atoms (Ge K-edge)	0	0		
Cu atoms (Cu K-edge)	6 – 8	7 - 9		

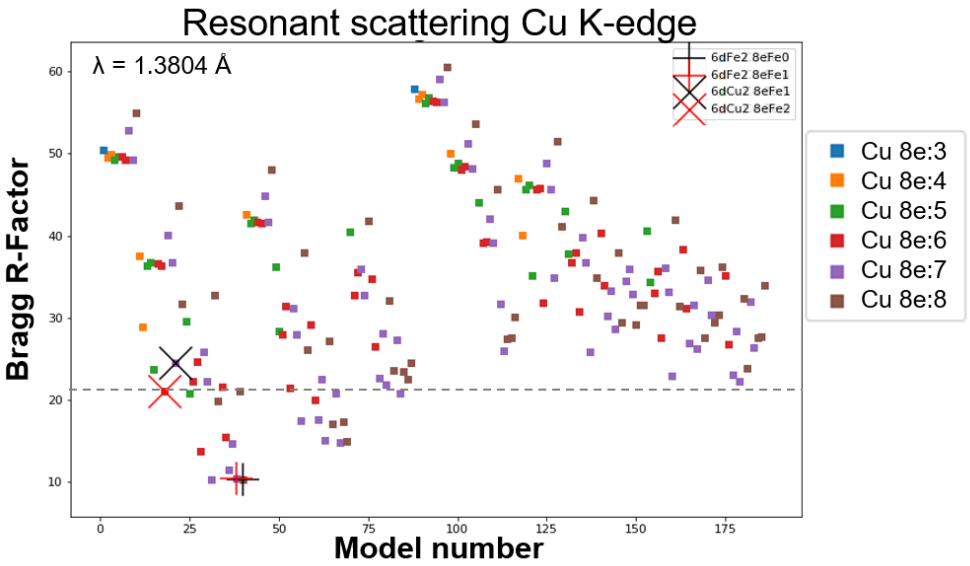

Figure 4.12. Bragg R-Factors obtained from the Rietveld refinement of the 186 structural models at Cu K-edge. A color identifies each 8e occupation. The dashed line serves as a guide to identify the best models.

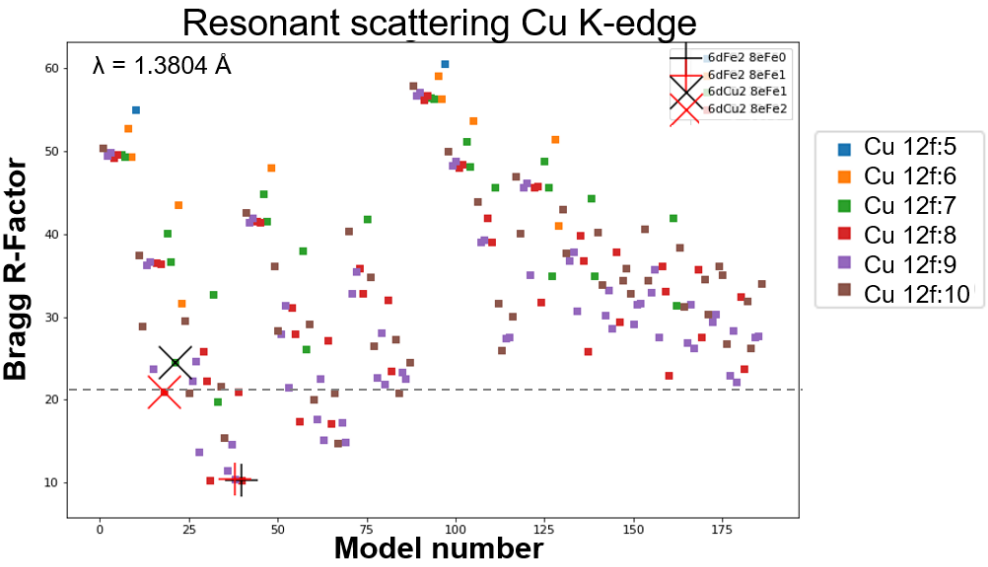

Figure 4.13. Bragg R-Factors obtained from the Rietveld refinement of the 186 structural models at Cu K-edge. A color identifies each 12f occupation. The dashed line serves as a guide to identify the best models.

4.3.4.2 Occupation of the 6*c* and 6*d* sites

Figure 4.14 depicts the *Bragg R-Factors* obtained from the Rietveld refinement of the diffraction pattern collected a Ge K-edge with the 186 structural models. The data are plotted with different color depending on the Ge occupation of the 6*c* site. Additionally, the plot is divided in three zones corresponding to the Ge occupation of the 6*d* site. The structural models where the 4 Ge atoms are either on the 6*c* or 6*d* site, stand out for their lowest average *Bragg R-Factors*. Indeed, based on crystallographic evidences previously presented, the calculated intensity of the (210) peak is optimized when the electronic count difference between the 6*c* and 6*d* sites is the largest. Moreover, considering the *M*-S distances of the 6*c* and 6*d* sites, obtained by Rietveld refinement of NPD data (Table 4.9), we expect the Ge atoms to preferably occupy the 6*d* site due to its significantly smaller ionic radii (0.39 Å) than that of Fe^{3+}, Cu^{+} and Cu^{2+} (0.49 Å, 0.60 Å and 0.57 Å, respectively).[195] Thereby, the 6*d* site is most likely occupied by 4 Ge atoms and the 6*c* site by 0 Ge atom.

Table 4.9. Average interatomic distances deduced from Rietveld refinement of neutron powder diffraction data recorded at RT.

	Distance (Å)
M_{2a}-S_1	4×2.33(4)
M_{6c}-S_2	4×2.36(7)
M_{6d}-S_2	4×2.14(1)
M_{12f}-S_1	2×2.34(9)
M_{12f}-S_2	2×2.30(5)
M_{8e}-S_1	1×2.2(5)
M_{8e}-S_2	3×2.31(8)

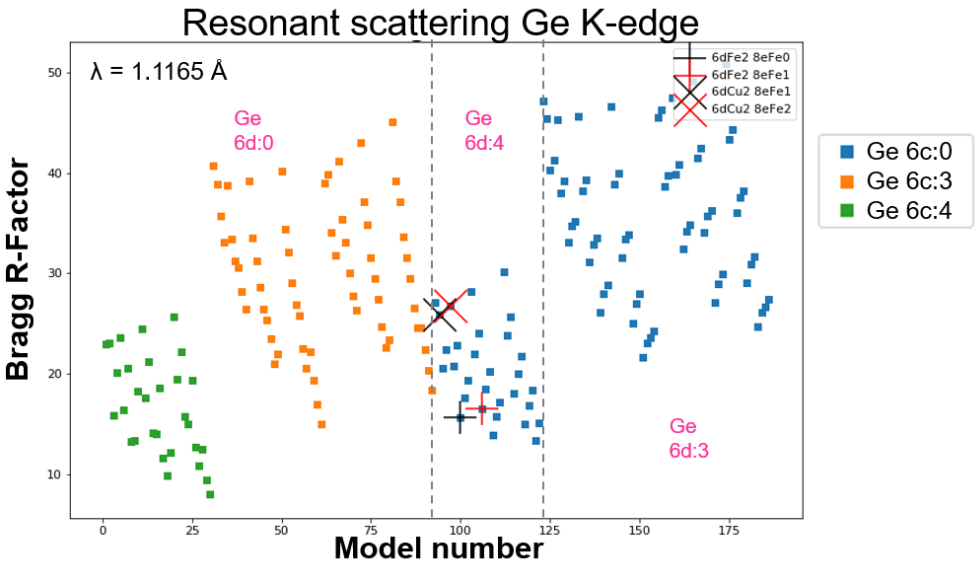

Figure 4.14. Bragg R-Factors obtained from the Rietveld refinement of the 186 structural models at Ge K-edge. The plot is divided in 3 zones corresponding to the Ge occupation of the 6d site. A color identifies each 6c occupation.

Figure 4.15 shows the *Bragg R-Factors* obtained from the Rietveld refinement of data acquired in resonant conditions at Cu K-edge. The plot is divided in seven zones corresponding to the Ge occupation of the 6*c* site and the structural models are displayed with different colors depending on the Ge occupation of the 6*d* site. Interestingly, within each of the seven occupation zones, we observe a decrease of the *Bragg R-Factors* with the gain in contrast between the 6*c* and 6*d* sites occupation. For instance, in the zone where the 6*c* site contains 6 Cu (first on the left), the highest *Bragg R-Factors* are observed where the 6*d* site contains 3 Cu (a higher Cu content is precluded by the constraints) and decrease upon the occupation by 2, 1 and 0 Cu atoms. Additionally, in agreement with the *M*-S lengths, a Cu-rich occupation of the 6*c* site (with low Cu content on 6*d*) yields better agreement factors than for the 6*d* site (with low Cu content on 6*c*). Also, the average *Bragg R-Factor* is increasing with the decreasing Cu content of 6*c*. Thus, we concluded the 6*d* site most likely contains 0 – 2 Cu atoms and the 6*c* site 6 Cu atoms.

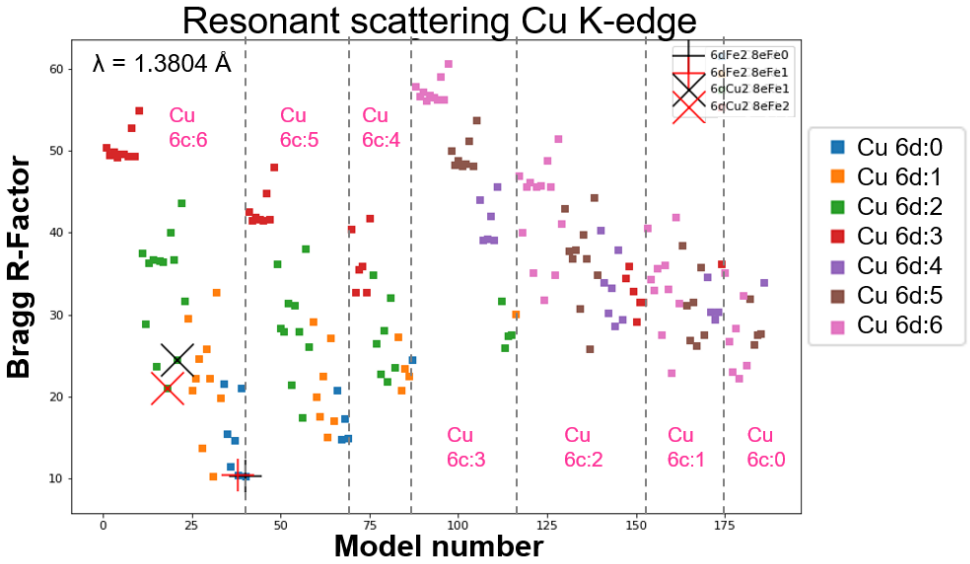

Figure 4.15. Bragg R-Factors obtained from the Rietveld refinement of the 186 structural models at Cu K-edge. The plot is divided in 7 zones corresponding to the Ge occupation of the 6c site. A color identifies each 6d occupation.

Figure 4.16 and Figure 4.17 display the *Bragg R-Factors* obtained from the refinement of the pattern measured at Fe K-edge by Rietveld method, represented as a function of the Fe content on the 6*c* and 6*d* sites, respectively. The occupation of the 6*c* or 6*d* sites by 0, 1 or 2 Fe atoms yield similar agreements. However, for the 6*c* site the Fe content will be fixed to 0 to agree with the Cu content. The optimal occupation of the 8*e*, 12*f*, 6*c* and 6*d* sites are summarized in Table 4.10.

Table 4.10. Continuation of the summary table on the optimal cationic occupation at each site.

	8*e*	**12*f***	**6*c***	**6*d***
Fe atoms (Fe K-edge)	0 -2	3 – 5	0	0 - 2
Ge atoms (Ge K-edge)	0	0	0	4
Cu atoms (Cu K-edge)	6 – 8	7 - 9	6	0 - 2

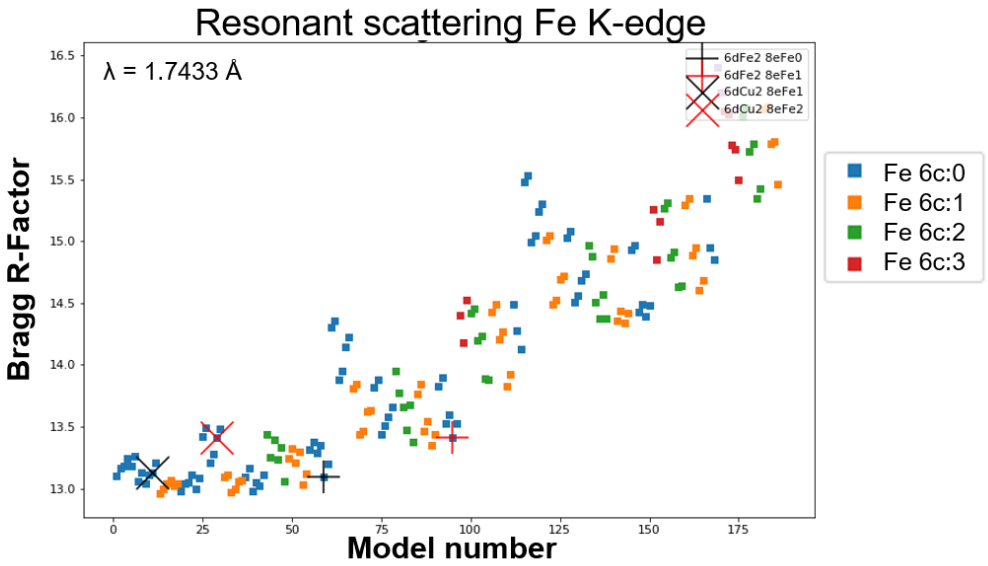

Figure 4.16. Bragg R-Factors obtained from the Rietveld refinement of the 186 structural models at Fe K-edge. A color identifies each 6c occupation.

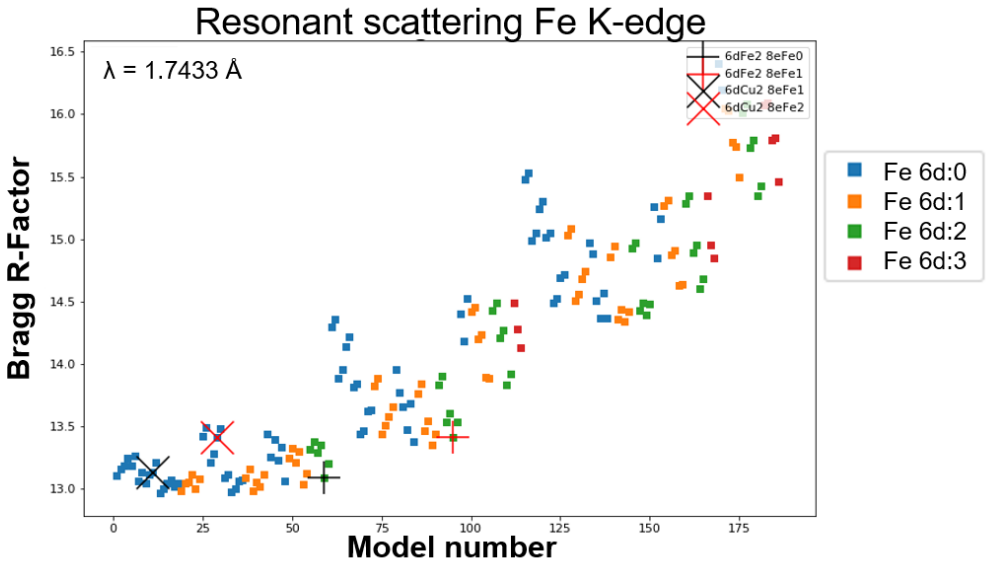

Figure 4.17. Bragg R-Factors obtained from the Rietveld refinement of the 186 structural models at Fe K-edge. A color identifies each 6d occupation.

4.3.5 Structural model propositions for germanite $Cu_{22}Fe_8Ge_4S_{32}$

The combination of the most favorable occupations yielded four structural models summarized in Table 4.11. The Fe atoms are distributed on three different crystallographic sites as predicted by the ^{57}Fe Mössbauer analysis, but unlike it

was predicted, the 12*f* site contains more than two Fe atoms. This might be explained by an erroneous interpretation of the spectrum (see the approximations p.154).

Table 4.11. Structural models with the lowest Bragg R-Factors of the refinement of the patterns around Cu K-edge and Ge K-edge.

2a	Fe_2	Fe_2	Fe_2	Fe_2
6c	Cu_6	Cu_6	Cu_6	Cu_6
6d	Fe_2Ge_4	Fe_2Ge_4	Cu_2Ge_4	Cu_2Ge_4
12f	Cu_9Fe_3	Cu_8Fe_4	Cu_8Fe_4	Cu_7Fe_5
8e	Cu_7Fe_1	Cu_8	Cu_6Fe_2	Cu_7Fe_1

Systematic Rietveld refinements of the patterns acquired at K-edge energies were performed with the four models. Figure 4.18a displays the diffraction pattern measured at Cu K-edge refined with a structural model containing 2 Cu atoms on the site 6*d*, namely $[Fe_2]_{2a}[Cu_6]_{6c}[Cu_2Ge_4]_{6d}[Cu_8Fe_4]_{12f}[Cu_6Fe_2]_{8e}$ ($[Fe_2]_{2a}[Cu_6]_{6c}[Cu_2Ge_4]_{6d}[Cu_7Fe_5]_{12f}[Cu_7Fe_1]_{8e}$ is similar). Figure 4.18b presents the refinement of the same pattern with a structural model containing 2 Fe atoms on the site 6*d*, namely $[Fe_2]_{2a}[Cu_6]_{6c}[Fe_2Ge_4]_{6d}[Cu_8Fe_4]_{12f}[Cu_8]_{8e}$ ($[Fe_2]_{2a}[Cu_6]_{6c}[Fe_2Ge_4]_{6d}[Cu_9Fe_3]_{12f}[Cu_7Fe_1]_{8e}$ is similar). The refinements with the models containing 2 Cu atoms on the 6*d* site yield intensity discrepancies on many reflections, especially the (210) reflection. This translate a high contribution of the Cu atoms to the structure factor of the reflection (210). To fit the peak intensity, a larger structure factor is necessary. Since the 6*d* and 6*c* sites contribute equally but in opposite sign to the structure factor of the (210), a larger structure factor can be obtained with the occupation of only one of the two sites by Cu atoms, *i.e.* the models $[Fe_2]_{2a}[Cu_6]_{6c}$ $[Fe_2Ge_4]_{6d}[Cu_{8+x}Fe_{4-x}]_{12f}[Cu_{8-x}Fe_x]_{8e}$ (x = 0, 1).

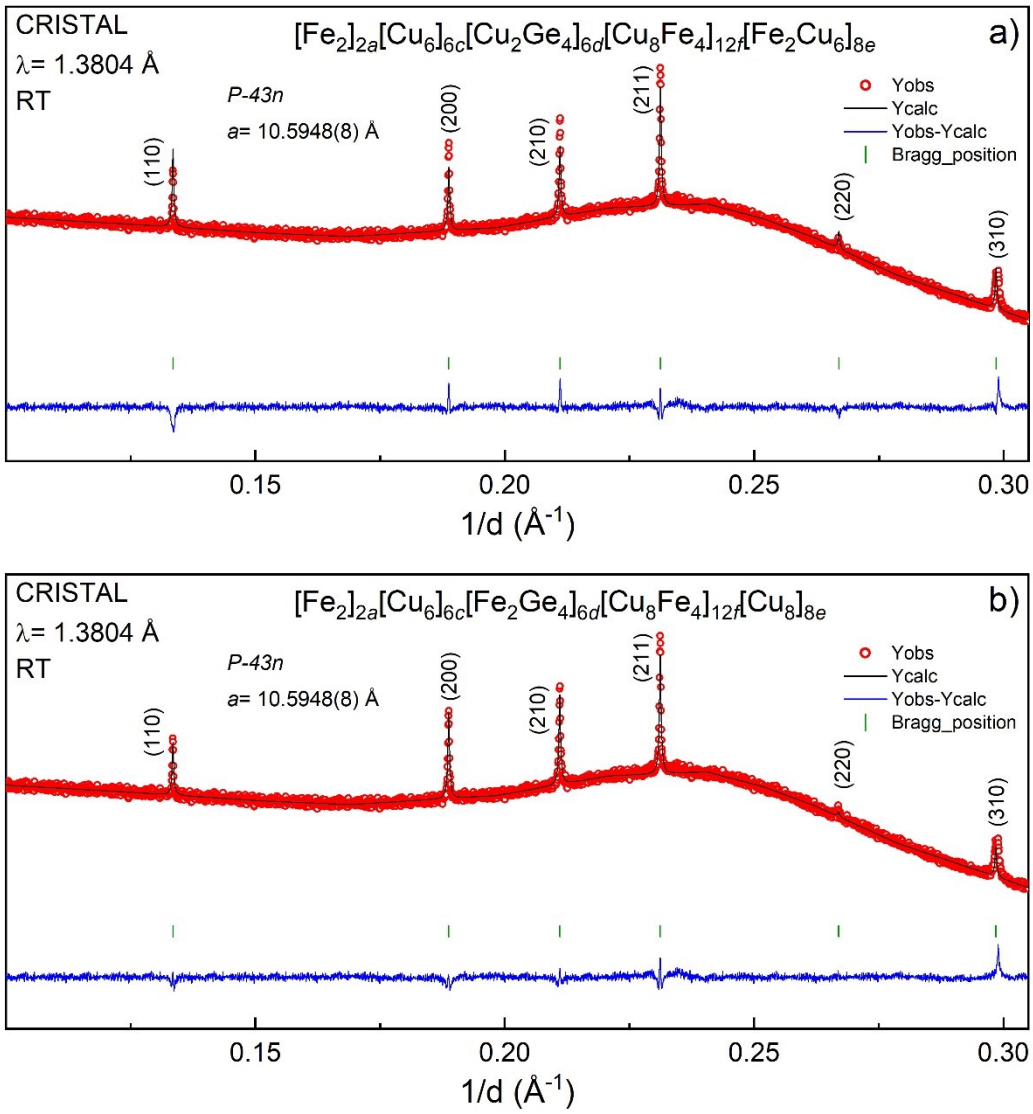

Figure 4.18. The Rietveld refinement of a germanite powder sample at Cu K-edge with the structural models a) $[Fe_2]_{2a}[Cu_6]_{6c}[Cu_2Ge_4]_{6d}[Cu_8Fe_4]_{12f}[Cu_8]_{8e}$ and b) $[Fe_2]_{2a}[Cu_6]_{6c}[Fe_2Ge_4]_{6d}[Cu_8Fe_4]_{12f}[Cu_6Fe_2]_{8e}$

The Rietveld refinement of the patterns acquired in resonant conditions allowed the discrimination of several site occupations. Thereby, the structural model the most likely for germanite $Cu_{22}Fe_8Ge_4S_{32}$ is $[Fe_2]_{2a}[Cu_6]_{6c}[Fe_2Ge_4]_{6d}[Cu_{8+x}Fe_{4-x}]_{12f}[Cu_{8-x}Fe_x]_{8e}$ with x = 0, 1. Indeed, a deviation from the nominal stoichiometry is anticipated for synthetic germanite due to the non-negligible presence of a semi-crystalline germanite-type phase and a bornite phase. To account of such deviation and to test the robustness of the models, several Rietveld fits were performed while freeing the occupancy.

4.3.6 Stoichiometric deviations in synthetic germanite

In Chapter 2, we showed that the germanite samples produced by sealed tube synthesis were commonly formed together with a bornite Cu_5FeS_4 phase and a semi-crystalline germanite-like phase because of sulfur loss. Hence, while the $Cu_{22}Fe_8Ge_4S_{32}$ stoichiometry was a fair assumption to determine the cationic occupation of the five crystallographic sites, this initial stoichiometry is certainly not that of the germanite phase. This stoichiometry deviation is illustrated by the discrepancies of the calculated profile with the observed peaks (110), (200) and (210) with the models $[Fe_2]_{2a}[Cu_6]_{6c}[Fe_2Ge_4]_{6d}[Cu_{8+x}Fe_{4-x}]_{12f}[Cu_{8-x}Fe_x]_{8e}$ (Figure 4.19 with $x = 0$, $x = 1$ is similar).

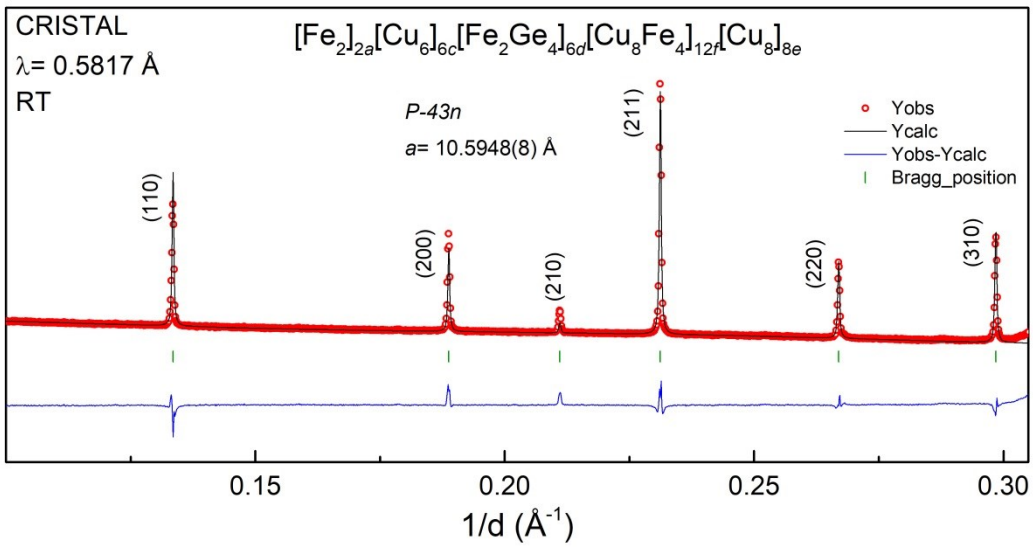

Figure 4.19. Rietveld refinement of the pattern measured at high energy with the structural model: $[Fe_2]_{2a}[Cu_6]_{6c}[Fe_2Ge_4]_{6d}[Cu_8Fe_4]_{12f}[Cu_8]_{8e}$.

In order to determine the ‘‘real’’ stoichiometry of germanite, a combined Rietveld refinement of the patterns measured at the elemental K-edges and high energy was performed. The weight contribution of each pattern was chosen to ensure an optimal scattering contrast among the elements to accurately determine their occupancy. For instance, the pattern acquired at Fe K-edge has a contribution to the refinement of only 1.0 % due to its few peaks with low signal-to-noise ratio. Also, the weight contribution of the pattern measured at high energy is 10 %

because of its lower scattering contrast compared to the patterns acquired at elemental K-edges. In that manner, the remaining 89 % was divided between the patterns measured at Ge K-edge (45 %) and Cu K-edge (44 %) due to their acute sensitivity to Ge and Cu.

The combined Rietveld refinements of the structural models $[Fe_2]_{2a}[Cu_6]_{6c}[Fe_2Ge_4]_{6d}[Cu_{8+x}Fe_{4-x}]_{12f}[Cu_{8-x}Fe_x]_{8e}$ (x = 0, 1) at all elemental K-edges (with no Ge stoichiometric constraints) converged to an occupation of the 6*d* site by 5 - 6 Ge atoms, hence suggesting a Ge-rich composition compared to the nominal stoichiometry. In fact, based on results presented in Chapter 2, a Ge-rich composition for the germanite samples prepared by sealed tube is expected to balance the secondary phases formation (which are found to be Ge poor in nature).[196] Also, mineral compounds of space group $P\bar{4}3n$ with a related chemical formula are found in nature, namely maikainite $Cu_{20}(Fe, Cu)_6Mo_2Ge_6S_{32}$, ovamboite $Cu_{20}(Fe, Cu, Zn)_6W_2Ge_6S_{32}$ and colusite $Cu_{26}(V, Nb, Ta, Cr)_2Ge_6S_{32}$.[197] The possible chemical formulas were determined regarding the following premises: a neutral electrical charge, a number of cations equal to 34 (from single crystal data), a Ge content between 4 and 6 atoms (resonant XRPD data) and a Cu^{2+} content between 1 and 2 atoms (0 Cu^{2+} was excluded because germanite is a *p*-type semiconductor and a higher content than 2 Cu^{2+} is not expected to be stable due to Jahn-Teller effects[151]). Following this, the investigated composition containing 1 Cu^{2+} per unit were determined by $Cu_{22+x}Fe_{7-3x}Ge_{5+2x}S_{32}$ with x = -0.5, -0.25, 0, 0.25, 0 and those containing 2 Cu^{2+} per unit by $Cu_{22+x}Fe_{8-3x}Ge_{4+2x}S_{32}$ with x = 0, 0.25, 0.5, 0.75, 1. Note that only the compositions leading to the improvement of the *Bragg R-Factors* compared to the nominal composition are presented in this manuscript. Hence, giving the following formulas: $Cu_{21.75}Fe_{7.75}Ge_{4.5}S_{32}$, $Cu_{22}Fe_7Ge_5S_{32}$, $Cu_{22.25}Fe_{6.25}Ge_{5.5}S_{32}$, $Cu_{22.5}Fe_{5.5}Ge_6S_{32}$, $Cu_{22.25}Fe_{7.25}Ge_{4.5}S_{32}$, $Cu_{22.5}Fe_{6.5}Ge_5S_{32}$, $Cu_{22.75}Fe_{5.75}Ge_{5.5}S_{32}$ and $Cu_{23}Fe_5Ge_6S_{32}$. For each formula, characterized by a Cu^{2+} content (*e.g.* 1 Cu^{2+} or 2 Cu^{2+}), a structural model based on the occupation preferences found for $Cu_{22}Fe_8Ge_4S_{32}$ is proposed. The structural model of each stoichiometry along with the *Bragg R-Factor* and global χ^2 at each collection energies, *i.e.* Cu K-edge (λ = 1.3804 Å), Ge K-edge (λ = 1.1165 Å), Fe K-edge (λ = 1.7433 Å) and high energy (λ = 0.5817 Å) are summarized in Table 4.12 and Table

4.13. Note that the occupation of the site 2*a* and 6*c*, *e.g.* $[Fe_2]_{2a}[Cu_6]_{6c}$, is constant and hence is not displayed in the tables.

Table 4.12. Bragg R-Factors at the Cu, Fe, Ge K-edges and high energy for the stoichiometries: $Cu_{22}Fe_8Ge_4S_{32}$, $Cu_{22.25}Fe_{7.25}Ge_{4.5}S_{32}$, $Cu_{21.75}Fe_{7.75}Ge_{4.5}S_{32}$, $Cu_{22.5}Fe_{6.5}Ge_5S_{32}$ and $Cu_{22}Fe_7Ge_5S_{32}$.

	$Cu_{22}Fe_8Ge_4S_{32}$	$Cu_{22.25}Fe_{7.25}Ge_{4.5}S_{32}$	$Cu_{21.75}Fe_{7.75}Ge_{4.5}S_{32}$	$Cu_{22.5}Fe_{6.5}Ge_5S_{32}$	$Cu_{22}Fe_7Ge_5S_{32}$
	$[Fe_2Ge_4]_{6d}$	$[Fe_{1.5}Ge_{4.5}]_{6d}$	$[Fe_{1.5}Ge_{4.5}]_{6d}$	$[Fe_1Ge_5]_{6d}$	$[Fe_1Ge_5]_{6d}$
	$[Cu_8Fe_4]_{12f}$	$[Cu_{8.25}Fe_{3.75}]_{12f}$	$[Cu_{7.75}Fe_{4.25}]_{12f}$	$[Cu_{8.5}Fe_{3.5}]_{12f}$	$[Cu_8Fe_4]_{12f}$
	$[Cu_8]_{8e}$	$[Cu_8]_{8e}$	$[Cu_8]_{8e}$	$[Cu_8]_{8e}$	$[Cu_8]_{8e}$
λ = 0.5817 Å	26.3	23.5	22.5	21.4	20.8
λ Cu = 1.3804 Å	29.1	28.4	30.4	27.9	30.0
λ Ge = 1.1165 Å	14.9	11.8	13.3	9.43	10.6
λ Fe = 1.7433 Å	6.93	6.06	6.82	8.06	7.14
Av. Bragg R-Fac.	19.3	17.4	18.3	16.7	17.1
Global χ^2	8.58	8.14	8.13	7.87	7.85
	2 Cu^{2+}	2 Cu^{2+}	1 Cu^{2+}	2 Cu^{2+}	1 Cu^{2+}

Table 4.13. Bragg R-Factors at the Cu, Fe, Ge K-edges and high energy for the stoichiometries: $Cu_{22.75}Fe_{5.75}Ge_{5.5}S_{32}$, $Cu_{22.25}Fe_{6.25}Ge_{5.5}S_{32}$, $Cu_{23}Fe_5Ge_6S_{32}$ and $Cu_{22.5}Fe_{5.5}Ge_6S_{32}$.

	$Cu_{22.75}Fe_{5.75}Ge_{5.5}S_{32}$	$Cu_{22.25}Fe_{6.25}Ge_{5.5}S_{32}$	$Cu_{23}Fe_5Ge_6S_{32}$	$Cu_{22.5}Fe_{5.5}Ge_6S_{32}$
	$[Fe_{0.5}Ge_{5.5}]_{6d}$	$[Fe_{0.5}Ge_{5.5}]_{6d}$	$[Ge_6]_{6d}$	$[Ge_6]_{6d}$
	$[Cu_{8.75}Fe_{3.25}]_{12f}$	$[Cu_{8.25}Fe_{3.75}]_{12f}$	$[Cu_9Fe_3]_{12f}$	$[Cu_{8.5}Fe_{3.5}]_{12f}$
	$[Cu_8]_{8e}$	$[Cu_8]_{8e}$	$[Cu_8]_{8e}$	$[Cu_8]_{8e}$
λ = 0.5817 Å	19.9	20.4	19.7	21.3
λ Cu = 1.3804 Å	29.6	30.3	31.5	32.2
λ Ge = 1.1165 Å	8.25	8.51	7.52	7.00
λ Fe = 1.7433 Å	10.5	9.64	13.1	12.2
Av. *Bragg R-Fac.*	17.1	17.2	18.0	18.2
Global χ^2	7.81	7.78	7.94	7.92
	2 Cu^{2+}	1 Cu^{2+}	2 Cu^{2+}	1 Cu^{2+}

The highest *Bragg R-Factors* and global χ^2 are obtained for the nominal composition $Cu_{22}Fe_8Ge_4S_{32}$ (Table 4.12). The increase of the Ge content (> 4) causes a decrease of the *Bragg R-Factor* of the high energy and Ge K-edge pattern refinements. The highest *Bragg R-Factors* at Cu K-edge were obtained for the models where the Ge content is the highest, *i.e.* the stoichiometries that deviate the most from the nominal (Table 4.13). The distribution of the Fe atoms on only two site in the structural model of the composition $Cu_{23}Fe_5Ge_6S_{32}$ and $Cu_{22.5}Fe_{5.5}Ge_6S_3$ is in disagreement with the ^{57}Fe Mössbauer results and this reflects in their high

Bragg R-Factors. Interestingly, the models with the worst agreement of the Fe K-edge pattern, happens to have the best agreement factors of the Ge-Kedge pattern, namely where 6 Ge atoms are on the 6*d* site (Table 4.13). This is because the increase in Ge content induces a decrease in the Fe content and the calculated profile agreement of the pattern measured at Fe K-edge is optimized for the highest Fe content. Similarly, the agreement of the pattern measured at Ge K-edge is optimized for the highest Ge content. Consequently, the stoichiometries $Cu_{22}Fe_8Ge_4S_{32}$, $Cu_{23}Fe_5Ge_6S_{32}$ and $Cu_{22.5}Fe_{5.5}Ge_6S_{32}$ led to the best and the worst agreements depending on the edge energy. The lowest average *Bragg R-factors* and global χ^2 were obtained for the compositions $Cu_{22.5}Fe_{6.5}Ge_5S_{32}$ (2 Cu^{2+}) and $Cu_{22.25}Fe_{6.25}Ge_{5.5}S_{32}$ (1 Cu^{2+}), respectively (Table 4.12 and Table 4.13).

Figure 4.20 represents the Rietveld refinements of the patterns acquired at all the elemental edges and high energy with three structural models of different composition, namely $Cu_{22}Fe_8Ge_4S_{32}$, $Cu_{22.5}Fe_{6.5}Ge_5S_{32}$ and $Cu_{23}Fe_5Ge_6S_{32}$ (all containing 2 Cu^{2+}). While, the $Cu_{23}Fe_5Ge_6S_{32}$ composition yields an improved calculated profile for the pattern measured at Ge K-edge compared to that of $Cu_{22}Fe_8Ge_4S_{32}$, it decreases the quality of the calculated profile for the pattern measured at Cu K-edge. Thus, as it was evidenced by the lower *Bragg R-factors*, the composition $Cu_{22.5}Fe_{6.5}Ge_5S_{32}$ is a good compromise between all the patterns measured at the different edges.

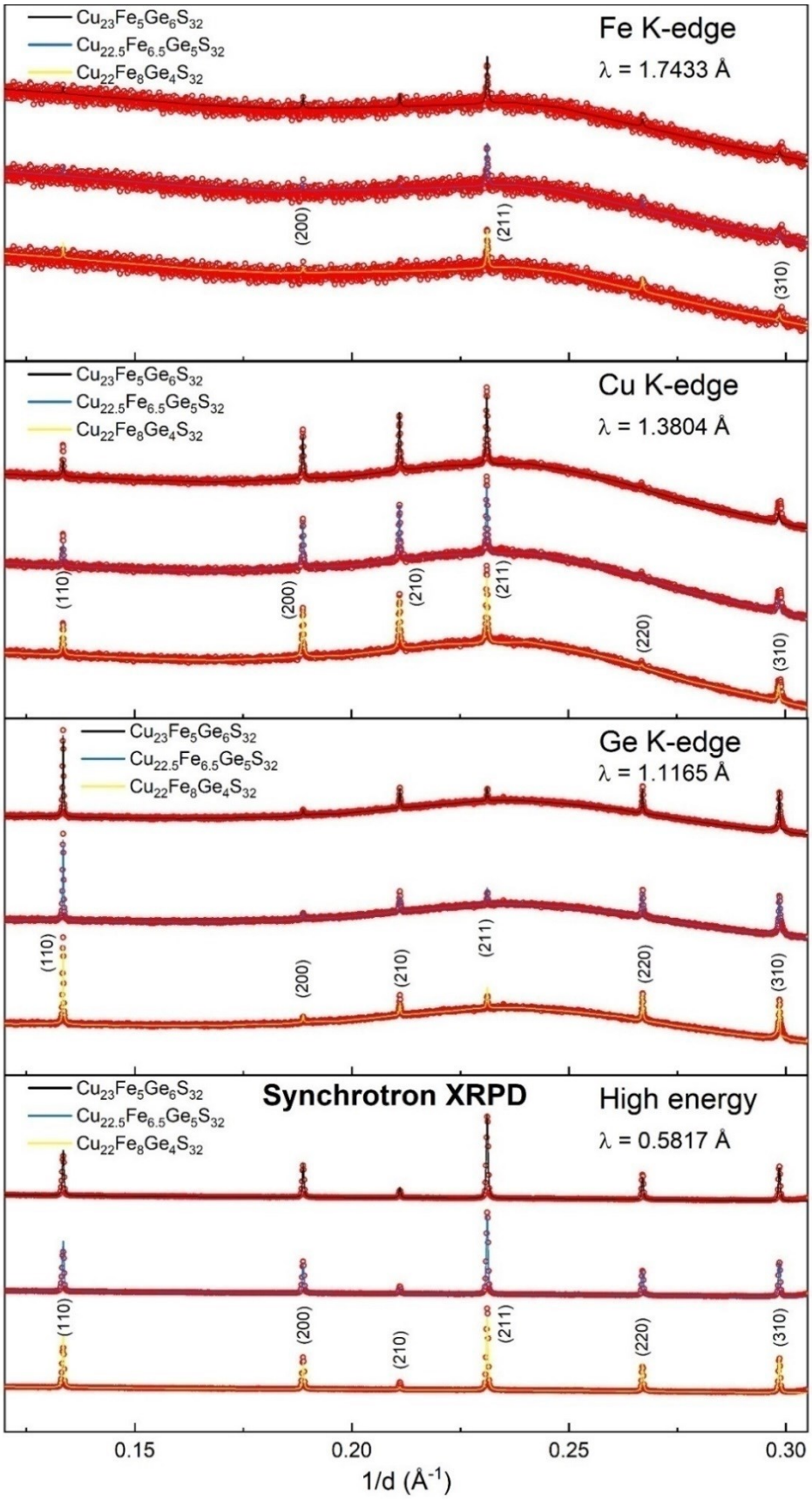

Figure 4.20. Rietveld refinements of germanite at high energy, Ge K-edge, Cu K-edge and Fe K-edge for $Cu_{22}Fe_8Ge_4S_{32}$, $Cu_{22.5}Fe_{6.5}Ge_5S_{32}$ and $Cu_{23}Fe_5Ge_6S_{32}$.

Next, we proceeded to perform Rietveld refinements with two different structural models for both compositions, namely:

- $[Fe_2]_{2a}[Cu_6]_{6c}[Fe_1Ge_5]_{6d}[Cu_{8.5}Fe_{3.5}]_{12f}[Cu_8]_{8e}$
- $[Fe_2]_{2a}[Cu_6]_{6c}[Fe_1Ge_5]_{6d}[Cu_9Fe_3]_{12f}[Cu_{7.5}Fe_{0.5}]_{8e}$
- $[Fe_2]_{2a}[Cu_6]_{6c}[Fe_{0.5}Ge_{5.5}]_{6d}[Cu_{8.25}Fe_{3.75}]_{12f}[Cu_8]_{8e}$.
- $[Fe_2]_{2a}[Cu_6]_{6c}[Fe_{0.5}Ge_{5.5}]_{6d}[Cu_9Fe_3]_{12f}[Cu_{7.25}Fe_{0.75}]_{8e}$.

In this series of refinement, the B_{iso} were freed to accommodate the slight intensity discrepancies. Table 4.14 summarizes the *Bragg R-Factors* of the four structural models for the stoichiometry $Cu_{22.5}Fe_{6.5}Ge_5S_{32}$ (2 Cu^{2+}) and $Cu_{22.25}Fe_{6.25}Ge_{5.5}S_{32}$ (1 Cu^{2+}). For the pattern measured at Fe K-edge, the refinement of the thermal parameters B_{iso} lead to a drastic increase of the *Bragg R-Factor* due to low contribution assigned to this pattern (1 %). Also, the two structural models presenting the poorest agreement have the lowest Fe content on 12*f*, *e.g.* $[Cu_9Fe_3]_{12f}$. Similarly, the *Bragg R-Factor* of the pattern measured at the Cu K-edge decreases with the addition of Fe atoms on the 8*e* site for both stoichiometries. The refinement of the site 6*d* occupancies of the model $[Fe_{0.5}Ge_{5.5}]_{6d}[Cu_9Fe_3]_{12f}[Cu_{7.25}Fe_{0.75}]_{8e}$ results in a substitution of the 0.5 Fe atom on 6*d* by 0.5 Cu atom, *e.g.* $[Cu_{0.5}Ge_{5.5}]_{6d}[Cu_9Fe_3]_{12f}[Cu_{6.75}Fe_{1.25}]_{8e}$, which present the best global χ^2 and *Bragg R-Factors* at all energies, except Fe K-edge. However, in $[Fe_1Ge_5]_{6d}[Cu_{8.5}Fe_{3.5}]_{12f}[Cu_8]_{8e}$, the substitution of 1 Fe atom by 1 Cu atom on site 6*d* lead to less satisfying fits. Generally, the structural models of the $Cu_{22.25}Fe_{6.25}Ge_{5.5}S_{32}$ (2 Cu^{2+}) stoichiometry lead to an improvement of the agreement factors compared to $Cu_{22.5}Fe_{6.5}Ge_5S_{32}$ (2 Cu^{2+}) and thus is preferred. However, considering the decreasing the charge carrier concentration observed in Chapter 2 (section 2.4.3) for the germanite produced by ST (*i.e.* the sample the most likely to present stoichiometric deviation) compared to the germanite produced by mechanical alloying, a chemical formula which contain 1 Cu^{2+} is more probable such as $Cu_{22.25}Fe_{6.25}Ge_{5.5}S_{32}$ or $Cu_{22}Fe_7Ge_5S_{32}$.

Table 4.14. Bragg R-Factors of four structural models with the stoichiometry $Cu_{22.5}Fe_{6.5}Ge_5S_{32}$ and $Cu_{22.25}Fe_{6.25}Ge_{5.5}S_{32}$ obtained from the Rietveld refinement of the B_{iso}.

	$Cu_{22.5}Fe_{6.5}Ge_5S_{32}$			$Cu_{22.25}Fe_{6.25}Ge_{5.5}S_{32}$		
	$[Fe_1Ge_5]_{6d}$	$[Fe_1Ge_5]_{6d}$	$[Cu_1Ge_5]_{6d}$	$[Fe_{0.5}Ge_{5.5}]_{6d}$	$[Fe_{0.5}Ge_{5.5}]_{6d}$	$[Cu_{0.5}Ge_{5.5}]_{6d}$
	$[Cu_{8.5}Fe_{3.5}]_{12f}$	$[Cu_9Fe_3]_{12f}$	$[Cu_8Fe_4]_{12f}$	$[Cu_{8.25}Fe_{3.75}]_{12f}$	$[Cu_9Fe_3]_{12f}$	$[Cu_9Fe_3]_{12f}$
	$[Cu_8]_{8e}$	$[Cu_{7.5}Fe_{0.5}]_{8e}$	$[Cu_{7.5}Fe_{0.5}]_{8e}$	$[Cu_8]_{8e}$	$[Cu_{7.25}Fe_{0.75}]_{8e}$	$[Cu_{6.75}Fe_{1.25}]_{8e}$
λ = 0.5817 Å	21.1	21.4	21.9	19.9	20.4	19.5
λ Cu = 1.3804 Å	26.5	24.4	29	27.2	23.1	21.9
λ Ge = 1.1165 Å	10.2	9.34	10.6	8.84	8.59	7.47
λ Fe = 1.7433 Å	14.0	15.8	10.8	14.5	17.0	16.3
Av. *Bragg R-Fac.*	18.0	17.7	18.1	17.6	17.3	16.3
Global χ^2	7.87	7.91	7.82	7.72	7.77	7.65
	2 Cu^{2+}			1 Cu^{2+}		

However, even though the $Cu_{22.25}Fe_{6.25}Ge_{5.5}S_{32}$ (1 Cu^{2+}) chemical formula leads to better fits than the nominal $Cu_{22}Fe_8Ge_4S_{32}$ (2 Cu^{2+}) formula, the acceptation of this chemical formula as the ''real'' stoichiometry of synthetic germanite will require experimental evidences such as the synthesis of a pure sample and EDS. Meanwhile, the Rietveld refinement on the full 2θ range, of neutron and X-ray diffraction powder patterns of nominal $Cu_{22}Fe_8Ge_4S_{32}$ with the structural model $[Fe_2]_{2a}[Cu_6]_{6c}[Fe_2Ge_4]_{6d}[Cu_8Fe_4]_{12f}[Cu_8]_{8e}$ of will be presented in the following section.

4.3.7 Rietveld refinements of synthetic germanite of NPD and XRPD patterns

The Rietveld refinements (on the full 2θ range) of a germanite sample produced by sealed tube synthesis acquired by X-ray diffraction are displayed in Figure 4.21. The calculated profile with the structural model $[Fe_2]_{2a}[Cu_6]_{6c}[Fe_2Ge_4]_{6d}[Cu_8Fe_4]_{12f}[Cu_8]_{8e}$ (Figure 4.21a) is in good agreement with the observed data and is a clear improvement compared to Tettenhorst model (Figure 4.21b). The Rietveld refinement on the full 2θ range gives an overall χ^2 = 16.1, which comprises a germanite $Cu_{22}Fe_8Ge_4S_{32}$ phase refined with a $P\bar{4}3n$ space group and lattice parameter a = 10.5952(2) Å (*Bragg R-Factor* = 2.90, compared to 4.20 for Tettenhorst) and a bornite phase refined with a $Fm\bar{3}m$ space group and a

= 10.893(1) Å (*Bragg R-Factor* = 27.9). The superstructure peaks are mostly correctly accounted with the new structural model, except for (110) and (211), which are overestimated (inset Figure 4.21a).

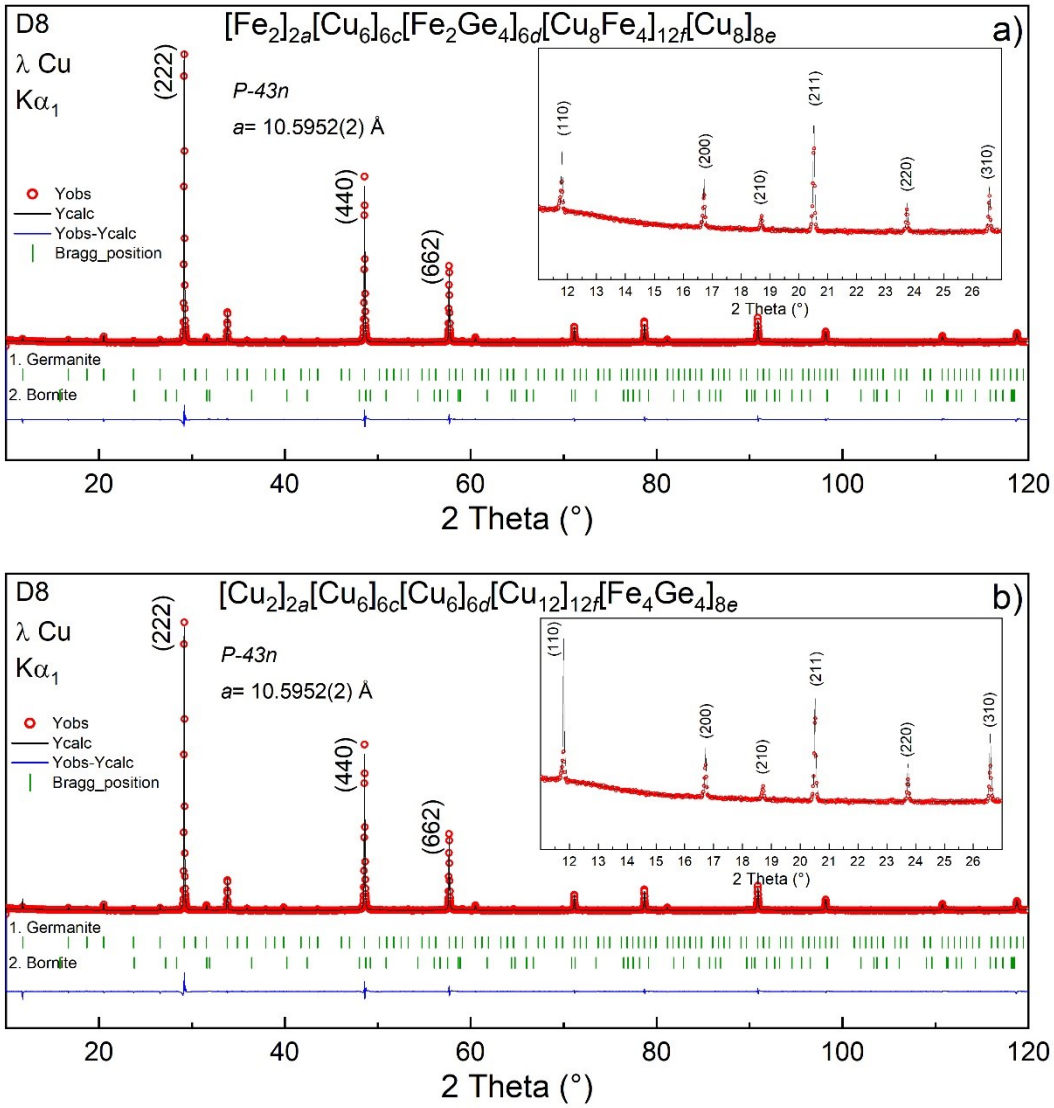

Figure 4.21. Rietveld refinements of a germanite sample synthesized by ST a) with the new structural model $[Fe_2]_{2a}[Cu_6]_{6c}[Fe_2Ge_4]_{6d}[Cu_8Fe_4]_{12f}[Cu_8]_{8e}$ and b) with Tettenhorst structural model $[Cu_2]_{2a}[Cu_6]_{6c}[Cu_6]_{6d}[Cu_{12}]_{12f}[Fe_4Ge_4]_{8e}$.

Figure 4.22 illustrates the Rietveld refinement of a germanite $Cu_{22}Fe_8Ge_4S_{32}$ sample with the model $[Fe_2]_{2a}[Cu_6]_{6c}[Fe_2Ge_4]_{6d}[Cu_8Fe_4]_{12f}[Cu_8]_{8e}$ on a neutron powder diffractogram. The Rietveld refinement of the pattern between 10 - 128° in 2θ gives an overall χ^2 = 11.3, which includes a germanite $Cu_{22}Fe_8Ge_4S_{32}$ phase refined with a $P\bar{4}3n$ space group and a = 10.5947(3) Å (*Bragg R-Factor* = 15.3) and

a bornite phase refined with a $Fm\bar{3}m$ space group and a = 10.894(1) Å (*Bragg R-Factor* = 19.0). Due to the presence of a semi-crystalline phase giving an anomalously large base to each main peaks of the germanite phase, the calculated profile underestimate the intensity of the main peaks. Additionally, the structural model $[Fe_2]_{2a}[Cu_6]_{6c}[Fe_2Ge_4]_{6d}[Cu_8Fe_4]_{12f}[Cu_8]_{8e}$ adequately describes all the superstructure peaks except for the (210) peak. This intensity discrepancy of the (210) peak might be due to a magnetic arrangement of the structure. Indeed, the peaks (210) and (220) disappear at high temperature before the rest of the superstructure peaks, as seen in Chapter 2, section 2.3.3.

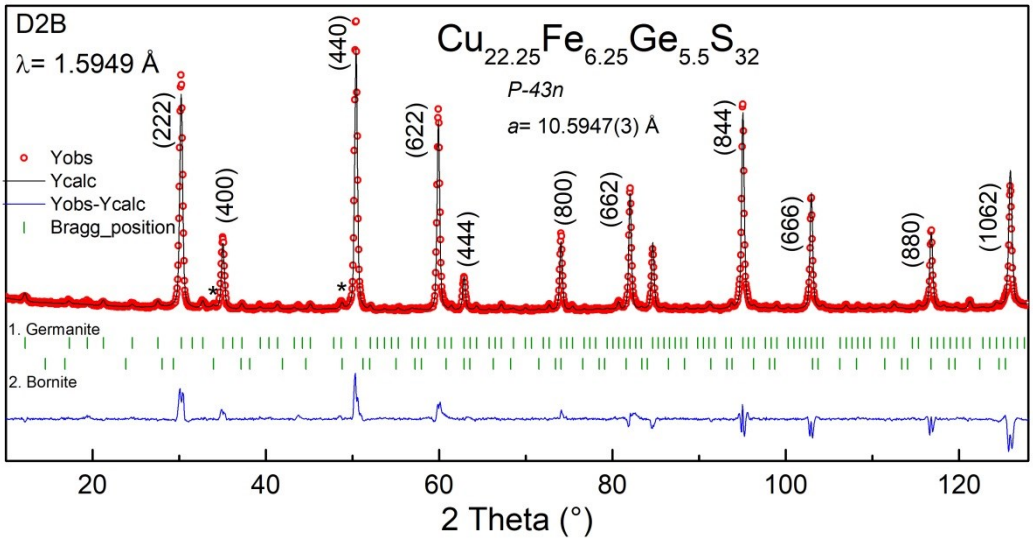

Figure 4.22. Rietveld refinement of a germanite sample measured by NPD on D2B with model $[Fe_2]_{2a}[Cu_6]_{6c}[Fe_2Ge_4]_{6d}[Cu_8Fe_4]_{12f}[Cu_8]_{8e}$. Asterisks identify the contributions of bornite.

4.4 Conclusion

A new structural model for synthetic germanite was proposed with respect to the space group and lattice parameter of the mineral material, $P\bar{4}3n$ and a = 10.595 Å. A reinterpretation of the ^{57}Fe Mössbauer spectra found that Fe is distributed on at least three crystallographic sites; 2 Fe on the interstitial 2a site of high symmetry, 2 Fe on the 12f site, which forms a metallic complex with the 2a

site, and the rest of the atoms on another site. The occupation of the 2*a* site by 2 Fe, in disagreement with Tettenhorst study on natural germanite (*i.e.* $[Cu_2]_{2a}$), was confirmed by single crystal X-ray data and supported by neutron powder diffraction. Unlike most materials, the resolution of a structural model on single crystal X-ray diffraction alone is not sufficient for germanite. Indeed, due to the electronic similarity of Cu, Fe and Ge, the symmetry resemblance of the crystallographic sites in $P\bar{4}3n$ and the mixed occupation of some sites, it is arduous to have a chemical contrast. Nonetheless, the diffraction patterns collected in resonant conditions at different elemental edges, *i.e.* Cu, Fe and Ge, allowed a sufficient scattering contrast to differentiate structural models by the quality of the Rietveld refinements. Hence, the 8*e* site was said to be occupied by 6 – 8 Cu atoms (0 - 2 Fe atoms) and the 12*f* site by 7 – 9 Cu atoms (3 – 5 Fe atoms). Also, the structural models where all 4 Ge atoms were on the 6*d* site and 6 Cu on the 6*c* site, presented the best agreement factors. From the combination of the most favorable occupation and the optimization of the calculated intensity of the (210) peak we proposed these two structural models for germanite $Cu_{22}Fe_8Ge_4S_{32}$:

- $[Fe_2]_{2a}[Cu_6]_{6c}[Fe_2Ge_4]_{6d}[Cu_8Fe_4]_{12f}[Cu_8]_{8e}$
- $[Fe_2]_{2a}[Cu_6]_{6c}[Fe_2Ge_4]_{6d}[Cu_9Fe_3]_{12f}[Cu_7Fe_1]_{8e}$

They both lead to a clear improvement of the calculated profiled compared to the model of natural germanite proposed by Tettenhorst.

Moreover, for the length of this thesis, the germanite was assumed to have the nominal stoichiometry: $Cu_{22}Fe_8Ge_4S_{32}$. From the refinement of the crystallographic sites occupancy on patterns measured in resonant conditions proposed two alternate stoichiometry for germanite: $Cu_{22.5}Fe_{6.5}Ge_5S_{32}$ and $Cu_{22.25}Fe_{6.25}Ge_{5.5}S_{32}$. However, the acceptation of either one of these stoichiometry would require experimental evidences.

General Conclusion & Perspectives

The research carried in this thesis focused on the synthesis, structural characterization and evaluation of the thermoelectric performance of the germanite family. The greatest strength, but also the greatest difficulty of this thesis is that it is dedicated to the study of a single material. The strength is obviously the completeness of the study and the depth of the analysis, which is crucial for such a fascinating and complex compound as germanite. The greatest difficulty was that all of the studies were carried out simultaneously, because a lot of the characterizations have been performed on large scale facilities and generally it take more than 6 months between the submission of the proposal and the experiment. Therefore, it forbids to follow the standard research ''timeline'', *e.g.* synthesis, structural characterization, properties measurement and conclusion.

As a consequence of this "fractured timeline", the germanite samples produced by sealed tube synthesis, namely the Sn-substituted series $Cu_{22}Fe_8Ge_{4-x}Sn_xS_{32}$ ($0 \leq x \leq 4$) and the $Cu_{22}Fe_8Ge_4S_{32}$ ST_SPS and ST_HP samples, were respectively sintered at 773 K and 873 K, which is way above the stability temperature (650 K) determined later. This possibly explains the decrease of the transport properties compared to the germanite samples synthesized by mechanical alloying, which responded differently to the densification since they undergo reactive sintering. Therefore, this implies that in future work we should sinter the sample produced by sealed tube at 600 K or lower. The main inconvenient of this sintering temperature, apart from the eventuality that the material does not sinter, is that it is less likely to yield structural disorder, which is desired to lower the lattice thermal conductivity. Hence, we suggest to induce cationic disorder by preparing sample with a sulfur sub stoichiometry. In addition, this investigation on the conditions of the processes drag attention to the significant impact of powder synthesis and sintering methods on the transport properties of complex quaternary Cu-based chalcogenides.

The classical experimental approach for phase exploration in solid state synthesis is oblivious to important information such as the formation temperature of the product (*e.g*. during an isotherm, heating or cooling) and the formation of

reactive intermediates and secondary phases. This lack of awareness hinders our ability to identify new materials or to devise successful synthetic processes for desired complex materials such as germanite. In this context, real time *in situ* reactions on powders in sealed tube by neutron powder diffraction is really advantageous and while it is a common approach for different synthesis method, to the best of our knowledge, it is a novelty.

Throughout this work we attempted to increase the thermoelectric figure of merit of germanite. Among the several approaches presented in Chapter 1, we focused on the effect of cationic substitution on the electrical and transport properties. In this context, we reported for the first time a crossover from the germanite to the renierite-type structure with a Cu to Zn substitution, *i.e.* $Cu_{22-x}Zn_xFe_8Ge_4S_{32}$, as the zinc content increases from $x = 0$ to $x = 2$, with a biphasic state for $x = 0.8$. We showed that the cationic disorder in the copper network increases with the Zn content and results in a decrease of the thermal conductivity that ultimately becomes lower for renierite with respect to germanite. Moreover, we suggested that this decrease in lattice thermal conductivity could also result from the additional number of crystallographic sites and the higher cationic disorder in the renierite-type compounds, induced by the tetragonal distortion, which provides an effective way of scattering heat carrying phonons. However, increasing the Zn concentration in the copper network leads to a decrease in the concentration of hole carriers, *i.e.* an increase of the electrical resistivity and Seebeck coefficient in renierite compared to germanite. This explains the very similar figures of merit observed for both structural types independently of the zinc content. It is the most interesting investigation because we managed to rationalized the electrical properties in the absence of a structural model by putting to profit ^{57}Fe Mössbauer spectroscopy together with precession electron diffraction tomography (PEDT).

The solid solution $Cu_{22}Fe_8Ge_{4-x}Sn_xS_{32}$ ($0 \leq x \leq 4$) is probably the most fascinating series and most promising to bring information regarding the relation structure properties. The substitution of Ge by a larger isovalent cation led to the decrease of electrical resistivity and Seebeck coefficient due to the decreasing of

the effective mass. In addition, the reduction of lattice thermal conductivity for the samples that contain both Ge and Sn was assigned to enhanced point defect scattering of the heat carrying because of mass, size, and bonding strength disparities due to the Sn-incorporation. Overall, the thermoelectric figure of merit *ZT* at 650 K was increased with the Sn content from 0.21 ($Cu_{22}Fe_8Ge_4S_{32}$) to 0.33 ($Cu_{22}Fe_8Sn_4S_{32}$) due to the contribution of higher power factor and to the lower thermal conductivity. A question left unanswered for this series of sample is: where do the Sn atoms are distributed and how this effects the crystal structure and the transport properties. We hope to answer this in the shortest delay with the interpretation of the resonant scattering and single crystal diffraction data.

The most challenging obstacle we have overcome was the determination of the crystal structure of synthetic germanite. At first glance, the crystal structure of germanite seems simple, its cubic and it contains only five crystallographic sites all coordinated in sulfur tetrahedra, but in fact, this high symmetry is precisely where the difficulty lie. Moreover, due to the electronic similarity of Cu, Fe and Ge, it is arduous to have a chemical contrast. Thus, from the analyses of diffraction patterns measured in resonant scattering at the K-edge of the three cations coupled to single crystal XRD, neutron diffraction and ^{57}Fe Mössbauer spectroscopy, we proposed a new structural model for synthetic germanite, which is in agreement with the space group and lattice parameter of the mineral product ($P\bar{4}3n$, a = 10.595 Å). In conclusion, the originality of the research work realized during this thesis lies in the experimental approach that was developed to overcome the inherent complexity of the germanite family.

5 Appendices

5.1 Molybdenum clathrate for thermoelectric applications

According to the phonon glass-electron crystal (PGEC) concept discussed in Chapter 1 (section 1.6.2.1), efficient thermoelectric materials are likely to be found among narrow band gap semiconductors with cage-like structures and atoms or molecules trapped inside the cages. The rattling of guest atoms provide effective scattering of the heat carrying phonons thus decreasing the lattice thermal conductivity, while charge carrier transport occurs through the covalent framework. Two classes of materials fulfill requirements of the PGEC concept, skutterudites and clathrates. The sp^3 covalently bonded framework of the clathrate conducts electrons through the structure; while loosely holding guest atoms inside with the function to scatter phonons thus significantly reducing the overall thermal conductivity. Moreover, the metallic cations quantity and nature alters the electron count that governs the electrical properties. This degree of freedom provides a simple fine-tuning parameter of the electron count for the optimization of the thermopower and electrical resistivity. Consequently, clathrates often have thermal conductivities below 3 W m^{-1} K^{-1} with metallic or semiconducting electrical properties. These electrical properties, combined with inherently low thermal conductivity, raised exciting perspectives to achieve a high dimensionless thermoelectric figure of merit *ZT*. The stannide clathrate class contains several material with *ZT*s above 1 in the mid-range temperature (480 K -550 K),[75–79] as $Ba_8Ga_{5.23}Al_{10.52}Sn_{30.26}$ with a maximum of ZT_{480K} = 1.2,[75] due to their relatively low conductivities 0.48 - 0.81 W $m^{-1}K^{-1}$ and high absolute Seebeck coefficient 175 - 245 mV K^{-1} at 300 K. Chevrel phases of formula $M_xMo_6Q_8$ (*M* = transition metal or rare-earth metal, *x* = 0–4, and *Q* = S, Se, or Te) have also been investigated for their thermoelectric and supraconductor properties.[80–86] These octahedral molybdenum units compounds can accommodate different metal cations or ligands, thus giving the possibility to easily tune their optical and electrical properties.[81,87–89]

Acknowledging the relatively good performances predicted for those chalcogenide molybdenum clusters, we took interest in the sulfur molybdenum compounds. The clathrate $Cs_{2.32}Mo_{4.21}S_4Cl_{8.22}$, an inorganic cluster of complex structure (V ≈ 78000 Å^3), is composed of [5^{12}] and [$5^{12}6^4$] cages formed by tetrahedral $Mo_4S^i{}_4Cl^a{}_{12}$ cluster units connected by shared chloride. Inside the cages, there is either a Cs^+ cation, a Cl^- anion or a $[Mo_6Cl_{14}]^{2-}$ unit for an overall formula of $[(Cs_2Mo_6Cl_{14})_{4.77}(CsCl)_{138}Cs_{47}][(CsCl)_{97}Cs_{24}][Mo_4S_4C_{l6}]_{136}$. The crystal structure of the latter was determined from a single crystal X-ray diffraction investigation as well as low temperature properties.[198] The goal of this study is to synthesize large powders batch of pure $Cs_{2.32}Mo_{4.21}S_4Cl_{8.22}$ in order to measure its TE properties. Figure 5.1 displays each polyhedron represented by a sphere of the corresponding color. The hexakaidecahedra (orange) are arranged in a diamond-like tetrahedral framework by sharing all of their hexagonal faces. Each hexakaidecahedron is surrounded by twelve pentagonal dodecahedra (blue) in a truncated tetrahedral fashion.

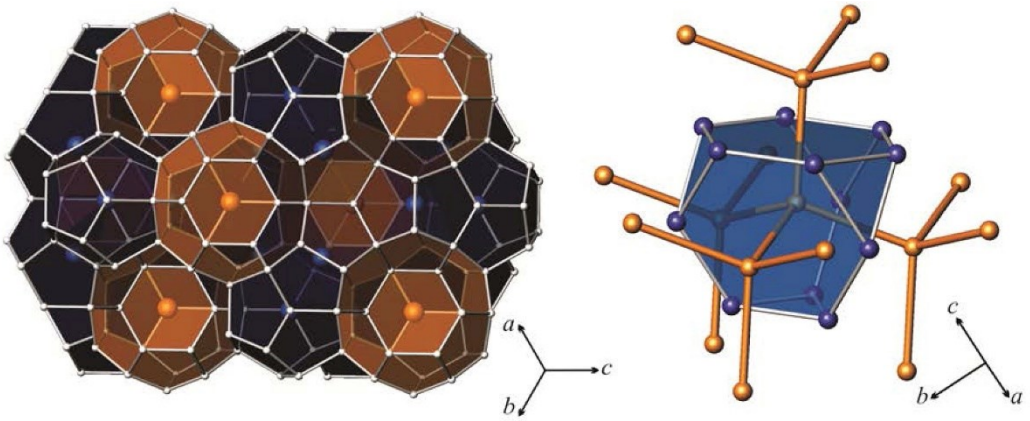

Figure 5.1 The crystal structure of clathrate II: (Left) Polyhedral view showing two types of polyhedral cages, pentagonal dodecahedra (blue) and hexakaidecahedra (orange); Right: connectivity diagram showing how polyhedra of each type are connected.[199]

Most clusters are synthesized under harsh conditions at temperatures above 1300 K for several days.[200–202] Since that is not well adapted for sulfur containing clusters, different low temperature technique were developed. First, through a low-temperature (673 K – 773 K) diffusion technique, Tarascon *et al.* [203,204] inserted rattling elements (*M*) inside the channels of a binary or pseudo-

binary chalcogenide phase Mo_6S_8, Mo_6Se_8 or $Mo_6(S_{8-x}Se_x)$. Anyhow the synthesis of high purity binary Mo_6S_8 is laborious.[205,206] Another approach to produce clusters at low temperature is by using reactant with analogous structures as building blocks such as Mo_6Cl_{12} and $Cs_2Mo_6Cl_{14}$.[207–213] The reactant Mo_6Cl_{12} structure (an octahedral molybdenum cluster) consist of cubic $Mo_6Cl_8^{4+}$ clusters interconnected one to the others by chloride ligands. Also, this cluster converts readily to a salt of the dianion $[Mo_6Cl_{14}]^{2-}$. For the cesium salt, $Cs_2Mo_6Cl_{14}$, each Mo bears one terminal chloride and is part of a Mo_6 octahedron embedded inside a cube defined by eight chloride centers. Mo_6Cl_{12} and $Cs_2Mo_6Cl_{14}$ are easily accessible reactants because their synthesis is a knowhow in CSM laboratory. Hence, this work aimed to synthesize the $Cs_{2.32}Mo_{4.21}S_4Cl_{8.22}$ molybdenum cluster by the low temperature diffusion technique using easily accessible or purchasable reactants. The next paragraphs resume the various reactants used with the specific reaction conditions.

For the synthesis the reactants from commercial origins were: Mo (99.95% Alfa Asar), S (99.5%, Alfa Aesar) and CsCl (99.9% Alfa Aesar), K_2S (44% Merck, the rest is K_2S_x). Prior to use, Mo powders were reduced under H_2 flowing gas at 1273 K during 10 h to eliminate any traces of oxygen. High purity Mo_6Cl_{12} (*Cmca*, a = 14.030(5) Å b = 11.263(9) Å c = 11.247(1) Å) and $Cs_2Mo_6Cl_{14}$ (*P*31*c*, a = 9.796(5) Å c = 14.236(1) Å) were synthesized in the laboratory (verified by XRD). Reactants were weighted and ground in an agate mortar in stoichiometric amount. The powders were synthesized by batch of 0.5 g and by 4 g for the reactions that worked best. The powders were placed in sealed silica tubes evacuated down to a pressure of 10^{-2} mbar from an argon atmosphere. The reactions took place in a furnace with a heating rate of 2 K min^{-1} and a plateau at 723 K for 48 h. The reactions were cooled down to 300 K at a natural cooling rate. The optimization work to find the time and temperature conditions for the clathrate formation were done by Corentin Breslau during his second year internship from the IUT *Mesures Physiques* from Saint-Nazaire, France.

The stoichiometry of the reactants was calculated to either yield the total stoichiometry of the clathrate $Cs_{2.32}Mo_{4.21}S_4Cl_{8.22}$, that of the cages $Mo_4S_4Cl_{12}$ or to react with a side product. Table 5.1 resumes all the reactants used and their proportion. Unsurprisingly, the low temperature synthesis promotes the formation of many secondary phases analogous to the reactant such as Cs_2MoCl_6, $Cs_3Mo_2Cl_9$, Mo_6Cl_{12}, $Mo_3S_7Cl_{14}$ and MoS_2. While it's possible to eliminate most of those phases without degrading the clathrate by an extraction with sulfuric acid H_2SO_4, the MoS_2 has proven to be tenacious as it can only be eliminated by an extraction with *aqua regia*, however the clathrate is not stable in these conditions. Thus, for clarity purposes the secondary phases removable by a H_2SO_4 extraction do not appear in the summary table. Quantification of the MoS_2 phase is not possible by Rietveld refinement due to its semi-crystalline nature. Hence, its presence is marked by a Yes or (-) in case of absence. The reaction of Mo_6Cl_{12} with S, K_2S or CsCl do not allow the formation of the clathrate (LPF110, LPF111 and LPF113). The reaction of Mo with sulfur and CsCl do not yield the clathrate either (LPF118) because reactions with metallic reactants usually needs much higher temperature and reaction time. The four conditions that generated the clathrate are LPF116 (88 wt.%), LPF117 (64 wt.%), LPF112 (50 wt.%) and LEM154 (59 wt.%). From these result it's possible to conclude that the clathrate synthesis requisite at least $Cs_2Mo_6Cl_{14}$ and sulfur as starting reactants and that the stoichiometry and the addition of Mo or Mo_6Cl_{12} as reactants vary the total yield of the reaction and the nature of the secondary products. Also, the addition of x CsCl to $Cs_2Mo_6Cl_{14}$ +3 S prevented the clathrate formation and promoted the formation of MoS_2 for x = 3 (LPF144 and LPF148). Figure 5.2, shows the diffractogram of the four synthesis that yield the clathrate between 5 – 23° in 2θ where a MoS_2 peak is observable. Among them, LEM154 (59 wt.% of clathrate) obtained from $Cs_2Mo_6Cl_{14}$ and the required stoichiometric sulfur amount to form $Cs_{2.32}Mo_{4.21}S_4Cl_{8.22}$ (x S = 5.7), generates the least MoS_2. Thus, it was decided to optimize the stoichiometric amount of sulfur to obtain the most clathrate with the least MoS_2 from these conditions.

Table 5.1 Formation of the clathrate and secondary phase MoS_2 for different reactants and stoichiometry.

Sample	Reactants				MoS_2	Clathrate
LPF110	Mo_6Cl_{12}	2 S	4 CsCl		-	-
LPF111	2/3 Mo_6Cl_{12}	3 S	K_2S		Yes	-
LPF113	2/3 Mo_6Cl_{12}	4 S			Yes	-
LPF118	4 Mo	4 S	6 CsCl		-	-
LPF112	2/3 $Cs_2Mo_6Cl_{14}$	6.22 S	2.22 Mo		Yes	50 %
LPF116	$Cs_2Mo_6Cl_{14}$	12 S	4 Mo	Mo_6Cl_{12}	Yes	88 %
LPF117	2 $Cs_2Mo_6Cl_{14}$	20 S	7 Mo	1/2 Mo_6Cl_{12}	Yes	64 %
LEM154	$Cs_2Mo_6Cl_{14}$	5.7 S			Yes	59 %
LPF144	$Cs_2Mo_6Cl_{14}$	3S	3 CsCl		Yes	-
LPF148	$Cs_2Mo_6Cl_{14}$	3S	CsCl		-	-

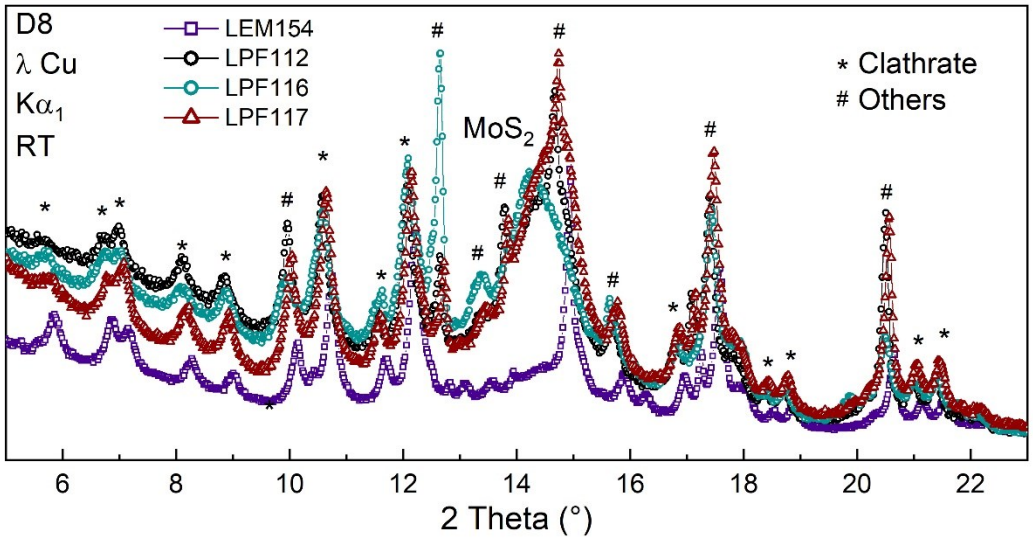

Figure 5.2 Diffractogram section of the four conditions that generate the clathrate: LPF116 (teal), LPF117 (wine), LPF112 (black) and LEM153 (purple) between 5 – 23° in 2θ to display a MoS_2 peak. Asterisks indicate the clathrate contributions and hashs other contributions.

The optimization of the $Cs_2Mo_6Cl_{14}$ to sulfur ratio demonstrates that the clathrate is formed within the ratio $3 \leq x \leq 8$. The clathrate is formed in small proportion (6.0 wt.%) for the ratio $x = 3$ as the main products are $Cs_3Mo_2Cl_9$ (55 wt.%) and Mo_6Cl_{12} (19 wt.%), also it is clear that the reaction is incomplete as there is still 20 wt.% of the reactant $Cs_2Mo_6Cl_{14}$. Furthermore, the clathrate formation is promoted with the increasing sulfur ratio until $x = 5.7$ (59 wt.%),

which is the precise amount of sulfur $Cs_2Mo_6Cl_{14}$ needs to form $Cs_{2.32}Mo_{4.21}S_4Cl_{8.22}$. Additionally, x = 5.7 is a turnover ratio for the secondary phases, $Cs_3Mo_2Cl_9$ (6 wt.%) and Mo_6Cl_{12} (0 wt.%) disappear almost completely and Cs_2MoCl_6 (35 wt.%) appears as a secondary phase for the first time. Higher sulfur content leads to the increase of Cs_2MoCl_6 and $Mo_3S_7Cl_{14}$, thus decreases the clathrate content. Consequently, going from a ratio of x = 5.7 to x = 6 drastically lowers the clathrate formation by a factor of two (from 59 wt.% to 24 wt.%) to the benefit of Cs_2MoCl_6 which increases by a factor of two (from 35 wt.% to 74 wt.%). Further increase of the sulfur ratio decreases the clathrate concentration and promotes Cs_2MoCl_6 and $Mo_3S_7Cl_{14}$. The highest sulfur ratio x = 9 do not generate the clathrate and Cs_2MoCl_6 (51 wt.%) and $Mo_3S_7Cl_{14}$ (49 wt.%) are produced equivalently. MoS_2 proportion is increasing with the sulfur ratio over the full range $3 \leq x \leq 9$. The weight percentages obtained by Rietveld refinement only represent the proprotion of the crystallized phases. Considering all these results, the $Cs_2Mo_6Cl_{14}$ to sulfur ratio x = 3.5 is considered the best synthesis as it yields the least MoS_2. However, the elimination of 84 wt.% of the crystallized phases by sulfuric acid revealed that the MoS_2 to clathrate ratio is high and was only camouflaged by the presence of secondary phases. Nonetheless, the wt.% should be used with precaution as the MoS_2 mass contribution is non-negligible, fluctuating and not taken into account. Table 5.2 resume the secondary phases and their proportion as a function of the ratio x of sulfur added to the reactant $Cs_2Mo_6Cl_{14}$.

Table 5.2 The weight percentage of the clathrate and the secondary phases obtained for different $Cs_2Mo_6Cl_{14}$ to sulfur ratio

x	$Cs_2Mo_6Cl_{14}$	$Cs_3Mo_2Cl_9$	Mo_6Cl_{12}	Cs_2MoCl_6	$Mo_3S_7Cl_{14}$	MoS_2	Clathrate
3	20 %	55 %	19 %	-	-	-	6.0 %
3.5	-	59 %	25 %	-	-	-	16 %
4	-	57 %	22 %	-	-	-	21 %
4.5	-	55 %	16 %	-	-	Yes	29 %
5.7	-	6 %	-	35 %	-	Yes	59 %
6	-	-	2.0 %	74 %	-	Yes	24 %
7	-	-	-	60 %	26 %	Yes	14 %
8	-	-	-	51 %	40 %	Yes	9.0 %
9	-	-	-	51 %	49 %	Yes	-

In conclusion, the bulk synthesis of the clathrate $Cs_{2.32}Mo_{4.21}S_4Cl_{8.22}$ by low temperature diffusion from related building blocks did not yield a pure product due to the presence of MoS_2. Also, it was shown that the clathrate synthesis required at least $Cs_2Mo_6Cl_{14}$ and sulfur as starting reactants and that the stoichiometry and the addition of Mo or Mo_6Cl_{12} as reactants varied the total yield of the reaction and the secondary phases nature. These last ranged from $Cs_3Mo_2Cl_9$, Mo_6Cl_{12}, Cs_2MoCl_6, $Mo_3S_7Cl_{14}$ and MoS_2 and were all eliminated by a sulfuric acid extraction except for MoS_2. Consequently, the reaction of $Cs_2Mo_6Cl_{14}$ with sulfur (LEM154) was selected as it produced the least MoS_2. Even more, optimization works on the $Cs_2Mo_6Cl_{14}$ to sulfur ratio demonstrated that the clathrate formation is promoted with the increasing ratio until x = 5.7, which is the precise amount of sulfur $Cs_2Mo_6Cl_{14}$ needs to form $Cs_{2.32}Mo_{4.21}S_4Cl_{8.22}$. Future works should focus on the elimination of MoS_2 yielded by the reaction $Cs_2Mo_6Cl_{14}$ + 5.7 S.

5.2 Conception and structural characterization

This thesis sprouted from a collaboration between the Institut des Sciences Chimiques de Rennes (ISCR) in Rennes and the Laboratoire de CRistallographie et Science des MATériaux (CRISMAT) in Caen. Thanks to the complementary skills and expertise of the two laboratories, a broad range of knowhow and equipment were accessible, the syntheses and characterizations were rendered accordingly. During the first 18 months at ISCR, focus was set on synthesis and crystallography. Additionally, all of the sealed tube syntheses were realized there, as well as most of the X-ray Powder Diffraction (XRPD), XRPD in temperature, Differential Scanning Calorimetry (DSC) analysis and Hot Press sintering. The second half of the thesis was completed at CRISMAT, where the objectives were to characterize the electrical properties and microstructure of the materials. Therefore, alongside mechanical alloying (MA), Spark Plasma Sintering (SPS) and XRPD, a multitude of characterizations were accomplished such as: electrical resistivity measurement, thermal conductivity measurement, Hall effect, Scanning Electron Microscopy (SEM) and Transmission Electron Microscopy (TEM). Moreover, some collaborations granted to perform further characterization like Mössbauer spectroscopy and monocristal XRD with the Institut Jean Lamour. Most of all, along the term of this work multiple visits were made at the Institut Laue Langevin (ILL) neutron facility in Grenoble for Neutron Powder Diffraction (NPD) experiments on D1B and D2B beamlines. Finally, resonant scattering experiments on CRISTAL beamline at SOLEIL synchrotron facility were also realized.

5.2.1 Process

Both sealed tube and mechanical alloying were used for the generation of the samples. The next two subsections address some specificities and experimental conditions of the syntheses. Additionally, in this work Hot Pressing (HP) and Spark Plasma Sintering (SPS) were used for reactive and non-reactive sintering and to shape the powders into pellets. A study of the process impact on the microstructure and TE properties of germanite is presented in Chapter 2 (section 2.4).

5.2.1.1 Sealed tube synthesis

The synthesis most commonly used in solid state chemistry laboratories is sealed tube (ST) synthesis. Because of the low diffusion rate at solid state, ST synthesis requires a substantial amount of time at high temperature, making it optimal for the synthesis of thermodynamically stable compound. Also, the slow reaction time has proven to be an ally for the generation of monocristal. Moreover, ST synthesis is well suited for exploratory purposes in the academic context because of its simple implementation. On the other hand, the downsides of ST lie in the stoichiometry deviations, low reaction kinetic along with the difficulty to scale up. In the context of this work, the materials benefited of an improved homogeneity and faster reaction time because sulfur melt/vapor fostered the contact and diffusion of the elements (*e.g.* sulfur T_m ~ 388 K, T_{vap} ~ 717 K). However, the sulfur propensity to vaporize sometimes led to the formation of undesirable secondary phases and/or sulfur sub-stoichiometry compositions.

In a glove box, the commercial powders (Table 5.3) were weighed in a stoichiometric ratio with a precision of ± 2 mg, grinded together in a agate mortar and finally put into pellets of ~ 0.5 g each in a Φ = 5 mm die. To avoid any pollution or overpressure from water, the silica tubes were torch-dried before the insertion of the pellets. The silica tubes dimension depended on the powders nature and quantity to allow the smallest headspace possible to reduce sulfur loss, whilst not being a safety hazard. Finally, the tubes were sealed under secondary vacuum (~ 3×10^{-2} mbar) and put in a vertical cylindrical oven for thermal treatment. For germanite and germanite-derivate samples, the powders were heated at 2 K min^{-1} to 973 K for 24 h and then cooled to 773 K with oven inertia and finally cooled to RT by an air quench. Chapter 2 was partially dedicated to the optimization of those conditions (section 2.2). All of the precursors used for sealed tube synthesis in Rennes are summarized in the table below.

Table 5.3 Supplier, lot number and purity of the precursors used for ST synthesis.

Product	**Supplier**	**Lot #**	**Purity (%)**
Copper	Strem Chemicals	19702800	0.99
Iron	Aldrich	MKBX5426V	0.995
Germanium	Alfa Aesar	K27Z021	0.99999
Tin	Alfa Aesar	61000952	0.998
Sulfur	Acros Organic	A0376534	0.995

5.2.1.2 Mechanical alloying

Mechanical alloying is a solid-state powder processing technique involving repeated welding, fracturing, and rewelding of powder particles in a high-energy ball mill. Originally developed to produce nickel and iron based superalloys for applications in the aerospace industry, MA has proven to be an effective method to synthesize a variety of equilibrium and non-equilibrium alloy phases from blended elemental powders. Mechanical alloying main advantage for sulfur-containing compounds lies in its low reaction temperature (no heating). It prevents sulfur loss via vaporization, hence grants a better control of the stoichiometry compared to the synthesis by ST. Mechanical alloying gives poorly crystallized homogenous powder. The synthesis conditions have a substantial impact on microstructure as well as grain size and morphology. Mechanical collisions caused by the riotous movement of the balls induce crystallographic defaults such as dislocations, fallacious stacking, vacancies, etc... The promotion of structural defaults prompt to scatter phonons and/or charge carriers can either have a positive or a negative influence on the thermoelectric properties. Optimization of such microstructural features is achievable through the control of several parameters such as the balls diameter and number, the power weight to jar volume ratio and the milling velocity and time. Such optimization work for the germanite samples was done was done by Pavan Kumar *et al.*.[151]

In a glove box, the commercial powders were weighed in a stoichiometric ratio with a precision of ± 2 mg and ground together in an agate mortar. Two batches of 4 g each were prepared and put into two 45 mL tungsten carbide jars along with a total of 14 balls with a diameter of Φ = 10 mm, for a 13:1 ball-to-powder weight ratio. The jars were closed inside the glove box to trap argon inside

and then placed in a planetary mill (Pulverisette 7 Premium line, *Fritsch*). The milling lasted for 360 min at 600 rpm decomposed in 24 cycles of 15 min each with 1 min pause and a reverse of the milling direction. of the milling direction. Table 5.4 summarizes the precursor located in Caen used for the samples synthesized by mechanical alloying.

Table 5.4. Supplier, lot number and purity of the precursors used for the MA samples

Product	**Supplier**	**Lot #**	**Purity (%)**
Copper	Alfa Aesar	W10B046	99
Iron	Alfa Aesar	61600270	99.90
Germanium	Alfa Aesar	M16D098	100.00
Tin	Alfa Aesar	N09B011	99.85
Sulfur	Alfa Aesar	Y30B024	99.50

5.2.1.3 Hot Pressing sintering

In a HP furnace (Figure 5.3) heat and uniaxial pressure are simultaneously applied for the densification or reaction of a sample. An electrical resistance or an induction coil heats the sample. In any case, heat exchanges through air convection with a low speed and is non-homogeneous. The main difference with conventional furnace sintering is the addition of pressure. The latter allows the synthesis of materials at lower temperature, hence opening new synthesis route to a host of compounds that were inaccessible before in reason of their low stability at high temperature. In this work, the samples were densified using a VAS (*Vide et Appareils Scientifiques*) hot press with a graphite resistor furnace. During samples preparation, loose powders were placed in a graphite die (Φ = 10 mm) between two pistons of the same material. A graphite sheet is placed at the sample/die interface and the sample / pistons interface to smoothen the movement and avoid pollution issues. The experiences were realized under a primary vacuum, the heating and cooling rate were equal to 15 K min^{-1} and a holding time of 60 min at 873 K under 64 MPa applied at room temperature.

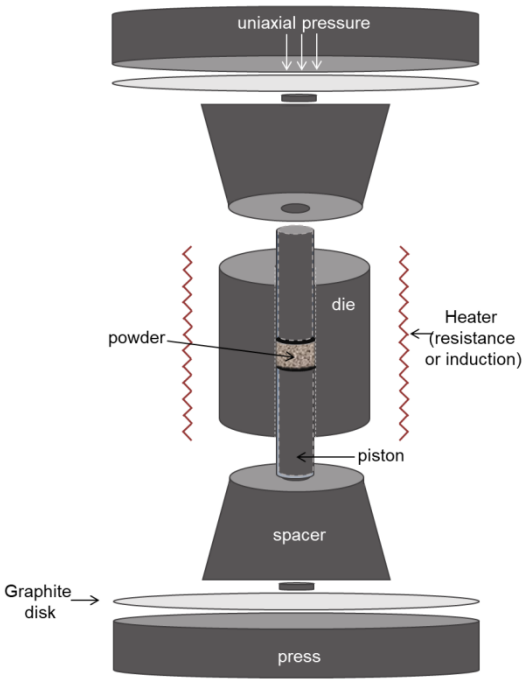

Figure 5.3 Schematic representation of a Hot Pressing furnace.

5.2.1.4 Spark Plasma Sintering

Like hot pressing, Spark Plasma Sintering is achieved under simultaneous application of uniaxial pressure and heating. However in this case the sample is heated by the passage of an electric current through it, giving a faster and better control of the temperature, a big gain over air convection heating. Finally, it is expected to gain control on sulfur stoichiometry over HP sintering because of the faster sintering time. The SPS system is a HP D 25/1 commercialized by FCT. During samples preparation, loose powders were put into a die (Φ = 10 mm) in the same manner as HP and sintered at 873 K under a uniaxial pressure of 150 MPa for the tungsten carbide die and 64 MPa for the graphite die with a heating rate of 50 K min^{-1} and cooling rate of 30 K min^{-1} and holding time of 30 minutes under vacuum. Again those conditions were optimized by Pavan Kumar *et al*..[151]

5.2.2 Diffraction

More than a century has passed since the discovery of ‘‘X-rays diffraction by crystals’’ by Max Von Laue (Physic Nobel Prize 1914), which can be regarded as a key experiment for both diffraction and experimental crystallography. Of course,

this breakthrough is only one of the milestones that lead diffraction to be used daily in research, either in form of single crystal diffraction or powder diffraction, either in laboratory environment or in large-scale research facilities such as synchrotrons and neutron sources. Finally, these fundamental and instrumental gains were strengthened up by Rietveld's computer assisted whole powder pattern fitting concept.

5.2.2.1 X-ray powder diffraction

Systematic X-ray diffraction measurements were performed on the samples to verify their purity and stability after treatments such as synthesis, sintering and electrical properties measurement. The outcome of a standard elastic diffraction experiment is the counts (*i.e.* intensity) of scattered particles over an angular range. Prior to measurements, the powders were finely grinded in an agate mortar and put on a sample holder within a suspension of cyclohexane. The data were collected over the angular 2θ range 5 – 80° with a step size of 0.019699° and a step time of 7 s. A long collection time was necessary to observe the superstructure peaks. A total of five diffractometers were used depending on my location and/or the nature of measurement. The first two diffractometers belong to CSM in Rennes and the last three belong to CRISMAT in Caen.

- A two-circle diffractometer D8 Advance (*Bruker*) equipped with a copper anticathode ($K\alpha_1$ = 1.5406 Å) and a silicium band LynxEye detector. The $K\alpha_2$ and $K\beta$ radiation are filtered out by a Ge[111] monochromator. The geometry configuration of the diffractometer is Debye-Scherrer.

-A two-circle diffractometer D8 Advance (*Bruker*) equipped with a molybdenum anticathode ($K\alpha_1$= 0.709300 Å and $K\alpha_2$= 0.713590Å) and a silicium band LynxEye High energy detector. The $K\beta$ radiation is eliminated by a goebel mirror. The diffractometer geometry configuration is Debye-Scherrer.

- A two-circle diffractometer X'PERT Pro MPD PANalytical (*Phillips*) equipped with a cobalt anticathode ($K\alpha_1$ = 1.7890 Å and $K\alpha_2$ = 1.7929 Å) and an X'Celerator detector. It is also equipped with an iron filter to eliminate $K\beta$ cobalt radiation. The diffractometer geometry configuration is Bragg-Brentano θ-2θ.

- A two-circle diffractometer X'PERT Pro MPD PANalytical (*Phillips*) equipped with a copper anticathode ($K\alpha_1$ = 1.5406 Å and $K\alpha_2$ = 1.5444 Å) and a PIXcel^{3D} detector. It is also equipped of a nickel filter to eliminate $K\beta$ copper radiation. The diffractometer geometry configuration is Bragg-Brentano θ-2θ.

- A two-circle diffractometer D8 Advance Vario1 (*Bruker*) equipped with a copper anticathode ($K\alpha_1$ = 1.5406 Å) and a silicium band LynxEye detector. The $K\alpha_2$ and $K\beta$ radiation are filtered out by a Ge[111] monochromator. The diffractometer geometry configuration is Debye-Scherrer.

5.2.2.2 X-Ray Powder Diffraction with synchrotron radiation

The experiments were carried out on CRISTAL beamline at SOLEIL light source facility, Saclay, France. CRISTAL is a high-performance undulator-based beamline providing techniques such as coherent diffraction, time-resolved diffraction, high angular and high spatial resolution diffraction and anomalous scattering. For the high energy elastic XRPD measurements, the data were acquired at 21 keV (possibility to tune from 4 to 30 keV) in order to have a high statistic while limiting fluorescence, microabsorption or anomalous effects. All powders were sieved with 100 μm cloth sieves prior to fill the borosilicate capillaries ($\Phi_{external}$ = 0.3 mm). The acquisitions were performed on a two-circles diffractometer positioned at the end of the beamline, well adapted for high resolution experiments on capillaries. Two detectors were used in parallel: twenty-one Si[111] crystal analyzers designed and built by *Laboratoire de Physique des Solides* (Orsay) and SOLEIL for optimal resolution and nine MYTHEN 1D-strip detector sold by *Dectris* for higher statistics.

5.2.2.3 Neutron Powder Diffraction

NPD data were collected at the Institut Laue Langevin (ILL, Grenoble, France) neutron facility on D1B and D2B beamlines. The D1B beamline is a high intensity two-axis powder diffractometer equipped with different environments set up such as a cryostat for magnetic measurements and a vanadium furnace for *in situ* measurements. The neutron beam is tunable at two wavelengths: λ = 2.52 Å with a pyrolytic graphite [002] monochromator and λ = 1.28 Å with a Ge[311] monochromator. While λ = 2.52 Å has a higher flux (20×), in some cases the λ = 1.28 Å was used in order to perceive more peaks in the 2θ interval (Figure 5.4). The ^{3}He multi detector contains 1280 cells covering a 128° angular range in a Debye-Scherrer geometry.

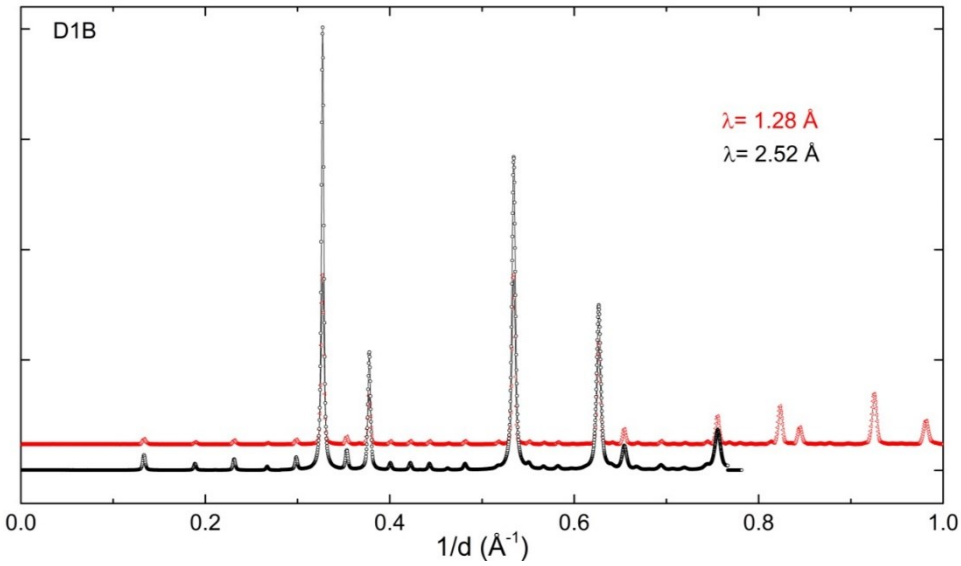

Figure 5.4 $Cu_{22}Fe_8Ge_4S_{32}$ pattern simulation for λ = 1.28 Å and λ = 2.52 Å.

The D2B beamline is a high-resolution two-axis diffractometer in Debye-Scherrer geometry. The term ‘‘high-resolution’’ does not refer to a smaller peak width in the powder diffraction pattern, but to the instrumental resolution function giving narrow peaks at high scattering angle. A complete diffraction pattern is obtained after 25 steps of 0.05° in 2θ, since the 128 ^{3}He detectors are spaced at 1.25° intervals. Such scans take typically 30 min and are repeated to improve statistics. From the many available wavelengths, λ = 1.594 Å with a Ge[335] monochromator was used.

5.2.2.4 X-Ray Single crystal Diffraction

The single crystal data were acquired on specimens found in powders produced by sealed tube synthesis by Pr. Malaman from the Institut Jean Lamour of Nancy. The data acquisitions were performed at 300 K using a Bruker APEX-II diffractometer equipped with CCD detector using Mo *Kα* radiation (λ = 0.71073 Å). Cell refinement and data reduction were carried out with the APEX2 Software.[214] The conditions of data collection and structure refinements are gathered in Table 5.5.

Table 5.5. Summary of single-crystal data collection and structure refinement conditions of different ST germanite sample.

Structural formula	**$Cu_{22}Fe_8Ge_4S_{32}$**	**$Cu_{22}Fe_8Ge_2Sn_2S_{32}$**	**$Cu_{22}Fe_8Sn_4S_{32}$**
Space group	$P\bar{4}3n$	$P\bar{4}3n$	$P\bar{4}3n$
Temperature (K)	293(2)	293(2)	293(2)
Formula weight	3160.96	2428.03	3345.36
Wavelength (Å)	0.71073	0.71073	0.71073
Crystal system	cubic	cubic	cubic
a (Å)	10.604(5)	10.668(4)	10.7217(19)
b (Å)	10.604(5)	10.668(4)	10.7217(19)
c (Å)	10.604(5)	10.668(4)	10.7217(19)
V (Å^3)	1192.4(17)	1214.0(15)	1232.5(7)
Z	1	1	1
Calculated density (g.cm^{-3})	4.402	4.450	4.507
Absorption coefficient (mm^{-1})	15.802	15.312	14.876
F(000)	1486	1522	1558
Crystal size (mm)	0.020 × 0.020 × 0.020	0.020 × 0.020 × 0.020	0.020 × 0.020 × 0.020
Crystal color	grey	grey	grey
Theta range (°)	2.716 - 24.913	2.700 - 36.577	2.687 - 24.952
Data collected	-11 ≤ *h* ≤ 12	-17 ≤ *h* ≤ 5	-11 ≤ *h* ≤ 12
	-10 ≤ *k* ≤ 9	-11 ≤ *k* ≤ 14	-12 ≤ *k* ≤ 1
	-7 ≤ *l* ≤ 12	-17 ≤ *l* ≤ 3	-12 ≤ *l* ≤ 10
R_{int}	0.0415	0.0553	0.0279
Reflections collected	2963	5573	3517
Reflections unique [I > 2σ]	356	1003	372
Completeness	1.000	1.000	1.000
Data/restraints/ parameters	356/0/26	1003/0/26	372/0/31

5.2.2.5 Pattern fitting

Hugo Rietveld revolutionized powder diffraction by providing a mathematical tool to separate overlapping data, thereby allowing an accurate determination of the structure. The latter is illustrated in Figure 5.5 where a broad peak is deconvoluated into three peaks belonging to two different phases. He also realized that with the emerging computer calculus capacity, it would be possible to obtain more realistic structural model by correcting some instrumental parameters. The method has been so successful that nowadays crystal structures are routinely being determined from powder diffraction.

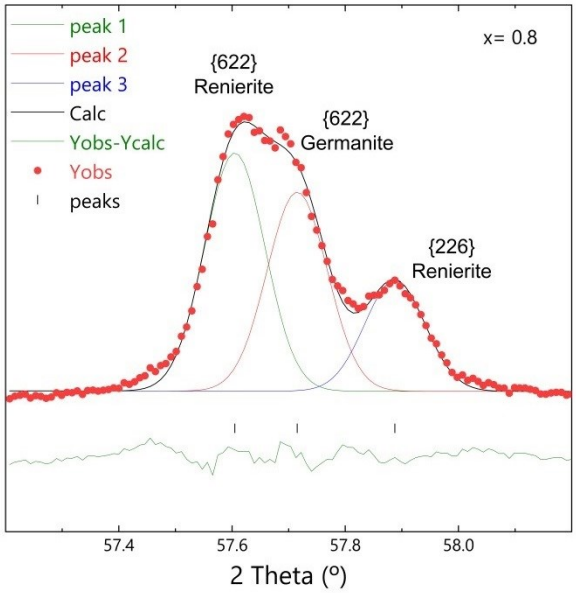

Figure 5.5. Deconvolution of overlapping peaks of a XRP diffractogram containing two related phases.

FullProf[215] software was used for all the pattern fitting works in this thesis for many reasons. First of all, it is free and the developers are actively improving the software (update available semi-annually). Second, it is possible to do pattern simulation, profile matching, multipattern and sequential refinement on XRPD and NPD (TOF and magnetic structures) among other things. Third, there are many implemented applications like WinPlotr[216] to plot powder diffraction patterns, FPstudio and Vesta to visualize crystal structures, BondStr for distances,

angles and bond-valences calculation, etc... Finally, the user has a deep control of the refined parameters.

Rietveld method principle is to minimize a least-squares function *M* which verifies the difference between a calculated profile *y(calc)* and observed data *y(obs)* such as:

$$M = \sum_i W_i \left\{ y_i^{obs} - \frac{1}{c} y_i^{calc} \right\}^2 \qquad \textit{Equation 5-1}$$

Where W_i is the statistical weight and c is an overall scale factor such that $y_i^{calc} = c\, y_i^{obs}$. Moreover, Rietveld needs a structural model to generate the intensities (Jbt = 0) from the structure factor such as:

$$\mathrm{I_h} = \{\mathrm{LAPCF^2}\}_\mathrm{h} \qquad \textit{Equation 5-2}$$

Where L contains the Lorentz multiplicity and polarization factors, A is the absorption correction, P is the preferred orientation function, C includes special corrections (non linearity, efficiencies, special absorption corrections, extinction, etc.) and F^2 is the square of the structure factor.

Le Bail refinement [217] also called profile matching fits the reflection permitted by the space group with proper shape parameters and constant scale factor (Jbt = 2). In this mode, the scale factor is fixed and the integrated intensities are individually refined using Rietveld formula iteratively. Prior to the refinement, an *hkl* file (containing the intensities) must be generated (Irf = 0) by running a couple of cycle with 0 refined parameters. Additionally since FullProf cannot calculate theoretical line intensities, all *hkl* values permitted by the space group are considered and included in the refinement (which sometimes means a lot of reflections). While using this type of refinement it is important to keep in mind that the starting cell parameters and resolution function determine to a large extent the intensity parameters. To conclude, profile matching is a convenient tool when there are no suitable structural models or when the starting point of a congruent Rietveld refinement is too far (a distant starting model leads to divergences in the early stage of refinement hence giving false minima).

The profile function approximation used is this work was mostly the pseudo-voight approximation (Npr = 5), a linear combination of a Lorentzian (L') and Gaussian (G') distribution (Equation 1-5) with shared FWHM (H) parameters. The latter are calculated from (Equation 1-6).

$$pV(x) = \eta L'(x) + (1-\eta)G'(x) \qquad \textit{Equation 5-3}$$

$$H^2 = (U + D_{ST}^2)\tan^2\theta + V\tan\theta + W + \frac{I_G}{\cos^2\theta} \qquad \textit{Equation 5-4}$$

Where η is the peak shape comprised between 0 and 1, U, V, W, are shape parameters, D_{ST} a microstrain coefficient and I_G an isotropic size parameter of Gaussian character.

The concordance between the observed and calculated profiles can be measured by a series of conventional factors such as: reduced chi square(χ^2), goodness of fit indicator (S), Bragg R-factor (R_{Bragg}) and crystallographic factor (R_F). Two indice sets are calculated in FullProf with different meaning of the integer n. In the first set (R_p, R_{wp}), n is the total number of refined points (total number of points in the pattern minus the total number of points excluded). In the second set (R_{exp}), n is the number of points included in Bragg peaks.

Profile Factor

$$R_p = 100\frac{\sum_{i=1,n}|y_i - y_{c,i}|}{\sum_{i=1,n} y_i} \qquad \textit{Equation 5-5}$$

Weighted Profile Factor

$$R_{wp} = 100\left[\frac{\sum_{i=1,n} w_i|y_i - y_{c,i}|^2}{\sum_{i=1,n} w_i {y_i}^2}\right]^{1/2} \qquad \text{Equation 5-6}$$

Expected Weighted Profile Factor

$$R_{exp} = 100\left[\frac{n-p}{\sum_i w_i {y_i}^2}\right]^{1/2} \qquad \textit{Equation 5-7}$$

Reduced Chi²

$$\chi^2 = \left[\frac{R_{wp}}{R_{exp}}\right]^2 \qquad \textit{Equation 5-8}$$

Where y_i is the collected data, y_{ic} the calculated data, w_i the weight, (n-p) the number of degrees of freedom and p the number of refined parameters. All equations appearing in this subsection come from Fullprof user guide.

5.2.3 Spectroscopy

Spectroscopy is the study of the interaction of electromagnetic radiation with molecules, compounds, atoms or the nucleus. The spectroscopy type therefore depends on the electromagnetic radiation (γ-rays, UV, IR) and the nature of its interactions with matter (absorption, emission, resonance, etc...). The experimental conditions of the Mössbauer spectroscopy and resonant scattering measurements are detailed in the following subsections.

5.2.3.1 Mössbauer

All measures and interpretations were done by Pr. Bernard Malaman at IJL and by Pr. Gérard Le Caër at IPR. Mössbauer spectra were fitted with a least-squares method program assuming Lorentzian peaks.

^{57}Fe Mössbauer spectra were measured at T = 300 K in transmission geometry with a spectrometer operated in the conventional constant-acceleration mode. Polycrystalline absorbers, with natural abundance of ^{57}Fe and thickness of 5 mg cm^{-2}, were used. Sources were kept at RT to collect ^{57}Fe Mössbauer spectra. The source was ^{57}Co in Rh matrix with a nominal strength of 25 mCi. Velocity calibration was performed against a 12 μm thick α-Fe foil at RT. ^{57}Fe isomer shifts (δ) are referred to α-Fe at RT.

^{119}Sn Mössbauer measurements were carried out using a 1024-channel constant-acceleration spectrometer in standard transmission geometry. A polycrystalline absorber with natural abundance of ^{119}Sn isotope and a thickness of ~10 mg cm^{-2} was used. The spectra were recorded at 300 K and 15 K using a liquid helium cryostat (JANIS). The source, kept at room temperature, was $Ba^{119}SnO_3$ with a nominal strength of 10 mCi. A palladium foil of 0.5 mm thickness was used as a critical absorbed for tin X-rays. Velocity calibration was performed against a 12 μm thick α-Fe foil at RT. ^{119}Sn isomer shift (IS or δ) is referred to $BaSnO_3$ at RT. ^{119}Sn Mössbauer uses the 23.87 keV level which is populated by the decay of 245 day.

5.2.3.2 Resonant scattering

The resonant scattering experiments were performed on CRISTAL beamline at SOLEIL light source facility. The diffractograms were acquired on ST germanite $Cu_{22}Fe_8Ge_4S_{32}$ powders in capillaries. All powders were sieved with 100 μm cloth sieves prior to fill the ($\Phi_{external}$ = 0.3 mm) borosilicate capillaries. The acquisitions were performed on a two-circles diffractometer positioned at the end of the beamline, well adapted for high resolution experiments on capillaries. The patterns were collected by nine MYTHEN 1D-strip detector mounted on a goniometer head, over the angular range 0 - 115° in 2θ with a step size of 0.003998°. The calibrated energy and resonant factors f^{II} were obtained from an X-ray absorption spectra of the germanite sample. Then, the f^{I} were calculated by a Kramers-Kronig relation. The collection energies have been chosen from such calculation. The nominal and calibrated incident beam energies, wavelength of the calibrated energies and the resonant factors are summarized in Table 5.6 to Table 5.8.

Table 5.6. Nominal and calibrated incident beam energies, wavelength of the calibrated energies and the resonant factors f^{I} and f^{II} of Fe (K-edge highlighted).

Nominal energy (eV)	Calibrated energy (eV)	λ (Å)	f^{I}	f^{II}
7000	7040	1.7611	-4.028939	0.561076
7070	7110	1.7438	-6.752462	0.661836
7072	7112	1.7433	-7.175967	1.026116
7076	7116	1.7423	-9.509273	1.411211
7080	7120	1.7414	-7.406057	3.331952

Table 5.7. Nominal and calibrated incident beam energies, wavelength of the calibrated energies and the resonant factors f^{I} and f^{II} of Cu (K-edge highlighted).

Nominal energy (eV)	Calibrated energy (eV)	λ (Å)	f^{I}	f^{II}
8 910	8 939	1.3870	-5.1176	0.480775
8 946	8 975	1.3814	-6.9340	0.585357
8 953	8 982	1.3804	-8.2818	1.165950
8 956	8 985	1.3799	-8.9642	2.557440

Table 5.8. Nominal and calibrated incident beam energies, wavelength of the calibrated energies and the resonant factors f^{I} and f^{II} of Ge (K-edge highlighted).

Nominal energy (eV)	Calibrated energy (eV)	λ (Å)	f^{I}	f^{II}
11 060	11 063	1.1207	-5.4130	0.516559
11 096	11 099	1.1171	-8.1986	0.810940
11 102	11 105	1.1165	-11.7572	3.499780
11 104	11 107	1.1163	-9.1899	7.702930

5.2.4 Electronic Microscopy

Electron Microscopes use a beam of highly energetic electrons as illumination source to probe objects on a very fine scale. As the wavelength of an electron can be up to 100 000 times shorter than that of visible light photons, electron microscopes have a higher resolving power than light microscopes and can reveal the structure of smaller objects. It yields information on the topography (fractures, porosities), morphology (shape and size of the particles), chemical composition and crystallographic information. The main electronic microscopic techniques are scanning electron microscopy (SEM) and transmission electronic microscopy (TEM). The next two subsections are dedicated to the description of

the experimental conditions used for SEM microscopy and TEM microscopy respectively.

5.2.4.1 Scanning Electron Microscopy

In this type of microscopy the surface is scanned with a focused beam of electrons. The electrons interact with atoms in the sample, producing various signals that contain information about the surface topography and composition of the sample. The SEM observations were performed on fractured cross-section of densified pellets using a ZEISS Supra 55 field emission scanning electron microscope. Fractured cross-section of densified pellets were performed using a ZEISS Supra 55 field emission scanning electron microscope.

5.2.4.2 Transmission Electron Microscopy

TEM is a microscopy technique in which a beam of electrons is transmitted through a specimen to form an image. The specimen is most often an ultrathin section less than 100 nm thick or a suspension on a grid. An image is formed from the interaction of the electrons with the sample as the beam is transmitted through the specimen. TEM analyses including electron diffraction (ED) and high angle annular dark field scanning TEM (HAADF-STEM) studies were performed by using a JEM200F cold FEG image and probe aberration microscope operated at 200 kV, equipped with CENTURIO EDX detector and Quantum GIF. The TEM samples were prepared by crushed powder in agate mortar, suspended in n-butanol and then deposited on a Ni holey carbon grid.

5.2.5 Thermal and electrical properties

Thermal measurements were performed to characterize the samples thermoelectric performance and stability. To do so the Seebeck coefficient, the electrical resistivity, the thermal conductivity, the charge carrier's concentration and the magnetic properties were measured as a function of temperature. Additionally, differential scanning calorimetry (DSC) was used to monitor phase transitions.

After the sintering process, the graphite sheet was removed from the pellets with a manual polishing machine. After, the pellets are cut to give two bars (~ 3 × 3 × 8 mm^3) for electrical resistivity and Seebeck measurements, two squares (~ 6 × 6 × 1 mm^3) for thermal diffusivity and one square for Hall Effect measurements (~ 3 × 3 × 0.5 mm^3). The cuttings are rendered with a precision chain saw Secotom-50 provided by *Struers*. All characterizations were measured perpendicular to the force applied during the sintering process. The considered relative uncertainties of the measures are: 6.0 % for Seebeck coefficient, 8.0 % for electrical resistivity, 11.2 % for the power factor, 11 % for thermal conductivity and 16 % for the overall figure of merit.

5.2.5.1 Electrical resistivity and Seebeck coefficient

The temperature dependent electrical resistivity (ρ) and Seebeck (S) coefficient were measured on a ZEM-3 *Ulvac Riko* system under vacuum to prevent oxidization and a partial pressure of helium (10 kPa) to ease the stabilization of the temperature gradient. The properties are measured on (~ 3 × 3 × 8 mm^3) bars between RT and 673 K (possibility to go up to 1073 K).

The electrical resistivity is determined by a four point measurement. Once the set point is stabilized, an electric current is applied between the two nickel electrodes. Then, the electric potential differential is measured between the two thermocouples. Finally, the electrical resistivity is calculated from Ohm's law (Equation 5-9) with (R) the material resistance, (a) the contact area and (l) the distance between the thermocouples.

$$\rho = R\frac{a}{l} \qquad \textit{Equation 5-9}$$

To estimate the Seebeck coefficient as a function of temperature, a heater is placed below the bottom electrode to set up a temperature gradient (ΔT) in the sample. The two thermocouples measure both the potential (ΔV) and the temperature differentials. Once the set point stabilized, the electrical potential is measured for three temperature gradients (ΔT = 20 K, 30 K, 40 K). The Seebeck coefficient is determined from the slope of these three points.

5.2.5.2 Thermal Conductivity

A *Netzsch* 457 microflash laser flash system was used to assess the thermal diffusivity under dynamic N_2 flow. The latter is equipped with a laser (λ = 1064 nm) and an infrared InSb detector cooled by liquid nitrogen. The measures are done in an airtight furnace under a nitrogen atmosphere between 300 K and 700 K with 50 K increment on a 6 × 6 mm^2 and 1 mm thick sample.

Following the sample irradiation by a short laser impulsion (< 1 ms), the heat propagate through the sample until homogenization. Then the sample cools down to the set point. The temperature evolution is monitored by the mean of an infrared detector outside of the furnace. Thus, the half-life time ($t_{1/2}$) required to attain half of the maximal temperature is measured. The diffusivity is calculated from Equation 5-10.

$$D = \frac{1.37x^2}{\pi^2 t_{1/2}} \qquad \textit{Equation 5-10}$$

Where D is thermal diffusivity ($m^2\ s^{-1}$), x is sample thickness (m) and $t_{1/2}$ is half-life time (s). Additionally, for a better estimation each temperature is measured three times.

Thermal conductivity κ was calculated (Equation 5-11) from the product of thermal diffusivity (D), density (d) and heat capacity (C_p) using Dulong-Petit approximation (Equation 5-12). The density was obtained using the mass and volume of the sintered pellets.

$$\kappa = \mathrm{D}\ C_p\ d \qquad \textit{Equation 5-11}$$

$$C_p = \frac{3nN_a k_B}{M} \qquad \textit{Equation 5-12}$$

Where, κ is the thermal conductivity (W m^{-1} K^{-1}), d is the density (kg m^{-3}), C_p is the specific heat (J kg^{-1} K^{-1}), n is the number of atoms in chemical formula, N_a is Avogadro number (6.022×10^{23} mol^{-1}), k_B is Boltzmann constant (1.381×10^{-23} kg m^2 s^{-2} K^{-1}) and M is the molar weight (kg mol^{-1}).

5.2.5.3 Charge carrier concentration measurements

The charge carrier concentration by Hall measurements were done using the van der Pauw method in a PPMS (Physical Properties Measurements System) commercialized by *Quantum Design*. A fluctuating magnetic field of -7 T - 7 T was applied during the hall measurements to verify the accuracy of the data. The properties were acquired between 5 K and 300 K. The square sample (~ 3 × 3 × 0.5 mm^3) was linked to the system by 4 copper wires connected to the corners by an indium welding. The charge carrier concentration is calculated from Equation 5-13 and the carrier mobility from Equation 5-14.

$$n_H = \frac{1}{eR_H} \qquad \textit{Equation 5-13}$$

$$\mu_H = \frac{1}{\rho\ e\ n_H} \qquad \textit{Equation 5-14}$$

Where n_H is the charge carrier concentration (m^{-3}), e is the elemental charge (1.602×10^{-19} C), R_H is the Hall constant (m^3 C^{-1}) and μ_H is the charge carrier mobility (m^2 V^{-1} s^{-1}).

5.2.5.4 Magnetic measurements

Round-shaped samples with a mass of ~ 30 mg were prepared from the SPS pellets. The magnetization (M) was measured as a function of temperature and magnetic field using a MPMS 5S Superconducting Quantum Interference Device (SQUID, *Quantum Design*, USA). Zero-field-cooled (ZFC) and field-cooled (FC) susceptibilities were measured subsequently in settle mode, applying a constant magnetic field of 0.1 T. Measurements were performed between 2 K – 300 K. The magnetic susceptibility (χ) was calculated as follows:

$$\chi = \frac{\mu M}{m H} \qquad \textit{Equation 5-15}$$

Where μ, M, m and H correspond to the measured magnetic moment, molar mass, sample mass and magnetic field, respectively.

5.2.5.5 Differential Scanning Calorimetry

Differential scanning calorimetry is a technique in which the heat flux (power) of the sample is monitored against time or temperature. A single heater is used in the heat-flux DSC to increase the temperature of both the sample and the empty reference. The difference in heat flux between the sample and an empty reference is monitored, small temperature differences due to exothermic or endothermic effects in the sample are recorded as a function of the programmed temperature.

A DSC 404 F3 Pegasus by *Netzsch* (maximal T = 1873 K) was used to scan materials domain of stability. To reflect ST reaction conditions, around 30 mg of sample were put in a small flat bottomed sealed tube (maximum height ~ 3 cm, $\Phi_{external}$ = 6 mm) as shown in Figure 5.6. An empty sealed tube of comparable dimensions and weight is used as reference. Typically, the samples were measured for two cycles in a row. The furnace is under a continuous flow of nitrogen as it heat up from RT to 1273 K at a 2 K min^{-1} rate.

Figure 5.6. Flat bottomed vial to reproduce sealed tube conditions-like during DSC measurements.

Bibliography

[1] OECD and IEA (2016) World Energy Outlook 2016. .

[2] Rowe, D.M. (1999) Thermoelectrics, an environmentally-friendly source of electrical power. *Renewable Energy*. 16 (1–4), 1251–1256.

[3] Slack, G.A. and Rowe, D.M. (1995) New Materials and Performance Limits for Thermoelectric Cooling. in: CRC Handb. Thermoelectr., pp. 407–440.

[4] Bell, L.E. (2008) Cooling, heating, generating power, and recovering waste heat with thermoelectric systems. *Science*. 321 (5895), 1457–1461.

[5] Bourgès, C., Gilmas, M., Lemoine, P., Mordvinova, N.E., Lebedev, O.I., Hug, E., Nassif, V., Malaman, B., Daou, R., and Guilmeau, E. (2016) Structural analysis and thermoelectric properties of mechanically alloyed colusites. *J. Mater. Chem. C*. 4 (4), 7455–7463.

[6] Suekuni, K., Tsuruta, K., Ariga, T., and Koyano, M. (2012) Thermoelectric Properties of Mineral Tetrahedrites $Cu_{10}Tr_2Sb_4S_{13}$ with Low Thermal Conductivity. *Applied Physics Express*. 5 (5), 051201.

[7] (n.d.) UN Environment Annual Report 2018.

[8] IPCC (2013) Climate Change 2013 The Physical Change Basis. *Climate Change 2013: The Physical Science Basis. Contribution of Working Group I to the Fifth Assessment Report of the Intergovernmental Panel on Climate Change*.

[9] Kosaka, Y. and Xie, S.P. (2013) Recent global-warming hiatus tied to equatorial Pacific surface cooling. *Nature*. 501 (7467), 403.

[10] England, M.H., Mcgregor, S., Spence, P., Meehl, G.A., Timmermann, A., Cai, W., Gupta, A. Sen, Mcphaden, M.J., Purich, A., and Santoso, A. (2014) Recent intensification of wind-driven circulation in the Pacific and the ongoing warming hiatus. *Nature Climate Change*. 4 (3), 222.

[11] Earth Science Communications Team (2018) Climate Change: Vital Signs of the Planet: Sea Level. *Nasa*.

[12] (n.d.) When Sea Levels Attack! | Visual.ly.

[13] Edenhofer, O., Madruga, R.P., Sokona, Y., Seyboth, K., Matschoss, P., Kadner, S., Zwickel, T., Eickemeier, P., Hansen, G., Schlömer, S., and von Stechow, C.

(2011) Renewable energy sources and climate change mitigation: Special report of the intergovernmental panel on climate change. Cambridge University Press, .

[14] Lu, Y., Nakicenovic, N., Visbeck, M., and Stevance, A.-S. (2015) Policy: Five priorities for the UN Sustainable Development Goals. *Nature News*. 520 (7548), 432.

[15] Abbasi, T., Premalatha, M., and Abbasi, S.A. (2011) The return to renewables: Will it help in global warming control? *Renewable and Sustainable Energy Reviews*. 15 (1), 891.

[16] Seebeck, T.J. (1826) Ueber die magnetische Polarisation der Metalle und Erze durch Temperaturdifferenz. *Annalen Der Physik*. 82 (3), 253–286.

[17] Ørsted, H.C. (1823) An electromagnetic experiment. *Annales de Chimie et de Physique*. 22 201–203.

[18] Park, R., Carroll, R., Burns, G., Desmaris, R., Hall, F., Herzkovitz, M., MacKenzie, D., McGuire, E., Reed, R., Sparks, L., and Wang, T. (1974) Manual on the Use of Thermocouples in Temperature Measurement. fourth edi ASTM International, .

[19] Peltier, J.C.A. (1834) Nouvelles Experiences sur la Caloricite des Courans Electriques. *Annales de Chimie et de Physique, LVI*. 56 371–387.

[20] Thomson, W. (1857) On a Mechanical Theory of Thermo-Electric Currents. *Proceedings of the Royal Society of Edinburgh*. 3 91–98.

[21] Ioffe, A.F., Stilbans, L.S., Iordanishvili, E.K., Stavitskaya, T.S., and Gelbtuch, A. (1959) Semiconductor thermoelements and thermoelectric Cooling. *Physics Today*. 12 (5), 42.

[22] Vedernikov, M.V. and Iordanishvili, E.K. (1998) A.F. Ioffe and origin of modern semiconductor thermoelectric energy conversion. in: .

[23] Nolas, G.S., Sharp, J., and Goldsmid, J. (2013) Thermoelectrics: basic principles and new materials developments. .

[24] Zhang, X. and Zhao, L.D. (2015) Thermoelectric materials: Energy conversion between heat and electricity. *Journal of Materiomics*. 1 (2), 92–105.

[25] Ioffe, A.F. (1960) Physics of semiconductors. *Infosearch*.

[26] Franz, R. and Wiedemann, G. (1853) Ueber die Wärme Leitungsfähigkeit der

Metalle. *Annalen Der Physik*. 165 (8), 457–531.

[27] Shi, X., Chen, L., and Uher, C. (2016) Recent advances in high-performance bulk thermoelectric materials. *International Materials Reviews*. 61 (6), 379–415.

[28] Kim, H.-S.S., Gibbs, Z.M., Tang, Y., Wang, H., and Snyder, G.J. (2015) Characterization of Lorenz number with Seebeck coefficient measurement. *APL Materials*. 3 (4), 041506.

[29] Ravich, Y.I., Efimova, B.A., and Smirnov, I.A. (1970) Semiconducting Lead Chalcogenides. *Plenum Press*. 299 (25), 181.

[30] Wang, H., Pei, Y., LaLonde, A.D., and Jeffrey Snyder, G. (2013) Material Design Considerations Based on Thermoelectric Quality Factor. in: Thermoelectr. Nanomater., pp. 3–32.

[31] Sootsman, J.R., Chung, D.Y., and Kanatzidis, M.G. (2009) New and Old Concepts in Thermoelectric Materials. *Angewandte Chemie International Edition*. 48 (46), 8616–8639.

[32] Mehdizadeh Dehkordi, A., Zebarjadi, M., He, J., and Tritt, T.M. (2015) Thermoelectric power factor: Enhancement mechanisms and strategies for higher performance thermoelectric materials. *Materials Science and Engineering R: Reports*. 97 1–22.

[33] Tan, G., Zhao, L.-D.D., and Kanatzidis, M.G. (2016) Rationally Designing High-Performance Bulk Thermoelectric Materials. *Chemical Reviews*. 116 (19), 12123–12149.

[34] Zeier, W.G., Zevalkink, A., Gibbs, Z.M., Hautier, G., Kanatzidis, M.G., and Snyder, G.J. (2016) Thinking Like a Chemist: Intuition in Thermoelectric Materials. *Angewandte Chemie - International Edition*. 55 (24), 6826–6841.

[35] Polozine, A., Sirotinskaya, S., and Schaeffer, L. (2014) History of development of thermoelectric materials for electric power generation and criteria of their quality. *Materials Research*. 17 (5), 1260–1267.

[36] Snyder, G.J. and Toberer, E.S. (2008) Complex thermoelectric materials. *Nature Materials*. 7 105–114.

[37] Heremans, J.P., Jovovic, V., Toberer, E.S., Saramat, A., Kurosaki, K., Charoenphakdee, A., Yamanaka, S., and Snyder, G.J. (2008) Enhancement of

thermoelectric efficiency in PbTe by distortion of the electronic density of states. *Science*. 321 (5888), 554–557.

[38] Zhao, L.D., Wu, H.J., Hao, S.Q., Wu, C.I., Zhou, X.Y., Biswas, K., He, J.Q., Hogan, T.P., Uher, C., Wolverton, C., Dravid, V.P., and Kanatzidis, M.G. (2013) All-scale hierarchical thermoelectrics: MgTe in PbTe facilitates valence band convergence and suppresses bipolar thermal transport for high performance. *Energy and Environmental Science*. 6 (11), 3346–3355.

[39] Herve, E. and Zaoui, A. (1990) Modelling the effective behavior of nonlinear matrix-inclusion composites. *European Journal of Mechanics, A/Solids*. 9 (6), 505–515.

[40] Wright, D.A. (1958) Thermoelectric Properties of Bismuth Telluride and its Alloys. *Nature*. 181 (4612), 834–834.

[41] DiSalvo, F.J. (1999) Thermoelectric Cooling and Power Generation. *Science*. 285 (5428), 703.

[42] Candolfi, C., Gougeon, P., Gall, P., Potel, M., Dauscher, A., and Lenoir, B. (2019) Thermoelectric Properties of Ternary and Quaternary Mo_6 and Mo_9 Cluster Selenides. in: .

[43] Alleno, E., Bérardan, D., Godart, C., Puyet, M., Lenoir, B., Lackner, R., Bauer, E., Girard, L., and Ravot, D. (2006) Double filling in skutterudites: A promising path to improved thermoelectric properties. *Physica B: Condensed Matter*.

[44] Chen, G., Dresselhaus, M.S., Dresselhaus, G., Fleurial, J.-P., and Caillat, T. (2003) Recent developments in bulk thermoelectric materials. *Int. Mater. Rev.* 48 (1), 45–66.

[45] Riffat, S.B. and Ma, X. (2003) Thermoelectrics: A review of present and potential applications. *Applied Thermal Engineering*. 23 (8), 913–935.

[46] Minnich, A.J., Dresselhaus, M.S., Ren, Z.F., and Chen, G. (2009) Bulk nanostructured thermoelectric materials: current research and future prospects. *Energy & Environmental Science*. 2 (5), 466.

[47] Vineis, C.J., Shakouri, A., Majumdar, A., and Kanatzidis, M.G. (2010) Nanostructured Thermoelectrics: Big Efficiency Gains from Small Features. *Advanced Materials*. 22 (36), 3970–3980.

[48] Seifert, U. (2012) Stochastic thermodynamics, fluctuation theorems and molecular machines. *Reports on Progress in Physics*. 75 (12), 126001.

[49] Zebarjadi, M., Esfarjani, K., Dresselhaus, M.S., Ren, Z.F., and Chen, G. (2012) Perspectives on thermoelectrics: from fundamentals to device applications. *Energy Environ. Sci.* 5 (1), 5147–5162.

[50] Zeng, W., Shu, L., Li, Q., Chen, S., Wang, F., and Tao, X.-M. (2014) Fiber-Based Wearable Electronics: A Review of Materials, Fabrication, Devices, and Applications. *Advanced Materials*. 26 (31), 5310–5336.

[51] Yin, Y., Tudu, B., and Tiwari, A. (2017) Recent advances in oxide thermoelectric materials and modules. *Vacuum*. 146 356–374.

[52] Steele, M.C. and Rosi, F.D. (1958) Thermal conductivity and thermoelectric power of germanium-silicon alloys. *Journal of Applied Physics*. 29 (11), 1517–1520.

[53] Liu, M.L., Huang, F.Q., Chen, L.D., and Chen, I.W. (2009) A wide-band-gap p -type thermoelectric material based on quaternary chalcogenides of Cu_2ZnSnQ_4(Q=S,Se). *Applied Physics Letters*. 94 (20), 46–49.

[54] Hicks, L.D. and Dresselhaus, M.S. (1993) Effect of quantum-well structures on the thermoelectric figure of merit. *Physical Review B*. 47 (19), 12727.

[55] Ohta, H., Kim, S., Mune, Y., Mizoguchi, T., Nomura, K., Ohta, S., Nomura, T., Nakanishi, Y., Ikuhara, Y., Hirano, M., Hosono, H., and Koumoto, K. (2007) Giant thermoelectric Seebeck coefficient of a two-dimensional electron gas in $SrTiO_3$. *Nature Materials*. 6 (2), 129.

[56] Mune, Y., Ohta, H., Koumoto, K., Mizoguchi, T., and Ikuhara, Y. (2007) Enhanced Seebeck coefficient of quantum-confined electrons in $SrTiO_3$/ $SrTi_{0.8}Nb_{0.2}O_3$ superlattices. *Applied Physics Letters*. 91 (19), 192105.

[57] Venkatasubramanian, R., Siivola, E., Colpitts, T., and O'Quinn, B. (2001) Thin-film thermoelectric devices with high room-temperature figures of merit. *Nature*. 413 (6856), 597.

[58] Winkler, M., Liu, X., Schürmann, U., König, J.D., Kienle, L., Bensch, W., and Böttner, H. (2012) Current status in fabrication, structural and transport property characterization, and theoretical understanding of Bi_2Te_3/Sb_2Te_3 superlattice systems. *Zeitschrift Fur Anorganische Und Allgemeine Chemie*. 638 (15), 2441–2454.

[59] Vaqueiro, P. and Powell, A. V. (2010) Recent developments in

nanostructured materials for high-performance thermoelectrics. *Journal of Materials Chemistry*. 20 (43), 9577–9584.

[60] Heikes, R.R. and Ure, R.W. (1961) Thermoelectricity: Science and Engineering Interscience. Interscience Publishers, New-York.

[61] Rosi, F.D., Hockings, E.F., and Lindenblad, N.E. (2003) Semiconductor materials for thermoelectric power generation. *Advanced Energy Conversion*. 1 151.

[62] Wood, C. (1988) Materials for thermoelectric energy conversion. *Reports on Progress in Physics*. 51 (4), 459–539.

[63] Poudel, B., Hao, Q., Ma, Y., Lan, Y., Minnich, A., Yu, B., Yan, X., Wang, D., Muto, A., Vashaee, D., Chen, X., Liu, J., Dresselhaus, M.S., Chen, G., and Ren, Z. (2008) High-thermoelectric performance of nanostructured bismuth antimony telluride bulk alloys. *Science*.

[64] Tang, X., Xie, W., Li, H., Zhao, W., Zhang, Q., and Niino, M. (2007) Preparation and thermoelectric transport properties of high-performance p-type Bi_2Te_3 with layered nanostructure. *Applied Physics Letters*.

[65] Wang, X.W., Lee, H., Lan, Y.C., Zhu, G.H., Joshi, G., Wang, D.Z., Yang, J., Muto, A.J., Tang, M.Y., Klatsky, J., Song, S., Dresselhaus, M.S., Chen, G., and Ren, Z.F. (2008) Enhanced thermoelectric figure of merit in nanostructured n-type silicon germanium bulk alloy. *Applied Physics Letters*. 93 (19), 193121.

[66] Joshi, G., Lee, H., Lan, Y., Wang, X., Zhu, G., Wang, D., Gould, R.W., Cuff, D.C., Tang, M.Y., Dresselhaus, M.S., Chen, G., and Ren, Z. (2008) Enhanced thermoelectric figure-of-merit in nanostructured p-type silicon germanium bulk alloys. *Nano Letters*. 8 (12), 4670–4674.

[67] Lalonde, A.D., Pei, Y., and Snyder, G.J. (2011) Reevaluation of $PbTe_{1-x}I_x$ as high performance n-type thermoelectric material. *Energy and Environmental Science*. 4 (6), 2090–2096.

[68] Pei, Y., Lalonde, A., Iwanaga, S., and Snyder, G.J. (2011) High thermoelectric figure of merit in heavy hole dominated PbTe. *Energy and Environmental Science*. 4 (6), 2085–2089.

[69] Skrabek, E.A. and Trimmer, D.S. (1995) Properties of the General TAGS System. in: D.M. Rowe (Ed.), CRC Handb. Thermoelectr., CRC, Boca Raton, pp. 267–275.

[70] Hsu, K.F. (2004) Cubic $AgPb_mSbTe_{2+m}$: Bulk Thermoelectric Materials with High Figure of Merit. *Science*. 303 (5659), 818–821.

[71] National Research Council (2015) Minerals, Critical Minerals, and the U.S. Economy. .

[72] Ge, Z.H., Zhao, L.D., Wu, D., Liu, X., Zhang, B.P., Li, J.F., and He, J. (2016) Low-cost, abundant binary sulfides as promising thermoelectric materials. *Materials Today*. 19 (4), 227–239.

[73] Slack, G.A. (1995) CRC Handbook of Thermoelectrics - CRC Press Book. in: Handb. Thermoelectr., .

[74] Maciá, E. (2015) Thermoelectric materials: advances and applications. 1st Editio Jenny Stanford Publishing, New-York.

[75] Deng, S., Saiga, Y., Suekuni, K., and Takabatake, T. (2011) Effect of Al substitution on the thermoelectric properties of the type VIII clathrate $Ba_8Ga_{16}Sn_{30}$. in: J. Electron. Mater., Springer US, pp. 1124–1128.

[76] Deng, S., Saiga, Y., Suekuni, K., and Takabatake, T. (2010) Enhancement of thermoelectric efficiency in type-VIII clathrate $Ba_8Ga_{16}Sn_{30}$ by Al substitution for Ga. *Journal of Applied Physics*. 108 (7), 073705.

[77] Saiga, Y., Du, B., Deng, S., Kajisa, K., and Takabatake, T. (2012) Thermoelectric properties of type-VIII clathrate $Ba_8Ga_{16}Sn_{30}$ doped with Cu. *Journal of Alloys and Compounds*. 537 303–307.

[78] Deng, S., Li, D.-C., Shen, L.-X., Hao, R.-T., and Takabatake, T. (2012) Sn-based type-VIII single-crystal clathrates with a large figure of merit. *Chinese Physics B*. 21 (1), 017401.

[79] Chen, Y., Du, B., Kajisa, K., and Takabatake, T. (2014) Effects of in substitution for Ga on the thermoelectric properties of type-VIII clathrate $Ba_8Ga_{16}S_{30}$ single crystals. *Journal of Electronic Materials*. 43 (6), 1916–1921.

[80] Caillat, T. and Fleurial, J.-P. (1998) Thermoelectric properties of the semiconducting Chevrel phase $Mo_2Re_4Se_8$. *Journal of Physics and Chemistry of Solids*. 59 (6–7), 1139–1144.

[81] Caillat, T., Fleurial, J.-P., and Snyder, G.J. (1999) Potential of Chevrel phases for thermoelectric applications. *Solid State Sciences*. 1 (7–8), 535–544.

[82] Tsubota, T., Ohtaki, M., and Eguchi, K. (2011) Thermoelectric Properties of

Chevrel-Type Sulfides AMo_6S_8. (A = Fe, Ni, Ag, Zn, Sn, Pb, Cu). *Journal of the Ceramic Society of Japan*. 107 (1248), 697–701.

[83] McGuire, M.A., Schmidt, A.M., Gascoin, F., Snyder, J.G., and DiSalvo, F.J. (2006) Thermoelectric and structural properties of a new Chevrel phase: $Ti_{0.3}Mo_5RuSe_8$. *Journal of Solid State Chemistry*. 179 (7), 2158–2163.

[84] Ohta, M., Obara, H., and Yamamoto, A. (2009) Preparation and Thermoelectric Properties of Chevrel-Phase $Cu_xMo_6S_8$. *Materials Transactions*. 50 (9), 2129–2133.

[85] Nishiate, H., Ohta, M., Yamamoto, A., Obara, H., Lee, C.H., and Ueno, K. (2011) Preparation of single-phase Pb-filled chevrel-phase sulfide and its thermoelectric properties. *Materials Transactions*. 52 (8), 1535–1538.

[86] Chevrel, R., Sergent, M., and Prigent, J. (1971) Sur de Nouvelles Phases Sulfurees Ternaires du Molybdene. *Journal of Solid State Chemistry*. 3 515–519.

[87] Robinson, L.M., Bain, R.L., Shriver, D.F., and Ellis, D.E. (1995) Effect of Coordination Environment on the Electronic Structure and Properties of Mo_6-Based Systems: A Density Functional Treatment. *Inorganic Chemistry*. 34 (22), 5588–5596.

[88] Cotton, F.A. and Stanley, G.G. (1978) Ground state electronic structures of some metal atom cluster compounds. *Chemical Physics Letters*. 58 (3), 450–453.

[89] Nunes, R.W., Mazin, I.I., and Singh, D.J. (1998) Theoretical search for Chevrel phase based thermoelectric materials. *Physical Review B*. 59 (12), 7969.

[90] Vaqueiro, P. (2010) Hybrid materials through linkage of chalcogenide tetrahedral clusters. *Dalton Transactions*. 39 (26), 5965–5972.

[91] Terasaki, I., Sasago, Y., and Uchinokura, K. (1997) Large thermoelectric power in $NaCoO_4$ single crystals. *Phys. Rev. B*. 56 (20), 12685.

[92] Fujita, K., Mochida, T., and Nakamura, K. (2001) High-temperature thermoelectric properties of $Na_xCoO_{2-\delta}$ single crystals. *Japanese Journal of Applied Physics, Part 1: Regular Papers and Short Notes and Review Papers*.

[93] Masset, A., Michel, C., Maignan, A., Hervieu, M., Toulemonde, O., Studer, F., Raveau, B., and Hejtmanek, J. (2000) Misfit-layered cobaltite with an anisotropic giant magnetoresistance in $Ca_3Co_4O_9$. *Physical Review B* -

Condensed Matter and Materials Physics. 62 (1), 166–175.

[94] Leligny, H., Grebille, D., Pérez, O., Masset, A.-C., Herveieu, M., Michel, C., and Raveau, B. (1999) A bismuth cobaltite with an intrinsically modulated misfit layer structure: $Bi_{0.87}SrO_{22}CoO_{21.8}$. *Comptes Rendus de l'Académie Des Sciences - Series IIC - Chemistry*. 2 (7–8), 409–414.

[95] Powell, A. V. and Vaqueiro, P. (2017) Chalcogenide thermoelectric materials. in: RSC Energy Environ. Ser., .

[96] Hicks, L.D., Harman, T.C., and Dresselhaus, M.S. (1993) Use of quantum-well superlattices to obtain a high figure of merit from nonconventional thermoelectric materials. *Applied Physics LettersMRS Online Proceedings Library Archive*. 326.

[97] Suekuni, K. and Takabatake, T. (2016) Research Update: Cu-S based synthetic minerals as efficient thermoelectric materials at medium temperatures. *APL Materials*. 4 (10), 104503.

[98] Moëlo, Y., Makovicky, E., Mozgova, N.N., Jambor, J.L., Cook, N., Pring, A., Paar, W., Nickel, E.H., Graeser, S., Karup-Møller, S., Balic-Žunic, T., Mumme, W.G., Vurro, F., Topa, D., Bindi, L., Bente, K., Shimizu, M., et al. (2008) Sulfosalt systematics: a review. Report of the sulfosalt sub-committee of the IMA Commission on Ore Mineralogy. *European Journal of Mineralogy*. 20 (1), 7–46.

[99] Dexter, M., Gao, Z., Bansal, S., Chang, C.-H., and Malhotra, R. (2018) Temperature, Crystalline Phase and Influence of Substrate Properties in Intense Pulsed Light Sintering of Copper Sulfide Nanoparticle Thin Films. *Scientific Reports*. 8 (1), 2201.

[100] Will, G., Hinze, E., and Abdelrahman, A.R.M. (2002) Crystal structure analysis and refinement of digenite, $Cu_{1.8}S$, in the temperature range 20 to 500 C under controlled sulfur partial pressure. *European Journal of Mineralogy*. 14 (3), 591–598.

[101] Chakrabarti, D.J. and Laughlin, D.E. (1983) The Cu-S (Copper-Sulfur) system. *Bulletin of Alloy Phase Diagrams*. 4 (3), 254.

[102] Ge, Z.H., Zhang, B.P., Chen, Y.X., Yu, Z.X., Liu, Y., and Li, J.F. (2011) Synthesis and transport property of $Cu_{1.8}S$ as a promising thermoelectric compound.

Chemical Communications. 47 (47), 12697–12699.

[103] Hirahara, E. (1951) The Physical Properties of Cuprous Sulfides-Semiconductors. *Journal of the Physical Society of Japan*. 6 (6), 422–427.

[104] Kanazawa, Y., Koto, K., and Morimoto, N. (1978) Bornite (Cu_5FeS_4): Stability and crystal structure of the intermediate form. *Canadian Mineralogist*. 16 (3), 397–404.

[105] Qiu, P., Zhang, T., Qiu, Y., Shi, X., and Chen, L. (2014) Sulfide bornite thermoelectric material: a natural mineral with ultralow thermal conductivity. *Energy and Environmental Science*. 7 (12), 4000–4006.

[106] Guélou, G., Powell, A. V., and Vaqueiro, P. (2015) Ball milling as an effective route for the preparation of doped bornite: Synthesis, stability and thermoelectric properties. *Journal of Materials Chemistry C*. 3 (40), 10624–10629.

[107] Pavan Kumar, V., Barbier, T., Lemoine, P., Raveau, B., Nassif, V., and Guilmeau, E. (2017) The crucial role of selenium for sulphur substitution in the structural transitions and thermoelectric properties of Cu_5FeS_4 bornite. *Dalton Transactions*. 46 (7), 2174–2183.

[108] Li, J., Tan, Q., and Li, J.F. (2013) Synthesis and property evaluation of $CuFeS_{2-x}$ as earth-abundant and environmentally-friendly thermoelectric materials. *Journal of Alloys and Compounds*. 551 143–149.

[109] Long, S.O.J., Powell, A. V., Vaqueiro, P., and Hull, S. (2018) High Thermoelectric Performance of Bornite through Control of the Cu(II) Content and Vacancy Concentration. *Chemistry of Materials*. 30 (2), 456–464.

[110] Wuensch, B.J. (1964) The crystal structure of tetrahedrite, $Cu_{12}Sb_4S_{13}$. *Zeitschrift Fur Kristallographie - New Crystal Structures*.

[111] Charlat, M. and Lévy, C. (1974) Substitutions multiples dans la serie tennantite-tetraedrite [Multiple substitutions in the tennantite-tetrahedrite series]. *Bull. Soc. Fr. Mineral. Cristallogr.* 97 241–250.

[112] Charlat, M. and Lévy, C. (1975) Influence des principales substitutions sur le parametre cristallin dans la serie tennantite-tetraedrite [Influence of main substitutions on the lattice constant in the tennantite-tetrahedrite series]. *Bull. Soc. Fr. Mineral. Cristallogr.* 98 152–158.

[113] Johnson, N.E., Craig, J.R., and Rimstidt, J.D. (1986) Compositional trends in

tetrahedrite. *Canadian Mineralogist*.

[114] Charnock, J.M., Garner, C.D., Pattrick, R.A.D., and Vaughan, D.J. (1989) Coordination sites of metals in tetrahedrite minerals determined by EXAFS. *Journal of Solid State Chemistry*. 82 (2), 279–289.

[115] Lu, X., Morelli, D.T., Xia, Y., Zhou, F., Ozolins, V., Chi, H., Zhou, X., and Uher, C. (2013) High Performance Thermoelectricity in Earth-Abundant Compounds Based on Natural Mineral Tetrahedrites. *Advanced Energy Materials*. 3 (3), 342–348.

[116] Suekuni, K., Tsuruta, K., Kunii, M., Nishiate, H., Nishibori, E., Maki, S., Ohta, M., Yamamoto, A., and Koyano, M. (2013) High-performance thermoelectric mineral $Cu_{12-x}Ni_xSb_4S_{13}$ tetrahedrite. *Journal of Applied Physics*. 113 (4), 043712.

[117] Weller, D.P. and Morelli, D.T. (2017) Rapid synthesis of zinc and nickel co-doped tetrahedrite thermoelectrics by reactive spark plasma sintering and mechanical alloying. *Journal of Alloys and Compounds*. 710 794–799.

[118] Harish, S., Sivaprahasam, D., Battabyal, M., and Gopalan, R. (2016) Phase stability and thermoelectric properties of $Cu_{10.5}Zn_{1.5}Sb_4S_{13}$ tetrahedrite. *Journal of Alloys and Compounds*. 667 323–328.

[119] Lu, X., Morelli, D.T., Xia, Y., and Ozolins, V. (2015) Increasing the Thermoelectric Figure of Merit of Tetrahedrites by Co-Doping with Nickel and Zinc. *Chemistry of Materials*. 27 (2), 408–413.

[120] Battiston, S., Fanciulli, C., Fiameni, S., Famengo, A., Fasolin, S., and Fabrizio, M. (2017) One step synthesis and sintering of Ni and Zn substituted tetrahedrite as thermoelectric material. *Journal of Alloys and Compounds*. 702 75–83.

[121] Chetty, R., Bali, A., Naik, M.H.H., Rogl, G., Rogl, P., Jain, M., Suwas, S., and Mallik, R.C.C. (2015) Thermoelectric properties of Co substituted synthetic tetrahedrite. *Acta Materialia*. 100 266–274.

[122] Barbier, T., Rollin-Martinet, S., Lemoine, P., Gascoin, F., Kaltzoglou, A., Vaqueiro, P., Powell, A. V., and Guilmeau, E. (2016) Thermoelectric Materials: A New Rapid Synthesis Process for Nontoxic and High-Performance Tetrahedrite Compounds. *Journal of the American Ceramic Society*. 99 (1),

51–56.

[123] Bouyrie, Y., Candolfi, C., Ohorodniichuk, V., Malaman, B., Dauscher, A., Tobola, J., and Lenoir, B. (2015) Crystal structure, electronic band structure and high-temperature thermoelectric properties of Te-substituted tetrahedrites $Cu_{12}Sb_{4-x}Te_xS_{13}$ ($0.5 \leq x \leq 2.0$). *Journal of Materials Chemistry C*. 3 (40), 10476–10487.

[124] Vaqueiro, P., Guélou, G., Kaltzoglou, A., Smith, R.I., Barbier, T., Guilmeau, E., and Powell, A. V. (2017) The Influence of Mobile Copper Ions on the Glass-Like Thermal Conductivity of Copper-Rich Tetrahedrites. *Chemistry of Materials*.

[125] Lemoine, P., Bourgès, C., Barbier, T., Nassif, V., Cordier, S., and Guilmeau, E. (2017) High temperature neutron powder diffraction study of the $Cu_{12}Sb_4S_{13}$and $Cu_4Sn_7S_{16}$ phases. *Journal of Solid State Chemistry*. 247 (October 2016), 83–89.

[126] Barbier, T., Lemoine, P., Gascoin, S., Lebedev, O.I., Kaltzoglou, A., Vaqueiro, P., Powell, A. V., Smith, R.I., and Guilmeau, E. (2015) Structural stability of the synthetic thermoelectric ternary and nickel-substituted tetrahedrite phases. *Journal of Alloys and Compounds*. 634 253–262.

[127] Hall, S.R. and Stewart, J.M. (1973) The crystal structure refinement of chalcopyrite, $CuFeS_2$. *Acta Crystallographica Section B Structural Crystallography and Crystal Chemistry*. 29 (3), 579–585.

[128] Tsujii, N. and Mori, T. (2013) High thermoelectric power factor in a carrier-doped magnetic semiconductor $CuFeS_2$. *Applied Physics Express*. 6 (4), 043001.

[129] Tsujii, N. (2013) Possible enhancement of thermoelectric properties by use of a magnetic semiconductor: Carrier-doped chalcopyrite $Cu_{1-x}Fe_{1+x}S_2$. *Journal of Electronic Materials*. 42 (7), 1974–1977.

[130] Tsujii, N., Mori, T., and Isoda, Y. (2014) Phase stability and thermoelectric properties of $CuFeS_2$-based magnetic semiconductor. *Journal of Electronic Materials*. 43 (6), 2371–2375.

[131] Li, Y., Zhang, T., Qin, Y., Day, T., Jeffrey Snyder, G., Shi, X., and Chen, L. (2014) Thermoelectric transport properties of diamond-like $Cu_{1-x}Fe_{1+x}S_2$ tetrahedral compounds. *Journal of Applied Physics*. 116 (20), 203705.

[132] Carr, W.D. and Morelli, D.T. (2016) The Thermoelectric Properties and Solubility Limit of $CuFeS_{2(1-x)}Se_{2x}$. *Journal of Electronic Materials*. 116 (20), 203705.

[133] Liang, D., Ma, R., Jiao, S., Pang, G., and Feng, S. (2012) A facile synthetic approach for copper iron sulfide nanocrystals with enhanced thermoelectric performance. *Nanoscale*. 4 (20), 6265–6268.

[134] Verma, S., Singh, M., Ahuja, D., Shimose, H., Nishino, S., Miyata, M., Mott, D., Koyano, M., and Maenosono, S. (2014) Chalcopyrite nanocomposite material for sustainable thermoelectrics. *Japanese Journal of Applied Physics*.

[135] Goto, Y., Naito, F., Sato, R., Yoshiyasu, K., Itoh, T., Kamihara, Y., and Matoba, M. (2013) Enhanced thermoelectric figure of merit in stannite-kuramite solid solutions $Cu_{2+x}Fe_{1-x}SnS_{4-y}$ (x = 0-1) with anisotropy lowering. *Inorganic Chemistry*. 52 (17), 9861–9866.

[136] Spry, P.G., Merlino, S., Su Wang, Xiaomao Zhang, and Buseck, P.R. (1994) New occurrences and refined crystal chemistry of colusite, with comparisons to arsenosulvanite. *American Mineralogist*.

[137] Frank-Kamenetskaya, O. V., Rozhdestvenskaya, I. V., and Yanulova, L.A. (2002) New data on the crystal structures of colusites and arsenosulvanites. *Journal of Structural Chemistry*. 43 (1), 89–100.

[138] Suekuni, K., Kim, F.S., Nishiate, H., Ohta, M., Tanaka, H.I., and Takabatake, T. (2014) High-performance thermoelectric minerals: Colusites $Cu_{26}V_2M_6S_{32}$ (M = Ge, Sn). *Applied Physics Letters*. 105 (13), 132107.

[139] Kikuchi, Y., Bouyrie, Y., Ohta, M., Suekuni, K., Aihara, M., and Takabatake, T. (2016) Vanadium-free colusites $Cu_{26}A_2Sn_6S_{32}$ (A = Nb, Ta) for environmentally friendly thermoelectrics. *Journal of Materials Chemistry A*. 4 (39), 15207–15214.

[140] Bouyrie, Y., Ohta, M., Suekuni, K., Jood, P., and Takabatake, T. (2018) Addition of Co, Ni, Fe and their role in the thermoelectric properties of colusite $Cu_{26}Nb_2Ge_6S_{32}$. *Journal of Alloys and Compounds*. 735 1838–1845.

[141] Bourgès, C., Bouyrie, Y., Supka, A.R., Al Rahal Al Orabi, R., Lemoine, P., Lebedev, O.I., Ohta, M., Suekuni, K., Nassif, V., Hardy, V., Daou, R., Miyazaki, Y., Fornari, M., and Guilmeau, E. (2018) High-Performance Thermoelectric Bulk

Colusite by Process Controlled Structural Disordering. *Journal of the American Chemical Society*. 140 (6), 2186–2195.

[142] Pavan Kumar, V., Supka, A.R., Lemoine, P., Lebedev, O.I., Raveau, B., Suekuni, K., Nassif, V., Al Rahal Al Orabi, R., Fornari, M., and Guilmeau, E. (2019) High Power Factors of Thermoelectric Colusites $Cu_{26}T_2Ge_6S_{32}$ (T = Cr, Mo, W): Toward Functionalization of the Conductive "Cu–S" Network. *Advanced Energy Materials*. 9 (6), 1803249.

[143] De Jong, W.E. (1930) Die Kristallstruktur von Germanit. *Zeitschrift Fur Kristallographie*. 73 176–180.

[144] Sclar, C.B. and Geier, B.H. (1957) The paragenetic relationships of germanite and renierite from Tsumeb, South-West-Africa. *Economic Geology*. 52 (6), 612–631.

[145] Lévy, C. (1966) Contribution a la mineralogie des sulfures de cuivre du type Cu_3XS_4. *Mem. Bur. Rech. Géol. Minières*. 54 3–178.

[146] Springer, G. (1969) Microanalytical investigation into germanite, renierite, briartite and gallite. *Neues Jahrbuch Für Mineralogie*. 3 435–440.

[147] Tettenhorst, R.T. and Corbato, C.E.E. (1984) Crystal Structure of Germanite, $Cu_{26}Ge_4Fe_4S_{32}$, Determined by Powder X-Ray Diffraction. *American Mineralogist*. 69 (9–10), 943–947.

[148] Spiridonov, E.M. (1987) sostave germanita (On the composition of germanite). *Doklady Akademii Nauk SSSR*. 295 (2), 477–481.

[149] Spiridonov, E.M., Kachalovskaya, V.M., Kovachev, V. V., and Krapiva, L. V. (1992) Germanokolysit $Cu_{26}V_2(Ge,As)_6S_{32}$- novyi mineral (Germanocolusite, $Cu_{26}V_2(Ge,As)_6S_{32}$'a new mineral). *Vestnik Moskovskogo Universiteta*. (6), 50–54.

[150] Nenasheva, S.N. (2003) On the chemical composition of germanite. *New Data on Minerals*. 38 34–40.

[151] Pavan Kumar, V., Paradis-Fortin, L., Lemoine, P., Caignaert, V., Raveau, B., Malaman, B., Le Caër, G., Cordier, S., and Guilmeau, E. (2017) Designing a Thermoelectric Copper-Rich Sulfide from a Natural Mineral: Synthetic Germanite $Cu_{22}Fe_8Ge_4S_{32}$. *Inorganic Chemistry*. 56 (21), 13376–13381.

[152] Bourgès, C., Lemoine, P., Lebedev, O.I., Daou, R., Hardy, V., Malaman, B., and Guilmeau, E. (2015) Low thermal conductivity in ternary $Cu_4Sn_7S_{16}$

compound. *Acta Materialia*. 97 180–190.

[153] Barbier, T., Lemoine, P., Martinet, S., Eriksson, M., Gilmas, M., Hug, E., Guélou, G., Vaqueiro, P., Powell, A. V., and Guilmeau, E. (2016) Up-scaled synthesis process of sulphur-based thermoelectric materials. *RSC Advances*. 6 (12), 10044–10053.

[154] Yang, J. and Caillat, T. (2006) Thermoelectric Materials for Space and Automotive Power Generation. *MRS Bulletin*. 31 (03), 224–229.

[155] Chen, X., Wada, H., Sato, A., and Mieno, M. (1998) Synthesis, Electrical Conductivity, and Crystal Structure of $Cu_4Sn_7S_{16}$ and Structure Refinement of Cu_2SnS_3. *Journal of Solid State Chemistry*. 139 (1), 144–151.

[156] Jemetio, J.-P.F., Zhou, P., and Kleinke, H. (2006) Crystal structure, electronic structure and thermoelectric properties of $Cu_4Sn_7S_{16}$. *Journal of Alloys and Compounds*. 417 (1–2), 55–59.

[157] Yund, R.A. and Kullerud, G. (1966) Thermal stability of assemblages in the Cu-Fe-S system. *Journal of Petrology*. 7 (3), 454–488.

[158] Cabri, L.J. (1973) New data on phase relations in the Cu-Fe-S system. *Economic Geology*. 68 (4), 443–454.

[159] Stephens, P.W. (1999) Phenomenological model of anisotropic peak broadening in powder diffraction. *Journal of Applied Crystallography*. 32 (2), 281–289.

[160] Gialanella, S., Girardi, F., Ischia, G., Lonardelli, I., Mattarelli, M., and Montagna, M. (2010) On the goethite to hematite phase transformation. *Journal of Thermal Analysis and Calorimetry*. 102 (3), 867–873.

[161] Calamiotou, M., Lampakis, D., Zhigadlo, N.D., Katrych, S., Karpinski, J., Fitch, A., Tsiaklagkanos, P., and Liarokapis, E. (2016) Local lattice distortions vs. structural phase transition in $NdFeAsO_{1-x}F_x$. *Physica C: Superconductivity and Its Applications*. 527 55–62.

[162] Suekuni, K., Shimizu, Y., Nishibori, E., Kasai, H., Saito, H., Yoshimoto, D., Hashikuni, K., Bouyrie, Y., Chetty, R., Ohta, M., Guilmeau, E., Takabatake, T., Watanabe, K., and Ohtaki, M. (2019) Atomic-scale phonon scatterers in thermoelectric colusites with a tetrahedral framework structure. *Journal of Materials Chemistry A*. 7 (1), 228–235.

[163] Bernstein, L.R. (1986) Renierite, $Cu_{10}ZnGe_2Fe_4S_{16}$-$Cu_{11}GeAsFe_4S_{16}$: a coupled solid solution series. *American Mineralogist*. 71 (1–2), 210–221.

[164] Doverspike, K., Kershaw, R., and Dwight, K. (1988) Preparation and properties of the system $Cu_2Zn_{1-x}Fe_xGeS_4$. *Materials Research Bulletin*. 23 (7), 959–964.

[165] Schafer, W. and Nitsche, R. (1974) Tetrahedral quaternary chalcogenides of the type Cu_2-II-IV-S_4(Se_4). *Material Research Bulletin*. 9 (5), 645–654.

[166] Guen, L. and Glaunsinger, W. (1979) Physical properties of the quarternary chalcogenides Cu_2IBIICIVX_4 (BII = Zn, Mn, Fe, Co; CIV = Si, Ge, Sn; X = S, Se). *Materials Research Bulletin*. 14 (4), 463–467.

[167] Guen, L. and Glaunsinger, W. (1980) Electrical, magnetic, and EPR studies of the quaternary chalcogenides Cu_2AIIBIVX_4 prepared by iodine transport. *Journal of Solid State Chemistry*. 35 (1), 10–21.

[168] Wintenberger, M. (1979) Etude de la structure cristallographique et magnetique de Cu_2FeGeS_4 et remarque sur la structure magnetique de Cu_2MnSnS_4. *Materials Research Bulletin*. 14 (9), 1195–1202.

[169] Quintero, M., Marquina, J., Quintero, E., Moreno, E., Álvarez, S., Rincón, C., Grima, P., Bocaranda, P., Rivero, D., Henao, J.A., and Macías, M.A. (2014) X-ray diffraction analysis of stannite, wurtz-stannite and pseudo-cubic quaternary compounds by rietveld method. *Revista Mexicana de Fisica*. 60 (2), 16–175.

[170] Bernstein, L.R., Reichel, D.G., and Merlino, S. (1989) Renierite crystal structure refined from Rietveld analysis of powder neutron-diffraction data. *American Mineralogist*. 74 (9–10), 1177–1181.

[171] Suryanarayana, C. (2001) Mechanical alloying and milling. *Progress in Materials Science*. 46 (1–2), 1–184.

[172] Slack, G.A. (1972) Thermal Conductivity of II-VI Compounds and Phonon Scattering by Fe^{2+} Impurities. *Physical Review B*. 6 (10), 3791–3800.

[173] Ioffe, A.V. and Ioffe, A.F. (1960) Thermal conductivity of semiconductor solid solutions. *Soviet Physics-Solid State*. 2 (5), 719–728.

[174] Le Caër, G. and Brand, R.A. (1998) General models for the distributions of electric field gradients in disordered solids. *Journal of Physics: Condensed Matter*. 10 (47), 10715–10774.

[175] Hightower, A., Delcroix, P., Caër, G. Le, Huang, C.K., Ratnakumar, B. V., Ahn,

C.C., and Fultz, B. (2000) ^{119}Sn Mössbauer spectrometry study of Li-SnO anode materials for Li-ion cells. *Journal of the Electrochemical Society*. 147 (1), 1–8.

[176] Imbert, P., Varret, F., and Wintenberger, M. (1973) Etude par effet Mössbauer de la briartite (Cu_2FeGeS_4). *Journal of Physics and Chemistry of Solids*. 34 (10), 1675–1682.

[177] Suekuni, K., Kim, F.S., and Takabatake, T. (2014) Tunable electronic properties and low thermal conductivity in synthetic colusites $Cu_{26-x}Zn_xV_2M_6S_{32}$ ($x \leq 4$, M = Ge, Sn). *Journal of Applied Physics*. 116 (6), 063706.

[178] Pavan Kumar, V., Barbier, T., Caignaert, V., Raveau, B., Daou, R., Malaman, B., Caër, G. Le, Lemoine, P., and Guilmeau, E. (2017) Copper Hyper-Stoichiometry: The Key for the Optimization of Thermoelectric Properties in Stannoidite $Cu_{8+x}Fe_{3-x}Sn_2S_{12}$. *The Journal of Physical Chemistry C*. 121 (30), 16454–16461.

[179] Pavan Kumar, V., Supka, A.R., Lemoine, P., Lebedev, O.I., Raveau, B., Suekuni, K., Nassif, V., Al Rahal Al Orabi, R., Fornari, M., and Guilmeau, E. (2019) High Power Factors of Thermoelectric Colusites $Cu_{26}T_2Ge_6S_{32}$ (T = Cr, Mo, W): Toward Functionalization of the Conductive "Cu–S" Network. *Advanced Energy Materials*. 9 (6), 1803249.

[180] Kovalenker, V. A. Evstigneeva, T.L., Malov, V.S., Trubkin, N. V., Gorshkov, A.I., and Geinke, V.R. (1984) Nekrasovite $Cu_{26}V_2Sn_6S_{32}$ –a new mineral of the colusite group. *Mineralogicheskii Zhurnal*. 1 (6), 88–97.

[181] Kim, F.S., Suekuni, K., Nishiate, H., Ohta, M., Tanaka, H.I., and Takabatake, T. (2016) Tuning the charge carrier density in the thermoelectric colusite. *Journal of Applied Physics*. 119 (17), 175105.

[182] He, Y., Day, T., Zhang, T., Liu, H., Shi, X., Chen, L., and Snyder, G.J. (2014) High thermoelectric performance in non-toxic earth-abundant copper sulfide. *Advanced Materials*. 26 (23), 3974–3978.

[183] Goto, Y., Sakai, Y., Kamihara, Y., and Matoba, M. (2015) Effect of Sn-substitution on thermoelectric properties of copper-based sulfide, famatinite Cu_3SbS_4. *Journal of the Physical Society of Japan*. 84 (4), 044706.

[184] Wei, T.R., Wang, H., Gibbs, Z.M., Wu, C.F., Snyder, G.J., and Li, J.F. (2014)

Thermoelectric properties of Sn-doped p-type Cu_3SbSe_4: A compound with large effective mass and small band gap. *Journal of Materials Chemistry A*. 2 (33), 13527–13533.

[185] Zeier, W.G., Zhu, H., Gibbs, Z.M., Ceder, G., Tremel, W., and Snyder, G.J. (2014) Band convergence in the non-cubic chalcopyrite compounds Cu_2MGeSe_4. *Journal of Materials Chemistry C*. 2 (47), 10189–10194.

[186] Klemens, P.G. (1955) The scattering of low-frequency lattice waves by static imperfections. *Proceedings of the Physical Society. Section A*. 68 (12), 1113–1128.

[187] Abeles, B. (1963) Lattice thermal conductivity of disordered semiconductor alloys at high temperatures. *Physical Review*. 131 (5), 1906–1911.

[188] Sears, V.F. (1992) Neutron scattering lengths and cross sections. *Neutron News*. 3 (3), 26–37.

[189] Cromer, D.T. and Liberman, D.A. (1981) Anomalous dispersion calculations near to and on the long-wavelength side of an absorption edge. *Acta Crystallographica Section A: Crystal Physics, Diffraction, Theoretical and General Crystallography*. 37 (2), 267–268.

[190] Brennan, S. and Cowan., P.L. (1992) A suite of programs for calculating X-ray absorption, reflection and diffraction performance for a variety of materials at arbitrary wavelengths. *Review of Scientific Instruments*. 63 (1), 850–853.

[191] Kronig, R. de L. and Kramers, H.A. (1928) Zur Theorie der Absorption und Dispersion in den Röntgenspektren. *Zeitschrift Für Physik*. 48 (3–4), 174–179.

[192] Bancroft, G.M. (1973) Mössbauer Spectroscopy: An Introduction for Inorganic Chemists and Geochemists. Halsted Press, New York.

[193] Goldanskii, V.I. and Makarov, E.F. (1968) Fundamentals of gamma-resonance spectroscopy. in: Chem. Appl. Mössbauer Spectrosc., Academic Press New York, pp. 1–113.

[194] Hanh, T., Ed. (2006) Space group 218. in: Int. Tables Crystallogr. Vol. A, 5th ed., Springer, pp. 664–665.

[195] Shannon, R.D. (1976) Revised effective ionic radii and systematic studies of interatomic distances in halides and chalcogenides. *Acta Crystallographica Section A*. 32 (5), 751–767.

[196] Belissont, R., Munoz, M., Boiron, M.-C., Luais, B., and Mathon, O. (2016) Distribution and oxidation state of Ge, Cu and Fe in sphalerite by u-XRF and K-edge u-XANES: insights into Ge incorporation, partitioning and isotopic fractionation. *Geochimica et Cosmochimica Acta*. 177 298–314.

[197] Spiridonov, E.M. (2003) Maikainite $Cu_{20}(Fe, Cu)_6Mo_2Ge_6S_{32}$ and ovamboite $Cu_{20}(Fe, Cu, Zn)_6W_2Ge_6S_{32}$: New minerals in massive sulfide base metal ores. *Doklady Earth Sciences*. 393 (9), 1329–1332.

[198] Shestopalov, M.A., Ledneva, A.Y., Cordier, S., Hernandez, O., Potel, M., Roisnel, T., Naumov, N.G., and Perrin, C. (2011) Tetrahedral Mo_4clusters as building blocks for the design of clathrate-related giant frameworks. *Angewandte Chemie - International Edition*. 50 (32), 7300–7303.

[199] Dolyniuk, J.-A., Owens-Baird, B., Wang, J., Zaikina, J. V., and Kovnir, K. (2016) Clathrate thermoelectrics. *Materials Science and Engineering: R*. 108 1–46.

[200] Perrin, C., Sergent, M., Le Traon, F., and Le Traon, A. (1978) Nouveaux thiochlorures de molybdène(II): $Mo_6Cl_{10}Y$ (Y = S, Se, Te): Structure et propriétés magnétiques et électriques. *Journal of Solid State Chemistry*. 25 (2), 197–204.

[201] Potel, M., Chevrel, R., Sergent, M., Armici, J.C., and Decroux, M. (1980) New pseudo-one-dimensional Metals: $M_2Mo_6Se_6$ (M= Na, In, K, Tl), $M_2Mo_6S_6$ (M= K, Rb, Cs), $M_2Mo_6Te_6$ (M= In, Tl). *Journal of Solid State Chemistry*. 35 (2), 286–290.

[202] Lepetit, R., Monceau, P., Potel, M., Gougeon, P., and Sergent, M. (1984) Superconductivity of the Linear Chain Compound $TI_2Mo_6Se_6$. *Journal of Low Temperature Physics*. 56 (3–4), 219–235.

[203] Tarascon, J.M., Di Salvo, F.J., Waszczak, J. V., and Hull, G.W. (1985) Synthesis and peculiar properties of $InMo_6S_{8-x}Se_x$,$TlMo_6S_{8-x}Se_x$ and $Hg_yMo_6S_{8-x}Se_x$. *Physical Review B*. 31 (2), 1012–1021.

[204] Tarascon, J.M., DiSalvo, F.J., Murphy, D.W., Hull, G., and Waszczak, J. V. (2002) New superconducting ternary molybdenum chalcogenides $InMo_6Se_8$,$T_1Mo_6S_{86}$, and $T_1Mo_6Se_8$. *Physical Review B*. 29 (1), 172–180.

[205] Even-Boudjada, S., Burel, L., Chevrel, R., and Sergent, M. (1998) New synthesis route of $PbMo_6S_8$ superconducting chevrel phase from ultrafine

precursor mixtures: II. PbS, Mo_6S_8, and Mo powders. *Materials Research Bulletin*. 33 (2), 237–252.

[206] Chevrel, R., Sergent, M., and Prigent, J. (1974) Un nouveau sulfure de molybdene : Mo_3S_4 preparation, proprietes et structure cristalline. *Materials Research Bulletin*. 9 (11), 1487–1498.

[207] Tsuge, K. (1996) Syntheses and structures of tetranuclear cluster complexes of molybdenum $[Mo_4(\mu_3\text{-}S)_2(\mu_2\text{-}S)\ 4X2\text{-}(PMe_3)_6]$ (X= SH, Cl, Br, I, SCN). *Journal of Cluster Science*. 7 (3), 407–421.

[208] Saito, G., Hosoda, H., Yoshida, Y., Hagiwara, J., Nishimura, K., Yamochi, H., Otsuka, A., Hiramatsu, T., Shimazaki, Y., Kirakci, K., Cordier, S., and Perrin, C. (2012) Synthesis and properties of charge-transfer solids with cluster units $[Mo_6X_{14}]$ 2- (X = Br, I). *Journal of Materials Chemistry*. 22 (37), 19774–19791.

[209] Cordier, S., Grasset, F., Molard, Y., Amela-Cortes, M., Boukherroub, R., Ravaine, S., Mortier, M., Ohashi, N., Saito, N., and Haneda, H. (2015) Inorganic Molybdenum Octahedral Nanosized Cluster Units, Versatile Functional Building Block for Nanoarchitectonics. *Journal of Inorganic and Organometallic Polymers and Materials*. 25 (2), 189–204.

[210] Saito, T. (1996) Group 6 Metal Chalcogenide Cluster Complexes and their Relationships to Solid-State Cluster Compounds. in: Adv. Inorg. Chem., pp. 45–91.

[211] Saito, N., Lemoine, P., Dumait, N., Amela-Cortes, M., Paofai, S., Roisnel, T., Nassif, V., Grasset, F., Wada, Y., Ohashi, N., and Cordier, S. (2017) From $Cs_2Mo_6Cl_{14}$ to $Cs_2Mo_6Cl_{14}{\cdot}H_2O$ and Vice Versa: Crystal Chemistry Investigations. *Journal of Cluster Science*. 28 (2), 773–798.

[212] Kirakci, K., Cordier, S., and Perrin, C. (2005) Synthesis and characterization of $Cs_2Mo_6X_{14}$ (X = Br or I) hexamolybdenum cluster halides: Efficient Mo_6 cluster precursors for solution chemistry syntheses. *Zeitschrift Fur Anorganische Und Allgemeine Chemie*. 631 (2–3), 411–416.

[213] Saito, N., Wada, Y., Lemoine, P., Cordier, S., Grasset, F., Ohsawa, T., Saito, N., Cross, J.S., and Ohashi, N. (2016) Theoretical and experimental determination of the crystal structures of cesium-molybdenum chloride. *Japanese Journal of Applied Physics*. 55 (7), 075502.

[214] Bruker AXS Inc (2006) M86-E01078 APEX2 User Manual. in: M86-E01078

APEX2 User Man., Bruker AXS Inc, Madison.

[215] Rodríguez-Carvajal, J. (1993) Recent advances in magnetic structure determination by neutron powder diffraction. *Physica B: Condensed Matter*. 192 (1–2), 55–69.

[216] Roisnel, T. and Rodríguez-Carvajal, J. (2001) WinPLOTR: A windows tool for powder diffraction pattern analysis. *Materials Science Forum*. 378 (1), 118–123.

[217] Le Bail, A., Duroy, H., and Fourquet, J.L. (1988) Ab-initio structure determination of $LiSbWO_6$ by X-ray powder diffraction. *Materials Research Bulletin*. 23 (3), 447–452.

Abstract: Germanite derivative materials: synthesis, crystallographic structure from multi-scale characterizations and thermoelectric properties

The work presented in this Ph.D. thesis deals with the synthesis, the structural and electronic properties characterization of the $Cu_{22}Fe_8Ge_4S_{32}$ copper sulfide, a material derived of the germanite mineral with promising thermoelectric properties. The first two chapters are dedicated to the optimization of the thermoelectric properties. The last chapter is an in-depth structural study of $Cu_{22}Fe_8Ge_4S_{32}$. First, the specific synthesis conditions to yield a ''pure'' germanite sample by sealed tube are investigated by the means of in situ reactions. Then, two different powder synthesis approaches are compared, namely mechanical alloying and conventional sealed tube synthesis, combined with two different densification methods: spark plasma sintering and hot pressing. This study drags attention to the process impact on the transport properties of complex Cu-based sulfides. Second, the series of compounds $Cu_{22-x}Zn_xFe_8Ge_4S_{32}$ ($0 \leq x \leq 2$) and $Cu_{22}Fe_8Ge_{4-x}Sn_xS_{32}$ ($0 \leq x \leq 4$) were investigated in the hope to enhance the TE properties through enhanced phonon scattering due to differences in atomic mass. In fact, in addition to lowering the κ_{Latt}, the Cu by Zn substitution in $Cu_{22-x}Zn_xFe_8Ge_4S_{32}$ leads to a decrease in the concentration of hole carriers. In addition, a reduction of $\kappa_{Latt}$is observed with the Sn-incorporation due to point defect scattering enhancement of the heat carrying phonons as a result of mass, size, and bonding strength disparities. Finally, a new structural model for synthetic germanite was proposed with respect to the space group and lattice parameter of the mineral material, $P\bar{4}3n$ and $a \approx 10.595$ Å. The crystal structure is proposed based on the complementarity from powder and single crystal XRD, ^{57}Fe Mössbauer spectroscopy and resonant scattering. The originality of this work lies in the experimental approach that was developed to overcome the inherent complexity of germanite cationic distribution.
Keywords: thermoelectricity, complex structure, germanite, $Cu_{22}Fe_8Ge_4S_{32}$, sphalerite, quaternary Cu-S

Résumé: Matériaux dérivés de la germanite: synthèse, structure cristallographique à partir de caractérisations multi-échelles et propriétés thermoélectriques

Le travail présenté dans cette thèse porte sur la synthèse, la caractérisation des propriétés structurelles et électroniques du sulfure de cuivre $Cu_{22}Fe_8Ge_4S_{32}$, un matériau dérivé de la germanite ayants des propriétés thermoélectriques prometteuses. Les deux premiers chapitres sont consacrés à l'optimisation des propriétés thermoélectriques par différentes approches. Le dernier chapitre est une étude structurelle approfondie de la germanite $Cu_{22}Fe_8Ge_4S_{32}$. Premièrement, les conditions spécifiques de la synthèse permettant de produire un échantillon ''pure'' de germanite par tube scellé sont examinées par le biais de réactions *in situ*. Ensuite, deux approches différentes de synthèse sont comparées, à savoir l'alliage mécanique et la synthèse en tube scellé, combinées à deux méthodes de densification différentes: le frittage SPS et le pressage à chaud. Deuxièmement, les séries de composés $Cu_{22-x}Zn_xFe_8Ge_4S_{32}$ ($0 \leq x \leq 2$) et $Cu_{22}Fe_8Ge_{4-x}Sn_xS_{32}$ ($0 \leq x \leq 4$) ont été étudiées dans l'espoir d'améliorer les propriétés thermoélectriques en augmentant la diffusions des phonons. En plus de la diminution de la κ_{Latt}, l'augmentation de la concentration en Zn dans le réseau de cuivre entraîne une diminution de la concentration en trous. De plus, l'incorporation de Sn diminue la κ_{Latt} en augmentant la diffusion des phonons par des défauts ponctuels due à des disparités de masse, de taille et de force de liaison. Enfin, un nouvelle structure crystalline pour la germanite synthétique a été proposé en conservant le groupe d'espace et le paramètre de maille du matériau minéral ($P\bar{4}3n$ and $a \approx 10.595$ Å). La détermination de la structure cristalline a été possible par la complémentarité des techniques de DRX sur poudre et monocristal, de spectroscopie Mössbauer ^{57}Fe et de diffusion résonante. L'originalité de ce travail réside dans l'approche expérimentale développée pour surmonter la complexité inhérente à la distribution cationique de germanite.
Mots clés : thermoélectricité, structure complexe, germanite, $Cu_{22}Fe_8Ge_4S_{32}$, sphalérite, Cu-S quaternaire